University of Pennsylvania
ScholarlyCommons

Publicly Accessible Penn Dissertations

Summer 8-14-2009

Multiscale Modeling of Electrocatalysis

Liang Qi
University of Pennsylvania, liangqi@seas.upenn.edu

Follow this and additional works at: http://repository.upenn.edu/edissertations

 Part of the Materials Chemistry Commons, Other Materials Science and Engineering Commons, and the Physical Chemistry Commons

Recommended Citation
Qi, Liang, "Multiscale Modeling of Electrocatalysis" (2009). *Publicly Accessible Penn Dissertations*. 14.
http://repository.upenn.edu/edissertations/14

This paper is posted at ScholarlyCommons. http://repository.upenn.edu/edissertations/14
For more information, please contact libraryrepository@pobox.upenn.edu.

Multiscale Modeling of Electrocatalysis

Abstract
In proton-exchange-membrane (PEM) fuel cells, electrochemical oxygen reduction reaction (ORR) on the cathode is a critical step at which large energy loss occurs. Theoretical tools at different scales are discussed in this thesis in order to find ORR catalysts with both higher activity and better durability than current Pt and Pt alloys. For catalytic activity, a relatively simple model reaction, ORR by hydrogen molecule under ultra-high-vacuum (UHV) conditions, is studied by first-principles methods on various metallic surfaces, which shows that good catalytic activities of Pt and its alloys originate from moderate adsorption strengths for atoms and molecules involved in the reaction. Then first-principles methods are also applied to study the reaction mechanisms of electrochemical ORR: detailed analyses in the electronic structures of ORR intermediates confirm that all the electron transfers in ORR occur through proton-coupled electron transfer (PCET) mechanism, which is accomplished by proton transfer along hydrogen-bond network from hydrated proton (hydronium) to ORR intermediates on the surface. Furthermore, first-principles methods are also used to search and design new alloy surfaces with optimal activity based on a simple kinetic model. However, the inaccuracy of this simple model makes a comprehensive multiscale ORR model necessary. Thus, a reaction network of ORR elementary steps on limited surface sites is built, and the steady-state solutions provide current density j at given electrode potential U; then a multiscale model of electrode-electrolyte interfacial structure is proposed for function U (σM), where σM is excess surface electron density on metallic electrode; finally, we discuss the principles to achieve a self-consistent multiscale ORR model to output both U and current I to the external circuit. For the stability of Pt as catalyst, we study its surface oxide formation and surface adatom diffusion, which result in the corrosion and coarsening of Pt nanocrystals respectively. It is found that different anti-corrosion stabilities of Pt facets can be explained by their maximum abilities to keep oxygen atoms adsorbed on the top surface layer, and Pt adatom diffusion barriers change with the surface coverage conditions at different U.

Degree Type
Dissertation

Degree Name
Doctor of Philosophy (PhD)

Graduate Group
Materials Science & Engineering

First Advisor
Ju Li

Keywords
Electrocatalysis, Oxygen Reduction Reaction, Multiscale Modeling, Fuel Cell Catalysts, Electrical Double Layer, Pt Oxidation

This dissertation is available at ScholarlyCommons: http://repository.upenn.edu/edissertations/14

Subject Categories
Materials Chemistry | Other Materials Science and Engineering | Physical Chemistry

This dissertation is available at ScholarlyCommons: http://repository.upenn.edu/edissertations/14

MULTISCALE MODELING OF ELECTROCATALYSIS

Liang Qi

A DISSERTATION

in

Materials Science and Engineering

Presented to the Faculties of the University of Pennsylvania

in

Partial Filfillment of the Requirements for the

Degree of Doctor of Philosophy

2009

Professor Ju Li

Supervisor of Dissertation

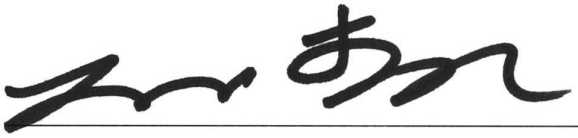

Professor Ju Li

Graduate Group Chairperson

Dedicated to my father and mother.

ACKNOWLEDGEMENT

I would like to express my deepest thanks to my advisor and mentor, Professor Ju Li, for his unlimited support and insightful guidance. He has taught me not only wealth of knowledge and techniques, but also how to be a devoted scientist.

I would like to thank Prof. Vasek Vitek, Prof. Andrew M. Rappe and Prof. Christopher B. Murray for serving on my thesis committee. It is a great honor for me to receive invaluable suggestions from these outstanding scientists. Their deep insights will lead my work to a higher level.

Many thanks to members of our Material Theory Group. I would like to thank Mr. Joshua Fujiwara, who brings me a lot of information and knowledge on fuel cell research and industry. I would like to thank Dr. Xiaofeng Qian, who treats me like a brother and teaches me a lot on density functional theory and programming. I would like to thank Dr. Jianguo Yu, who taught me basic modeling techniques when I was a fresh graduate student. I would like to thank Dr. Erik Bitzek, who makes a good organization to build and maintain our new computer cluster, where I ran a large amount of jobs for my thesis. I would like to thank Dr. Ji Feng, who teaches me a lot on electronic structures and helps me submit our paper when I was busy with my thesis. I would like to thank Amit Samanta, with whom I share the graduate student experience. I would like to thank Liu Cao, Zheng Li, Wei Liu and Wenbin Li; all of you give me a lot of help and support.

I would like to thank Mr. Mitsumoto Kawai for offering me an exciting internship experience at Honda Research Institute in Tokyo. I also would like to express my sincere thanks to my friends at Ohio State University and Upenn: Ning Zhou, Weiqi Luo, Wei Cai, $\cdots$; with all of you I have an enjoyable life in Columbus and Philadelphia.

Last, I would like to express my heartfelt gratitude to my parents. All of my achievements, which are small but I accomplished proudly by working hard, are founded on their

unselfish love and strict education.

ABSTRACT

MULTISCALE MODELING OF ELECTROCATALYSIS

Liang Qi

Dr. Ju Li

In proton-exchange-membrane (PEM) fuel cells, electrochemical oxygen reduction reaction (ORR) on the cathode is a critical step at which large energy loss occurs. Theoretical tools at different scales are discussed in this thesis in order to find ORR catalysts with both higher activity and better durability than current Pt and Pt alloys. For catalytic activity, a relatively simple model reaction, ORR by hydrogen molecule under ultra-high-vacuum (UHV) conditions, is studied by first-principles methods on various metallic surfaces, which shows that the good catalytic activities of Pt and its alloys originate from moderate adsorption strengths for atoms and molecules involved in the reaction. Then first-principles methods are also applied to study the reaction mechanisms of electrochemical ORR: detailed analyses in the electronic structures of ORR intermediates confirm that all the electron transfers in ORR occur through proton-coupled electron transfer (PCET) mechanism, which is accomplished by proton transfer along hydrogen-bond network from hydrated proton (hydronium) to ORR intermediates on the surface. Furthermore, first-principles methods are also used to search and design new alloy surfaces with optimal activity based on a simple kinetic model. However, the inaccuracy of this simple model makes a comprehensive multiscale ORR model necessary. Thus, a reaction network of ORR elementary steps on limited surface sites is built, and the steady-state solutions provide current density j at given electrode potential U; then a multiscale model of electrode/electrolyte interfacial structure is proposed for function $U(\sigma^{\mathrm{M}})$, where σ^{M} is excess surface electron density on metallic electrode; finally, we discuss the principles to achieve a self-consistent

multiscale ORR model to output both U and current I to the external circuit. For the stability of Pt as catalyst, we study its surface oxide formation and surface adatom diffusion, which result in the corrosion and coarsening of Pt nanocrystals respectively. It is found that different anti-corrosion stabilities of Pt facets can be explained by their maximum abilities to keep oxygen atoms adsorbed on the top surface layer, and Pt adatom diffusion barriers change with the surface coverage conditions at different U.

Contents

List of Tables

List of Figures

Chapter 1

Introduction

1.1 Background

A fuel cell is an electrochemical energy conversion device. It produces electricity from chemical reaction energy of fuels on the anode side and oxidants on the cathode side. Fuel cells have several prominent advantages compared with other energy conversion systems, such as combustion engines[98]. First, because they are not heat engines under the limitation of Carnot cycle, they usually have very high fuel efficiency ($>$50%). Second, they can use different types of renewable fuels, such as methanol, ethanol and hydrogen gas, other than fossil fuels with limited and nonrenewable sources. Third, because of high reaction efficiency and/or choices of clean fuels, they usually have less or even no output of greenhouse gas or other pollutants, such as carbon dioxide (CO_2) and nitrous oxide (N_2O). For these reasons, they provide promising technologies to help us solve the serious energy and environmental problems in modern society.

There are several types of fuel cells with different choices of fuels, oxidants and membranes, which are used to conduct ions between two electrodes. Among them, the proton exchange membrane (PEM) fuel cell uses H_2 as fuel and O_2 as oxidant, where the overall

reactions are shown as following:

$$\text{Hydrogen Oxidation Reaction (HOR) on anode: } H_2 \rightarrow 2H^+ + 2e^- \tag{1.1}$$

$$\text{Oxygen Reduction Reaction (ORR) on cathode: } O_2 + 4H^+ + 4e^- \rightarrow 2H_2O \tag{1.2}$$

Here both H_2 and O_2 are in gas states with partial pressure $\sim$ 1 atm, and both reactions occur at room temperature ($\sim$ 300 K) in the electrolyte with H_2O as solvent molecules. The proton involved in these reactions exists in the electrolyte as a hydrated state by combining with nearby water molecules; polymer membranes (Nafion®) are used to transport these hydrated protons between anode and cathode. The electrons involved in HOR and ORR come from the anode and cathode, respectively, and their free energies depend on electrode potentials. In addition, because there are large activation energy barriers for both HOR and ORR performing in homogeneous electrolyte phases, certain catalysts on the electrodes have to be used in order to make both reactions occur fast and smoothly at room temperature. The catalysts work by providing their surfaces as active reaction sites, where the activation energies significantly decrease, resulting from surface adsorption and dissociation of certain reactant atoms and molecules. In general, because of its low operation temperature and compact size, PEM fuel cell is a prime candidate for vehicles and other mobile applications, which need to be turned on/off frequently[6].

However, there are still many obstacles for the practical application of PEM fuel cell, especially in its catalysts. Currently, all high-performance catalysts for PEM fuel cell are made of precious Pt or Pt alloys; there are also technical problems for these expensive materials to perform as highly efficient and stable catalysts. First, on the anode side, the impurity in the fuel, such as carbon monoxide (CO), can poison the catalyst by strong adsorption at active reaction sites on Pt surface, which decreases the catalytic activity of Pt for HOR[72]; second, on the cathode side, neither pure Pt nor Pt alloys have high enough

Pt mass activity, defined as the ORR rate by using unit mass of Pt as catalysts, so that the total amount of Pt used is quite large and significantly increases the cost for its commercial applications[33]; third, all catalysts are deposited on electrodes in the form of nanocrystals to increase electrochemical active surface area (ECSA), but corrosion and coarsening gradually occur and result in catalytic performance degradation[119]. My research is mainly focused on the last two problems: the activity and durability of catalysts used on the cathode of PEM fuel cell, because ORR on the cathode has much smaller activity than HOR on the anode, which makes ORR the rate-determining step in the whole fuel cell reaction, and corrosion also occurs much faster on the cathode, which has higher electrode potential U than the anode.

In experiments, the activity and durability of catalysts can be evaluated by measuring electric current I and electrode potential U with different techniques, such as Tafel plot, cyclic voltammetry (CV) and Levich-Koutecky plot with rotating disk electrode (RDE)[7]. These measurements can also be used to investigate the reaction mechanisms based on assumptions of surface reaction models[22, 116, 78, 79]. However, there are still many controversies and uncertainties for mechanisms of both ORR and catalyst degradation. These uncertainties mainly result from two factors. First, unlike surface reactions under ultra-high vacuum (UHV) conditions where characterization techniques are abundant[63], it is still quite difficult to accurately obtain electronic and atomic information of electrochemical surface reaction because of the existence of liquid electrolyte. Second, both ORR and Pt corrosion are reactions with complex dynamics: ORR is a multiple-electron transfer process and consists of several elementary reaction steps with many possible reaction intermediates; Pt corrosion is a relatively slow process but can be accelerated by electrode potential cycling and corresponding Pt oxidation/reduction, which involve intricate Pt lattice distortions and reconstruction. For these reasons, theoretical studies are needed to understand these mechanisms and speed up the search for new catalysts with better activity

and durability.

There are several general types of theoretical and computational tools for materials science, such as classical molecular dynamics, Monte Carlo methods, kinetic Monte Carlo and first-principles methods[121, 71]. Density functional theory (DFT), a widely used first-principles method, provides a theoretical tool to study the physical and chemical properties of certain materials accurately and efficiently[101, 81]. In principle, DFT calculation is a quantum mechanical method depending only on the some universal constants such as Planck constant, speed of light, mass of ions and electrons (practically, it needs some material-independent parameters for the electron density functional and pseudopotentials of ions plus core electrons.). Its results are usually very accurate without the help of experimental measurements. In addition, because the degrees of freedom are single-electron wavefunction (Kohn-Sham) and electron density rather than many-body wavefunction in quantum chemistry methods, DFT can calculate larger systems with reasonable time and computer power consumption. For these reasons, DFT has been widely used in studies of surface reactions on the catalysts[44].

However, DFT methods alone are not enough to determine the whole picture of an electrochemical surface reaction such as Eq. 1.2. As a quantum mechanical method, DFT calculation is still very expensive so that it is usually used to deal with a system of $\sim$100 atoms with the size of $\sim$30 Å; on the other hand, an electrochemical surface reaction is affected by factors at different scales: on the catalyst surface the elementary reaction steps compete with each other for the limited reaction sites, so that statistical mechanical models are needed to consider these lateral interactions (*catalysis* model); away from the surface there are long-range diffusion layers of reactants and ions (100$\sim$10000 Å), which result in an electric field and its integral effect–electrode potential U; the surface reaction kinetics has a self-consistent relation with the diffusion layers so that multiscale models are needed to clarify these complex pictures, especially for electrochemical ORR (*electrocatal-*

ysis model).

1.2 Detailed Outline

In Chapter 2, there is short introduction on the basic concepts and theories frequently used in my thesis. First, a short introduction is given on the subject of surface structure models. Then there are some fundamental theories in electrochemistry, such as electrode potential references, electrical double layer structures, Gouy-Chapman theory in charge-potential relation, electrode reaction kinetics and overpotentials. Finally some methodologies of simulation techniques, such as DFT and kinetic Monte Carlo, are briefly reviewed.

In Chapter 3, we start DFT studies of oxygen reduction by hydrogen molecule at ultra high vacuum (UHV) conditions, as shown in the following:

$$O_2 + 2H_2 \rightarrow 2H_2O \tag{1.3}$$

Although it is different from electrochemical ORR of Eq. 1.2 in both the reactant (H_2 vs. $H^+ + e^-$) and reaction environment, there are still several similarities. First, their final products are both H_2O molecules; second, the strong covalent bond of O_2 has to be broken in both reactions; third, Pt is the effective catalyst for both reactions. Besides these similarities, reaction in Eq. 1.3 is relatively easy to study by DFT, because there are only gas molecules and solid surface involved. The purpose of this study is to use a simple model reaction to understand the origin of catalytic activity in oxygen reduction on different surfaces, so DFT calculations are performed on (111) surfaces of different metals (Pt, Cu, Au and Pt alloys).

In Chapter 4, the topic is changed from ORR at UHV conditions of Eq. 1.3 back into electrochemical ORR of Eq. 1.2. Since there are multiple-electron transfers for a full

ORR path, which can be accomplished by numerous combinations of possible elementary steps depending on the charge states of ORR intermediates, it is essential to understand its detailed reaction mechanism before we build any accurate kinetic model. Thus, we use DFT methods to study electronic structure of every possible reaction intermediate, such as adsorbed oxygen molecule, in order to clarify the corresponding electron transfer sequence. After that, we also use DFT to study the dynamics of these electron transfer processes near electrode surfaces, so that we can obtain their activation barriers, which are useful for the kinetic studies in the next step. Meanwhile, because there is some simple ORR kinetic model whose input parameters are just the adsorption energies of critical ORR intermediates[94], we also use it to discover new catalysts for ORR by theoretically designing atomic structures and calculating their adsorption energies. Although it is not very accurate, it can be used as a quick and coarse filtering method to pick up possible candidates of better activity for detailed studies by more accurate kinetic models.

Chapter 5 illustrates the procedures to build a multiscale and self-consistent model of electrochemical ORR on catalyst surface. First, based on the reaction mechanisms and corresponding dynamics found in Chapter 4, we build a reaction network on limited surface sites. Here we do not only consider the competitions of reaction sites between elementary steps (*entropic interaction*), but also the repulsive interactions between ORR intermediates on the surface (*enthalpic interaction*). In mean-field approximation, the steady states of the reaction network can be numerically solved in order to obtain ORR rate and current density j at given U. Based on this model, we build a mathematical framework to perform the analyses on how each input parameter, such as adsorption energy of certain intermediate, can affect the final output of this reaction network. Besides mean-field results, the advantages of discrete model to accurately describe the lateral interactions and site competitions are also discussed. Second, the electrode-electrolyte interface, so called *double layer structure*, is studied by combining both DFT and classical statistical theories in order to determine U

as a function of excess surface electron density σ^M on metallic electrode, and the results can also be used to calculate the differential capacitance C_d, which is directly comparable with experiments. Finally, because σ^M depends on both the electron consumption rate by electrochemical surface reactions and the supply rate by current I from external circuit, we discuss the principles to achieve a self-consistent multiscale ORR model to output both U and I, such that a PEM fuel cell simulator *in silico* can be constructed.

In Chapter 6, the topic is changed to the durability of catalyst. The degradation of catalyst performance results from two mechanisms: the corrosion and coarsening of Pt nanocrystals. The corrosion is usually accelerated by Pt oxidation/reduction cycling, so the formation mechanisms of thin oxide layer on various Pt surfaces (low index facets such as (111) or (100), and high index facets such as (210)) are studied in order to find a possible method to impede oxidation process and subsequent corrosion. The coarsening is found by experiments to be accomplished by Pt adatom diffusion between Pt grains[153], so that Pt adatom diffusion is theoretically studied on Pt (111) surface with various surface adsorbates in order to explain potential-dependent coarsening rates and design special structures to deactivate this process.

Chapter 7 summaries all the results in my thesis and proposes some directions for future studies.

Chapter 2

Fundamental Concepts and Modeling Methodologies

2.1 Models of Solid Surface

Surface of solid is inherently different than the rest of the solid (the bulk): because there are less coordination numbers for the atoms on the surface than those in the bulk, the bonding at the surface is different than those in the bulk, resulting in various physical and chemical properties. In this thesis, all the (electro-)chemical reactions occur on the surface of certain solid material at gas-solid or liquid-solid interface, so it is essential to choose some proper models to describe the atomic structures of solid surface.

In general, there are two types of surface models:

- Cluster model, which uses a cluster composed of limited number of atoms, as shown in Fig. 2.1 (a).
- Slab model, where the surface is described as a slab with periodic boundary conditions along the surface directions, as shown in Fig. 2.1 (b) and (c).

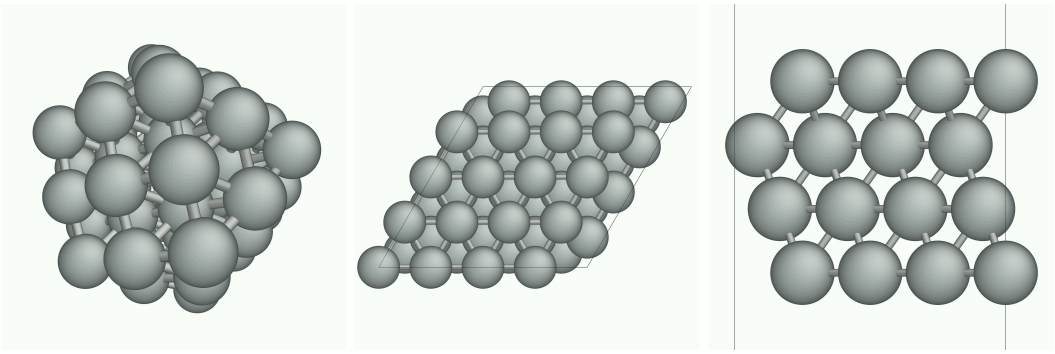

(a) (b) (c)

Figure 2.1: Models of solid surface. (a) Example of a cluster model, a 55-atom Pt cluster in FCC lattice structure, where both (100) and (111) facets are shown. (b) and (c): Top and side view of a slab model, a (4×4) Pt (111) surface in FCC lattice structure composed of 4 (111) layers.

In practical simulations, because of computational power limitation, a surface model can only have a small number of atoms (usually < 100). Thus, the cluster model has very small size and there may be several types of atoms with different coordination numbers, which result in various chemical properties at different surface sites. The heterogeneity of surface sites may increase our difficulty to compare the simulation results with the experimental measurements, where the real surface has much larger size and more uniform properties (the real surface still has many types of reactions sites such as steps and kinks, but not so high density as the cluster model in Fig. 2.1 (a)). Meanwhile, the electronic structures of the isolated clusters may be different from the surface of bulk solids. For these reasons, we usually apply slab model to study the (electro-)catalytic reaction on the surface[44].

2.2 Fundamental Concepts in Electrochemistry

2.2.1 Electrode Potential

A chemical reaction in which there are electrons provided or taken by an external source, such as HOR in Eq. 1.1 and ORR in Eq. 1.2, is called electrochemical reaction or electrode reaction, and the external electron source is called electrode. To calculate the free energy changes in an electrode reaction, an electron in the electrode should be assigned its own free energy and corresponding chemical potential, which can be quantitatively described only if a well-defined reference system, so-called *reference electrode*, is given. Thus *electrode potential* U of this electrode is defined as the free energy change to move one electron from the reference electrode to the studied electrode divided by electron charge $-e$, where e is the elementary charge equal to 1.6021×10^{-19} C; it is also the difference of Fermi level E_{F} between two electrodes divided by $-e$.

A common accepted reference is the *standard hydrogen electrode* (SHE), also called *normal hydrogen electrode* (NHE)[5, 7]. In SHE, electrons have the free energy so that the following HOR

$$\mathrm{H_2(gas,\ } a_{\mathrm{H_2}}=1) \leftrightarrow 2\mathrm{H^+(aqueous,\ } a_{\mathrm{H^+}}=1) + 2\mathrm{e^-} \tag{2.1}$$

is at thermodynamic equilibrium. Here $a_{\mathrm{H_2}}$ and $a_{\mathrm{H^+}}$ is the activity for hydrogen gas molecule and hydrate proton, respectively, defined as the following:

$$a_{\mathrm{gas}} = \frac{p_{\mathrm{gas}}}{p_0},\ \ a_{\mathrm{H^+}} = f_{\mathrm{H^+}}\frac{c_{\mathrm{H^+}}}{c_0} \tag{2.2}$$

where p_0 = 10^5 Pa and c_0 = 1 mol/L as the references, and $f_{\mathrm{H^+}}$ = 1 for the strong acid that dissociates completely in an aqueous solution. In addition, Pt electrode has to be used to

speed up the reaction rate to reach equilibrium. In this thesis, if not specially mentioned, all electrode potentials are relative to SHE. Using SHE, if electrons from an electrode can make the following ORR in thermodynamic equilibrium at room temperature (T = 298.15 K):

$$O_2(\text{gas},\ a_{O_2} = 1) + 4H^+(\text{aqueous},\ a_{H^+} = 1) + 4e^- \leftrightarrow 2H_2O(\text{aqueous}) \qquad (2.3)$$

the corresponding electrode potential U = +1.23 V vs. SHE. This value is obtained from the Gibbs free energy change of the reaction $2H_2(\text{gas},\ a_{H_2} = 1) + O_2(\text{gas},\ a_{O_2} = 1) \rightarrow 2H_2O(\text{aqueous})$ divided by $-4e$[5].

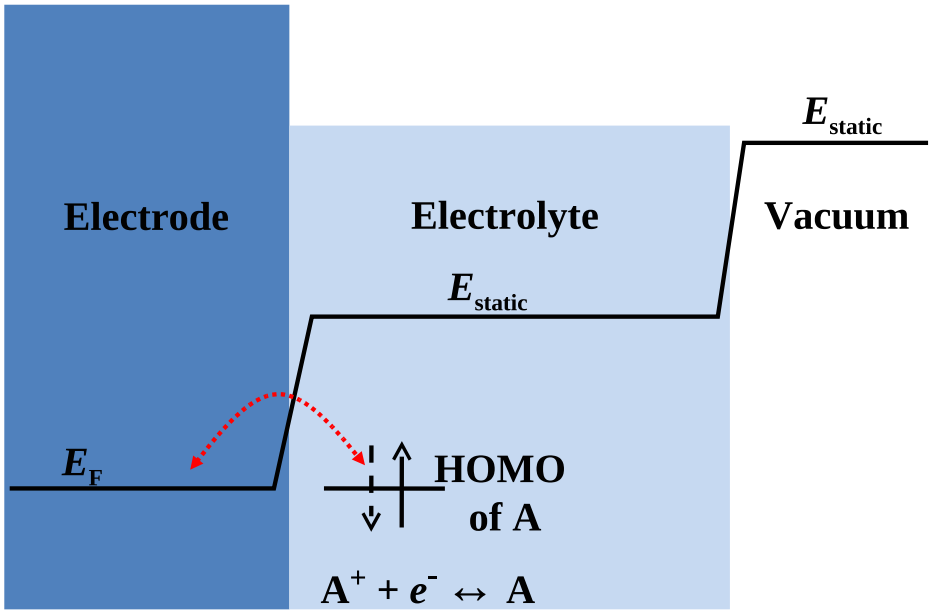

Figure 2.2: Illustration of electrode potential and absolute electrode potential. Here Fermi level of the electrode, E_F, equals the energy level of *highest occupied molecular orbital* (**HOMO**) of A, so reaction of $A^+ + e^- \leftrightarrow A$ is at thermodynamic equilibrium. E_{static} is the average electrostatic energy of an electron in the electrolyte and vacuum, respectively.

Unfortunately, such macroscopic system with two electrodes is difficult to handle by

ordinary microscopic simulation methods, so it is better to find a reference system for a single electrode for theoretical studies. A good choice is **absolute electrode potential** U_{abs}[135], which is defined as the free energy change to move one electron from the vacuum area just outside the electrolyte-vacuum interface to the electrode divided by $-e$, as shown in Fig. 2.2. For an isolated electron in vacuum, its free energy only comes from the electrostatic potential, thus

$$U_{\text{abs}} = -(E_{\text{F}} - E_{\text{static}})/e \tag{2.4}$$

where E_{F} is Fermi level of the electrode and E_{static} is electrostatic energy of one electron in the vacuum just outside the electrolyte-vacuum interface[131]. Meanwhile, experimental results show that U_{abs} of SHE is 4.6 ± 0.2 V[135, 136], providing a conversion method between the absolute electrode potential of certain electrode and its counterpart relative to conventional reference systems, such as SHE.

2.2.2 Electrical Double Layer

Physically, electrode potential U results from the opposite excess charges accumulated on the two sides of electrode-electrolyte interface. This interface behaves like a capacitor, where there are excess electrons, q^{M}, on the metal electrode, and opposite charges, $q^{\text{S}} = -q^{\text{M}}$, in the electrolyte. Here q^{M} can be either negative, meaning there are more electrons than the positive charges of metallic ions, or positive, meaning less electrons than the metallic ions' charge. They are distributed in a very thin layer ($<\sim$ 1Å) on the metal surface. The charges in electrolyte, q^{S}, result from excess of either cations or anions in the vicinity of the electrode surface ($10 \sim 10^4$Å from the surface). Usually q^{M} and q^{S} are expressed by excess surface electron/charge densities, such as $\sigma^{\text{M}} = q^{\text{M}}/A$ in unit of μC/cm^2, where A is the surface area. The whole structure of the excess/deficient charge species on both sides of electrode-electrolyte interface is called **electrical double layer**.

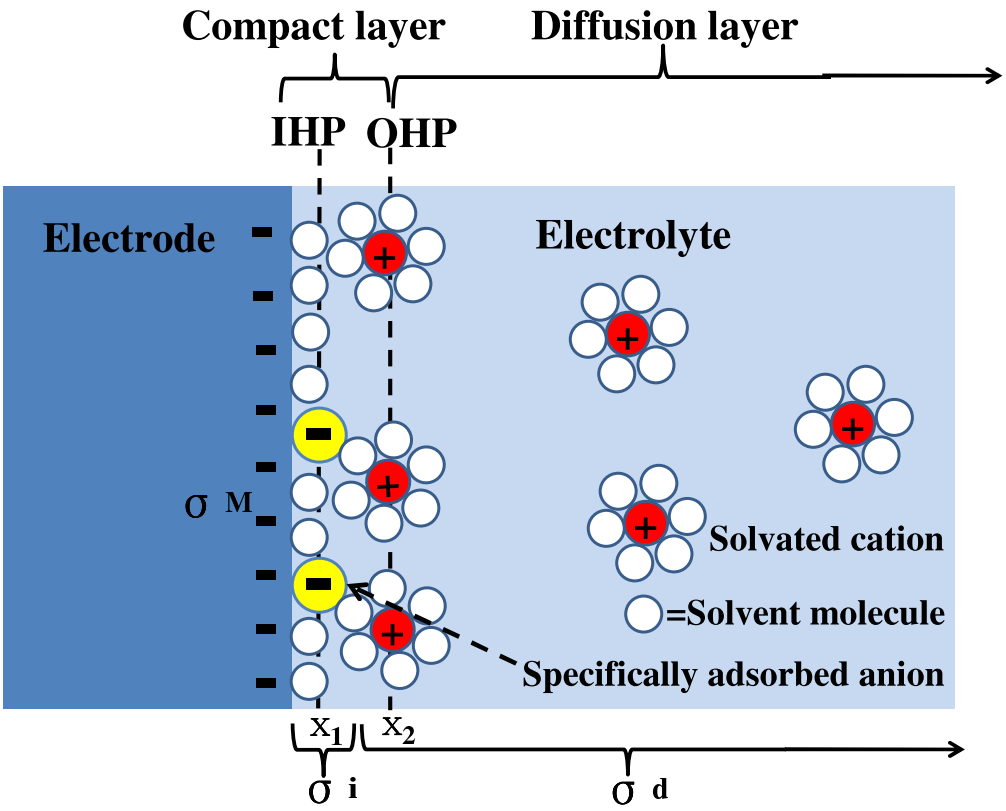

Figure 2.3: Illustration of electrical double-layer structure under conditions where anions are specifically adsorbed, copying from Fig. 1.2.3 in reference [7].

Both thermodynamics and kinetics of interfacial electrochemistry are affected by electrical double layer, which has complex structure, as shown in Fig. 2.3. On the metal electrode side, the distribution of excess/deficient electrons on the surface is different from metal-vacuum interface because of dielectric properties of the electrolyte near the surface. The electrolyte side can be conceptually divided into several "layers". Closest to the electrode, it is the *inner layer* or *compact layer*, which contains solvent molecules adsorbed on the surface in a compact arrangement and sometimes other *specifically adsorbed* species (ions or molecules). The locus of the electrical centers of specifically adsorbed ions is called the *inner Helmholtz plane* (IHP), which is at a distance of x_1 to the electrode surface. The total charge density from specifically adsorbed ions in the inner layer is $\sigma^{i}(\mu C/cm^2)$. The solvated ion, which is made of a bare ion plus a surrounding solvent molecule shell,

can only approach the metal to a distance $x_2 > x_1$, and there are only electrostatic interactions between the charged electrode and these solvated ions, which can also be called *non-specifically adsorbed* ions. The locus of the electrical centers of the non-specifically adsorbed ions in their position of closest approach is called *outer Helmholtz plane* (OHP). The non-specifically adsorbed ions are distributed in the region extended from OHP into the bulk of electrolyte, which is called *diffusion layer*. The excess charge density in the diffusion layer is σ^{d}. Thus, the total excess charge density on the electrolyte side of electrical double layer, σ^{S}, is given by

$$\sigma^{\mathrm{S}} = \sigma^{\mathrm{i}} + \sigma^{\mathrm{d}} = -\sigma^{\mathrm{M}} \tag{2.5}$$

Gouy-Chapman Theory

Besides the graphical model of double layer structures, we need a theory to quantitatively describe how the electrode potential is generated by excess electron/charge density on two sides of double layer. A simple model for this metal-electrolyte interface was developed by Gouy [38] and Chapman [18] as early as 1910. The basic idea is to consider the electrode as a perfect conductor and the electrolyte as point ions distributed in the dielectric continuum, and the detailed distributions of ions satisfy with basic electrostatics and Boltzmann statistics. If we choose the coordinate system so that a planar electrode is at the place of $x = 0$ for simplification, we can get *Poisson-Boltzmann equation*:

$$\frac{d^2\phi}{dx^2} = -\frac{e}{\varepsilon\varepsilon_0}\sum_i n_i^0 z_i \exp\left(\frac{-z_i e\phi}{k_{\mathrm{B}}T}\right) \tag{2.6}$$

where ϕ is electrostatic potential measured with respect to the bulk electrolyte far away from the electrode; ε_0 is vacuum permittivity; ε is dielectric constant of the electrolyte; n_i^0 is bulk concentration of ion i far away from electrode; z_i is the charge number for ion i; k_{B} is Boltzmann constant and T is temperature. If there is only one cation-anion pair with

charge number $+z/-z$ in the electrolyte, Eq. 2.6 can be rewritten as

$$\frac{d^2\phi}{dx^2} = -\frac{zen^0}{\varepsilon\varepsilon_0}\left[\exp\left(-\frac{ze\phi(x)}{k_{\mathrm{B}}T}\right) - \exp\left(\frac{ze\phi(x)}{k_{\mathrm{B}}T}\right)\right] \tag{2.7}$$

If the ion concentration is very low so that the potential fluctuation is very small ($\frac{ze\phi(x)}{k_{\mathrm{B}}T} \ll 1$), Eq. 2.7 can be simplified as linear equation (Debye-H*ü*ckel limit[14]):

$$\frac{d^2\phi}{dx^2} = \approx \kappa^2\phi(x) \tag{2.8}$$

where κ is defined as Debye inverse length:

$$\kappa = \left(\frac{2(ze)^2 n^0}{\varepsilon\varepsilon_0 k_{\mathrm{B}}T}\right)^{\frac{1}{2}} \tag{2.9}$$

which semi-quantitatively shows the thickness of diffusion layer in the electrolyte with varying ion concentration, as shown in Table 2.1.

Table 2.1: Debye length for an aqueous solution with completely dissociated 1-1 electrolyte at room temperature T = 300 K and $\varepsilon = 78.4$. Copying from Table 3.1 in reference [115].

Concentration n^0 [mol/L]	10^{-4}	10^{-3}	10^{-2}	10^{-1}
Debye Length $1/\kappa$ [Å]	305.0	96.4	30.5	9.6

Considering the boundary condition $\phi(+\infty) = 0$ and charge balance condition of Eq. 2.5, solutions of Eq. 2.8 can be:

$$\phi(x) = \frac{\sigma^{\mathrm{M}}}{\varepsilon\varepsilon_0\kappa}\exp(-\kappa x) \tag{2.10}$$

$$\rho(x) = -\sigma^{\mathrm{M}}\kappa\exp(-\kappa x) \tag{2.11}$$

where σ^{M} is the excess surface electron density on the electrode. The nonlinear Poisson-

Boltzmann equation 2.7 can also be solved explicitly, and the result is

$$\tanh\left(\frac{ze\phi(x)}{4k_{\mathrm{B}}T}\right)=\frac{\sqrt{1+\alpha^2(\sigma^{\mathrm{M}})^2}-1}{\alpha\sigma^{\mathrm{M}}}\exp(-\kappa x) \tag{2.12}$$

where $\alpha=(8k_{\mathrm{B}}Tn^0\varepsilon\varepsilon_0)^{-\frac{1}{2}}$. And the differential capacitance, defined as $C_d\equiv\frac{\partial\sigma^{\mathrm{M}}}{\partial\phi}$, is

$$C_d=\varepsilon\varepsilon_0\kappa\cosh\left(\frac{ze\phi(0)}{2k_{\mathrm{B}}T}\right) \tag{2.13}$$

When $\phi(0)=0$, the electrode carries no excess electrons, and the corresponding electrode potential is called *potential of zero charge*(PZC). So the differential capacity is

$$C_d=\varepsilon\varepsilon_0\kappa\cosh\left[\frac{ze(U-\mathrm{PZC})}{2k_{\mathrm{B}}T}\right]=\left(\frac{2(ze)^2\varepsilon\varepsilon_0n^0}{k_{\mathrm{B}}T}\right)^{\frac{1}{2}}\cosh\left[\frac{ze(U-\mathrm{PZC})}{2k_{\mathrm{B}}T}\right] \tag{2.14}$$

which is called *Gouy-Chapman capacitance*. It has a minimum value at PZC and goes into infinity when $U\rightarrow\pm\infty$. This V-shaped capacitance function resembles the experimental behaviors at low ion concentrations and at potentials not far away from the PZC[7, 115].

However, Gouy-Chapman theory is known to strongly overestimate ionic concentrations close to charged surfaces. The main reason for inaccuracies results from the finite size of ions in the electrolyte. The ions have finite sizes, which are larger than the isolated ions in vacuum because of the primary solution sheath, so they can not approach the surface any closer than the ionic radius, as shown in Fig. 2.3. Ideally, there are no ionic charges from the electrode surface to OHP if there are no specifically adsorbed ions on the electrode surface, so the electrostatic potential in the compact layer is assumed to behave like a linear function, as shown in Fig. 2.4, and its contribution to the total differential capacitance C_d is also different. If we assume that the dielectric constant in compact layer is the same as

bulk electrolyte, C_d can be calculated as following:

$$\frac{1}{C_d} = \frac{x_2}{\varepsilon\varepsilon_0} + \frac{1}{(\frac{2(ze)^2\varepsilon\varepsilon_0 n^0}{k_B T})^{\frac{1}{2}} \cosh[\frac{ze(U-\mathrm{PZC})}{2k_B T}]} = \frac{1}{C_H} + \frac{1}{C_D} \tag{2.15}$$

where x_2 is the distance between OHP and electrode surface, and the *Helmholtz capacitance* C_H corresponds to the capacitance contributed by compact layer inside OHP. This model, known as *Gouy-Chapman-Stern*(GCS) model, predicts the behaviors closer to real systems.

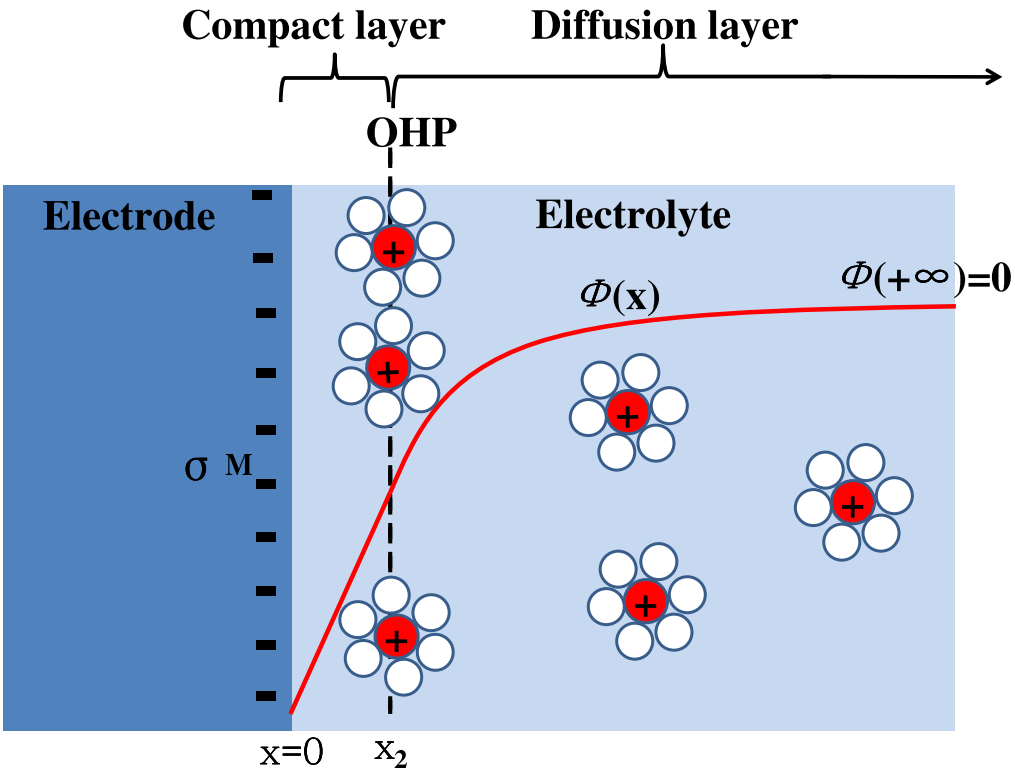

Figure 2.4: Potential distribution of electrical double layer by Gouy-Chapman-Stern (GCS) model. Meanings of difference signs are explained in the caption of Fig. 2.3.

Based on these theories, there are at least two more things we can improve further. First, in the real electrode-electrolyte interface, the dielectric constant in compact layer is different from bulk electrolyte because of the effect from electrode[114], so we want to build a multiscale model, which combines quantum mechanical methods and statistical mechanics, to obtain more accurate descriptions of double layer structures. Second, in

GCS model, electrode potential U is measured with respect to PZC, which is a variable depending on detailed electrode-electrolyte interface, so we need to obtain U relative to a fixed reference system, which is experimentally measurable, such as SHE. Both of them will be discussed in Section 5.2.

2.2.3 Electrode Reaction

For a general electrode reaction, O + ne^- $\rightarrow$ R, it can be accomplished by several steps, as shown in Fig. 2.5. First, the reactant O should move from bulk electrolyte to the area near electrode by mass transfer. There are three different modes of mass transfer:

- Migration. Movement of a charge body caused by an electric field.
- Diffusion. Movement of a species under the influence of a chemical potential gradient (usually it is concentration gradient.).
- Convection. Bulk movement of fluid accompanied by the transfer of species inside.

Second, when the reactant is close to the surface, it may need to be adsorbed on the electrode surface, marked as O^*. Third, electrons are transferred to O^*, accompanied by some other possible surface reactions, such as molecular dissociation and/or recombination, so O^* is transformed into R^* adsorbed on the surface. Finally, R^* departs from the surface to the bulk electrolyte by desorption and various mass transfer modes. It is also possible that neither O nor R needs to be adsorbed on the surface; they may gain or lose electrons and transform into each other once they are close to the electrode surface. As shown in Fig. 2.5, this reaction can also occur in a reverse direction by similar mechanisms.

In such a complex reaction pathway, each elementary step may contribute some barrier to impede the electrode reaction. For example, there may be a high free energy barrier, Q_{eq}, for electron transfer or other chemical reactions on the electrode surface when U equals the

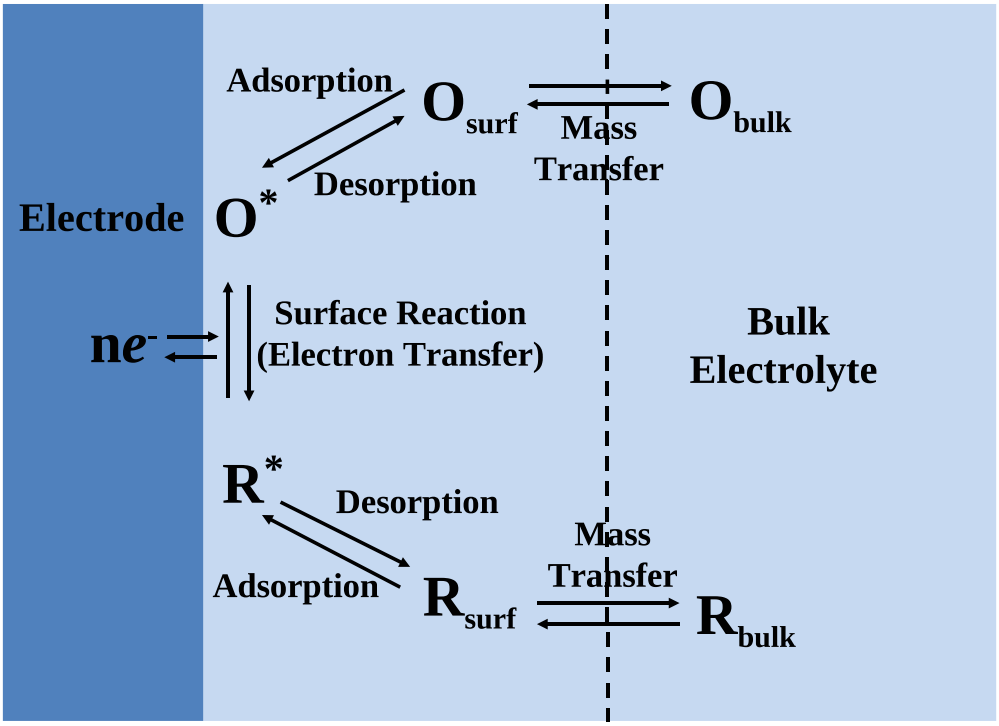

Figure 2.5: Pathway of a general electrode reaction O + ne^- ↔ R. Here O_{bulk}/R_{bulk} stands for O/R in the bulk electrolyte, O_{surf}/R_{surf} stands for O/R near the electrode surface, and O^*/R^* is the adsorbed state on the electrode surface.

thermodynamic equilibrium value U_{eq}. As shown in Fig. 2.6, Q_{eq} stands for the difference between the lowest point of free energy curve for (O + ne^-) and the intersection point of two curves for reactants (O + ne^-) and products (R). To decrease this huge barrier, U has to be reduced by a value of -η (here $\eta < 0$) so that the free energy curve for (O + e^-) is shifted up by -$n\eta e^-$, which also makes Q_{eq} change into a lower value, Q_U. As a result, the reaction on the surface can occur fast under this new potential $U = U_{eq} + \eta$. Thus η is called *overpotential*, defined as the additional potential beyond thermodynamic requirement, U_{eq}, needed to drive a reaction at certain rate. In addition, the ratio between the activation free energy change and reaction free energy change is called *transfer coefficient* or *symmetry*

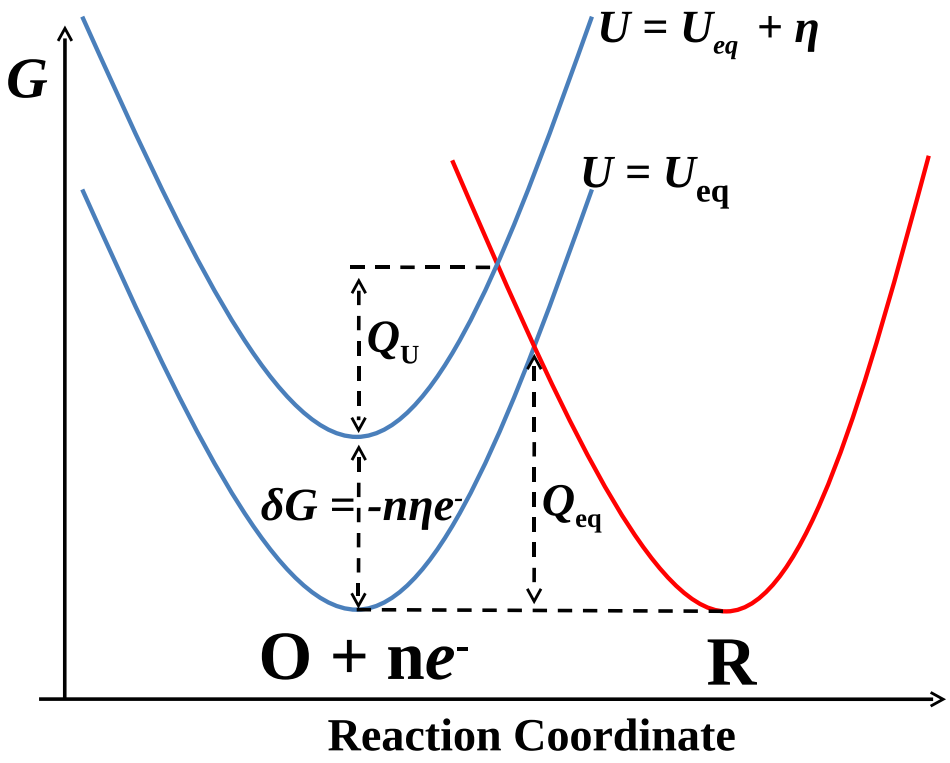

Figure 2.6: Effect of an overpotential η on activation free energy of reaction O + ne^- $\rightarrow$ R. Here U_{eq} is the equilibrium potential. Q_{eq}/Q_U is the corresponding activation free energy when U is $U_{eq}/(U_{eq} + \eta)$. Here η is negative to increase the free energy of the reactant (O + ne^-).

factor, defined as

$$\beta \equiv \frac{\delta Q}{\delta G} = \frac{Q_{eq} - Q_U}{-n\eta e^-} \tag{2.16}$$

Usually $\beta \approx \frac{1}{2}$ for general electrode reactions[7].

Besides surface and near-surface reactions (including electron transfer), mass transfer processes, as shown in Fig. 2.5, may also reduce the total reaction rate, so it can also make a considerable contribution to the overpotential, especially at large current density region. An efficient fuel cell system should generate large current density with a small magnitude of overpotential. Thus, both surface reactions and mass transfer need to be considered in order to improve the performance of a fuel cell. For ORR of Eq. 1.2 in PEM fuel cell, it is

found that the overpotential from surface reaction is larger than its counterpart from mass transfer[33], so we mainly focus on surface reaction mechanism of ORR in this thesis.

2.3 Materials Modeling Methodologies

2.3.1 Density Functional Theory

In order to study reactions on electrode surface at atomic scale, we need to accurately describe the electronic structures of atoms, molecules and solid surfaces, which can be achieved based on first-principles methods. In quantum mechanics, for a many-body system with N electrons in an external potential $V_{\text{ext}}(\mathbf{r})$, the total system can be rigorously described by many-body wavefunction $\psi(\mathbf{r}_1, \mathbf{r}_2, \ldots, \mathbf{r}_n)$ and its eigenvalue E_i solved from the following Schrödinger equation

$$\{-\sum_i \nabla_i^2 + \sum_i V_{\text{ext}}(\mathbf{r}_i) + \frac{1}{2}\sum_{i\neq j}\frac{1}{|\mathbf{r}_i - \mathbf{r}_j|}\}\psi(\mathbf{r}_1, \mathbf{r}_2, \ldots, \mathbf{r}_n) = E_i\psi(\mathbf{r}_1, \mathbf{r}_2, \ldots, \mathbf{r}_n) \quad (2.17)$$

Here Hartree atomic units are used, where $\hbar = m_e = e = 4\pi\varepsilon = 1$. However, when N is not small, this equation can not be solved by any analytical or numerical method because of large degrees of freedom in $\psi(\mathbf{r}_1, \mathbf{r}_2, \ldots, \mathbf{r}_n)$. For example, to express $\psi(\mathbf{r}_1, \mathbf{r}_2, \ldots, \mathbf{r}_n)$ numerically in a cubic of $10 \times 10 \times 10$ points, it requires totally 10^{3N} data, which is an astronomical figure even when $N > 10$ so that it can not be stored or manipulated by current computers.

Instead of directly dealing with many-body wavefunction, Kohn et al. provide another avenue to study the ground state of a many-body system based on electron density, so called *density functional theory* (DFT)[51, 61, 101, 81]. First, Hohenberg and Kohn strictly proved that for any system of interacting electrons in an external potential $V_{\text{ext}}(\mathbf{r})$, the potential $V_{\text{ext}}(\mathbf{r})$ is determined uniquely, except for a constant, by the ground state electron

density $n_0(\mathbf{r})$; second, a universal functional for the energy $E[n]$ in terms of the density $n(\mathbf{r})$ can be defined for external $V_{\text{ext}}(\mathbf{r})$ so that for any particular $V_{\text{ext}}(\mathbf{r})$, the exact ground state energy of the system is the global minimum value of this functional, and the density $n(\mathbf{r})$ that minimizes the functional is the exact ground state density $n_0(\mathbf{r})$[51].

Based on the above theorems, Kohn and Sham used variational methods and an auxiliary system of N non-interacting electrons, whose ground state energy E_0 and density $n_0(\mathbf{r})$ are the same with those of the system of N interacting electrons, to obtain the Kohn-Sham Schrödinger-like equations[61]:

$$(H_{\text{KS}} - \varepsilon_i)\psi_i(\mathbf{r}) = 0 \tag{2.18}$$

where $\psi_i(\mathbf{r})$ is the eigenfunction and ε_i is the corresponding eigenvalue for a non-interacting electron. H_{KS} is the effective Kohn-Sham Hamiltonian defined as

$$\begin{aligned} H_{\text{KS}} &= -\frac{1}{2}\nabla^2 + V_{\text{ext}}(\mathbf{r}) + \frac{\delta E_{\text{Hartree}}[n]}{\delta n(\mathbf{r})} + \frac{\delta E_{\text{xc}}[n]}{\delta n(\mathbf{r})} \\ &= -\frac{1}{2}\nabla^2 + V_{\text{ext}}(\mathbf{r}) + V_{\text{Hartree}}(\mathbf{r}) + V_{\text{xc}}(\mathbf{r}) \end{aligned} \tag{2.19}$$

Here $-\frac{1}{2}\nabla^2$ and V_{ext} stand for the kinetic energy and external potential energy for the non-interacting electrons, $E_{\text{Hartree}}[n]$ is classical Coulomb interaction energy defined as

$$E_{\text{Hartree}}[n] = \frac{1}{2}\int d^3r d^3r' \frac{n(\mathbf{r})n(\mathbf{r}')}{|\mathbf{r}-\mathbf{r}'|} \tag{2.20}$$

$E_{\text{xc}}[n]$ is so-called *exchange-correlation* energy including all the left many-body interactions. Similar with $E_{\text{Hartree}}[n]$, $E_{\text{xc}}[n]$ is also a materials-independent functional of density n; although its exact form is unknown, it can be approximately expressed by certain analytical formula based on n[101, 81].

For a system of N non-interacting electron obeying H_{KS}, the ground state has one

electron in each of the N orbitals $\psi_i(\mathbf{r})$ with lowest eigenvalues ε_i, so the ground state density is given by

$$n(\mathbf{r}) = \sum_{i=1}^{N} |\psi_i(\mathbf{r})|^2 \tag{2.21}$$

which is also the ground state density for the system of N interacting electrons, whose ground state energy can also be calculated based on $n(\mathbf{r})$.

Because of the usage of the non-interacting electron system, the degrees of freedom involved in calculations decrease significantly. If we still use a cubic of $10 \times 10 \times 10$ points, the system can be described by $(N_w + 1) \cdot 10^3$, where N_w is the number of wavefunction $\psi_i(\mathbf{r})$ and comparable with the number of electrons N. So it can be practically performed on computers. Meanwhile, every term in H_{KS} has exact analytical expression except $E_{\mathrm{XC}}[n]/V_{\mathrm{XC}}(\mathbf{r})$, whose contribution to total energy is relatively small compared with other terms in H_{KS} and efficient approximation forms can be found, so the results are usually very accurate. Thus, DFT based on Kohn-Sham equations is widely used in different areas of physics, chemistry and materials science[71, 81].

In practice, there are many numerical methods to perform DFT calculations, which can be categorized from two aspects:

- Basis sets

  The wavefunction in real calculation is not expressed totally numerically, but is constructed by combinations of many basis wavefunctions, so-called basis sets. There are two general types of basis: localized functions, such as atomic orbitals, and plane waves (including projector augmented wave (PAW) approach[13, 70]). Localized functions are usual choice in cluster-type models as shown in Fig. 2.1 (a), while plane waves are usually used in slab-type models as shown in Fig. 2.1 (b) and (c). Usually the core electrons of certain ions are not treated explicitly, because they require a large number of basis functions but do not affect the final physical and chemi-

cal properties we interest in most cases. So *pseudopotential* description of ionic core are used[42, 140]. Meanwhile, we should use enough basis functions to describe wavefunction accurately; in plane waves cases, this means the basis should include plane wavefunctions from those with low kinetic energies to those with high enough kinetic energies, so-called converging test of *cut-off energy*[81].

- Approximation on exchange and correlation functionals

  The major problem with DFT is that the exact functional for exchange and correlation, $E_{\mathrm{XC}}[n]$ in Eq. 2.19, is not known except for free electron gas[17]. However, approximations exist which permit the calculation of certain physical and chemical quantities quite accurately. The most widely used approximations are the local-density approximations (LDA), whose exchange and correlation functional depends only on the density at the coordinate where the functional is evaluated[144, 106, 19, 105]. DFT results from LDA approximations usually give a good description of atomic geometries of studied system, but may overestimate the binding energies between different species. A better solution comes from generalized gradient approximations (GGA)[104, 103, 43], which are local but also take into account the gradient of the electron density at the same coordinate. GGA usually gives good descriptions of the ground state energies[44], so it is widely used in surface chemistry areas, including most of calculations in this thesis (here we mainly use Perdew-Burke-Ernzerhof (PBE) exchange-correlation functional[103], a common type of GGA).

2.3.2 Kinetic Monte Carlo Simulation

DFT and other first-principles methods are usually used to deal with individual chemical reactions occurring locally on certain reaction sites. However, real surface (electro-)chemical reactions, which are usually composed of several elementary steps, are much more complex

because reactions at different surface sites are strongly affect each other[122, 63], so the reaction kinetics are difficult to obtain by only applying first-principles calculations. This problem can be solved with the help of *kinetic Monte Carlo* (kMC) simulation, also called dynamics Monte Carlo simulation, which is a general method for numerically simulating the stochastic time evolution of many coupled events[36, 32, 121, 71].

A typical kMC algorithm for simulating the time evolution of a system, where each process i occurs with known rates r_i, can be written as follows:

0. Set the time $t = 0$.

1. Form a list of r_i for all possible event i in the system.

2. Calculate the cumulative function $R_i = \sum_{j=1}^{i} r_j$ for i=1,...,N, where N is the total number of possible events, and denote $R = R_N$

3. Get a uniform random number $u' \in (0,1]$

4. Locate the event k, for which $R_{k-1} < u' < R_k$.

5. Carry out event k.

6. Due to the above transition, total number of possible events N and all rates r_i may have changed. So we need to recalculate the total number of events and their new rates to update N and the list of r_i accordingly.

7. Get a new uniform random number $u \in (0,1]$.

8. Update the time with $t = t + \Delta t$, where Δt is calculated by

$$\Delta t = -\frac{\log u}{R}. \tag{2.22}$$

9. Return to step 2.

For a system of surface reactions, each individual event is a possible elementary reaction step at one surface site and its r_i can be calculated from DFT methods. Thus, we can build a multiscale model, which combines DFT results and statistic methods such as kMC

together, to study the thermodynamics, dynamics and kinetics of certain (electro-)catalytic surface reactions.

Chapter 3

Oxygen Reduction at Vacuum Conditions–the Origin of Catalytic Activity

The oxygen reduction by hydrogen molecule at ultra-high-vacuum (UHV) conditions, as shown in Eq. 1.3, is a famous example of catalytic reaction. As early as the 1840s, it was already found that gaseous H_2 and O_2, which are almost impossible to react in homogeneous gas phases at room temperature, react smoothly to produce water on the surface of Pt crystals at room temperature and even below[29, 9]. Being a well-defined and characterized "model" system, this reaction is of fundamental importance to catalysis and electrocatalysis. In this chapter, (111) surfaces of FCC-lattice metals are used as the model of catalyst surface to study oxygen adsorption, dissociation and reduction at UHV conditions, and several types of metals (Pt, Pt alloys, Cu and Au) are applied. The results will help us understand the origin of catalytic activity for oxygen reduction under both UHV and electrochemical conditions.

3.1 Oxygen Reduction on Pt (111) Surface

Many theoretical calculations have been performed in the framework of DFT and other first-principles methods, not only for the whole oxygen reduction as Eq. 1.3[85], but also its elementary steps such as O_2 adsorption and dissociation [24, 25, 55]. While these calculations have contributed a great deal to our understanding, a complete reconciliation with experiments is not yet achieved. In particular, the predicted O_2 dissociation rate appears to be too slow compared to experiments, as well as the rate of H_2O formation above the water molecule desorption temperature T_{des}, which is $\sim$170 K on Pt(111) surface under UHV conditions.

Völkening *et al.* observed oxygen reduction reaction by hydrogen molecule in progress with scanning tunneling microscope (STM) and high-resolution electron energy loss spectroscopy (EELS) [143]. Two distinct temperature regimes were seen. Below T_{des}, the adsorbed water has an autocatalytic effect and the reduction occurs via disproportionation reactions. Above T_{des}, when water does not stay on the surface, it was postulated that water is formed by successive additions of adsorbed H (H^*) atoms to adsorbed O (O^*) atom:

$$H^* + O^* \rightarrow OH^* \tag{3.1}$$

$$H^* + OH^* \rightarrow H_2O^* \tag{3.2}$$

Michaelides and Hu studied this reaction pathway by DFT, starting from chemisorbed O^* and H^* atoms[85]. They found that reaction (3.1) is a highly activated process, with an activation barrier of 0.94 eV. The barrier of reaction (3.2), on the other hand, is very small, only 0.21 eV.

However, this scenario does not seem to be congruent with the experimental observation [95] that Pt is still a potent catalyst above T_{des}. Taking $T = 200$K [95] and trial

frequency $\nu = 10^{12}$/s, a barrier of 0.94 eV would correspond to O^* half-life of $\sim 10^4$ years. So either the DFT barrier for reaction (3.1) is off, or there may be alternative reaction pathways. Recent DFT calculations for oxygen reduction reaction (ORR) under aqueous electrochemical conditions have indicated the possibility of O_2^* reacting directly with hydronium $H_3O^+(H_2O)_2$ to form OOH^* intermediates [120, 147, 148]. Experimentally, there is also some hint for this possibility [142, 10]. It is therefore profitable for us to look at this hydroperoxyl-mediated pathway using DFT under non-aqueous condition.

H^* and O^* arise from the adsorption and dissociation of H_2 and O_2. The case of H_2 is simple and has been well-studied [99]: H_2 can dissociate without barrier upon contact with Pt (111) surface. The situation with O_2 is more complex. A common conclusion of several UHV experiments [37, 73, 100, 130, 91] is that the dissociation of O_2 on Pt (111) is a thermally activated process via molecular precursor states (MPS), such as O_2^{-*} (superoxo, paramagnetic) or O_2^{2-*} (peroxo, nonmagnetic). Using DFT, Eichler and Hafner identified two energetically nearly degenerate precursors (O_2^{-*} at bridge site and O_2^{2-*} at fcc site), in excellent agreement with experiments. However, they also found that the O_2^* dissociation barriers were 0.8$\sim$0.9 eV[24, 25], which is definitely contradictory to the low experimental O_2 dissociation temperature estimated to be $\sim$150 K[37]. Nolan *et al.* used EELS and molecular beam techniques to examine high translational energy adsorption of oxygen, and estimated the dissociation barrier to be 0.29 eV[91]. Šljivančanin and Hammer recalculated the O_2^* dissociation barriers on flat Pt (111) surface and found the lowest barrier to be 0.6 eV[145], which is a good improvement. Recently, Hyman and Medlin obtained the O_2 dissociation barrier to be 0.44 eV from a cluster calculation[55]. However, the disagreement of slab calculation with experiments in O_2^* dissociation still exists and needs further study.

In this section, we use DFT to study the whole reaction process of water formation, starting from the adsorption of O_2 and H_2 on Pt (111). We resolve the two contradictions

described above by searching for different reaction paths, and checking the dependence of the energetics on adsorbate coverage. The latter could be fulfilled by changing the unit cell used in the calculation. In Sec. 3.1.1, we give details of the calculation method. In Sec. 3.1.2, we discuss the problem of O_2 adsorption and dissociation. We find that if the unit cell is large enough ($(2\sqrt{3}\times 4)$ in our case), the O_2^* dissociation barrier becomes reasonable ($\sim$0.3 eV). This indicates strong dependence of the O_2^* dissociation barrier on oxygen coverage. In Sec. 3.1.3, we first verify the calculation by Michaelides and Hu for the (3.1)+(3.2) reaction by confirming that reaction barrier in Eq. 3.1 is as high as $\sim$1 eV, then we provide a new pathway starting from the direct protonation of O_2^* via the Langmuir-Hinshelwood mechanism to form OOH^* (hydroperoxyl), which only involves an energy barrier of $\sim$0.4 eV. This path may be important when P_{O_2} and P_{H_2} are both high, and its low activation barrier satisfies with the experimental observation of Pt as effective catalyst.

3.1.1 Computational Methods

The calculations are performed using the Vienna Ab-Initio Simulation Package (VASP), an efficient DFT code for extended systems[66, 67]. We use the projector augmented wave (PAW) approach[13, 70], with Perdew-Burke-Ernzerhof (PBE) exchange-correlation functional[103]. The PAW potentials are generally more accurate than the ultrasoft (US) pseudopotentials[140, 97] because the radial cutoffs (core radii) are smaller than the radii used for the US pseudopotentials, and because PAW implicitly invokes the exact valence wave function with all nodes in the core region during the variational minimization. In all cases, the calculations are performed in spin-polarized condition with the planewave expansion truncated at a cutoff kinetic energy of 400 eV.

The Pt (111) surface is modeled as a four-layer slab, separated by five layers equivalent of vacuum. In the most basic setup, we use a rectangular ($\sqrt{3}\times 2$) unit cell (leading to a

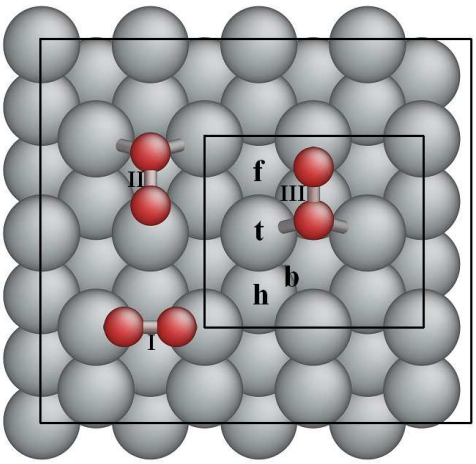

Figure 3.1: Surface cell and short-hand notation of special sites, where there are three O_2^* adsorbed on bridge, fcc and hcp hollow site, respectively. The larger rectangle stands for $(2\sqrt{3}\times4)$ unit cell and the smaller one is for $(\sqrt{3}\times2)$.

c(4×2) structure) where there are 4 Pt atoms in each layer, and we use a Monkhorst-Pack **k**-point grid of $4\times4\times1$ for Brillouin-zone integration[86]. To check the effect of adsorbate coverage, we also increase the size of calculation supercell to $(2\sqrt{3}\times4)$ (c(8×4)) where there are 16 atoms in each layer, with a $2\times2\times1$ Monkhorst-Pack grid. All calculations are performed at the equilibrium Pt lattice constant of 3.977 Å as found from VASP geometry optimization (experimental lattice constant is 3.92 Å), while Pt atoms on the top two layers and the adsorbate atoms are allowed to relax freely. Figure 3.1 shows the surface unit cell and some special sites on it (t-top, b-bridge, f-fcc hollow and h-hcp hollow).

Reaction pathways are searched with the climbing image nudged elastic band (CI-NEB) method[50]. The nudged elastic band (NEB) is a method for finding saddle points and minimum energy paths between known reactants and products[49, 155]. The method works by optimizing a number of intermediate images along the reaction path. Each image finds the lowest possible energy while maintaining equal spacing to neighboring images. This is done by adding spring forces along the band between images and by projecting out the force component parallel to the band due to the interatomic potential. The CI-NEB

is a small modification of the NEB method in which the highest-energy image is driven up to the saddle point, trying to maximize its energy along the band and minimize in all other directions. When the algorithm converges, the highest-energy image will be at an exact saddle point, so a smaller number of intermediate images is needed in CI-NEB than NEB. In this work, 4 intermediate images are used in searching for the saddle point of each elementary reaction step mentioned below, and the spring constant between adjacent images is 5.0 eV/Å^2.

3.1.2 O_2 Adsorption and Dissociation on Pt (111) Surface

In ($\sqrt{3}\times2$) unit cell, when H_2 molecule is close to the Pt surface, it would immediately dissociate into two H atoms adsorbed on the surface during relaxation, which means there are no or very low dissociation barriers. It is found that H atoms preferentially occupy hollow sites. Nevertheless, the difference in adsorption energy between various sites is very small, less than 0.02 eV. All these results agree well with previous DFT calculations[99, 151].

For oxygen in ($\sqrt{3}\times2$) unit cell, we first obtain the three chemisorbed O_2^* precursors [24], shown in Figure 3.1. Precursor I sits on the bridge site with molecular axis parallel to the surface and each oxygen atom binding to one Pt atom near the top site. Precursor II (III) sits on fcc (hcp) hollow site with one oxygen atom binding to Pt atom near the top site and another binding to two Pt atoms at the bridge site, respectively. The geometrical parameters are listed in Table 3.1. The adsorption energies at these three sites are similar with the results of Eichler[24], as shown in Table 3.2. The differences in geometries and adsorption energies may come from the usage of different pseudopotentials (Eichler used ultrasoft pseudopotentials). By inspecting the local density of states (LDOS) on oxygen atoms, we find that the most stable $(O_2^*)_{\text{bridge}}$ species is paramagnetic with left spin density surrounding oxygen atoms, while $(O_2^*)_{\text{fcc}}$ and $(O_2^*)_{\text{hcp}}$ are both nonmagnetic, also agreeing

with the results of Eichler[24]. Since electron transfer is not considered here, the detailed electronic structures and charge states of adsorbed oxygen molecules will be discussed in Chapter 4.

Table 3.1: O_2^* geometry in ($\sqrt{3} \times 2$) unit cell. The data in brackets are from Eichler's results[24]. Here O_2-surface distance is the perpendicular distance between O_2 molecule center and surface plane. O_2 tilt angle is formed by O_2 molecular axis and surface plane, so 0° means O_2 is parallel to surface. All lengths are in Å and angles in degree.

	O_2 bond length	O_2-surface distance	O_2 tilt angle
bridge	1.35(1.39)	1.91(1.92)	0.0(0.0)
fcc	1.39(1.43)	1.76(1.78)	8.9(10.1)
hcp	1.38(1.42)	1.82(1.81)	8.1(8.4)

We then increase the unit cell to ($2\sqrt{3}\times4$) and find the adsorption energy increases by $\sim$0.1 eV for O_2 at fcc site but is almost unchanged for the other two sites. The dissociation energy of O_2^* is calculated by placing two O atoms in two neighboring fcc or hcp hollow sites. Surprisingly, Table 3.2 shows that it increases a lot from the small unit cell to the large unit cell, especially for O atom at fcc hollow site, which is much more attractive for O than hcp hollow site [30]. This indicates the strong dependence of O atom adsorption energy on O coverage. It should also affect the dissociation barriers according to Bronsted-Evans-Polanyi relation[12].

Table 3.2: O_2 adsorption energy on different sites and unit cells. The data in brackets are from Eichler's results[24]. Here 2fcc (2hcp) means O_2 already dissociates into two O atoms in neighbor fcc (hcp) sites. All results are in eV.

	($\sqrt{3}\times2$) unit cell	($2\sqrt{3}\times4$) unit cell
bridge	-0.65(-0.72)	-0.67
fcc	-0.53(-0.68)	-0.66
hcp	-0.43(-0.58)	-0.46
2fcc	-1.68	-2.21
2hcp	-1.21	-1.49

The next step is to calculate the activation energy barrier in O_2 dissociation as the

Table 3.3: Geometries of O_2^* dissociation paths in $(2\sqrt{3}\times 4)$ unit cell. As Fig. 3.2 shows, $O_a(O_b)$ is the left(right) oxygen atom in the initial state. Here $d_{\text{O-O}}$ is the distance between two oxygen atoms. $d_{\text{Pt-O}}$ is the distance between O atom and its nearest Pt atom. d_z is the perpendicular distance between O atom and Pt surface. I, T1(T2) and F1(F2) stand for the initial, transition and final states for path 1(2). All lengths are in Å.

	$d_{\text{O-O}}$	$d_{\text{Pt-O}_a}$	$d_z(\text{O}_a)$	$d_{\text{Pt-O}_a}$	$d_z(\text{O}_b)$
I	1.35	2.04	1.90	2.04	1.90
T1	1.32	2.01	1.99	2.75	2.25
F1	3.01	2.03	1.14	2.04	1.14
T2	2.51	1.98	1.31	1.83	1.78
F2	3.02	2.03	1.24	2.03	1.25

following

$$O_2^* \rightarrow 2O^* \tag{3.3}$$

From the above we think that when the unit cell is small, there may be strong lateral interactions between O^*'s, which may be mediated via the competition for metal's electron. To minimize this effect on O_2 dissociation, we first use $(2\sqrt{3}\times 4)$ unit cell to calculate the dissociation barrier. O_2^* at bridge site is used as the initial state, and the final state will be two O^* in two hollow sites. Although O^* is much more stable at fcc hollow site than at hcp hollow site, two O^* at two hcp hollow sites could also be the final state of oxygen dissociation since it is also a local minimum and can be an intermediate state along the whole reaction path. For this reason, two different reaction paths are chosen, which are from bridge site to two fcc hollow sites, and from bridge site to two hcp hollow sites, respectively, as shown in Figure 3.2. In the first path, O_2 molecule rotates toward the fcc hollow site with one oxygen atom still bonding with Pt near top site and stays molecular at the transition state. In the second path, oxygen molecule rotates toward the hcp hollow site in a similar way. However, at the transition state, oxygen-oxygen bond is already broken. The geometries are given in Table 3.3. The barrier energies are 0.37 eV and 0.27 eV for path 1 and path 2 respectively. These low dissociation barriers agree well with several experimental results

[37, 91].

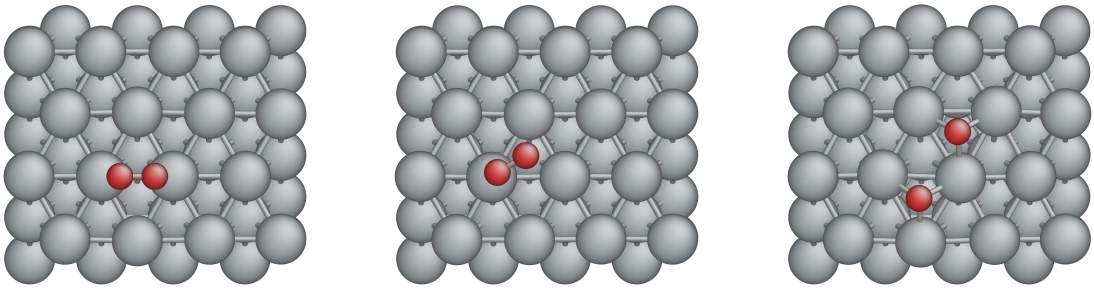

(a)

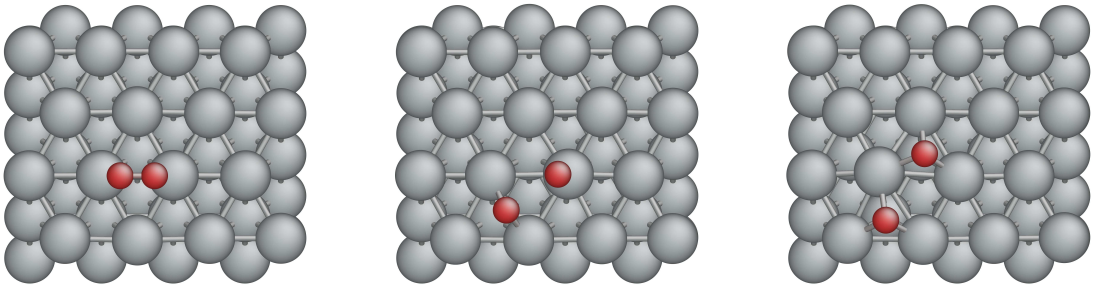

(b)

Figure 3.2: The initial, transition and final states for the reaction path of O_2 dissociation ($O_2^* \rightarrow 2O^*$) in ($2\sqrt{3}\times4$) unit cell. Although initial states are both O_2^* at bridge site, (a) shows the path to the final state with two O atoms at fcc sites and (b) shows the path to the final state with two O atoms at hcp sites.

However, if the unit cell decreases to ($\sqrt{3}\times2$), although the geometries of the saddle points do not change very much, the dissociation barriers increase a lot. The barrier of path 2 mentioned above increases to 0.52 eV, which again illustrates the strong dependence on oxygen coverage. This could also explain the overestimation of the dissociation barrier by previous DFT calculations. In Eichler's calculation, the unit cell was ($\sqrt{3}\times2$) and the

activation energy was explored only on fixed paths[24]. In Šljivančanin's calculation[145], a larger unit cell was used, but it was still smaller than ($2\sqrt{3}\times4$). Generally, a trend can be identified here that when O_2 coverage is small, it is much easier to dissociate.

3.1.3 Reaction Paths on Pt(111) Surface

After obtaining the chemisorbed O^* and H^* atoms, the work that remains is just to add H^* to O^* one by one. The calculations have been performed by Michaelides and Hu, and they are repeated here for consistency check. The energetic results from both sources are almost identical, as shown in Table 3.4.

Table 3.4: The reaction energy (ΔE) and activation barrier (E_a) of reaction path of water formation from O^* and H^* atoms. Data in brackets are from Michaelides and Hu[85].

	ΔE [eV]	E_a [eV]
$O^*+H^* \rightarrow OH^*$	-0.20	0.91(0.94)
$OH^*+H^* \rightarrow H_2O^*$	-0.75	0.14(0.21)

The detailed reaction path in ($\sqrt{3}\times2$) unit cell is shown in Figures 3.3 and 3.4 and some important geometrical parameters are given in Table 3.5 and 3.6, respectively. For reaction (3.1), the initial state is O at fcc hollow site and H at top site (Fig. 3.3), then O and H atoms come close to each other along <112> direction and finally OH stays at bridge site with O atom connected to two nearby Pt atoms. Meanwhile, it is calculated that OH at top site is only 0.02 eV less stable than OH at bridge site so we can consider them as nearly degenerate intermediate states. As Michaelides mentioned, a lot of the energy barrier comes from O^* diffusion, since at the saddle point O^* moves from fcc hollow site to a bridge-like site. We have calculated isolated O^* atom diffusion barrier from fcc site to neighboring hcp site to be 0.62 eV, which is a significant fraction of the reaction (3.1) barrier. After OH formation, adding another H to it is very easy. As shown in Fig. 3.4, during reaction (3.2) O atom always stays close to the top site and only H^* atom needs to make large movements, which

costs small amount of energy as calculated in Sec. 3.1.2. We also check the coverage effect on the barrier of OH formation and find that it just increases a little, from 0.91 to 1.0 eV, when the unit cell changes to $(2\sqrt{3}\times4)$. This means the coverage dependence of reaction (3.1) is smaller than that of oxygen dissociation.

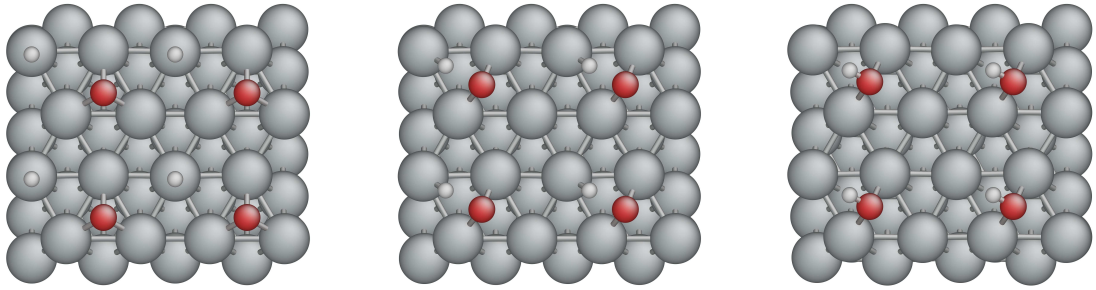

Figure 3.3: The initial, transition and final states for the reaction path of OH formation ($O^*+H^* \rightarrow OH^*$) in $(\sqrt{3}\times2)$ unit cell.

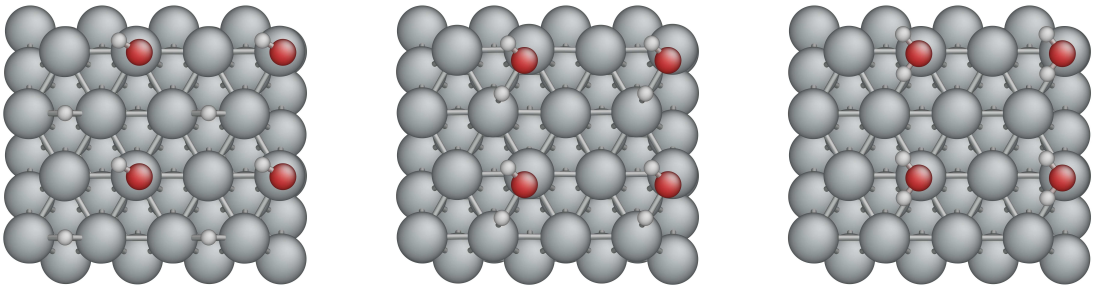

Figure 3.4: The initial, transition and final states for the reaction path of H_2O formation ($OH^*+H^* \rightarrow H_2O^*$) in $(\sqrt{3}\times2)$ unit cell.

As mentioned above, the barrier of OH formation seems too high for Pt to be a reasonably good catalyst above $T_{\rm des}$ ~170 K. There may be some explanations for this; for example, there could be other sites such as steps, kinks and other defects [141]. However, here we offer a possible intrinsic mechanism. It involves the direct protonation of O_2^* molecular precursors (Table 3.7),

Table 3.5: Geometries of initial (I), transition (T) and final (F) states of reaction (3.1) in $(\sqrt{3}\times 2)$ unit cell. The notation follows Table 3.3. All lengths are in Å.

	$d_{\text{O-H}}$	$d_{\text{Pt-O}}$	d_z(O)	$d_{\text{Pt-H}}$	d_z(H)
I	3.22	2.05	1.16	1.56	1.56
T	1.59	2.05	1.44	1.67	1.30
F	0.99	2.17	1.63	2.59	2.01

Table 3.6: Geometries of initial (I), transition (T) and final (F) states of reaction (3.2) in $(\sqrt{3}\times 2)$ unit cell. There are two H atoms and H_a is the one which is initially absorbed separately on Pt surface. The notation follows Table 3.3. All lengths are in Å.

	$d_{\text{O-H}_a}$	$d_{\text{Pt-O}}$	d_z(O)	$d_{\text{Pt-H}_a}$	$d_z(H_a)$
I	3.89	2.00	1.99	1.75	1.05
T	1.68	2.06	2.01	1.64	1.43
F	0.98	2.48	2.48	2.72	2.49

$$O_2^* + H^* \rightarrow OOH^* \tag{3.4}$$

followed by

$$OOH^* + H^* \rightarrow 2OH^* \tag{3.5}$$

and then reaction (3.2), because O_2^* has a finite lifetime on the platinum surface. Indeed, as shown in Sec. 3.1.2, the O_2^* dissociation barrier is strongly dependent on the coverage, so O_2^* may exist for a much longer time on Pt (111) surface if P_{O_2} is large. The Langmuir-Hinshelwood pathway we propose here differs from the Eley-Rideal pathways studied theoretically before[120, 147, 148], in that H^* is already adsorbed on the surface and stays close to the surface during the reaction.

Table 3.7: The reaction energy (ΔE) and activation barrier (E_a) of reaction path of water formation from O_2^* molecule and H^* atom.

	ΔE [eV]	E_a [eV]
O_2^*+H^* →OOH^*	-0.18	0.42
OOH^*+H^* →$2OH^*$	-2.19	0.31
OH^*+H^* →H_2O^*	-0.75	0.14

The path we obtain is described in the following. As shown in Figure 3.5, initially O_2^* is at bridge site and H^* at a top site nearby. Then H^* comes close to O_2^* and directly forms a hydroperoxyl intermediate OOH^*, which has one O atom connected to Pt at top site and the remaining OH part a little away from the surface. However, the two O atoms still connect to each other and stay around the bridge site. The geometry is given in Table 3.8. Although there are large movements of the two O atoms, they always stay bonded during the whole process, and it costs only 0.42 eV energy to reach the saddle point.

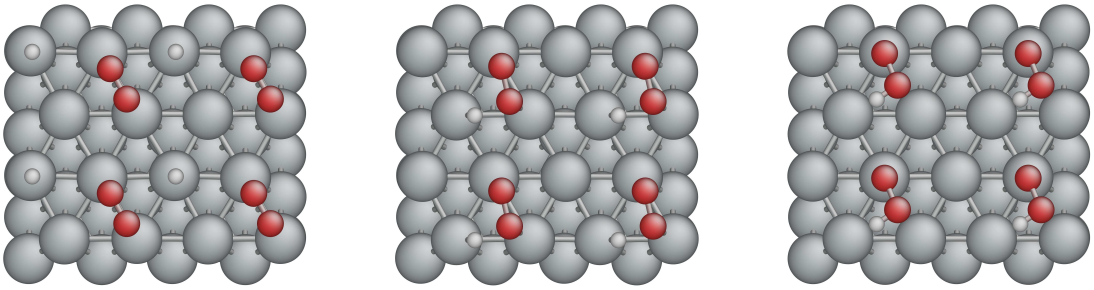

Figure 3.5: The initial, transition and final states for the reaction path of OOH formation (O_2^*+H^* $\rightarrow$$OOH^*$) in ($\sqrt{3}\times2$) unit cell.

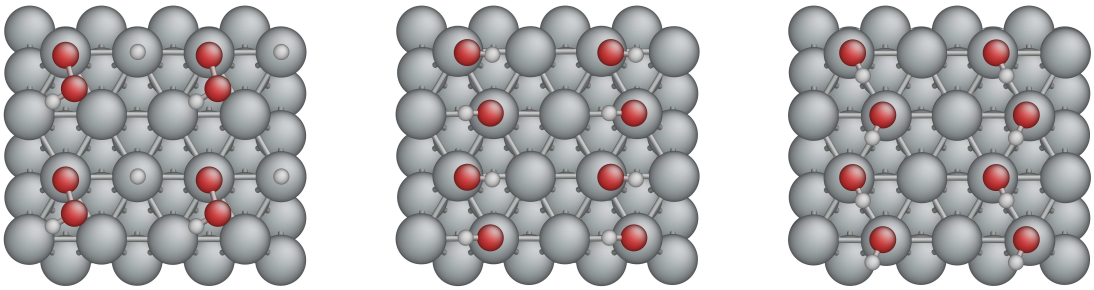

Figure 3.6: The initial, transition and final states for the reaction path of 2OH formation (OOH^*+H^* $\rightarrow$$2OH^*$) in ($\sqrt{3}\times2$) unit cell.

In the next step, there are two possible choices: one is that OOH^* dissociates to one O^* and one OH^*, but then it comes back to the previous reaction pathway where there is still

a large barrier to form OH^* from isolated O^*; the other is directly adding another H atom to this OOH^* to form two isolated OH^*. The minimum energy path is shown in Figure 3.6 and some geometrical parameters are given in Table 3.9. Initially, both OOH^* and H^* are at top sites. Finally there are two OH^* at two neighboring top sites, forming a chain of hydrogen bonds. The barrier energy is only 0.31 eV. The whole reaction can then finish via (3.2).

Table 3.8: Geometries of initial (I), transition (T) and final (F) states of reaction (3.4) in $(\sqrt{3}\times 2)$ unit cell. There are two O atoms: O_a is the one which is finally connected with H atom, and O_b is the other one. The notation follows Table 3.3. All lengths are in Å.

	$d_{O_a\text{-}H}$	$d_{O_a\text{-}O_b}$	$d_{Pt\text{-}O_a}$	$d_z(O_a)$	$d_{Pt\text{-}O_b}$	$d_z(O_b)$	$d_{Pt\text{-}H}$	$d_z(H)$
I	4.80	1.35	2.06	1.94	2.06	1.94	1.56	1.56
T	1.56	1.41	2.14	1.93	2.03	1.93	1.64	1.47
F	0.99	1.43	2.88	2.52	2.01	2.01	3.02	2.59

Table 3.9: Geometries of initial (I), transition (T) and final (F) states of reaction (3.5) in $(\sqrt{3}\times 2)$ unit cell. There are two O atoms: O_a is the one which is initially connected with H atom, and O_b is the other one. Similarly, H_a is the H atom initially connected with O atom and H_b is the other. The notation follows Table 3.3. All lengths are in Å.

	$d_{O_b\text{-}H_b}$	$d_{O_a\text{-}O_b}$	$d_{Pt\text{-}O_a}$	$d_z(O_a)$	$d_{Pt\text{-}O_b}$	$d_z(O_b)$	$d_{Pt\text{-}H_b}$	$d_z(H_b)$
I	2.87	1.43	2.87	2.48	2.02	2.02	1.56	1.56
T	1.50	1.48	2.47	2.33	2.16	2.04	1.67	1.42
F	1.01	2.70	2.00	1.99	1.99	1.99	2.44	2.22

The reason for the low barrier of (3.4) is that there is no motion of isolated O^* atom on the surface, which has been shown to involve a large energy barrier. Since the reaction starts from a whole O_2^* molecule, this path could be important when the oxygen coverage is high so that the O_2^* dissociation barrier is large enough to keep O_2^* existing for a while. This is possible, since in $(\sqrt{3}\times 2)$ unit cell O_2^* dissociation barrier is higher than the OOH^* formation barrier. Another problem with this new path is that OOH^* may not be a long-lived intermediate [10] because it could dissociate into O^* and OH^* quickly. However, if there are a lot of H^* and/or O^* atoms around (large P_{H_2} and/or P_{O_2}), this path is still

possible.

The whole reactions (3.1)+(3.2) and (3.4)+(3.5)+(3.2) are compared in Figure 3.7. Obviously, no matter which catalyst and which path are chosen, the total reaction energy should be a constant, which is -5.08 eV from isolated molecule DFT calculations with the parameter setting described in Sec. 3.1.1. However, this number cannot be obtained by simply adding the individual step reaction energies, due to lateral interactions in the small calculation cell. For example, in ($\sqrt{3}\times 2$) unit cell, if we compare the energy of surface plus one adsorbed O^* atom, surface plus one absorbed H^* atom and surface plus both adsorbed O^* and H^* atoms, it is found that there is a repulsion energy of 0.12 eV between O^* and H^*. So the real reaction energy of (3.1) should be added by 0.12 eV in ($\sqrt{3}\times 2$) unit cell. By adding these kinds of corrections to the initial and final states of all elementary reaction steps, the whole reaction paths are drawn in Figure 3.7, where the net reaction energy is -5.08 eV in both cases.

3.2 Oxygen Reduction on (111) Surfaces of Other FCC Metals

As DFT calculations in Section 3.1 confirm that Pt has good catalytic activity for oxygen reduction as Eq. 1.3 under UHV conditions, the following question is naturally raised that whether and why other metals instead of Pt can (not) be good catalyst. To answer this general question, we should get help from the famous Sabatier principle, which gives a qualitative criterion to choose good catalyst for certain reaction[112]. This principle says that the surface adsorption energies of the reactants, intermediates and products for the studied reaction should be in some optimal range for a good catalyst. The adsorption energies should be strong enough to induce surface reaction, such as dissociation of reactant molecules. However, they should not be too strong to assure only short residence time for

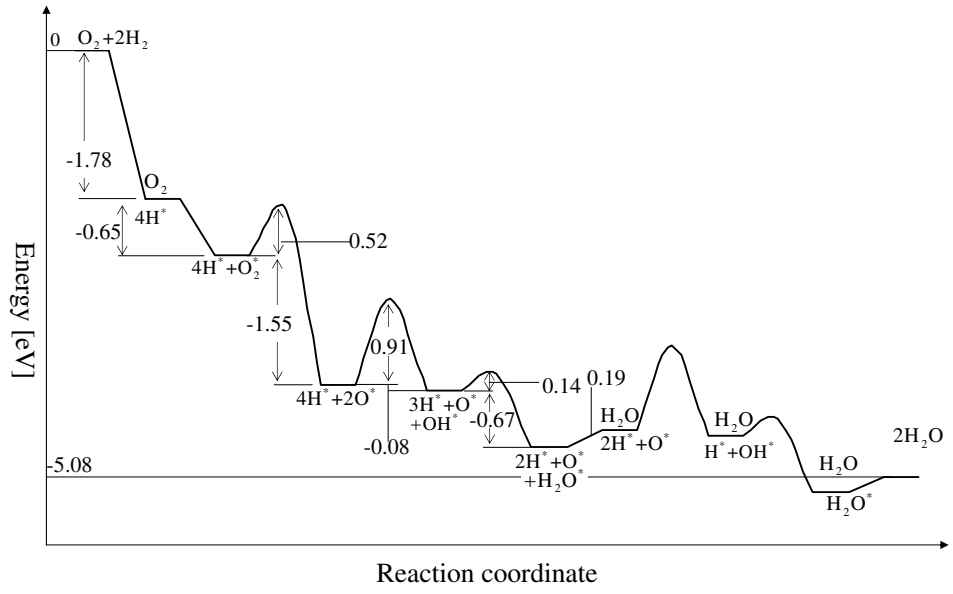

(a)

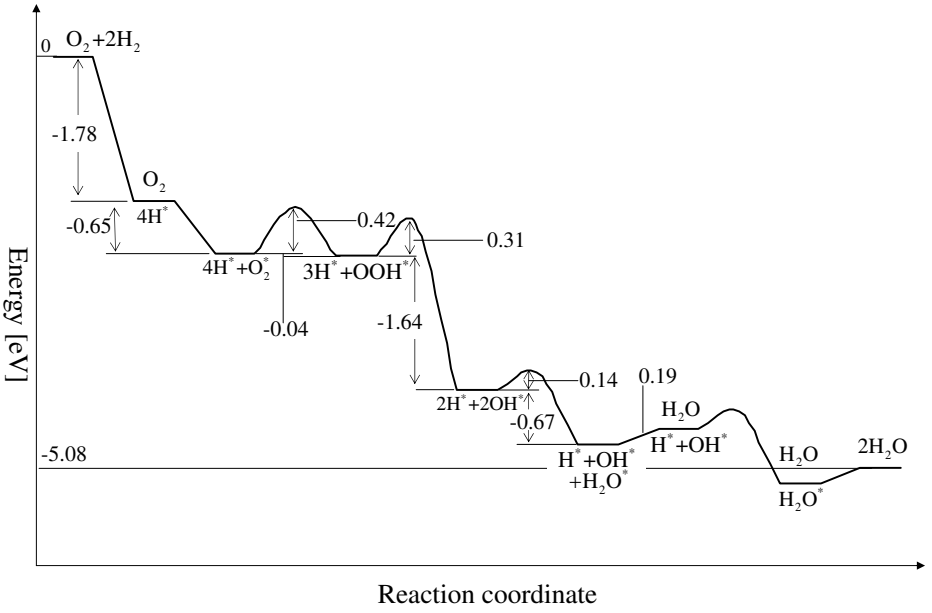

(b)

Figure 3.7: The whole reaction path of water formation: (a) shows the path starting by dissociation of O_2^*, (b) shows the path starting by formation of OOH^*.

the surface intermediates and rapid desorption of the product molecules. In this section, this principle is testified by DFT calculations for oxygen reduction reaction on (111) surface of two typical transition metals with FCC lattice structure, Cu and Au. The results indeed show that both Cu and Au have poor catalytic activity for reaction in Eq. 1.3, which result from opposite factors: Cu has too strong adsorption energies for surface adsorbates such as oxygen atom and hydroxyl, while Au has too weak adsorption energies for them. On the other hand, these adsorption energies on Pt (111), between the corresponding values on Cu and Au, happen to be close to the optimal values for good catalytic activity, supporting the validity of Sabatier principle.

3.2.1 Adsorption on Cu (111) and Au (111) Surfaces

Since adsorption energies and catalytic activity are correlated with each other according to Sabatier principle, the adsorptions of four important intermediates in oxygen reduction under UHV conditions, O_2 molecules, O atom, hydroxyl OH and H atom, are calculated on both Cu and Au (111) surface, and their adsorption energies are defined as the following:

$$E_{\text{ads}}^{\text{O}_2^*} = E_{\text{surface}+\text{O}_2^*} - E_{\text{surface}} - E_{\text{O}_2} \tag{3.6}$$

$$E_{\text{ads}}^{\text{O}^*} = E_{\text{surface}+\text{O}^*} - E_{\text{surface}} - \frac{1}{2}E_{\text{O}_2} \tag{3.7}$$

$$E_{\text{ads}}^{\text{OH}^*} = E_{\text{surface}+\text{OH}^*} - E_{\text{surface}} - E_{\text{OH}} \tag{3.8}$$

$$E_{\text{ads}}^{\text{H}^*} = E_{\text{surface}+\text{H}^*} - E_{\text{surface}} - \frac{1}{2}E_{\text{H}_2} \tag{3.9}$$

where * means intermediates in adsorption state. So for certain adsorbate, the more negative E_{ads} is, the stronger the adsorption is.

The results are listed in Table 3.10, which shows a general tendency that the adsorption energy for certain adsorbate always increases in the order Au $<$ Pt $<$ Cu. This trend origins from their different surface electronic structures[44]: when atoms/molecules contact with

Table 3.10: The adsorption energies of surface intermediates at different sites in a ($\sqrt{3}\times2$) unit cell of Pt(111) from Section 3.1.

	Cu	Pt	Au
$E_{\text{ads}}^{\text{O}_2^*}$	-0.48	-0.65	-0.02
$E_{\text{ads}}^{\text{O}^*}$	-1.47	-1.10	+0.04
$E_{\text{ads}}^{\text{OH}^*}$	-3.12	-2.40	-2.06
$E_{\text{ads}}^{\text{H}^*}$	-0.61	-0.50	-0.00

metal surface, there would be overlapping between electrons from adsorbates and metal d states, which raises the kinetic energies of electrons because of Pauli repulsion; The amount of energy increase is approximately proportional to the square of the adsorbate-metal d coupling matrix element V_{ad}^2, and V_{ad}^2 on Cu surface is only about $\frac{1}{4}$ of those on Pt or Au. Thus, Cu has the strongest adsorption energies for atoms/molecules. On the other hand, for Pt and Au whose V_{ad}^2 are similar with each other, the relative adsorption strengths can be explained by *d*-band center theory[45, 46, 84]: after adsorption, the HOMO of the adsorbate forms both bonding and anti-bonding orbitals by interaction with the continuous band structures of the surface; when the *d*-band structure of transition metal surface has lower average energy (the *d-band center*) relative to the Fermi level, the position of anti-bonding orbital also goes down, resulting in more filling of this orbital and weakening of adsorption. Thus, the lower the *d*-band center of the surface is, the weaker the adsorption for certain adsorbate is. DFT calculations indeed confirm that the *d*-band center of Au surface is 1.31 eV lower than Pt[44].

3.2.2 Reaction Paths on Cu (111) Surface

Compared with noble metals such as Pt, Au and Ag, Cu is much more chemically active. When exposed to air at room temperature, Cu surface can react with O_2, H_2O and CO_2 to form copper(II) carbonate, indicating that Cu surface has strong chemical affinity and adsorption energies for these small molecules and atoms, which have been confirmed by the

above DFT calculations. The strong adsorption energies would affect the minimum-energy paths for oxygen reduction on Cu (111) surface, whose reaction pathways are calculated by DFT+NEB methods in $(\sqrt{3}\times 2)$ unit cell as described in Sec. 3.1.1.

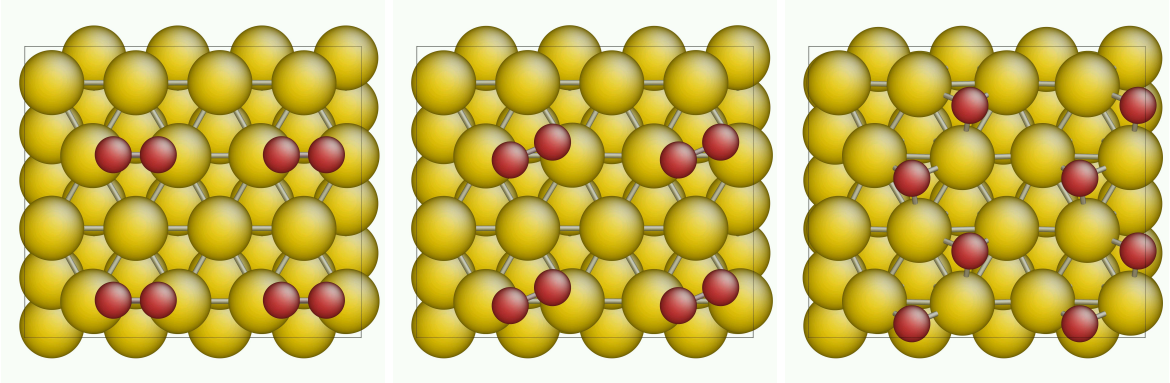

Figure 3.8: The initial, transition and final states for the reaction path of O_2 dissociation ($O_2^*\rightarrow 2O^*$) in ($\sqrt{3}\times 2$) unit cell of Cu (111) surface.

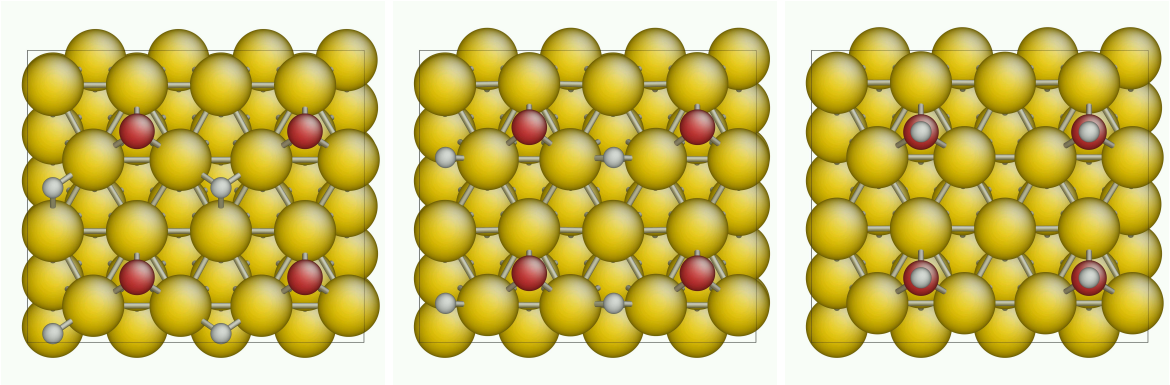

Figure 3.9: The initial, transition and final states for the reaction path of OH formation ($O^*+H^* \rightarrow OH^*$) in ($\sqrt{3}\times 2$) unit cell of Cu (111) surface.

First, the dissociated oxygen molecular adsorption is calculated; the energetic data (the reaction energy (ΔE) and activation barrier (E_a)) is shown in Table 3.11 and the configurations of minimum-energy path are shown in Fig. 3.8. Different from Pt (111) surface, there is almost no energy barrier for the dissociation of oxygen molecule because of the strong adsorption energy, which indicates almost spontaneous oxygen dissociation after

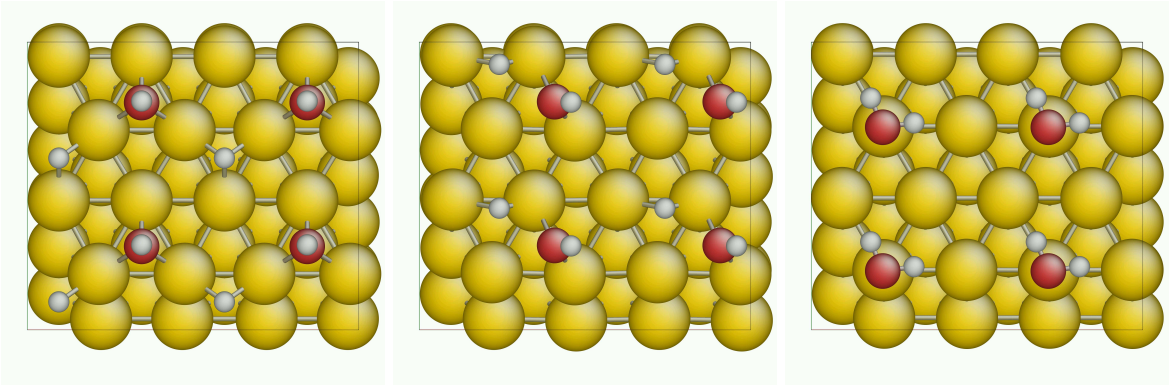

Figure 3.10: The initial, transition and final states for the reaction path of H_2O formation ($OH^*+H^* \rightarrow H_2O$) in ($\sqrt{3}\times 2$) unit cell of Cu (111) surface.

the adsorption. For this reason, the hydroperoxyl-mediated pathway proposed for Pt (111) surface may not occur on Cu (111) surface because of the short lifetime of adsorbed oxygen molecule.

Table 3.11: The reaction energies (ΔE) and activation barriers (E_a) of oxygen reduction on Cu (111) surface at UHV conditions.

	ΔE [eV]	E_a [eV]
$O_2^* \rightarrow 2O^*$	-1.58	0.02
$O^*+H^* \rightarrow OH^*$	-0.83	0.33
$OH^*+H^* \rightarrow H_2O^*$	-0.23	0.84

In the next two steps, OH formation (Eq. 3.1) and H_2O formation (Eq. 3.2) are also calculated with results shown in Table 3.11 and configurations shown in Fig. 3.9 and 3.10. Compared with the corresponding values on Pt (111) surface shown in Table 3.4, there are several significant changes for the minimum-energy paths on Cu (111) surface. First, the stability of adsorbed hydroxyl (OH^*) increases largely, which results in significant increase of ΔE for OH formation (-0.20 eV on Pt vs. -0.83 eV on Cu) and decrease of ΔE for H_2O formation (-0.75 eV on Pt vs. -0.23 eV on Cu) in ($\sqrt{3}\times 2$) unit cell. It is also observed that the most favorable adsorption site of OH on (111) surface changes: on Pt surface, the top and bridge sites are almost energy-degenerate favorable sites as shown in Fig. 3.3 and

3.4; on Cu surface the fcc hollow site is the most favorable site as shown in Fig. 3.9 and 3.10. Second, because of the significant changes in reaction driving forces, the activation energies E_a also vary. E_a for OH formation is only 0.33 eV, but E_a for H_2O formation is as large as 0.84 eV, which means the rate-determining step (RDS) for the whole oxygen reduction reaction on Cu (111) surface is its final elementary step, H_2O formation as Eq. 3.2. Because of the high E_a value for RDS, Cu (111) does not have high catalytic activity for oxygen reduction by hydrogen molecules, since it surface reaction sites would be covered by a lot of stable adsorbed hydroxyl (OH^*).

3.2.3 Reaction Paths on Au (111) Surface

Different from Cu with too strong affinity to small molecules, Au has the opposite effect: too weak interaction with its surface adsorbates. When one oxygen molecule is placed in a $(\sqrt{3} \times 2)$ unit cell of Au (111) surface, DFT calculation shows that the adsorption energy is almost zero (-0.02 eV) and the equilibrium distance of oxygen molecule to Au surface is as large as 3.21 Å. A similar situation occurs for the adsorption of hydrogen molecule. It only shows considerable adsorption energies for the unstable atoms and molecules with unpaired electrons, such as OOH, O and OH.

Table 3.12: The reaction energy (ΔE) and activation barrier (E_a) of reaction path of oxygen reduction from O_2^* molecule and H^* atom on Au (111) surface.

	ΔE [eV]	E_a [eV]
$O_2^*+H^* \rightarrow OOH^*$	-0.85	0.68
$OOH^*+H^* \rightarrow 2OH^*$	-2.42	0.09
$OH^*+H^* \rightarrow H_2O^*$	-1.86	0.05

Because of the weak adsorption energies, oxygen dissociation should have a huge energy barrier on Au (111) surface. So the hydroperoxyl-mediated pathway proposed for Pt (111) surface is a better choice for the minimum-energy path of oxygen reduction on

Au (111) surface. The calculation results are shown in Table 3.12 and the corresponding configurations shown in Fig. 3.11, 3.12 and 3.13. It indicates that hydroperoxyl (OOH^*) formation is the RDS with E_a=0.68 eV. Once OOH^* is produced, the next two steps ($OOH^*+H^* \rightarrow 2OH^*$ and $OH^*+H^* \rightarrow H_2O$) can proceed with small energy barriers (<0.1 eV). However, because of the high value of E_a for RDS, the total reaction rate is still negligible. In addition, it is found that even hydrogen dissociation on Au surface is quite difficult with E_a as high as 0.7 eV. Thus, when Au (111) surface is exposed to the mixture of oxygen and hydrogen molecules at room temperature, there is almost no H_2O produced and the surface would be very clean.

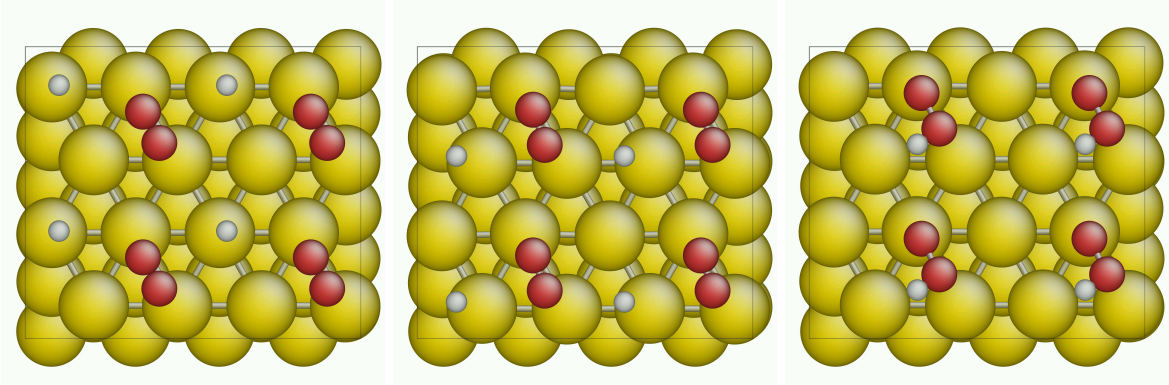

Figure 3.11: The initial, transition and final states for the reaction path of OOH formation ($O_2^*+H^* \rightarrow OOH^*$) in ($\sqrt{3}\times 2$) unit cell of Au (111) surface.

In conclusion, Cu/Au has very low catalytic activity for oxygen reduction at UHV conditions because of too strong/weak adsorption energies for the atoms and molecules on its surface, which satisfies the Sabatier principle. On the other hand, the adsorption energies on Pt surfaces may be just close to the optimal values, which would be the origin of its high catalytic activity. However, this Sabatier principle just gives us a qualitative criterion, but the optimal values of adsorption energies for best catalytic activity are still unknown. In the next section, DFT calculations on Pt alloy surfaces are performed in order to search for such optimal values.

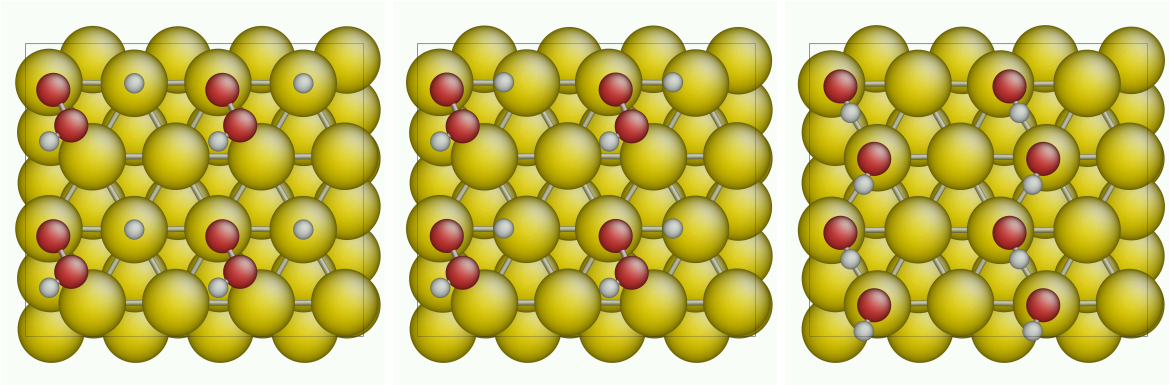

Figure 3.12: The initial, transition and final states for the reaction path of 2OH formation ($OOH^{*}+H^{*} \rightarrow 2OH^{*}$) in ($\sqrt{3}\times 2$) unit cell of Au (111) surface.

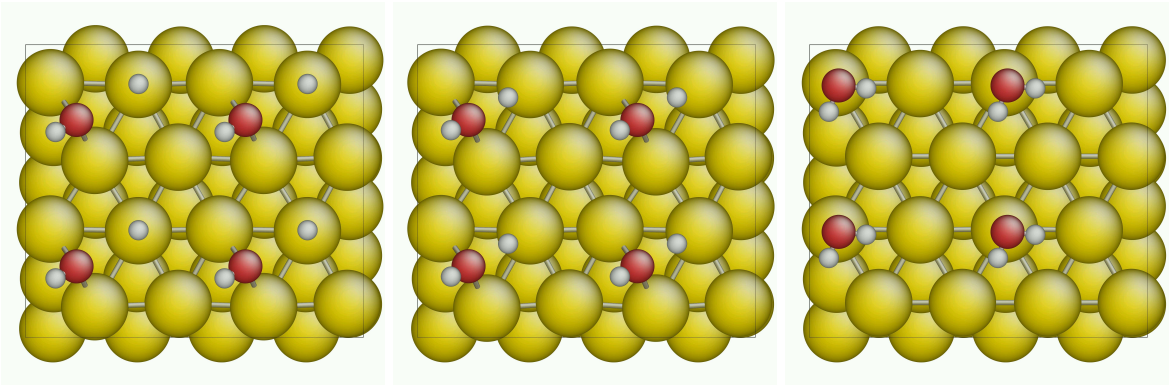

Figure 3.13: The initial, transition and final states for the reaction path of H_2O formation ($OH^{*}+H^{*} \rightarrow H_2O$) in ($\sqrt{3}\times 2$) unit cell of Au (111) surface.

3.3 Oxygen Reduction on (111) Surface of Pt Alloys

Calculations in Section 3.1 and 3.2 suggest that first-principles methods such as DFT can semi-quantitatively explain the good catalytic activity of pure Pt instead of other metals (Au and Cu) in oxygen reduction at UHV conditions. A following question is then naturally raised that whether DFT methods can reveal the catalytic activity of other materials, such as Pt alloys, which may have better catalytic activity than pure Pt for electrochemical oxygen reduction in PEM fuel cell. Thus, in this section, the same DFT calculation procedures as Section 3.1 are performed on (111) surfaces of several Pt alloys in order to check whether there is similar catalytic activity increase for oxygen reduction at UHV conditions.

There are a lot of studies of electrocatalytic activities of Pt alloys for oxygen reduction reaction (ORR). Mukerjee et al. investigated five carbon-supported binary Pt alloy electrocatalysts (PtCr, PtMn, PtFe, PtCo and PtNi with Pt:M all equal to 3:1) and found an increase of performance in all these alloys compared with Pt/C electrocatalyst[87, 88]. The electrocatalytic activities decrease in the order PtCr $>$ PtFe $>$ PtMn $>$ PtCo $>$ PtNi $>$ Pt. Meanwhile, the electrocatalytic activities of bulk Pt_3Ni and Pt_3Co were studied in perchloric and sulfuric acid[124]. In $HClO_4$ at 293 K the activity of Pt_3Co is the best and a factor of two higher than that of pure Pt. In sulfuric acid solution, affected by specific adsorption of bisulfate anions, the activities order changed to $Pt_3Ni > Pt_3Co >$ Pt. A benchmark experiment of electrocatalytic activity for Pt and Pt alloys for PEM fuel cell was accomplished and found Pt_xCo_{1-x}/C has almost twice mass activity compared with pure Pt/C[33]. Recently, Stamenkovic et al. showed that the electrocatalytic activities on Pt_3M (M=Ni, Co, Fe, Ti, V) surfaces for the ORR can be related to the experimentally determined surface electronic structures (*d*-band centers as discussed in Sec. 3.2.1), which decide the adsorption energies of reaction intermediates[125, 126].

Since catalytic performance of certain material usually depends on its surface struc-

tures, the atomic configurations of these Pt alloys are also well studied. When the 3d transition metal M is one of the elements in the periodic table from V through Ni, the ordered PtM alloys have the CuAu-type ($L1_0$) structure, whereas the Pt_3M and PtM_3 alloys usually have the Cu_3Au-type ($L1_2$) structure. Mukerjee et al. used XRD to confirm that at room temperature all the alloys (PtCr, PtMn, PtFe, PtCo and PtNi- all 3:1 Pt:M stocis) exist in high degree crystallized states composed primarily of Pt_3M in $L1_2$-type lattice[88]. Joyner et al. used low-energy ion scattering spectroscopy measurements (LEISS) to study the $Pt_{70}Cr_{30}$ alloy film and showed that the top layer is significantly enriched in Pt[60]. Particularly, Stamenkovic et al. found that (111) surface of Pt_3Ni, with pure Pt top layer and $L1_2$-structure bulk lattice, is the stable surface configuration and can have 10-fold more activity for the ORR than the corresponding Pt(111) surface. In the following, this (111) surface structure will be used by first-principles calculations to study the reaction paths of the catalytic oxygen reduction reaction of Eq. 1.3 and the corresponding activation energies on Pt_3M alloys.

Here three Pt_3M alloys (Pt_3Ti, Pt_3Cr and Pt_3Co) are chosen. All Pt_3M alloy (111) surfaces are modeled as a four-layer slab, which is composed of three Pt_3M layers in $L1_2$ structure and a top layer with pure Pt, separated by five layers equivalent of vacuum. In the most basic setup, we use a trigonal (2×2) unit cell where there are 4 atoms in each layer with a Monkhorst-Pack **k**-point grid of $5\times5\times1$ for Brillouin-zone integration[86]. All calculations are performed at the corresponding equilibrium Pt_3M (in $L1_2$ structure) lattice constant as found from VASP geometry optimization, as shown in Table 3.13. Atoms on the top two layers and the adsorbate atoms are allowed to relax freely. All other calculation parameters and techniques, such as NEB method for activation energies, are the same as those described in Section 3.1.1. Figure 3.14 shows the surface unit cell and some special sites on it (t-top, b-bridge, f-fcc hollow and h-hcp hollow). In the following text, we name this kind of structure Pt_3MPt in order to clarify its difference with pure Pt_3M alloy.

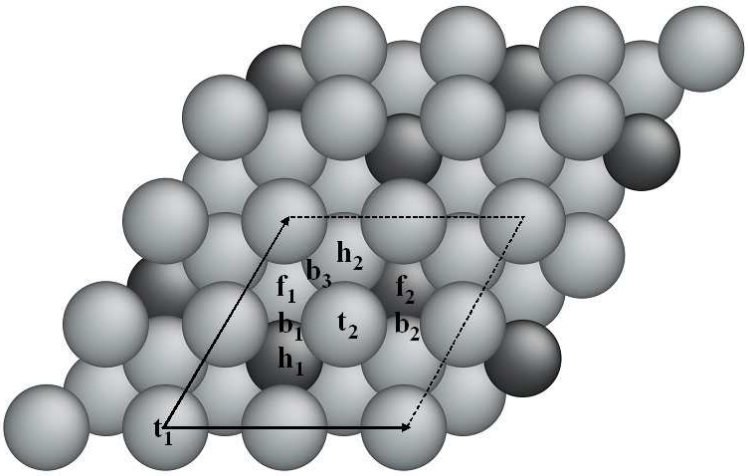

Figure 3.14: Unit cell of Pt_3M (111) surface and short-hand notation of special sites(t_i-top, b_i-bridge, f_i-fcc hollow and h_i-hcp hollow). Here subscripts stand for different sites because of different nearby atoms.

Table 3.13: The equilibrium lattice constant c_0 and the corresponding magnetization m obtained from VASP calculations for pure Pt and Pt_3M alloys

	c_0 (Å)	c_0 (Å,Experimental)	m/unit cell (μ_B)
Pt	3.977	3.924	0.00
Pt_3Co	3.893	3.85[88]	2.95
Pt_3Cr	3.920	3.88[16]	2.72
Pt_3Ti	3.945	N/A	0.00

3.3.1 Adsorptions on (111) Surfaces of Pt Alloys

On (111) surface of pure metals there are only four kinds of high symmetric adsorption sites (top, bridge, fcc hollow and hcp hollow) where surface intermediates exist in a stable or metastable state. Four important intermediates (O_2^*, O^*, OH^* and H^*) at these four sites on pure Pt (111) surface are summarized in Table 3.14. However, on the (111) surface of Pt_3MPt there are more different positions because of different atoms as nearest neighbors. As Fig. 3.14 shows, there are two kinds of top sites, three kinds of bridge sites, two kinds of fcc hollows and two kinds of hcp hollow sites. The adsorption energies on all these sites

are summarized in Table 3.15, 3.16, 3.17 and 3.18.

Table 3.14: The adsorption energy of surface intermediates at different sites in a ($\sqrt{3}\times2$) unit cell of Pt(111) from Section 3.1. N/A means the surface intermediates are quite unstable at the corresponding site compared with other sites. All results are in eV.

	top	bridge	fcc	hcp
$E_{ads}^{O_2^*}$	N/A	-0.65	-0.53	-0.43
$E_{ads}^{O^*}$	N/A	N/A	-1.10	-0.69
$E_{ads}^{OH^*}$	-2.38	-2.40	N/A	N/A
$E_{ads}^{H^*}$	-0.45	-0.44	-0.50	-0.45

Table 3.15: The adsorption energy of O_2, $E_{ads}^{O_2^*}$, at different sites of Pt_3MPt (111) surfaces. Here all letters with subscripts mean symmetric adsorption sites shown in Fig. 3.14 and all results are in eV.

	b_1	b_2	b_3	f_1	f_2
Pt_3CoPt	-0.33	-0.22	-0.32	-0.28	-0.01
Pt_3CrPt	-0.38	-0.30	-0.23	-0.31	-0.10
Pt_3TiPt	-0.34	-0.31	-0.32	-0.30	-0.09

Table 3.16: The adsorption energy of O atom, $E_{ads}^{O^*}$, at different sites of Pt_3MPt (111) surfaces. Here all letters with subscripts mean symmetric adsorption sites shown in Fig. 3.14 and all results are in eV.

	f_1	f_2	h_1	h_2
Pt_3CoPt	-0.81	-0.53	-0.42	+0.03
Pt_3CrPt	-0.87	+0.39	-0.48	-0.48
Pt_3TiPt	-0.91	-0.17	-0.39	-0.47

From Table 3.14 to 3.18, it is clearly shown that in all Pt_3MPt cases, the adsorption energies decrease a lot compared with those of pure Pt cases. Meanwhile, almost all adsorbates with oxygen atom (O_2^*, O^* and OH^*) prefer the adsorption sites near alloy atoms, such as b_1, f_1 and t_2, to the sites away from alloy atoms, such as b_2, f_2 and t_1 (The only exception is Pt_3CoPt case, where OH^* prefer t_1 to t_2.). However, for H^* cases the situation is a little more complex: on top sites, H^* likes t_1 site far away from second layer alloy atoms; on the other hand, when on the fcc hollow sites, it favors f_1 near the alloy atoms.

Table 3.17: The adsorption energy of OH, $E_{ads}^{OH^*}$, at different sites of Pt_3MPt (111) surfaces. Here all letters with subscripts mean symmetric adsorption sites shown in Fig. 3.14 and all results are in eV.

	b_1	b_2	b_3	t_1	t_2
Pt_3CoPt	-2.13	-2.04	-2.15	-2.23	-2.18
Pt_3CrPt	-2.18	-2.09	-2.18	-2.19	-2.24
Pt_3TiPt	-2.23	-2.07	-2.19	-2.20	-2.32

Table 3.18: The adsorption energy of H atom, $E_{ads}^{H^*}$, at different sites of Pt_3MPt (111) surfaces. Here all letters with subscripts mean symmetric adsorption sites shown in Fig. 3.14 and all results are in eV.

	t_1	t_2	f_1	f_2
Pt_3CoPt	-0.36	-0.21	-0.30	-0.19
Pt_3CrPt	-0.32	-0.22	-0.33	-0.18
Pt_3TiPt	-0.37	-0.20	-0.36	+0.02

In addition, there is an approximate tendency that the maximum adsorption energy for certain adsorbate on all the sites increase in the order $Pt_3CoPt < Pt_3CrPt < Pt_3TiPt < Pt$ (the only two exceptions are the maximum $E_{ads}^{O_2^*}$ on Pt_3CrPt is larger than Pt_3TiPt and the maximum $E_{ads}^{H^*}$ on Pt_3CoPt is larger than Pt_3CrPt.). This tendency satisfies with the results that the lattice constant also increases in the same order, as shown in Table 3.13. According to *d*-band center theory[45, 46, 84], when the surface atoms are subjected to tensile strain, the d-orbital overlap is decreased, resulting in a sharpening of the *d*-band and an upshift in its average energy (the *d*-band center). For simple adsorbates, such as H, O, and CO, this results in a stronger adsorption energy when compared to those of the unchanged metal surface. On the other hand, compressive strain on the surface results in lowering of *d*-band center and the adsorption energies of simple adsorbates are expected to decrease.

Besides strain factors, the electronic interaction between two metals, so-called ligand effect[75, 34], could also contribute to the modification of surface electronic structure and consequently the chemical properties in alloy systems. Fig. 3.15 shows the projected *d*-band density of states for the top layer Pt atoms on (111) surfaces of pure Pt, Pt_3MPt alloys

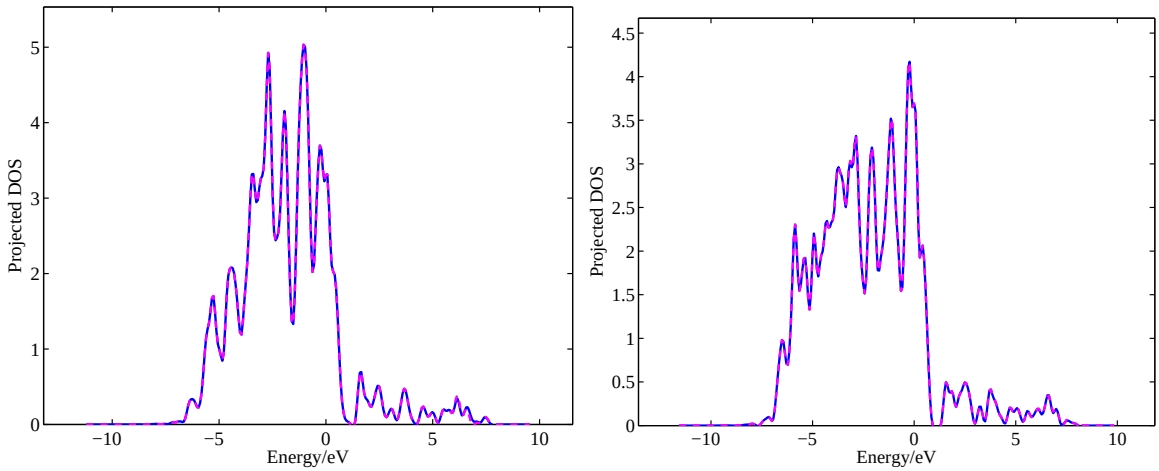

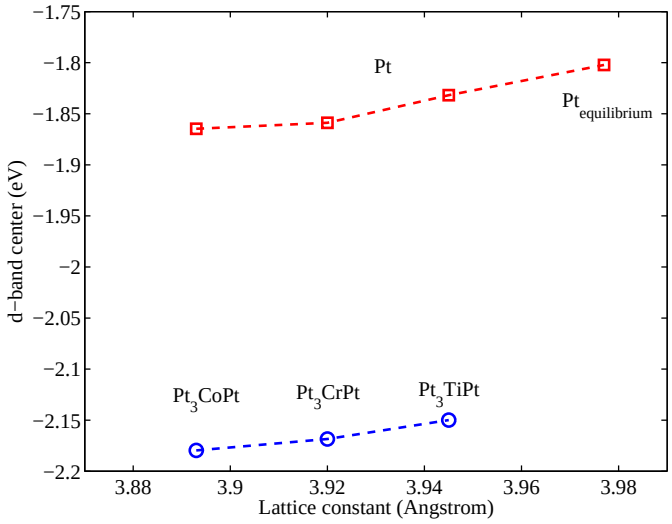

(c)

Figure 3.15: Projected density of states of Pt atoms at the top layer of Pt(a), Pt_3CoPt(b) (111) surfaces, where solid lines stand for spin-up *d*-band and dashed line for spin-down *d*-band, and zero point means Fermi energy level. (c) shows the shift of *d*-band center for these alloys surface and pure Pt surface with the same lattice constant of the corresponding alloy.

and pure Pt with the same lattice constants of Pt_3MPt, respectively. The projected density of states are obtained from projections of the wavefunctions onto spherical harmonics, such as *s*, *p*, *d* orbitals, centered at the positions of studied ions. Usually it requires a cutoff radius for the projection on certain ion, but because we use projector augmented wave (PAW) method[13, 70], a quick method for the calculation of *spd*- and site projected wave function character is applied so that no cutoff radius is needed, which is achieved by setting LORBIT =12 in VASP input parameters[66, 67]. The results indicate that in pure Pt(111) surface cases the compressive strain indeed lowers *d*-band center as expected, as Fig. 3.15(e) shows. Meanwhile, for three Pt_3MPt cases the *d*-band center also shifts up with increasing lattice constant. However, there is a large energy shift ($\sim$ 0.3 eV between Pt_3MPt and pure Pt with same lattice constant) of *d*-band center between pure Pt cases and those in Pt_3MPt case, which indicates that alloy elements largely change the electronic structure including *d*-band center. To compare the strain effect and ligand effect, we define strain contribution ratio C_{strain} to the adsorption energy change as the following:

$$C_{\text{strain}} = \frac{E_{\text{ads}}^{\text{Pt}} - E_{\text{ads}}^{\text{Pt-strain}}}{E_{\text{ads}}^{\text{Pt}} - E_{\text{ads}}^{\text{Alloy}}} \tag{3.10}$$

where $E_{\text{ads}}^{\text{Pt}}$ and $E_{\text{ads}}^{\text{Alloy}}$ are the adsorption energies on pure Pt and Pt alloy surfaces, respectively; $E_{\text{ads}}^{\text{Pt-strain}}$ is the adsorption energy on pure Pt (111) surfaces but with the same lattice constants of Pt_3MPt, as shown in Table 3.13. In Table 3.19, change of $E_{\text{ads}}^{\text{O}^*}$ from strain effect and the corresponding contribution ratio are listed, which show that strain effect indeed makes a significant contribution to the adsorption energy change $\triangle E_{\text{ads}}^{\text{O}^*}$. However, when lattice changes are relatively small, such as Pt_3TiPt (111), ligand effect is still dominant (C_{strain} <0.5); as lattice constant decreases further, the strain effect becomes dominate in the change of adsorption energy ($C_{\text{strain}} \approx 0.8$ for Pt_3CoPt (111) surface).

Table 3.19: The adsorption energy of O atom at fcc hollow site on (111) surface of Pt under the same lattice constant with Pt_3M alloy and its contribution ratio C_{strain} to the total adsorption energy change during alloying. All energy results are in eV.

Lattice constant Å	$E_{ads}^{O^*}$	C_{strain}
3.945 (Pt_3Ti)	-1.02	0.42
3.920 (Pt_3Cr)	-0.95	0.65
3.893 (Pt_3Co)	-0.87	0.79

3.3.2 Reaction Paths on (111) Surface of Pt Alloys

The same as (111) of pure Pt surface as Section 3.1, two different reaction paths are calculated on all Pt_3MPt surfaces. One is made up of oxygen dissociation ($O_2^* \rightarrow 2O^*$ as Eq. 3.3), OH formation ($H^* + O^* \rightarrow OH^*$ as Eq. 3.1) and H_2O formation ($H^* + OH^* \rightarrow H_2O^*$ as Eq. 3.2) sequentially, whose results for Pt_3MPt (111) surfaces are summarized in Table 3.20; the other is by OOH formation ($O_2^* + H^* \rightarrow OOH^*$ as Eq. 3.4), two OH formation ($OOH^* + H^* \rightarrow 2OH^*$ as Eq. 3.4)) and H_2O formation as Eq. 3.2, whose results for Pt_3MPt (111) surfaces are summarized in Table 3.21. Although there are different adsorption sites for certain adsorbates as shown in Fig. 3.14, which makes each elementary step occur at different sites with different activation/reaction energies, the calculations of adsorption in Sec. 3.3.1 show that some sites have stronger affinity to the surface adsorbates than others, so that all elementary steps for oxygen reduction at UHV conditions are calculated on/near these favorable sites.

Table 3.20: The activation energetics for every elementary step in oxygen reduction at UHV conditions on Pt_3MPt (111) surface, starting from oxygen dissociation. All results are in eV.

	$O_2^* \rightarrow 2O^*$	$H^* + O^* \rightarrow OH^*$	$H^* + OH^* \rightarrow H_2O^*$
Pt	0.52	0.91	0.19
Pt_3CoPt	0.68	0.83	0.28
Pt_3CrPt	0.64	0.84	0.37
Pt_3TiPt	0.52	0.94	0.55

Similar as Pt(111) surface, the activation energy for certain surface reaction comes

Table 3.21: The activation energetics for every elementary step in oxygen reduction at UHV conditions on Pt_3MPt (111) surface, starting from OOH formation. All results are in eV.

	$O_2^* + H^* \rightarrow OOH^*$	$OOH^* + H^* \rightarrow 2OH^*$	$H^* + OH^* \rightarrow H_2O^*$
Pt	0.42	0.31	0.19
Pt_3CoPt	0.19	0.25	0.28
Pt_3CrPt	0.19	0.30	0.37
Pt_3TiPt	0.18	0.39	0.55

from two parts: the first one is the repulsion energy between the reactants, the second part is from the "diffusion" contribution in the process that reactants have to move from local stable positions to the saddle point positions. In these catalytic oxygen reduction reactions, the reactants and intermediates with O atom (such as O^* and OH^*) have much higher adsorption energies and diffusion activation energies than H^* atom, so that in elementary reaction steps H^* atom moves a much longer distance than oxygen species, which finally results in two different effects as the following.

On one hand, the "diffusion" contributions of oxygen species such as O^* and OH^* to total activation barriers are mainly decided by the depth of the local potential wells, which can be quantitatively described by the adsorption energies at the corresponding local sites. As a result, a clear tendency of activation energy change for these Pt_3MPt alloys can be found that the energy barriers for oxygen dissociation (reaction 3.3), OH formation (reaction 3.1), two OH formation (reaction 3.5) and H_2O formation (reaction 3.2) always increase in the order $Pt_3CoPt < Pt_3CrPt < Pt_3TiPt$ as the adsorption energies for O^* and OH^* both increase in the same order. On the other hand, if compared with pure Pt, this tendency is not quite correct. For example, in H_2O formation (reaction 3.2), although pure Pt has larger adsorption energy of both OH and H atom, the activation barrier on Pt(111) surface is much lower than those on Pt_3MPt. The reason for such abnormality may result from the inhomogeneity of $E_{ads}^{H^*}$ on Pt_3MPt surface. Because H atom usually moves a large distance on the surface during each elementary reaction step, its "diffusion" contribution

to total reaction barrier is not only decided by local adsorption energy $E_{\mathrm{ads}}^{\mathrm{H}^*}$, but is also strongly affected by its inhomogeneity of $E_{\mathrm{ads}}^{\mathrm{H}^*}$ on different sites. As shown in Table 3.14, on pure Pt (111) surface, $E_{\mathrm{ads}}^{\mathrm{H}^*}$ is almost the same on different symmetric sites so there is almost no diffusion barriers for H atom. However, on Pt_3MPt surface, as Table 3.18 shows, there are distinct differences on different sites, which increase H diffusion barrier and the corresponding contribution to the activation energy of elementary reaction steps, such as reaction 3.2.

Generally speaking, the effect of alloying brings two competing factors to the activation energy in oxygen reduction at UHV conditions: the weaker adsorptions of intermediate species with oxygen atom (such as O^* and OH^*) decrease their "diffusion" contributions to activation energies, but the inhomogeneity of H adsorption energy makes a positive "diffusion" contribution to activation energies. Decided by two factors, the activation energies on Pt_3MPt alloy surface can be either larger or smaller than those on pure Pt surface.

If we compare the highest reaction barrier in either reaction path I (reaction 3.3, 3.1 and 3.2) or path II (reaction 3.4, 3.5 and 3.2), it is found the maximum activation energy in either path decreases in the order $Pt_3TiPt > Pt > Pt_3CrPt > Pt_3CoPt$, which suggests that the catalytic activity may increase in the order $Pt_3TiPt < Pt < Pt_3CrPt < Pt_3CoPt$ in both cases at UHV conditions. This activity sequence "accidentally" agrees with its counterpart for electrochemical oxygen reduction reaction.

In summary, for a catalytic reaction, the interaction strengths between the catalyst surface and the reaction intermediates determine the total reaction rate. For oxygen reduction at UHV conditions as Eq. 1.3, the good catalytic activity of Pt instead of other metal origins from its adsorption energies for certain oxygen species (oxygen molecule, oxygen atom, hydroxyl ...) close to the optimal values for the highest reaction rate, so that there are reaction paths with lower activation energies on Pt surface. To support this conclusion, we show two opposite cases, Cu/Au with too strong/weak adsorption strengths, and the rate

determining steps with huge activation barriers are found on both surfaces. In addition, the activation energies on Pt surface can be further decreased on Pt alloy, where the adsorption energies decrease from pure Pt. To obtain the exact optimal values, a statistical model of total oxygen reduction reaction is needed to obtain the accurate reaction rate at certain temperature and partial pressures. Since our purpose is to understand electrochemical oxygen reduction, we did not build such a model for this reaction at UHV conditions.

Chapter 4

First-Principles Studies of Electrochemical Oxygen Reduction Reaction

Electrochemical oxygen reduction reaction (ORR) on the cathode of PEM fuel cell (Eq. 1.2) is much more complex than its counterpart at ultra-high-vacuum (UHV) conditions (Eq. 1.3). On the cathode, hydrogen species are supplied by hydrated proton combined with water molecules, so-called hydronium $H_3O^+(H_2O)_n$ where n is a variant integer and usually $n = 2 \sim 3$. Meanwhile, as mentioned in Chapter 1 and 2, electrochemical surface reactions have self-consistent relations with a long-range diffusion layer and electric field in electrolyte. Furthermore, electrochemical ORR is a multielectron transfer reaction and can be accomplished through many combinations of elementary reaction steps; generally, electrochemical ORR could occur in two possible pathways: (i) a "direct" four-electron reduction, wherein four electrons for each O_2 molecule are transferred jointly; (ii) a "serial" pathway that involves H_2O_2 as an intermediate. Each of them is usually divided into several

elementary steps and envisioned to proceed as the following mechanisms:

$$O_2 + * \rightarrow O_2^* \tag{4.1}$$

$$O_2^* + H^+ + e^- \rightarrow OOH^* \tag{4.2}$$

Here $*$ means adsorbed state or free adsorption site. In a "direct" pathway, the whole reaction could continue as following:

$$OOH^* \rightarrow OH^* + O^* \tag{4.3}$$

or

$$OOH^* + H^+ + e^- \rightarrow H_2O + O^* \tag{4.4}$$

then reductions for the left O^* and OH^* occur as the following:

$$O^* + H^+ + e^- \rightarrow OH^* \tag{4.5}$$

$$OH^* + H^+ + e^- \rightarrow H_2O \tag{4.6}$$

Another possible mechanism of a "direct" pathway is that after O_2 adsorption as Equation 4.1, O_2^* dissociates directly on electrode surface:

$$O_2^* + * \rightarrow O^* + O^* \tag{4.7}$$

And the left O^* atoms react with protons and electrons to produce OH^* and H_2O finally as Equation 4.5 and 4.6.

On the other hand, in "serial" pathway, the reaction after OOH^* formation as Equation

4.2 continues as

$$OOH^* + H^+ + e^- \rightarrow H_2O_2^* \tag{4.8}$$

$$H_2O_2^* + H^+ + e^- \rightarrow OH + H_2O \tag{4.9}$$

Then the left OH^* continuously reacts with a proton and an electron to produce H_2O as Equation 4.6.

Different mechanisms would perform at various reaction conditions. The "serial" pathway usually occurs on the electrode surface where the adsorption energies of O_2 molecule and O atom are weak, such as Au[27]. On Pt electrode, the "direct" pathway is assumed to dominate since very small fluxes of H_2O_2 are observed on Pt rotating ring-disk (RRD) electrode as electrode potential U above 0 V (SCE)[78]. However, surface blocking by adsorbed atoms sometimes changes the reduction mechanism from "serial" to "direct" pathway[2].

For all the mechanisms mentioned above, the reaction intermediates on both sides of above equations, O_2^*, $H_2O_2^*$, OOH^*, O^* and OH^*, are all assumed to be charge neutral, so every electron transfer always occurs concurrently with the corresponding proton (hydronium) transfer from the electrolyte, i.e., all electron transfers are proton-coupled (PCET) [21]. Otherwise, ORR could occur through charged reaction intermediates by transferring proton and electron independently as the following:

$$O_2 + * + e^- \rightarrow O_2^{-*} \tag{4.10}$$

$$O_2^{-*} + H^+ \rightarrow OOH^* \tag{4.11}$$

$$OOH^* + H^+ + 2e^- \rightarrow H_2O + O^{-*} \tag{4.12}$$

In these mechanisms, because the charge states of ORR intermediates may be variant num-

bers (0, -1, -2,...), the possible reaction paths and total reaction mechanism would become much more complicated than those with PCET.

There have been several attempts to study electrochemical ORR by DFT and other first-principles methods[120, 94, 147, 56]. However, because DFT can only handle limited number of electrons and atoms, most models lack the ability to accurately describe the total electrochemical ORR. One of the most successful results is provided by Nørskov[94]: based on the assumed elementary reaction steps in "direct" pathway (Equation 4.1 to 4.7) and the usage of experimental results on the relation between electrode potential and reaction free energies, Nørskov et al. proposed a model to plot the free-energy landscape of the electrochemical ORR as a function of the electrode potential U by simply calculating the energies of idealized reaction intermediates by DFT method[94] (detailed methods discussed in Section 4.3). This model can successfully explain the origin of the ~ 0.4 volt cathode overpotential for ORR, as well as rank alloy catalytic activities in significant agreement with experiments. They also claimed that the most critical parameter for the good catalytic activity is the adsorption energy of oxygen atom on the surface $E_{\mathrm{ads}}^{\mathrm{O}^*}$, and there is an optimal value of $E_{\mathrm{ads}}^{\mathrm{O}^*}$ to achieve the best possible catalytic effect, which provides a semi-quantitative criteria to search for active ORR catalyst.

In this chapter, first-principles methods are used in two areas. First, both the static (Section 4.1) and dynamic (Section 4.2) structures, especially charge states, of reaction intermediates on catalyst surface are studied in order to understand the detailed electron transfer mechanisms in ORR, which are critical not only for the validation of the assumptions used in Nørskov's model[94], but also crucial for the multiscale model of ORR discussed in Chapter 5. Second, based on Nørskov's semi-quantitative criteria that can be directly calculated by DFT methods, quick and comprehensive search and design of alloy structures are performed in order to discover new efficient and stable ORR catalysts.

4.1 Electronic Structures of Intermediates in ORR

In Nørskov's ORR model[94], near-neutrality of all reaction intermediates on the catalyst surface is a critical assumption, because it uses "direct" pathway (Equation 4.1 to 4.7) as ORR mechanism and the adsorption free energies of all the reaction intermediates in this pathway, O_2^*, OOH^*, O^* and OH^*, are assumed to be weakly affected by electrode potential U. This insensitivity to U can be satisfied if there is negligible dipole moment change in the surface normal direction before and after the adsorption of each intermediate, which is synonymous with the above near-neutrality assumption. This direct connection between the dipole changes and the charge states results from the geometric configurations of ORR intermediates: after relaxation in DFT calculations, all ORR intermediates keep certain distances from Pt (111) surface (1.5$\sim$2.0 Å for O_2^*, OOH^* and OH^*, 1.1 Å for O^*, as shown in Section 3.1), so large/small charge transfer between Pt and ORR intermediates would result in significant/negligible dipole and potential (work function) changes on the surface.

However, the near-neutrality of all reaction intermediates is still uncertain. For example, there has been a long debate in charge states of O_2^* as the intermediate in ORR[1]. Although the atomic geometries of O_2^* can be accurately observed via several techniques[37, 129, 100, 130], its charge state can only be inferred by indirect means, such as vibrational frequency measurements. Two bands of stretching mode of O_2^* on Pt (111) surface, 860-880 cm^{-1} and 690-700 cm^{-1}, were identified and assigned as superoxide O_2^- and peroxide O_2^{2-} ion, respectively[37, 129, 100]. Eichler and Hafner used DFT calculations to study O_2 adsorption and identified superoxide O_2^- as a paramagnetic chemisorbed precursor at the bridge site of Pt(111) surface, and peroxide O_2^{2-} as a nonmagnetic precursor at the fcc hollow site[24, 25]. The formal charge assignments $^{1-}$ and $^{2-}$ were based on magnetic moments, vibrational frequencies and the *shape* of charge difference density $\Delta\rho \equiv$

ρ(Pt(111)+O_2)-ρ(Pt(111))-ρ(O_2) for these two O_2^* precursors. Since the vertical distance between O_2^* and the surface is about 2 Å[24, 25, 108], these charge assignments would indicate large induced dipoles, defined as the difference in supercell total dipole before and after O_2 adsorption. However, this contradicts results of Hyman and Medlin, who used DFT to calculate the adsorption of oxygen molecule and atom on Pt(111) surface in the presence of homogeneous electric field, and confirmed that the induced electric dipole moments for O_2^* and O^* are indeed very small (0.07 and 0.04 Åe, respectively)[55].

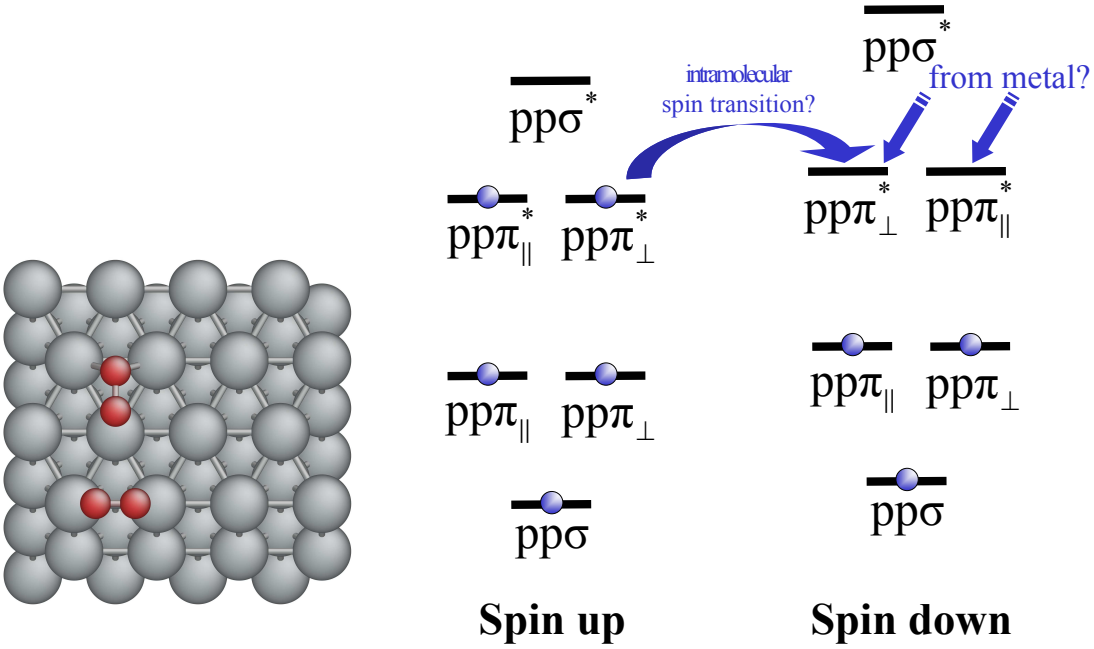

(a) (b)

Figure 4.1: (a) Configurations of two chemisorbed O_2 molecular precursors at the bridge site and fcc hollow site. (b) Molecular orbital energy diagram for O_2.

To reconcile the above with the observations of Eichler and Hafner [24, 25] and obtain a comprehensive and accurate picture of electron transfer mechanism in ORR, we make a detailed and quantitative analysis on the charge states of adsorbed oxygen molecules and other ORR intermediates (OOH^*, $H_2O_2^*$, OH^* and O^*)[107]. The calculations are performed using the Vienna Ab-Initio Simulation Package (VASP) [69, 67]. We use projec-

tor augmented wave (PAW) potentials[13] with Perdew-Burke-Ernzerhof (PBE) exchange-correlation functional[103] in spin-polarized condition. The Pt(111) surface is modeled by a four-layer slab with a rectangular ($\sqrt{3} \times 2$) unit cell of total 16 Pt atoms, separated by 12 Å thick vacuum layer. Only one ORR intermediate is adsorbed on one side of the slab, as shown in Fig. 4.1. The molecule and Pt atoms at the top two layers are fully relaxed. Brillouin zone integrations are performed on a grid of $4 \times 4 \times 1$ $\vec{k}$ points, using first-order Methfessel-Paxton smearing of σ=0.2 eV. The calculations are performed at equilibrium lattice constant of a_0=3.977 Å. Dipole correction[76] on the electric potential and total energy is imposed to eliminate dipole-dipole interactions between image supercells. We have also checked the effects of larger supercell, symmetric adsorptions on both sides of the slab, larger vacuum region, higher density $\vec{k}$-points sampling in Brillouin zone and the usage of ultrasoft pseudopotentials with different functionals (LSD, PW91) in O_2 adsorption cases. In all cases, the changes in O_2^* charge state are not significant.

4.1.1 Charge States on O_2^*

Confirmation of Previous Calculations on O_2 Adsorption

Table 4.1 shows the optimized geometry, E_{ad}, magnetic moment m and stretching frequency ν of adsorbed O_2^*, most of which agree with Eichler and Hafner's results by ultrasoft pseudopotentials[24, 25]. There is a large difference in m for O_2^* at the bridge site; however, it is found to be inconsequential to the main conclusions of the charge states. There are also slight differences in the stretching frequencies; however, they are still near the experimental values [37, 129] and close to another DFT calculation[118]. The magnetic moment density and total charge difference density are plotted and their shapes are seen to match Eichler and Hafner's plots[24, 25]: for O_2^* at bridge site, its remaining magnetic moment density behaves like $\pi_{\|}^{\star}$ antibonding orbital; meanwhile, the *shape* of the

charge difference density $\Delta\rho$ is similar to the $\pi^{\star}_{\perp}$ antibonding orbital (the molecular orbital energies of free O_2 are illustrated in Fig. 4.1(b), $\parallel$ and $\perp$ means parallel and perpendicular to the metal surface, respectively), so it was suggested that about one electron transferred from Pt to $\pi^{\star}_{\perp}$ spin-down orbital. On the other hand, for O_2^* at fcc hollow site, there is no magnetic moment left and the shape of the charge difference density is like the sum of $\pi^{\star}_{\perp}$ and $\pi^{\star}_{\parallel}$, so it was suggested that about two electrons transferred from Pt to both $\pi^{\star}_{\perp}$ and $\pi^{\star}_{\parallel}$ spin-down orbitals. Until now, our results seem to agree with the charge assignments according to the observation of Eichler and Hafner[24, 25]

Table 4.1: DFT-PBE-PAW optimized ORR intermediates on Pt(111): the adsorption site, the equilibrium bond length b between two O atoms (except OH, where b is measured between O and H), shortest vertical distance z between adsorbates and surface, adsorption energy E_{ads} (references are the same intermediates in relaxed and isolated states plus relaxed clean surface), magnetic moment m of total unit cell, maximum stretching frequency ν_{max} of adsorbates, and induced vertical electric dipole P_z.

	site	b[Å]	z[Å]	E_{ads}[eV]	$m[\mu_{\mathrm{B}}]$	$\nu_{\mathrm{max}}[\mathrm{cm}^{-1}]$	$P_z[e\text{Å}]$
O_2^*	bridge	1.35	1.91	-0.65	0.93	913	0.06
O_2^*	fcc	1.39	1.74	-0.53	0.00	826	0.07
OOH^*	top	1.43	2.01	-1.12	0.00	3504	0.09
$H_2O_2^*$	top	1.47	2.41	-0.29	0.00	3496	-0.18
OH^*	top	0.97	1.99	-2.37	0.00	3663	0.13
O^*	fcc	/	1.11	-4.48	0.00	431	0.02

On the other hand, the small dipole changes P_z found by Hyman et al. [55] are also confirmed by our calculation. The induced dipole P_z, computed by direct charge integration in the supercell, is very small, only 0.06 and 0.07 eÅ for the bridge and fcc hollow site, respectively. The values can also be supported by experimental measurements, since the dipole changes are directly related to the work function changes before and after surface adsorptions, which are experimentally measurable.

We can theoretically obtain the work function change (δW) of Pt (111) surface due to

Table 4.2: Work function of Pt (111) surface with O_2^*: O_2 coverage θ_{O_2}, work function W and the change relative to clean surface δW.

	θ_{O_2}[ML]	W[V]	δW[V]
Clean Surface	0	5.752	0.0
O_2 at bridge	$\frac{1}{4}$	6.103	0.352
O_2 at fcc	$\frac{1}{4}$	6.181	0.430
O_2 at bridge	$\frac{1}{2}$	6.424	0.672

O_2 adsorption. First we can estimate δW by P_z as the following formula:

$$\delta W = P_z/(\varepsilon_0 \times \mathrm{A}) \tag{4.13}$$

where ε_0 is vacuum permittivity and A is the surface area of unit cell. In our calculation A = 27.400 Å^2, so δW = +0.376 V when $P_z = 0.06$ eÅ. According to the experiments by Gland[37], adsorption of saturation coverage of molecular oxygen on Pt(111) surface results in a work function change of +0.8 V. The difference between this experimental value and our calculation may result from different O_2 coverage. So we also calculate the work function change with different O_2 coverages. The calculation is performed with $(\sqrt{3} \times 2)$ unit cell and 8 (111) layers. The vacuum area between two surfaces in the unit cell is 20 Å and O_2 molecules are adsorbed on both surface sides. All other parameters are the same with the previous cases. The work function of surface is calculated from the difference between the electrostatic potential of the vacuum layer and Fermi level of the total system. As shown in Table 4.2, δW of $\frac{1}{2}$ monolayer (ML) O_2 at bridge site is only 0.13 V less than the experimental value [37]. We have also calculated the case of 1 ML of O_2 at both bridge and fcc sites and found that O_2 are finally desorbed from the surface, which indicates that the saturation coverage of O_2^* at Pt (111) surface is between $\frac{1}{2}$ and 1 ML. For these reasons, the experimental value (0.8 V), larger than 0.67 V but smaller than twice of it, agrees quite well with our calculation. In addition, δW of $\frac{1}{4}$ monolayer (ML) O_2 at bridge site almost

equals to the value calculated by Equation 4.13, which strongly supports the validity of small induced dipoles in O_2 adsorption process.

Quantitative Determination of O_2^* Charge States

Until now two contradictory conclusions (large charge assignments vs. small induce dipoles) are both confirmed by our calculations, so it is highly possible that something tricky is hidden in the detail electronic structures and charge states of O_2^*. To analyze the charge state in a fine-grained manner, we integrate the charge difference densities $\Delta\rho$ in *x*,*y* directions (parallel to the surface) and plot them with respect to *z* in Fig. 4.2(a) and (b) for paramagnetic and nonmagnetic case respectively. It is seen that in both cases the magnitude of $\Delta\rho$ is quite small and inside the metal $\Delta\rho$ is more of the Friedel oscillation type than a net transfer. Only the metal surface charge density beyond the outermost Pt atom ($z > z_{\mathrm{Pt}}$) shows appreciable net deficit, separated from the gain by O_2^* by a nodal structure at $z_{\mathrm{partition}} \approx 13$Å (indicated by the vertical dash lines in Fig. 4.2(a) and (b)). We may thus define roughly the total electron transfer from Pt(111) to O_2^* molecule as

$$\Delta N \equiv \int_{z_{\mathrm{partition}}}^{z=z_{\mathrm{O}}+\Delta z} dz \int\int dxdy\Delta\rho(x,y,z), \tag{4.14}$$

where we take $z_{\mathrm{partition}} = (z_{\mathrm{Pt}} + z_{\mathrm{O}})/2$, z_{Pt} (z_{O}) being the highest (lower) *z*-coordinate of Pt(111) atoms (O_2^* molecule), respectively, and Δz is a distance from z_{O} to make sure that the charge density of O_2^* decays to essentially zero (here we take Δz = 5Å). Consistent with the dipole results, it is found that ΔN for both the paramagnetic bridge and nonmagnetic fcc hollow O_2^* are very small, just 0.07*e* and 0.09*e*, respectively. To test the sensitivity on $z_{\mathrm{partition}}$, with arbitrary choice of $z_{\mathrm{partition}}$ between z_{Pt} and z_{O}, ΔN from charge difference integration is found to be always less than 0.13*e*.

These small ΔN values support the validity of small induced dipoles [55] and near-

neutrality assumptions used in Nøskov's model[94] instead of the charge assignments by Eichler and Hafner [24, 25]. To reconcile these contradictory results, we find it instructive to plot the *spin-charge difference*

$$\Delta\rho_\sigma \equiv \rho_\sigma(\mathrm{Pt}(111)+\mathrm{O}_2) - \rho_\sigma(\mathrm{Pt}(111)) - \rho_\sigma(\mathrm{O}_2) \tag{4.15}$$

in addition to the total charge difference, where σ denotes spin up/down state. The *xy* integral and isosurface of $\Delta\rho_\sigma$ are also shown in Fig. 4.2. We can see that changes in the spin charges are much larger in magnitude than change in the total charge, but there is a tremendous cancellation effect between $\Delta\rho_\uparrow$ and $\Delta\rho_\downarrow$. Using similar definition as Eq. (4.14) for ΔN_σ, the spin-charge transfer for paramagnetic O_2^* at bridge site is found to be $\Delta N_\uparrow = -0.64e$ and $\Delta N_\downarrow = 0.71e$. Meanwhile, the isosurfaces of $\Delta\rho_\uparrow$ and $\Delta\rho_\downarrow$ (Fig. 4.2(a)) indicate that most of the spin-charge changes result from the decreased occupation of $\pi_\perp^\star$ spin-up orbital and increased occupation of $\pi_\perp^\star$ spin-down orbital. Such $\pi_{\perp\uparrow}^\star \rightarrow \pi_{\perp\downarrow}^\star$ transfer, illustrated in Fig. 4.1(b), causes no change in the total charge density, and thus would *not be detectable* in the total charge difference $\Delta\rho$ plot.

For nonmagnetic O_2^* at fcc site, $\Delta N_\uparrow = -0.93e$ and $\Delta N_\downarrow = 1.02e$. The isosurfaces of $\Delta\rho_\uparrow$ and $\Delta\rho_\downarrow$ (Fig. 4.2(b)) show that both spin-charge differences have the similar shape, which is a combination of $\pi_\perp^\star$ and $\pi_\parallel^\star$ orbitals, but opposite in sign. Hence, our new interpretation of O_2^* electronic structure is: when O_2 is adsorbed at bridge site of Pt(111) surface, about half electron transfers from $\pi_\perp^\star$ spin-up orbital to $\pi_\perp^\star$ spin-down orbital, so that O_2^* is in a paramagnetic and almost neutral state; when O_2 is adsorbed at fcc hollow site, both spin-up $\pi_\perp^\star$ and spin-up $\pi_\parallel^\star$ give about half electron to their own spin-down orbitals, so that O_2^* is nonmagnetic and also almost neutral. The transfer of electron occupation from metal to the molecule is only a "second-order" process relative to the "first-order" intramolecular spin transition.

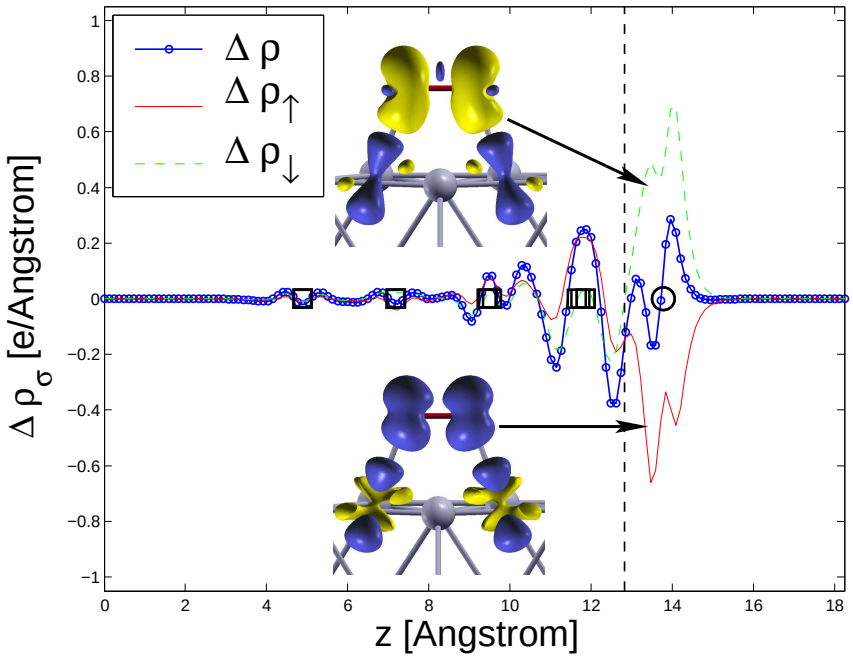

(a)

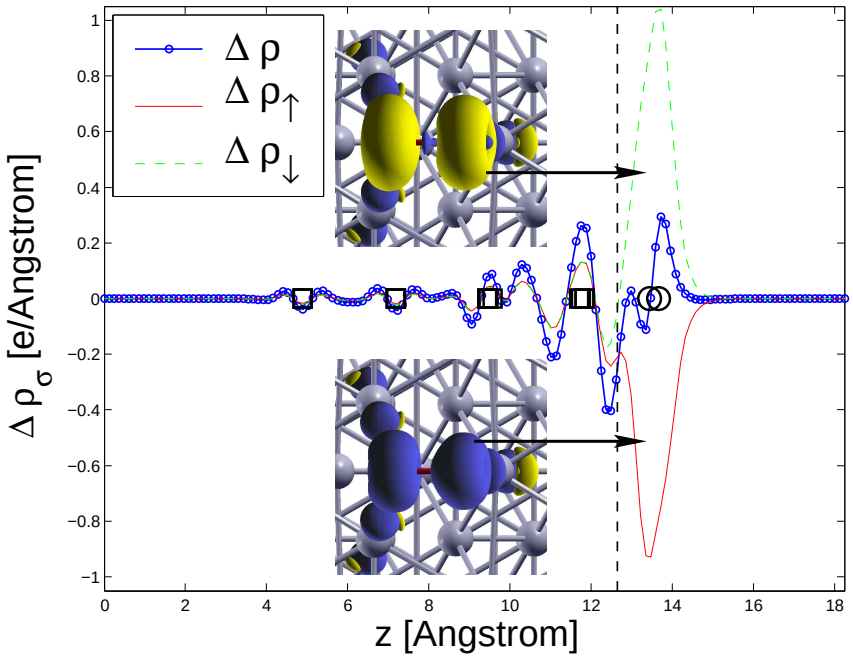

(b)

Figure 4.2: Charge/spin-charge difference density $\Delta\rho/\Delta\rho_\sigma$ along the surface normal direction z for O_2^* at bridge (a) and fcc hollow (b) site on Pt (111) surface. Black squares/circles stand for the z-coordinates of Pt/oxygen atoms and vertical dash lines stand for the middle position between highest Pt and lowest O atoms. The isosurfaces of $\Delta\rho_\uparrow$ and $\Delta\rho_\downarrow$ are plotted inside each sub-figure using XCySDen[62], where yellow and blue means positive and negative change respectively. The isovalues for all the isosurfaces are ± 0.04 eÅ^{-3}.

Further analyses of the projected density of states (PDOS) of O_2^* and associated molecular orbital (MO) character of the Bloch eigenfunctions $\psi_{n\vec{k}}$ confirm our new interpretation. We plot the isosurface of the periodic part of $\mathrm{Re}(\psi_{n\vec{k}})$ corresponding to peaks in PDOS of O_2^*, as indicated by arrows in Fig. 4.3. For O_2^* at bridge site, beside the strong peak of unoccupied spin-down $\pi_{\|}^{\star}$ (labeled as ψ_2 in Fig. 4.3 (a)), the spin up/down $\pi_{\perp}^{\star}$ (ψ_1 and ψ_3 in Fig. 4.3 (a)) states are seen to be half occupied. At fcc site, there is also a large number of unoccupied states (spectral strength) just above the Fermi level, which can be clearly identified as having $\pi_{\|}^{\star}$ (labeled as ψ_1 and ψ_3 in Fig. 4.3 (b)) and $\pi_{\perp}^{\star}$ (ψ_2 and ψ_4 in Fig. 4.3 (b)) character. We also integrate the PDOS below the Fermi level for both O_2^* and isolated O_2 molecule with the same bond length as its adsorbed state. It is found that compared with isolated O_2, there are only slight changes in the occupied PDOS integral for adsorbed O_2^* (from 9.57e to 9.75e for O_2^* at bridge site, and 9.50e to 9.73e for O_2^* at fcc site), which also suggests no large electron transfer from Pt to oxygen.

The next question is whether this small charge transfer during O_2 adsorption is just a special case for Pt(111) surface or a prevalent phenomena on different metal surfaces. So we have used the same method to calculate the charge transfer and induced dipole moment when O_2 is adsorbed at the (111) surface bridge site of several other fcc metals with different workfunctions, as shown in Fig. 4.4. Although the tendencies of increasing charge transfer and induced dipole with decreasing workfunction are very clear, it is found that even for Al, which is very active and easy to lose electron, ΔN is only about 0.2e. This result is consistent with a previous DFT calculation [52]. Under no circumstances can surface-adsorbed O_2^* be classified as a true integer anion [118]. Recently, Raebiger et al. found that transition metal impurities inside bulk ionic or semiconducting crystals maintain nearly constant local charge during redox [109]. Here we demonstrate a similar phenomenon in molecular adsorptions on metal surfaces. Both challenge conventional notions of literal integer charge transfer between adsorbates/impurities and crystals.

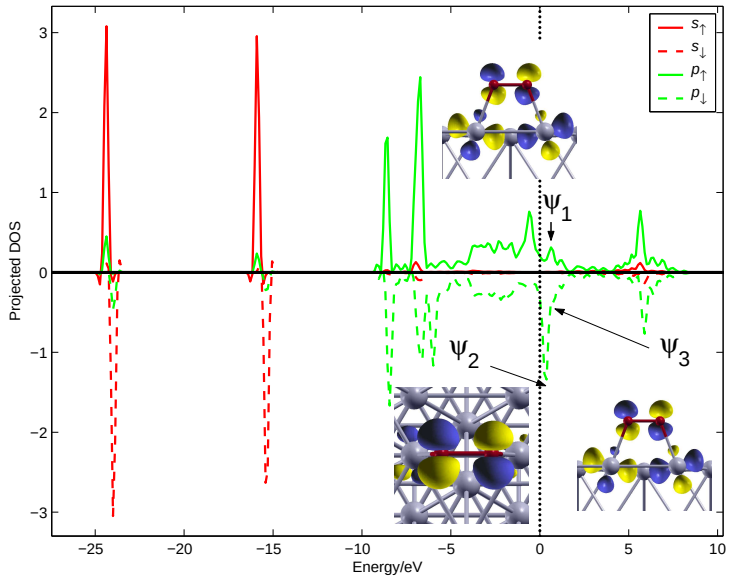

(a)

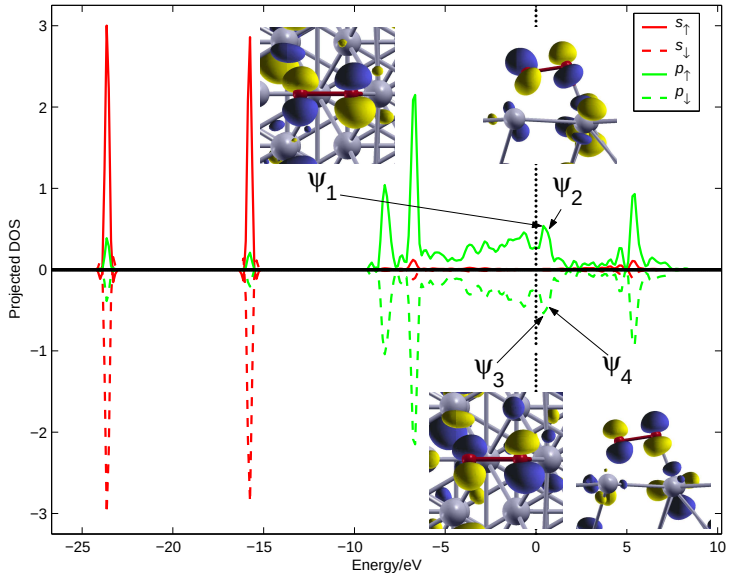

(b)

Figure 4.3: Projected DOS of O_2^* at bridge (a) and fcc hollow (b) sites on Pt (111) surface. Fermi energy is zero and spin-down states are plotted as negative. Isosurfaces of the real part of Bloch eigenfunctions $\mathrm{Re}(\psi_{n\vec{k}})$ at $\vec{k} = [\frac{1}{8}\frac{1}{8}0]$ of the first Brillouin zone are plotted for certain unoccupied peaks, as labeled in each subfigure. The absolute isovalues for all the isosurfaces are $\frac{1}{3}$ of the maximum absolute values of $\mathrm{Re}(\psi_{n\vec{k}})$ and yellow/blue means positive/negative value. For bridge-site case (a), the isosurfaces of ψ_1(n=90, ε=0.54 eV) and ψ_3(n=89, ε=0.65 eV) behave as spin-up/down $\pi_\perp^\star$, while spin-down ψ_2 (n=90, ε=0.32 eV) has the shape of $\pi_\parallel^\star$. For fcc-site case (b), isosurface of ψ_1/ψ_3 (n=89, ε=0.35 eV) behaves as spin-up/down $\pi_\parallel^\star$, while ψ_2/ψ_4 (n=90, ε=0.52 eV) is similar to spin-up/down $\pi_\perp^\star$.

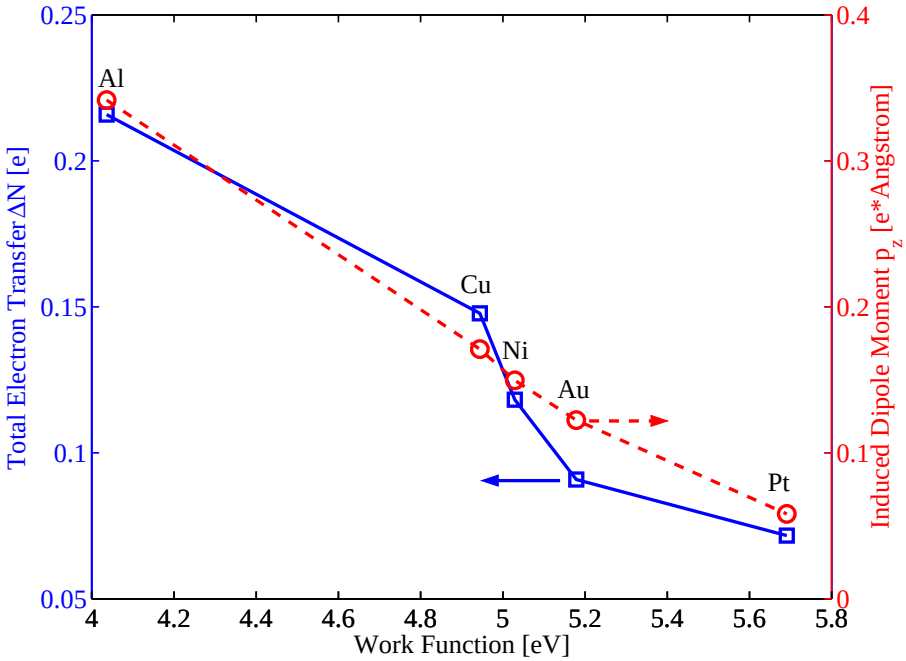

Figure 4.4: Electron transfer ΔN and induced dipole P_z of O_2^* at bridge site versus (111) surface workfunction of different metals. The bond length of O_2^* and its distance to the top surface layer are fixed as the optimized values on Pt(111).

All these intramolecular spin self-adjustments can be explained by the Anderson-Newns model of chemisorption[3, 89]: in free O_2 molecule, $\pi_\perp^\star$ and $\pi_\parallel^\star$ orbitals are degenerate and should have the same energy level E and self-exchange energy U^{ex}. Therefore the "width parameter" of virtual state Δ, which describes the interaction strength between molecular orbital and continuous bands of metal, decides their magnetic properties, as shown in Fig. 4 of [3]. After adsorption, the lower half of $\pi_\perp^\star$ orbital of O_2^* is closer to the surface so that it has a stronger interaction with the surface, thus, $\Delta_{\pi_\perp^\star}$ is comparable with $U^{\text{ex}}_{\pi_\perp^\star}$ so that $\pi^\star_{\perp\uparrow}$ and $\pi^\star_{\perp\downarrow}$ become equally occupied after adsorption. On the other hand, $\pi_\parallel^\star$ orbital is further away from the surface compared to $\pi_\perp^\star$ so that $\Delta_{\pi_\parallel^\star}$ is smaller, which makes $\pi_\parallel^\star$ spin-polarized at the (111) bridge site of many transition metals. However, the opposite situation, equal occupation of two $\pi_\parallel^\star$ spin orbitals, occurs at Pt(111) fcc hollow site and Al(111) bridge site. The former results from geometry, where there are more $O_{\pi_\parallel^\star}$-Pt in-

teractions (as Fig. 4.1(a) shows, at fcc hollow site $\pi^{\star}_{\|}$ would overlap with two Pt nearest neighbors); the latter likely arises from the angular bonding features of Al [97].

In conclusion, DFT calculations reveal that O_2^* adsorbed on a variety of metal surfaces has very little net charge (a few percent of *e*) and induced dipole. An intramolecular spin transition occurs when the molecule approaches the metal surface. So the adsorption energy and charge state of this important reaction intermediate is only weakly dependent on the electrode potential.

Further Analyses on the Accuracy of DFT

Although a more accurate and quantitative picture of O_2^* electronic structure has been obtained by detailed analyses of DFT calculation results, there may still be some problems in the accuracy of this DFT description because of certain intrinsic errors in approximate functionals of DFT. For this reason, some high-level quantum mechanical methods have to be applied in order to check the accuracy of DFT in these adsorption cases.

One possible error may come from the fact that current PAW-PBE functionals would overestimate the interaction of adsorbate's Lowest Unoccupied Molecular Orbital (LUMO) with the metal substrate, which would lead to an unrealistically large downshift and occupation of the LUMO [68]. To correct this error, on-site Coulomb interaction has to be applied to molecular orbital of the adsorbate in order to shift completely empty states to higher energies and increase the separation between its Highest Occupied Molecular Orbital (HOMO) and LUMO. In our results it is asserted that O_2^* on Pt (111) surfaces is near-neutral. However, if this overestimation of the interaction between O_2^* LUMO and Pt surface occurs in our DFT calculation, it would only strengthen our assertion instead of weakening it. The reason is that electron is supposed to transfer from Pt surface to O_2 LUMO; so if DFT overestimates substrate-LUMO interaction, yet the calculated charge transfer is still small, it will mean, in reality, the charge transfer will be even smaller. To verify this argument, we

use VASP to perform LSDA+U calculation on both isolated O_2 molecule and O_2 adsorption at bridge site cases, where Dudarevs formula of on-site Coulomb interaction is applied to *p* orbitals of each oxygen atom [23]. The results are shown in the Table 4.3.

Table 4.3: LSDA+U calculation of charge transfer for O_2^* at bridge site on Pt (111) surface, where Dudarevs formula of on-site Coulomb interaction is applied to *p* orbitals of each oxygen atom [23]: on-site Coulomb and exchange parameters U-J, the energy gap between LUMO and HOMO for isolated O_2, spin-up charge transfer $\Delta N_\uparrow$, spin-down charge transfer $\Delta N_\downarrow$, total charge transfer ΔN, induced vertical electric dipole P_z and magnetic moment m^* of O_2^*.

U-J[eV]	E_{LUMO}-E_{HOMO}[eV]	$\Delta N_\uparrow[e]$	$\Delta N_\downarrow[e]$	$\Delta N[e]$	$P_z[e\text{Å}]$	$m^*[\mu_B]$
0.0-0.0	2.2730	-0.638	0.708	0.071	0.057	0.631
0.7-0.09	2.4731	-0.624	0.693	0.069	0.056	0.662
1.4-0.18	2.6757	-0.611	0.678	0.067	0.053	0.691
2.8-0.36	3.0892	-0.584	0.644	0.061	0.048	0.756
5.6-0.72	3.9491	-0.531	0.581	0.050	0.039	0.881

Table 4.3 indicates that for isolated O_2, as the on-site Coulomb interaction correction, $U-J$ energy, to *p* orbital increases, LUMO shifts up a lot relative to Fermi energy and HOMO-LUMO gap increases. As a result, the overestimation of the interaction between the LUMO and the metal substrate may be corrected by applying LSDA+U to oxygen p orbital. Then for O_2^* at bridge site of Pt (111) surface, as on-site Coulomb interaction increases and LUMO shifts up, the interaction between LUMO and surface may decrease, so do the charge transfers (all ΔN,$\Delta N_{\uparrow/\downarrow}$ and P_z values), which further supports the near-neutrality of adsorbed O_2^*. Meanwhile, because there is less spin-up electron transferring to spin-down orbital after adsorption, the remaining magnetic moment around adsorbed O_2^*, m^*, increases as $(U-J)$ increases. But all these changes are not significant. For these reasons, these LSDA+U methods do not change the detailed conclusions of intramolecular spin transition in our studies (for O_2^* at bridge site, about half electron transfers from spin-up π orbital to spin-down π orbital, so that O_2 is in a paramagnetic and almost neutral state.).

4.1.2 Charge States of other ORR Intermediates

Charge States of OOH^*, $H_2O_2^*$, OH^* and O^*

Except for O_2^* cases, the optimized geometry, E_{ads}, magnetic moment m and stretching frequency ν of all other ORR intermediates (OOH^*, $H_2O_2^*$, OH^* and O^*) are also listed in Table 4.1, while their spin-charge difference integration plots and their contours are shown in Fig. 4.5 (OOH^* and $H_2O_2^*$) and Fig. 4.6 (OH^* and O^*). The results of charge transfer for all ORR intermediates adsorbed on Pt (111) surface are summarized in Table 4.4. Here the amount of spin/total charge transfer $\Delta N_{\uparrow/\downarrow}/\Delta N$ and magnetic moment m for each intermediate are calculated in the same integration method as Equation 4.14.

First, we start from the analysis of OOH, which has one unpaired electron in its HOMO orbital in isolated state. Once it is adsorbed on the top site of Pt (111) surface, its spin-up charge $N_\uparrow$ decreases by 0.46 e but spin-down charge $N_\downarrow$ increases by 0.52 e, so that the total charge transfer ΔN is as small as 0.06 e and induced dipole P_z is only 0.09 eÅ, and there is no magnetic moment left on either absorbed OOH^* and Pt surface. As Fig. 4.5(a) shows, both spin up and down charge difference densities behave as OOH's HOMO orbital, a π^* orbital on two oxygen atoms. Furthermore, in Fig. 4.7 (a) the analysis of PDOS for OOH^* shows that there are both unoccupied spin-up and down peaks whose corresponding Bloch eigenfunctions have π^* characters around oxygen atoms. Thus, similar with O_2 adsorbed on bridge site, when OOH is adsorbed on top site of Pt (111) surface, about half electron transfer from its spin-up HOMO orbital to its own spin-down HOMO orbital, and there is no significant charge transfer between Pt surface and OOH.

As an intermediate only appeared in "serial" pathway, the charge state of $H_2O_2^*$ adsorbed at the top site of Pt (111) surface is also analyzed, as shown in Fig. 4.5 (b). It is clear that there are only negligible changes for both spin-up and down electrons. This is readable, since H_2O_2 has closed-shell electron configuration and the interaction between

Table 4.4: Charge transfer results for ORR intermediates adsorbed on Pt (111) surface: the adsorption site, magnetic moment m of isolated intermediates, spin-up charge transfer $\Delta N_{\uparrow}$, spin-down charge transfer $\Delta N_{\downarrow}$, total charge transfer ΔN, magnetic moment m^* of adsorbed intermediates, and induced vertical electric dipole P_z.

	site	$m[\mu_B]$	$\Delta N_{\uparrow}[e]$	$\Delta N_{\downarrow}[e]$	$\Delta N[e]$	$m^*[\mu_B]$	$P_z[e\text{Å}]$
O_2^*	bridge	2.00	-0.64	0.71	0.07	0.63	0.0569
O_2^*	fcc	2.00	-0.93	1.02	0.09	0.00	0.0698
OOH^*	top	1.00	-0.46	0.52	0.06	0.00	0.0929
$H_2O_2^*$	top	0.00	-0.03	-0.03	-0.06	0.00	-0.18
OH^*	top	1.00	-0.43	0.57	0.14	0.00	0.1276
O^*	fcc	2.00	-0.88	1.04	0.16	0.00	0.0210

H_2O_2 and Pt surface is pretty weak: the distance between H_2O_2 and Pt is 2.42 Å and the adsorption energy E_{ad} is -0.29 eV, much smaller than E_{ad} =-0.65 eV for O_2 at bridge site.

The charge transfer between OH and Pt (111) surface is also similar with OOH case. In isolated state, OH has one unpaired electron in its HOMO orbital. Once it is adsorbed on the top site of Pt (111) surface, its spin-up charge $N_{\uparrow}$ decreases by 0.43 e but spin-down charge $N_{\downarrow}$ increases by 0.57 e, so that the total charge transfer ΔN is 0.14 e and induced dipole P_z is 0.13 eÅ, and there is no magnetic moment left on either absorbed OH^* and Pt surface. Although ΔN of OH^* is twice as those of O_2^* and OOH^*, it is still much small than 1 e. In addition, after adsorption there is no magnetic moment left on either absorbed OH^* and Pt surface. So the same as OOH^*, for OH^* at top site about half electron transfers from its spin-up orbital to its own spin-down orbital, and there is no significant charge transfer between Pt surface and OH.

The analysis of specific orbitals of OH provides more detailed information on the charge self-adjustment in its molecular orbitals. For isolated OH in DFT calculation, s orbital of oxygen atom and σ bond, formed by s orbital of H atom and p_x orbital of oxygen atom (here x stands for the direction along OH bond), have the lowest and second lowest eigenvalues, respectively. The left two p orbitals in oxygen atom, p_y and p_z, are energetically degenerate. In spin-up cases, both p_y and p_z are occupied by one electron; while in spin-down

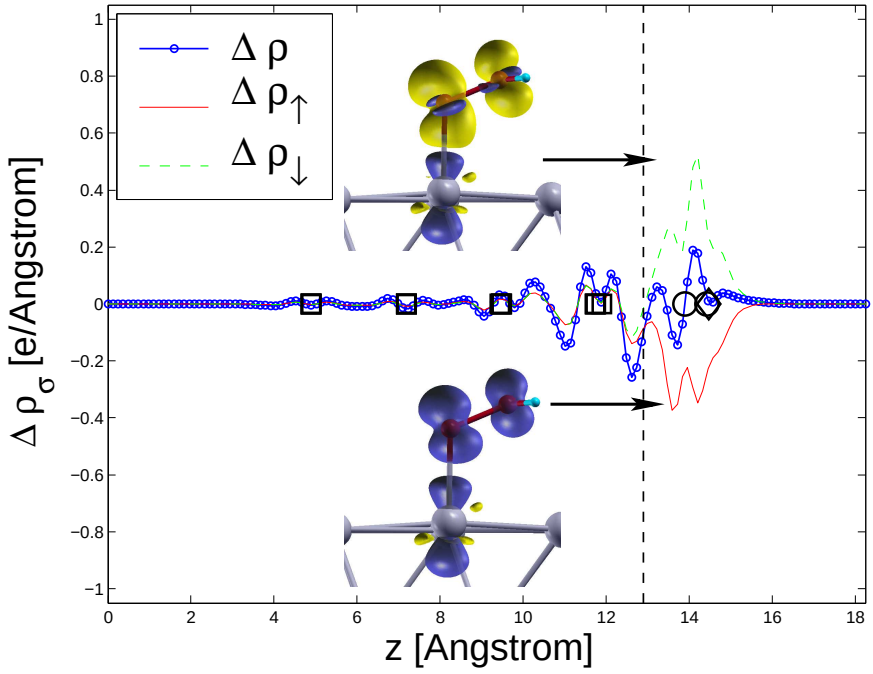

(a)

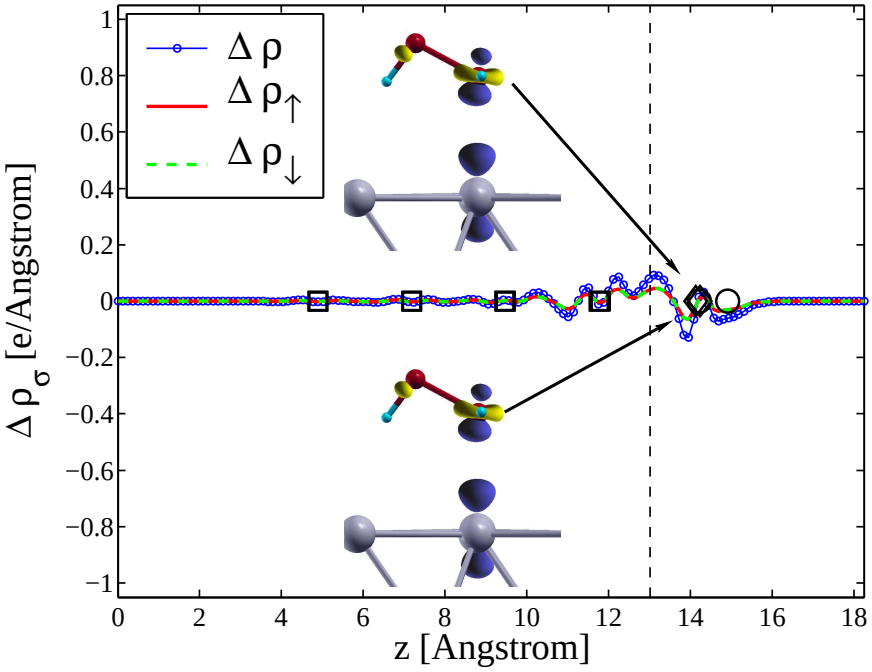

(b)

Figure 4.5: The integration and contours of charge/spin-charge difference density $\Delta\rho/\Delta\rho_\sigma$ for ORR intermediates on Pt(111) surface. (a) OOH^* at top site; (b) $H_2O_2^*$ at top site. Meanings of difference signs are explained in the caption of Fig. 4.2

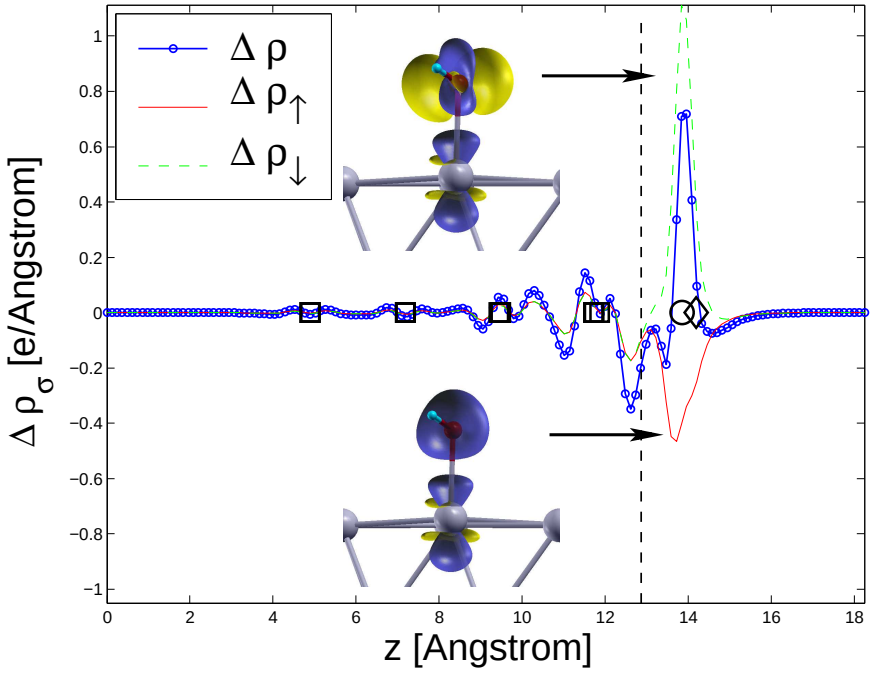

(a)

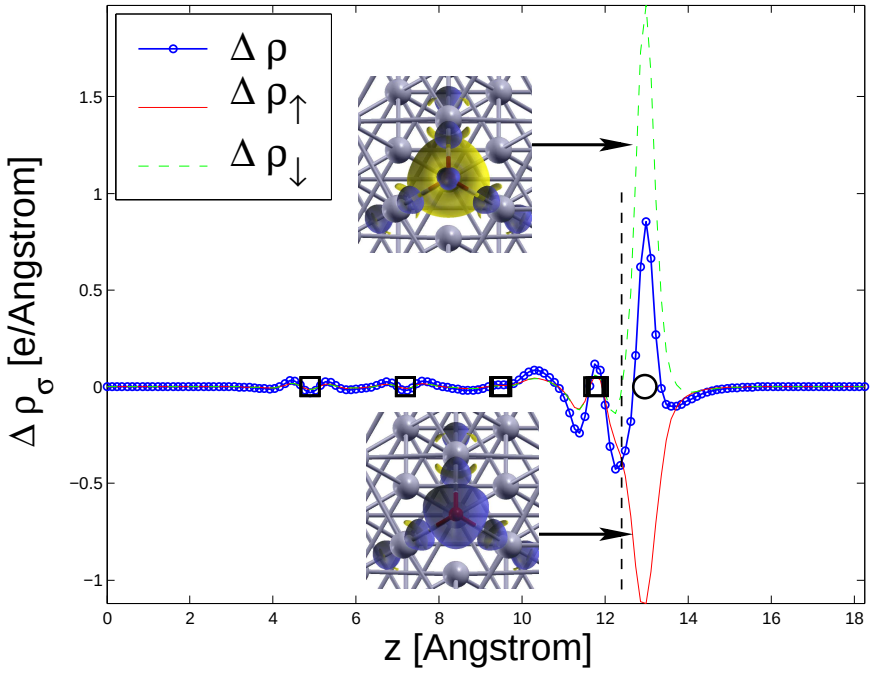

(b)

Figure 4.6: The integration and contours of charge/spin-charge difference density $\Delta\rho/\Delta\rho_\sigma$ for ORR intermediates on Pt(111) surface. (a) OH^* at top site; (b) O^* at fcc hollow site. Meanings of difference signs are explained in the caption of Fig. 4.2

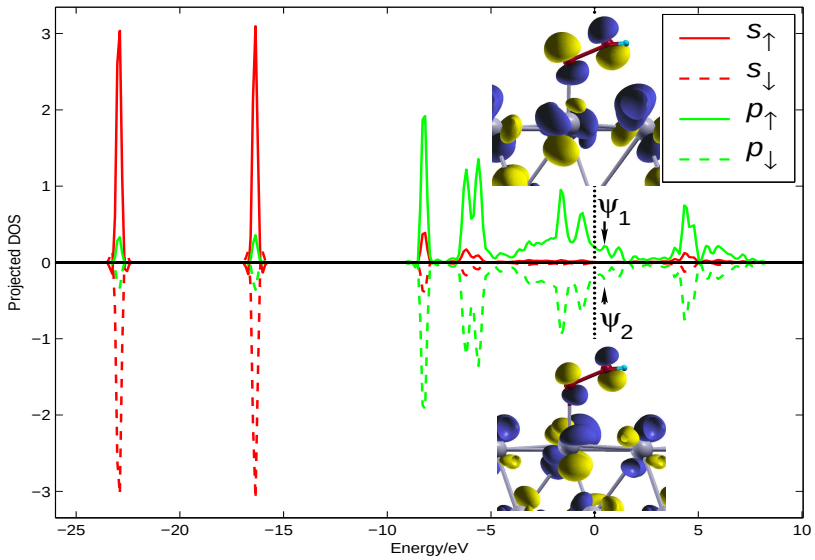

(a)

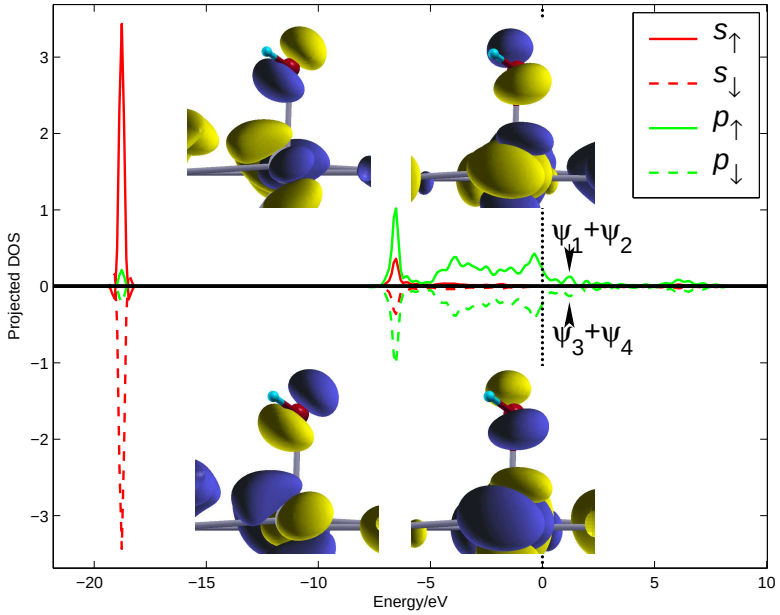

(b)

Figure 4.7: Projected DOS of OOH* (a) and OH* at top site on Pt (111) surface. Meanings of difference signs are explained in the caption of Fig. 4.3. Isosurfaces of the real part of Bloch eigenfunctions $\mathrm{Re}(\psi_{n\vec{k}})$ at $\vec{k} = [\frac{1}{8}\frac{1}{8}0]$ of the first Brillouin zone are plotted for certain unoccupied peaks, as labeled in each subfigure. For OOH* case (a), the isosurfaces of ψ_1(n=90, ε=0.40 eV) and ψ_2(n=90, ε=0.40 eV) behave as spin-up/down $\pi^\star$ on two oxygen atoms. For OH* case (b), isosurface of ψ_1/ψ_3 (n=89, ε=0.96 eV) and ψ_2/ψ_4 (n=90, ε=1.10 eV) are spin-up/down p orbitals of oxygen atom with component both perpendicular and parallel to Pt surface.

cases, both of them have the same higher eigenvalues because of exchange interactions and each of them is occupied by half an electron. After OH adsorption, there is negligible changes in both *s* orbital and σ bond because their eigenvalues are much lower than Fermi level. On the other hand, there are large self-adjustments in both p_y and p_z orbitals of oxygen atom. Ideally, both p_y and p_z spin-up orbitals would contribute $\frac{1}{4}$ electron to their own spin-down orbitals, so that $\Delta\rho_\uparrow$ and $\Delta\rho_\downarrow$ contour would have opposite values, but both of them behave as the combination of p_y and p_z orbitals: a circular shape around the oxygen atom and perpendicular to OH bond direction. However, since in our calculation cases, the unit cell is in rectangular shape and OH bond direction is not along any axis of unit cell, $\Delta\rho$ contours shown in Fig. 4.6 (a) look a little bit different: $\Delta\rho_\uparrow$ surrounding OH^* behaves like the combination of p_y and p_z orbital, but $\Delta\rho_\downarrow$ has more p_y feature (parallel to (111) surface) than p_z (perpendicular to surface). We can also observe unoccupied peaks in PDOS of OH^* with both p_z and p_y orbital characters, as shown in Fig. 4.7 (b). In conclusion, most of the charge self-adjustments in OH^* occur in two *p* orbitals perpendicular to OH bond so that both of them are partially occupied with equal amounts of electron in both spin-up and spin-down states.

We continue to use the same integration method to analyze charge transfer between adsorbed O atom and Pt surface. In isolated state, O atom has two unpaired spin-up electrons in its *p* orbitals. Once it is adsorbed on the top site of Pt (111) surface, its spin-up charge $N_\uparrow$ decreases by 0.88 *e* but spin-down charge $N_\downarrow$ increases by 1.04 *e*, so that the total charge transfer ΔN is 0.16 *e*, and there is no magnetic moment left on either absorbed O^* and Pt surface. Although its ΔN is even larger than the corresponding value of OH^*, the induced dipole P_z is only 0.02 *e*Å, much smaller than P_z of OH^* case. Because the vertical distance between O^* and Pt is only 1.11 Å, the previous method of charge difference integration as Equation 4.14 may be not very accurate. So we plot contours of $\Delta\rho$, $\Delta\rho_\uparrow$ and $\Delta\rho_\downarrow$ in Fig. 4.8 (a), where it is observed that most of charge changes occur surrounding O^* atom. For

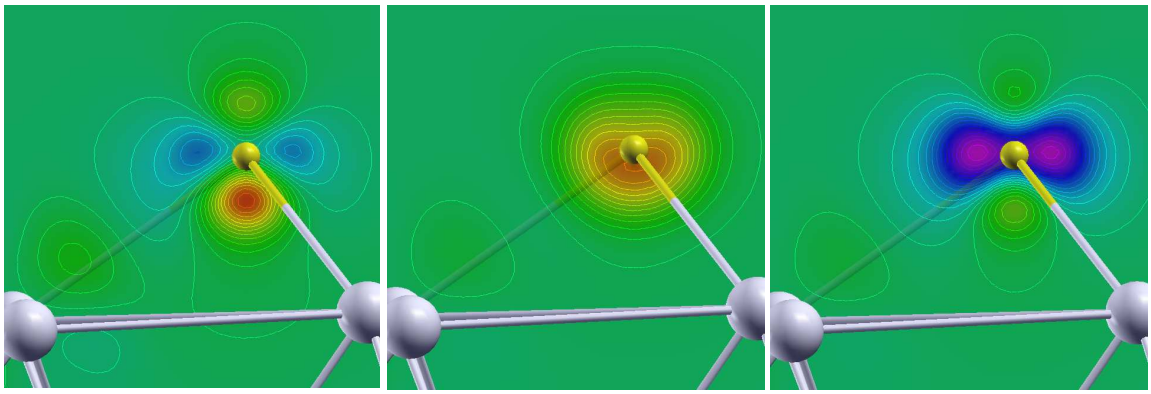

(a)

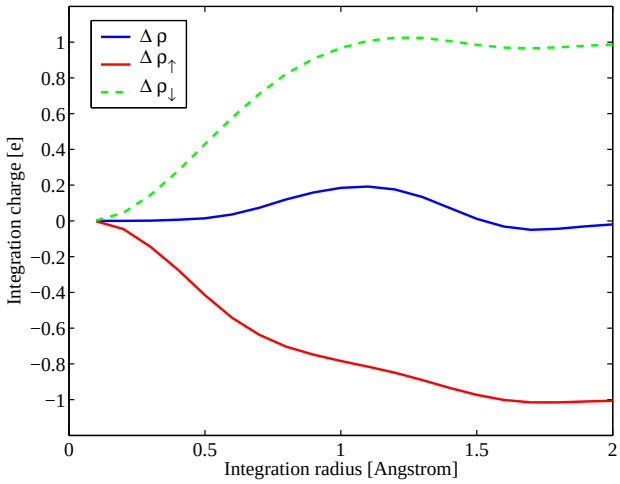

(b)

Figure 4.8: (a) Difference contours for total charge density $\Delta\rho$, spin-up charge density $\Delta\rho_{\uparrow}$ and spin-down charge density $\Delta\rho_{\downarrow}$ (from left to right) in the adsorption process of oxygen atom at fcc hollow site on Pt (111) surface. (b) Integration of $\Delta\rho$, $\Delta\rho_{\uparrow}$ and $\Delta\rho_{\downarrow}$ in spherical shape with O*'s position as the center. *x* axis stands for the change of integration radius and *y* axis shows total integration charge amounts.

$\Delta\rho_{\uparrow}$, all p orbitals lose electron, especially the part near Pt surface area, so the contours behave as spherical sharps. For $\Delta\rho_{\downarrow}$, p orbitals parallel to surface gain a large amount of electron, but p orbital perpendicular to surface, p_z, still loses some electron because of the strong repulsion from surface. For the total charge difference, p_x and p_y gain some electron, most of which is spin-down; while p_z loses some electron, most of which is spin-up. If we integrate the charge difference inside a sphere whose center is located in the position of O^*, the integrated charge difference changes with integration radius, as shown in Fig. 4.8(b). From this new integration method, it is clear that the total charge transfer is still very small compared with corresponding spin-charge changes. The maximum number is 0.2 *e*, which is larger than all other ORR intermediates, which is reasonable because the isolated oxygen atom has a larger electron affinity than O_2, OOH, H_2O_2 and OH. However, when the integration radius increases to $\sim$ 1.5 Å, total charge transfer again decreases to almost zero, while spin up/down charge difference approximately equals +/- 1, so that O^* is confirmed to be in near-neutral state.

Effects of electrode-electrolyte interface

Previous studies are all performed to investigate the charge transfer between Pt and ORR intermediates under UHV conditions. However, the results may be different in the real electrochemical environment. On electrode-electrolyte interface, there are many electrolyte molecules, usually H_2O. H_2O is a polarized molecule, which can also form strong hydrogen bond with ORR intermediates, especially those with H atom, such as OH^* and OOH^*. In addition, there is a strong external electric field applied by the separated excess charges on the two sides of electrode-electrolyte interface (*electrical double layer*). Both of these factors, H_2O molecules and electric fields, may affect the charges states of ORR intermediates, which are discussed here in detail.

The structure of H_2O molecules on metallic surface itself is a complex topic with many

experimental and theoretical studies [48]. Recently, Ogasawara et al. found that H_2O is adsorbed on Pt(111) in a flat monolayer with both metal-oxygen and metal-hydrogen bonding species[96]. Using this water structure, Nørskov et al. analyzed its effect on the stability of O^* and OH^* [94, 111]. For O^* case, they simply added H_2O monolayer on top of Pt (111) + O^* surface, and the result showed that there is negligible effect on the adsorption energy of O atom. So the change in charge state of O^* from water solvation effect should also be insignificant and is not investigated here. On the other hand, a hexagonal mixed network monolayer of H_2O and OH, first proposed by Feibelman [31], was used to calculate the interaction between H_2O and OH on Pt (111) surface, and the results show that H_2O strongly stabilizes OH^* due to strong hydrogen bonding. The structure of OH + H_2O mixed network is shown in Fig. 4.9(a), where both OH and H_2O have a coverage of $\frac{1}{3}$. In addition, the closest vertical distance between top Pt surface and O atom in OH^* increases from 1.987 Å under UHV conditions to 2.110 Å. Because of the changes in both adsorption energy and geometric configuration, we calculate the charge transfer between Pt surface and OH + H_2O monolayer.

Here the charge difference density is defined as $\Delta\rho \equiv \rho$(Pt(111) + OH + H_2O)-ρ(Pt(111))-ρ(OH + H_2O), where OH + H_2O monolayer is studied as a single species. The charge difference integration method is the same as Equation 4.14. In a unit cell shown in Fig. 4.9(a), there are two OH^* and two H_2O molecules. Although the (spin)-charge densities are integrated on the entire surface of the unit cell, the results are interpreted in $\Delta N_{\uparrow/\downarrow}/\Delta N$ for each OH^*+H_2O pair. The results show that $\Delta N_{\uparrow}$ is -0.46 e and $\Delta N_{\downarrow}$ is 0.52 e, so total charge transfer for each OH^*+H_2O pair is only 0.06 e and its induced dipole is as small as 0.017 eÅ. The integration plots and $\Delta\rho_{\uparrow/\downarrow}$ contours are shown in Fig. 4.9 (b), where it is clear that some spin-charge transfer occurs on H_2O molecule with the same sign of nearby $\Delta\rho_{\uparrow/\downarrow}$ on OH^*. So the $\Delta N_{\uparrow/\downarrow}$ of OH^* itself should be even smaller. The decrease of $\Delta N_{\uparrow/\downarrow}/\Delta N$ compared with OH^* under UHV conditions could result from two factors: first,

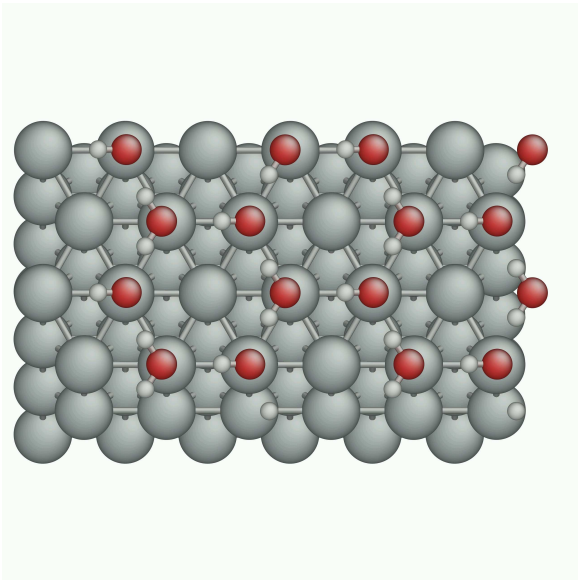

(a)

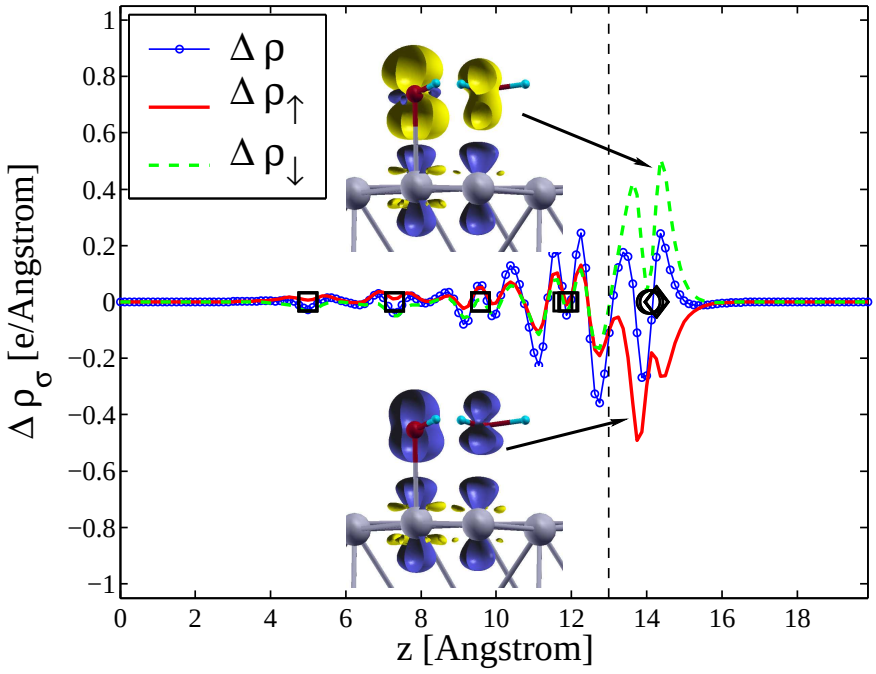

(b)

Figure 4.9: (a) Configurations of the hexagonal mixed network monolayer of OH + H_2O monolayer [31, 111]. (b) Charge/spin-charge difference density $\Delta\rho/\Delta\rho_\sigma$ along the surface normal direction for OH + H_2O monolayer. Meanings of difference signs are explained in the caption of Fig. 4.2.

dangling p orbital parallel the surface on O atom of OH^* is stabilized by nearby H_2O, so almost all $\Delta\rho_{\uparrow/\downarrow}$ are found on p_z orbital perpendicular to the surface; second, the increasing vertical distance between Pt and OH^* could decrease the interaction between p_z orbital of O atoms and Pt surface, which may further decrease spin-charge transfer. In conclusion, H_2O molecules on Pt surface not only stabilize OH^* but also impede the charge transfer from the surface, which makes OH^* closer to neutral state.

The next question is the effect of external field on the charge transfer between ORR intermediates and Pt surface. The electric field on electrode-electrolyte interface varies with electrode potential; even at constant potential, the electric field at different places on electrode surface could be different because of the variation of nearby electrolyte molecular structure. So we just add constant electric field to study charge transfer change tendency. The magnitude of electric field is estimated as the following: the normal range of ORR cathode potential V is $0.6 \sim 1.0$ volt with respect to the standard hydrogen electrode (SHE) and the potential of zero charge (PZC) for Pt(111)-aqueous 0.1 M $HClO_4$ interface is about 0.2 volt versus SHE[152]. Using the Gouy-Chapman-Stern model and supposing all the interfacial potential variation physically localizes within the outer Helmholtz plane (OHP), usually about 5 Å in thickness [7], the average electric field is still just $\sim$ 0.2 volt/Å. Considering the local oscillation, we add ± 0.5 volt/Å electric field on Pt (111) surface with ORR intermediates, where positive/negative field means to increase/decrease electrostatic potential far away from the surface, simulating the external potential gradient at cathode/anode.

Under external field, spin-change density difference is defined as

$$\Delta\rho \equiv \rho(\text{Pt(111)+Adsorbate+}E_{\text{ext}}) - \rho(\text{Pt(111)+}E_{\text{ext}}) - \rho(\text{Adsorbate+}E_{\text{ext}}) \qquad (4.16)$$

where E_{ext} means investigated species, including clean Pt (111) surface and adsorbate in

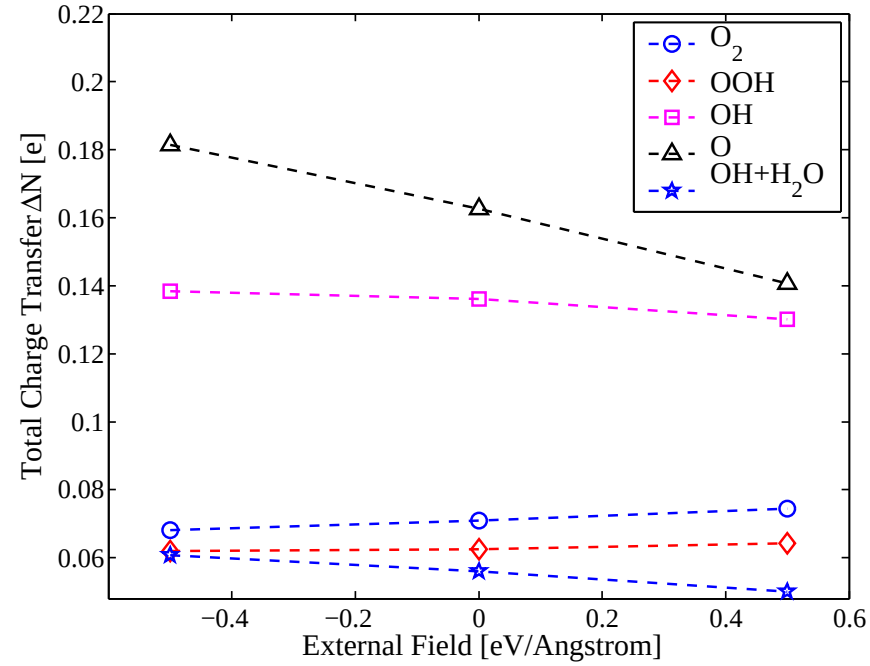

(a)

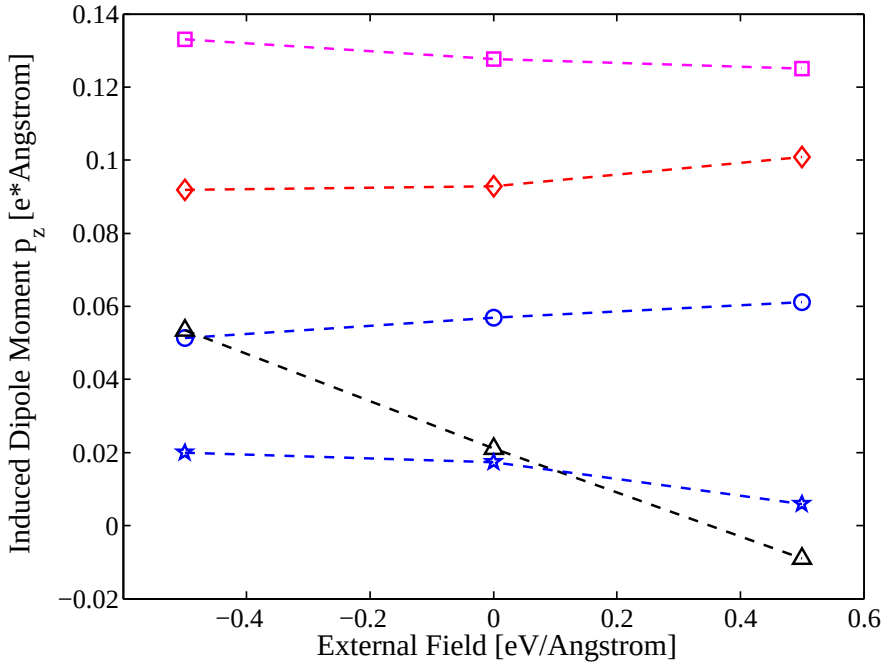

(b)

Figure 4.10: Changes of total charge transfer ΔN (a) and induced dipole moment p_Z (b) with external electric field for ORR intermediates, where positive/negative field means to increase/decrease electrostatic potential far away from the surface with adsorbates.

isolated state, are calculated under the same external field. The changes in total charge transfer ΔN and induce dipoles P_z with electric field are shown in Fig. 4.10. It is interesting to point out that for different intermediates, ΔN has different change tendencies: for O_2 and OOH, their ΔNs increase with positive electric field, but for O, OH and OH+H_2O, their ΔNs decrease with positive electric field. The induce dipole P_z for each intermediate changes in the same way as its ΔN, which supports our argument that induce dipole P_z is a good indicator of ΔN. Furthermore, instead of different tendencies, all the changes in both ΔN and P_z are quite small. Except for O atom, between $+0.5$ volt/Å and -0.5 volt/Å the differences in $\Delta N/P_z$ are always less than 0.02 e/0.02 eÅ for all ORR intermediates. The larger changes in O atom case reveal the inaccuracy of the integration method of Equation 4.14 because of the short vertical distance between O atom and Pt surface. However, its ΔN is still quite small compared with 1 e. So it is clear that during the whole range of interested potential, all ORR intermediates on Pt (111) surface are almost charge neutral, and all electron transfers between Pt and ORR intermediates occur through proton-coupled mechanisms as Eq. 4.1 to 4.7.

4.2 Dynamics of Proton-Coupled Electron Transfer in ORR

The above studies provide static pictures of ORR intermediates. However, the dynamics of proton-coupled electron transfer (PCET) process in ORR is still unclear. In Nørskov's model, at large electrode potential U some proton-coupled electron transfer step is up-hill in total free energy, so this positive reaction energy is used as its activation energy E_a[94], which means there is no extra barrier for this electron transfer step. This may be an over-simplified picture, because bare proton gets huge solvation energy ($\sim$ 10 eV [133]) by the surrounding H_2O shell so that it may need extra energy for proton to break this H_2O shell and meet ORR intermediates on the surface.

Generally there are two types of electron transfers at the electrode, *inner-sphere* and *outer-sphere*. The "outer-sphere" denotes an electron transfer reaction between two species remaining separated before, during and after the reaction, which includes the electron transfer between two ions in solvent (*homogeneous electron transfer*) or between the electrode and an ion in solvent (*heterogeneous electron transfer*); the "inner-sphere" means that two species process electron transfer by a shared chemical bridge between them, which includes the electrochemical ORR (Eq. 1.2) and HOR (Eq. 1.1) on Pt electrode. Outer-sphere electron transfer can be treated in a more straightforward way than inner-sphere processes[77, 90, 150], where specific chemical interactions, such as the surface adsorption on the electrode, may be important for the final reaction rate. So here we study the energetics and electronic structure evolution of PCET by calculating proton transfer process from hydronium near surface to ORR intermediates with DFT methods. The results may be helpful for us to build an analytical model of proton-coupled electron transfer based on the schemes of molecular orbitals and surface electronic structures[65, 113].

Proton-coupled electron transfer is completed in two sequential processes. The first step is proton transfer in the bulk electrolyte from the hydronium far away from the electrode to the hydronium on or close to the electrode surface, which can be considered as a "homogeneous" transfer process; the second step is proton transfer from the hydronium near the surface to the ORR intermediate adsorbed on the surface, where the proton meets the electron transferred from the electrode, so it can be regarded as a "heterogeneous" transfer process. For these reasons, it is better to deal with these two steps by different methods.

There have been a lot of studies for proton transfer in bulk electrolyte, which are composed of water molecules in most cases. Since protons in water always exist in the hydrated form, so called hydronium $H^+(H_2O)_n$, it is important to clarify the structure of hydronium. Generally, two main structural models have emerged for the hydrated proton. As shown in Fig 4.11, Eigen proposed the formation of an $H_9O_4^+$ complex in which an H_3O^+ core is

strongly hydrogen-bonded to three H_2O molecules[26]; Zundel provided the notion of an $H_5O_2^+$ complex in which the proton is shared between two H_2O molecules[156]. Marx et al. used *ab initio* path integral simulations to study the proton transfer in bulk water [83]. They found that the hydronium forms a fluxional defect in the hydrogen-bonded network, with both $H_9O_4^+$ and $H_5O_2^+$ occurring only in the sense of "limiting" or "ideal" structures. The defect can become delocalized over several hydrogen bonds owing to quantum fluctuations. For the proton transfer process, there is only a small barrier (< 0.05 eV) induced by solvent polarization, and the rate of proton diffusion is determined by thermally induced hydrogen-bond breaking in the second solvation shell.

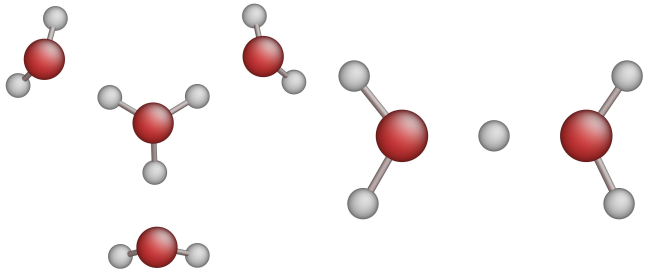

(a) (b)

Figure 4.11: Two structural models for hydronium. (a) an $H_9O_4^+$ complex proposed by Eigen[26]. (b) an $H_5O_2^+$ complex proposed by Zundel[156].

There are also a lot of first-principles studies of proton transfer from hydronium near the electrode to the ORR intermediate adsorbed on the electrode. A typical work is provided by Anderson et al.[120], where the hydronium is simulated by H_3O^+ connecting with two nearby H_2O molecules and the electrode is simulated by a two-atom-size Pt cluster. They used localized orbitals as the basis of wavefuntions, so that they can calculate the minimum energy paths of PCET at constant electrode potential U by fixing the gap between HOMO and LUMO. However, this system is too small to reveal the accurate electronic structures for the electrode, the ORR intermediates and the hydronium. For example, ORR interme-

diates on the small Pt clusters may have different electronic structures than those on large Pt electrode surface.

On the other hand, although plane-wave based first-principles methods plus periodic surface unit cell can describe the electronic structures of metallic electrode, it is difficult to use this method to simulate the reaction dynamics at constant U: in the typical plane-wave based DFT methods, the electrode potential can be estimated from the work function of metal-electrolyte interfacial structures[131]; however, this work function may vary if the configurations of certain species change in the interfacial structures, so does the electrode potential U.

4.2.1 PCET on Pt (111) Surfaces

Instead of obtaining very accurate dynamics of PCET at constant U, we study the proton transfer processes from hydronium near the electrode surface to ORR intermediates on Pt surface, which can be used as approximations as the corresponding process at constant U if the work function does not vary much during the transfer. The configuration of electrode-electrolyte interface model is constructed by (4×4) unit cell of Pt (111) surface plus one "hydronium", which is composed of one H_3O molecule and two H_2O molecules as a simple solvation shell, as shown in Fig. 4.12. Here two hydrogen atoms in H_3O form hydrogen bonds with two nearby H_2O molecules, while the third hydrogen atom points to the Pt surface. The ORR intermediates, such as O_2^*, O^* and OH^*, are initially adsorbed on the surface far away from the hydronium. Here it should be pointed out that the hydronium may not have exact +1 excess positive charge: when the hydronium is close to metallic surface, the solvation shell is partially broken, so the real charge surrounding the hydronium is uncertain and can change with detailed atomic configuration and electrode potential. In this simulation, the charge surrounding the hydronium structure is determined self-consistently by DFT calculation. Using the same method used in Section 4.1, we find that there is about

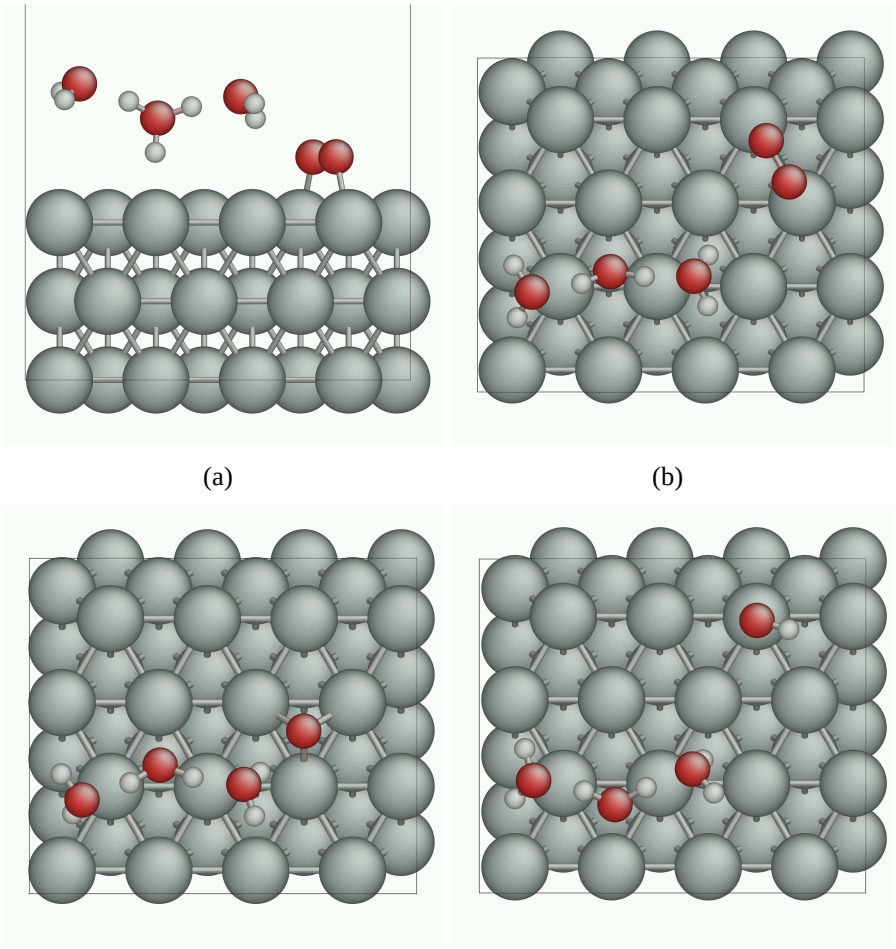

Figure 4.12: Side (a) and top (b) views of the coexistence of an H_7O_3 "hydronium" on top of Pt (111) surface and an O_2^* nearby. (c)/(d) is the top view the coexistence of an H_7O_3 "hydronium" and an O^*/OH^*. All of them are used as initial configurations to study PCET near Pt (111) surface.

+0.3 positive charge round the H_7O_3 hydronium, which is 3.4 Å away from the surface.

In the proton transfer process, first the hydronium and the ORR intermediate come close to each other through the diffusion of either the hydronium or the intermediate or both, then one hydrogen atom on the H_3O would transfer to the nearest H_2O that is close to the ORR intermediate. At almost the same time, this H_2O which just receives one more hydrogen atom would contribute one of its other two hydrogen atoms to the ORR intermediate adsorbed on the Pt surface. So the whole process is still like the proton transfer in the bulk water, where the distance of the movement for each hydrogen atom is very small ($\sim$ 1 Å) and the proton transfer processes through a chain reaction in a hydrogen bond network.

Table 4.5: Reaction energy δE and reaction energy E_a of PCET near Pt (111) surface by using the configurations shown in Fig. 4.12

	δE [eV]	E_a [eV]
$H_3O(H_2O)_2$+O_2^* $\rightarrow$$OOH^*$+$(H_2O)_3$	-0.16	0.09
$H_3O(H_2O)_2$+O^* $\rightarrow$$OH^*$+$(H_2O)_3$	+0.20	0.24
$H_3O(H_2O)_2$+O^* $\rightarrow$$H_2O^*$+$(H_2O)_3$	-0.60	0.00

Here we use DFT + NEB method to calculate these energy minimum paths for different ORR intermediate, as shown in Fig. 4.13, 4.14 and 4.15, and the energetic data are listed in Table 4.5. In the cases of proton transfer from hydronium to O_2^* and OH^*, the activation energies are less than 0.1 eV, and most of these barriers come from the diffusion of O_2^* or OH^* on Pt surface. At the real electrode-electrolyte interface, even such small diffusion barriers can be avoided, because the hydronium can easily come close to O_2^* or OH^* through the hydrogen bond network in the electrolyte. In the case of proton transfer from hydronium to O^* atom, the activation barrier increases to 0.24 eV. However, the reaction energy of this proton transfer process is also +0.2 eV, which means almost no extra activation barrier except the positive reaction energy. These low activation energies satisfy with the assumption of the activation barrier used by Nørskov[94], where the positive reaction energy is directly

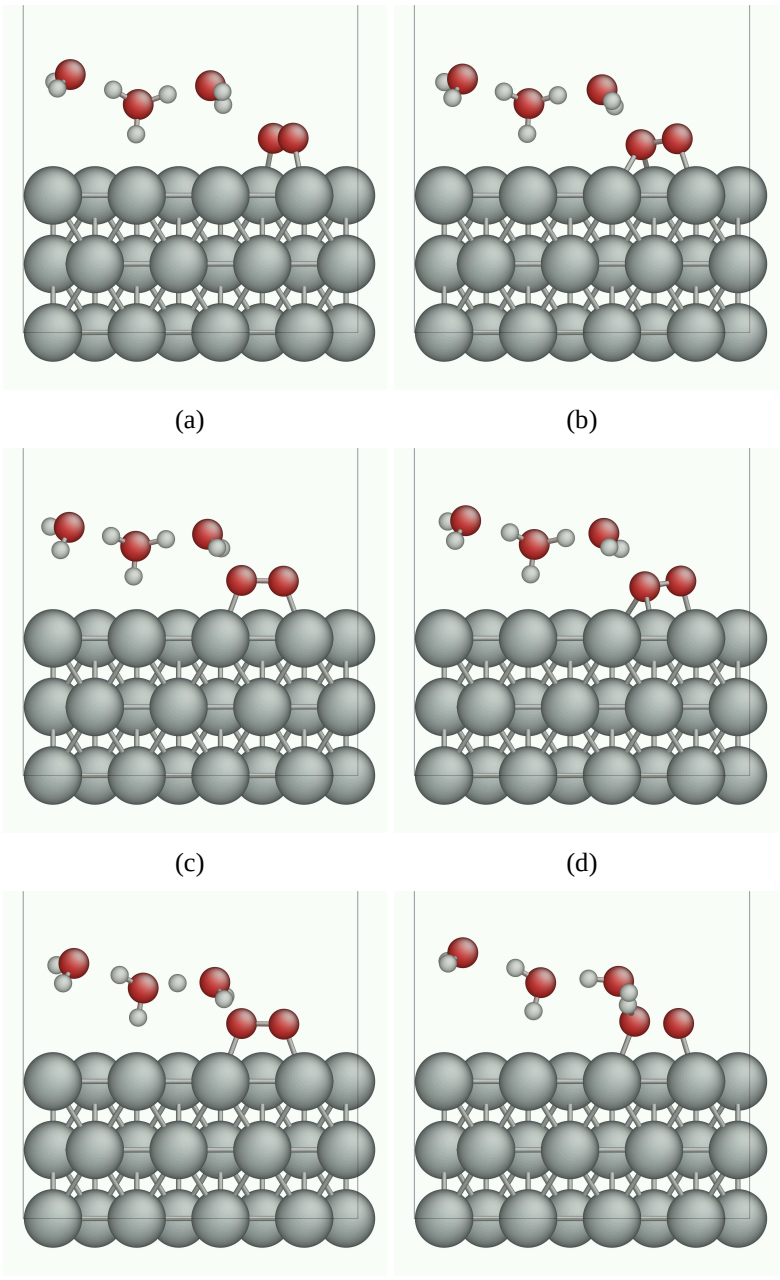

Figure 4.13: From (a) to (f): the minimum energy path of $O_2^* + H^+ + e^- \rightarrow OOH^*$ near Pt (111) surface, where (b) is the configuration of transition state.

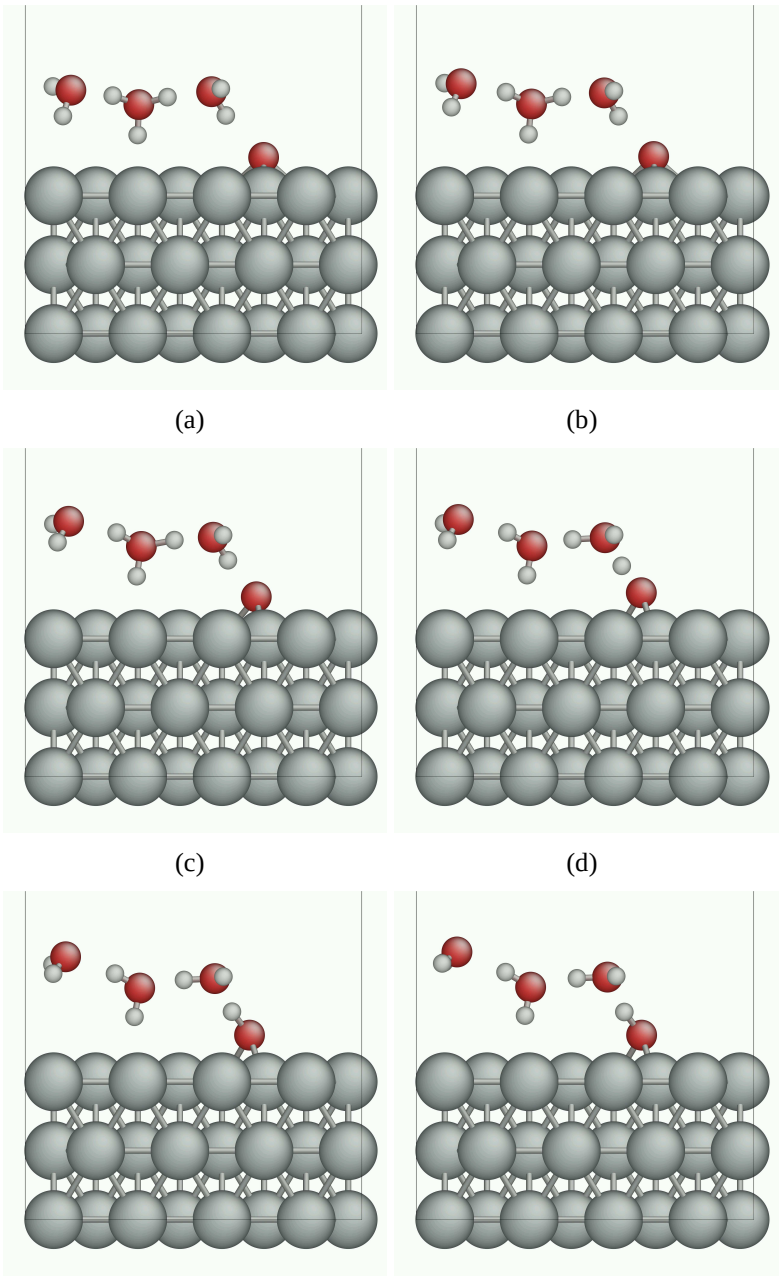

Figure 4.14: From (a) to (f): the minimum energy path of $O^* + H^+ + e^- \rightarrow OH^*$ near Pt (111) surface, where (d) is the configuration of transition state.

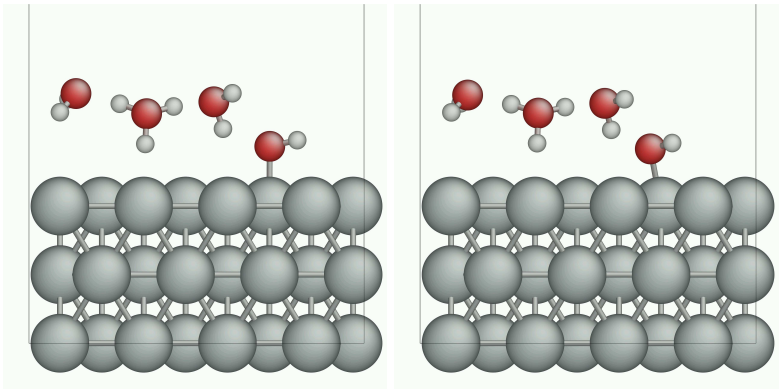

(a)

(b)

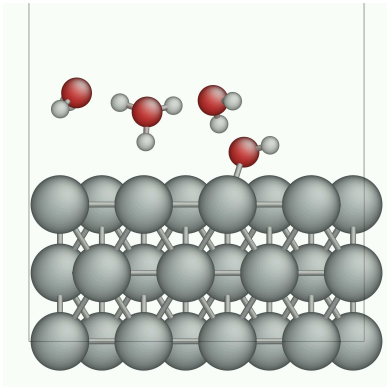

(c)

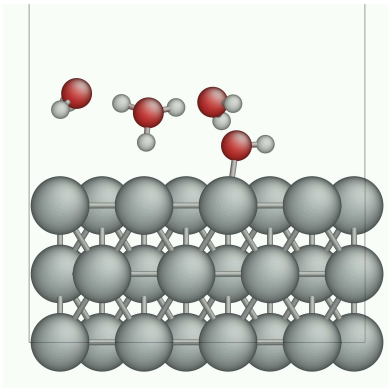

(d)

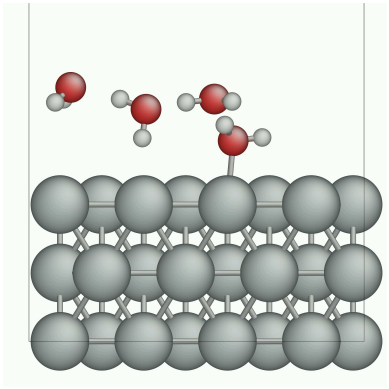

(e)

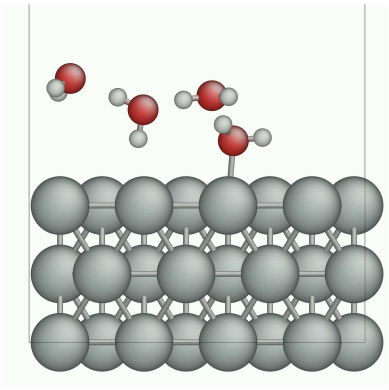

(f)

Figure 4.15: From (a) to (f): the minimum energy path of $OH^* + H^+ + e^- \rightarrow H_2O$ near Pt (111) surface, where the energy of each configuration keeps decreasing from initial (a) to final (f) state.

used as the activation energy to estimate the reaction rate.

4.2.2 General Pictures of PCET Dynamics

To test whether these small energy barriers are special cases for Pt surface or general phenomena on different metallic surfaces, the minimum energy path of proton transfer from hydronium to O* atom is also calculated on Au, Cu, Ni and Al (111) surfaces. The results of reaction energy and activation energy are listed in Table 4.6, where the stability of O^* relative to OH^* is also calculated, defined as the energy changes $\delta E_{O^* \to OH^*}$ of the following reaction:

$$O^* + \frac{1}{2}H_2 \to OH^* \tag{4.17}$$

In Table 4.6, there is a clear tendency that when the stability of O* relative to OH* increases as $\delta E_{O^* \to OH^*}$ becomes more positive, both the reaction energies and activation energies of the corresponding PCET also become more positive. On Au (111) surface, there is a large negative reaction energy and almost zero activation energy for proton transfer to O^*, while on Al (111) surface, the activation energy is relatively high. From the analysis of minimum energy path, it shows that most of the activation energies on Al, Ni and Pt come from the barrier to move O^* atom from fcc hollow site to bridge site at the transition state, instead of the proton transfer process inside the hydrogen bond network. Furthermore, even for Al the activation energy is only 0.3 eV larger than the reaction energy. So it is suitable to use the positive reaction energy as the approximate value of the activation energy in PCET, as long as the proton (hydronium) is close to the electrode surface.

However, as mentioned above, these DFT+NEB studies only reveal the dynamics of PCET near the electrode surface; a full PCET path is completed if we also consider how the proton is transferred from hydronium in the bulk electrolyte to hydronium near the surface.

Table 4.6: Reaction energy δE and reaction energy E_a of PCET to O^* near Au, Ni, Pt, Cu and Al (111) surface by using the configuration shown in Fig. 4.12 (c) ($H_3O(H_2O)_2$+$O^* \rightarrow OH^*$+$(H_2O)_3$). $\delta E_{O^* \rightarrow OH^*}$ is the reaction energy of Eq. 4.17.

	δE [eV]	E_a [eV]	δE (O^*+$\frac{1}{2}H_2 \rightarrow OH^*$)[eV]
Al	0.10	0.39	1.05
Ni	0.03	0.23	-0.20
Pt	0.20	0.24	-0.52
Cu	-0.81	0.00	-0.79
Au	-1.00	0.04	-1.34

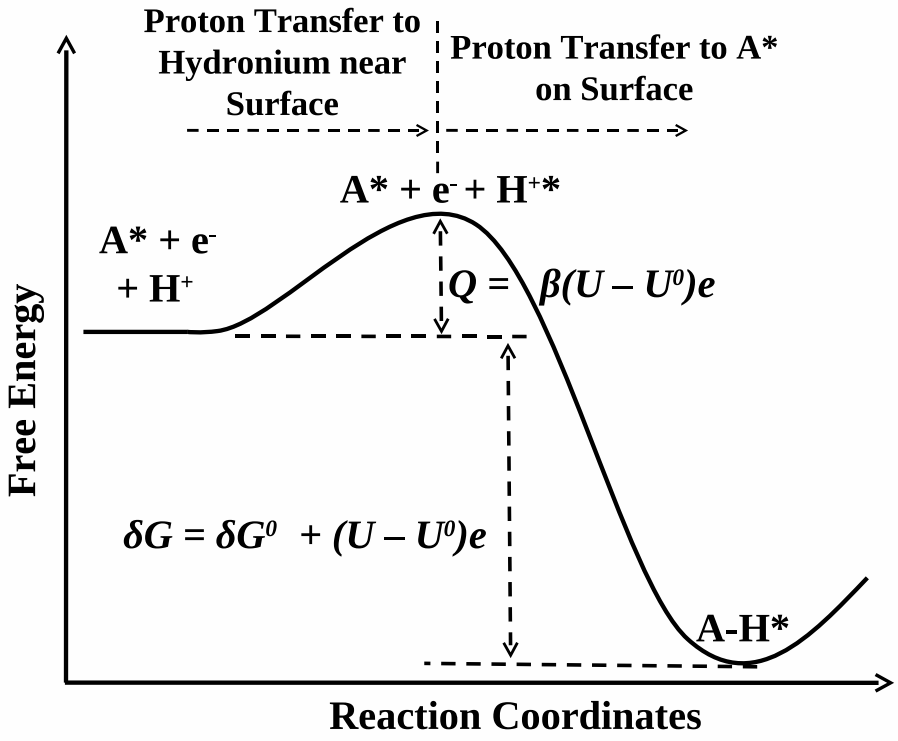

Figure 4.16: Reaction path of proton-coupled electron transfer (PCET) $A^* + H^+ + e^- \rightarrow AH^*$. Here Q_{PT} is the activation free energy for proton transferred from the hydronium in the bulk electrolyte to the hydronium near electrode surface; δG is the reaction free energy of the whole reaction; H^+* means proton is in the hydronium close to the electrode surface; β is symmetric factor and usually $\beta \approx \frac{1}{2}$[7, 78, 79, 80].

Usually this process requires excess energy, because the solvation field surrounding this hydronium would change and the electric field applied on this hydronium also changes. When electrode potential U increases, such excess energy would also increase, because more positive U results from more positive excess charges on the electrode surface, which would increase the repulsive energy between hydronium and electrode surface. So here we propose a hypothesis of PCET dynamics, as shown in Fig. 4.16: when proton is transferred from the hydronium in the bulk electrolyte to the hydronium near electrode surface, the activation free energy Q_{PT} changes with electrode potential U as the following equation

$$Q_{\mathrm{PT}} = \beta(U - U^0)e \tag{4.18}$$

where U^0 is the electrode potential at which Q_{PT} = 0, and β is called *symmetry factor*, defined in Section 2.2.3. For most cases in experiments, $\beta \approx \frac{1}{2}$[7, 78, 79, 80]. Then the proton is transferred to surface adsorbates A^* and meet the electron from the electrode. According to the above calculations and discussions, if this step is down-hill in free energy, there is no extra activation free energy; otherwise, the extra activation free energy equals the total free energy difference in this step. Thus, the total activation energy of whole PCET can be summarized as

$$\begin{aligned} Q &= Q_{\mathrm{PT}} = \beta(U - U^0)e \quad \text{if} \quad \delta G < Q_{\mathrm{PT}} \\ &= \delta G = \delta G^0 + (U - U^0)e \quad \text{otherwise} \end{aligned} \tag{4.19}$$

Because δG can be negative at low U (high overpotential) and positive at high U (low overpotential), the change of Q can have different linear relations with the change of U: $\delta Q = \beta \delta U e$ at low U but $\delta Q = \delta U e$ at high U. For electrochemical ORR, the reaction rate at low overpotential is more important to evaluate the activity of catalysts, thus, the usage

of δG as Q in Nøskov's model is a good approximation[94].

However, for the activation free energy of PCET at low U, the exact physical meaning of β is unclear. There are two possible explanations. The first explanation depends on partial electron transfer: when the hydronium comes close to electrode surface, it may not be still at +1 charge state; as the calculations in Sec 4.2.1 shown, part of one electron charge, such as βe^- with $\beta < 1$, may already transfer to the near-surface hydronium; as a result, when electrode potential changes by δU, the free energy of PCET's initial state and transition state, in which hydronium is close to the surface, may change by -δUe and -(1-β)$\cdot\delta Ue$, respectively; thus, their difference, defined as activation free energy Q, changes by (-(1-β)$\cdot\delta Ue$) - (-δUe) =$\beta\cdot\delta Ue$, so β can be defined as symmetry factor. The second possible explanation is from the potential distribution in the electrical double layer structures. As shown in Section 2.2.2, when hydronium comes close to the surface, the electrostatic potential is different from the bulk electrolyte far away; thus, when electrode potential changes by δU, the electrostatic potential surrounding the near-surface hydronium may change by (1-β)δU; as a result, the free energy of PCET's initial state and transition state may change by -δUe and -(1-β)$\cdot\delta Ue$ so that the corresponding Q changes by their difference, $\beta\cdot\delta Ue$. Both mechanisms are possible and a detailed analysis depends on a correct description on electronic structures and potential profile of electrode-electrolyte interface, which will be discussed in Section 5.2.

4.3 Search of New Catalysts by First-Principles Methods

The studies in the last two sections support the validity of the assumptions used in Nørskov's model[94]: the electron transfer mechanism and the approximation of activation energy. In this section, we try to use this model to search for new alloy structures with better catalytic performance than pure Pt. First, we use combinatorial methods to test (111) surfaces of

a lot of noble metal alloys. Then we study a series of special structures: Pt (111) surface with different types of Au clusters deposited on it.

4.3.1 Combinatorial Search of Noble Metal Alloys

According to Nørskov's ORR model, there is an optimal value of atomic oxygen adsorption energy $E^{O^*}_{opt-ads}$ to reach the highest ORR activity, and $E^{O^*}_{ads}$ on Pt (111) surface is only $\sim$0.2 eV stronger than $E^{O^*}_{opt-ads}$[94]. This agrees with the famous Sabatier principle, which states that a good catalyst should form chemical bonds of intermediate strength to the surface adsorbates[112, 122]. In experiments, it is found that certain Pt alloys, such as Pt_3Co, Pt_3Ni and Pt_3Fe in Cu_3Au ($L1_2$) lattice structure[134, 125, 126, 47], have better catalytic activity than pure Pt. DFT calculations indicate weaker binding of oxygen atom on these alloys than pure Pt, which may explain the activity enhancement according to Nørskov's ORR model[123]. In this section, we use this model to calculate ORR reaction rate on different designed alloy structures at certain electrode potential. In addition, because the stability of these alloys is also crucial to their practical application as electrocatalysts[119, 47], we also use a simple thermodynamic model to estimate their anti-corrosion stability.

We first start from a simple surface model as shown in Fig. 4.17. It is a ($\sqrt{3}\times 2$) unit cell of four (111) layers in FCC lattice structure, so 16 atoms are used in calculation, 15 of which belong to one type of metal as the basis element. Because it needs to have good anti-corrosion ability, only four kinds of noble metals, Pt, Pd, Ag and Au, are used as the basis elements. The left atom is used by another alloying element. It is placed at either the first or second layer depending on which configuration has lower energy. Then the adsorption energy of O* and OH* on these surfaces are calculated.

The total reaction rates of ORR are calculated by the methods used in Nørskov's model[94]. In this model, ORR activity can be estimated from the adsorption energies of O^*($E^{O^*}_{ads}$) and OH^*($E^{OH^*}_{ads}$) through the following mechanism: first, ORR is assumed to occur in three se-

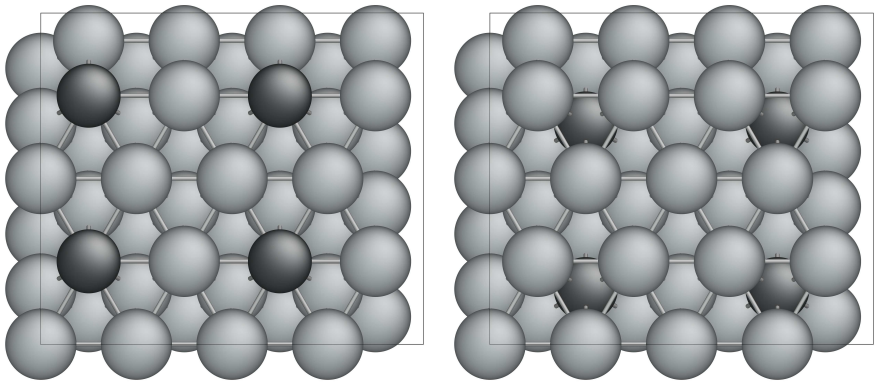

(a) (b)

Figure 4.17: (111) surface of noble metal alloys with alloying atom at (a) top layer and (b) second top layer. In a ($\sqrt{3}\times2$) unit cell there are four (111) layers and 16 atoms in total; 15 of them are basis element atoms in light color, the left one is the alloying atom in dark color.

quential steps: O_2 dissociated adsorption ($O_2 \rightarrow 2O^*$), oxygen protonation ($O^* + H^+ + e^- \rightarrow OH^*$) and hydroxyl protonation ($OH^* + H^+ + e^- \rightarrow H_2O$); then the activation energy of the first step can be obtained from an extrapolated increasing linear relation between O_2 dissociation barrier and $E_{\text{ads}}^{\text{O}^*}$ [12]; the reaction free energy of the last two steps, which are calculated from $E_{\text{ads}}^{\text{O}^*}$ and $E_{\text{ads}}^{\text{OH}^*}$ and can be positive values, are used as lower bounds of their activation energies. Thus, if $E_{\text{ads}}^{\text{O}^*}$ is a too high value, which means weak adsorption, O_2 dissociation becomes too difficult; on the other hand, if either $E_{\text{ads}}^{\text{O}^*}$ or $E_{\text{ads}}^{\text{OH}^*}$ is too negative, which means strong adsorption, the last two steps may become very slow. In addition, because the activation free energies of ORR change with U, catalytic activities of different surfaces are evaluated by the activation energy of ORR when electrode potential $U = 0.9$ vs. SHE, which is close to the working potential of PEM fuel cell[6].

Meanwhile, the anti-corrosion stability of these alloy structures is estimated by equilibrium potential U_{eq} for the corrosion of the alloying element atom, which is removed from the surface and becomes a solvated ion in the electrolyte after corrosion. Because the free energy of an ion in the electrolyte comes from a long range of solvation field, it is difficult

to use first-principles methods to accurately calculate U_{eq}. On the other hand, U_{eq}s for pure metals are well known from the experimental handbook. So here we can obtain U_{eq} for alloy surface with the help of these experimental data. For example, for an alloy surface $M_{15}X$ in the structure of Fig. 4.17, where M is the basis element and X is the alloying element, we first use DFT to calculate the reaction energy E_{seg} of the following segregation reaction

$$\mathrm{M_{15}X_{surface}} + \mathrm{M_{bulk}} \rightarrow \mathrm{M_{16-surface}} + \mathrm{X_{bulk}} \tag{4.20}$$

where $\mathrm{M_{15}X_{surface}}$ and $\mathrm{M_{16-surface}}$ are both in (111) surface structure as shown in Fig. 4.17, while $\mathrm{M_{bulk}}$ or $\mathrm{X_{bulk}}$ is one atom in the lattice structure of the pure bulk phase. From the experimental handbook, pure X in bulk phase can be oxidized as cation in the water with n^{+} charge above the equilibrium potential $U_{\mathrm{eq}}^{\mathrm{x}}$ as the following:

$$\mathrm{X_{bulk}} \rightarrow \mathrm{X}^{\mathrm{n}+} + \mathrm{n}e^{-} \tag{4.21}$$

Combining reactions in Eq. 4.20 and 4.21 together, we obtain the following reaction

$$\mathrm{M_{15}X_{surface}} + \mathrm{M_{bulk}} \rightarrow \mathrm{M_{16-surface}} + \mathrm{X}^{\mathrm{n}+} + \mathrm{n}e^{-} \tag{4.22}$$

Thus, the equilibrium electrode potential of this corrosion reaction is

$$U_{\mathrm{eq}} = U_{\mathrm{eq}}^{\mathrm{x}} + \frac{E_{\mathrm{seg}}}{\mathrm{n}e} \tag{4.23}$$

The final results are shown from Fig. 4.18 and 4.19 for Pt, Pd, Ag and Au alloys respectively. For Au and Ag, all their alloys have very high activation energy for ORR, indicating negligible catalytic activities. For Pt and Pd alloys, although some of them have considerable good catalytic activity, most of their U_{eq}s are lower than 0.9 V, a common working

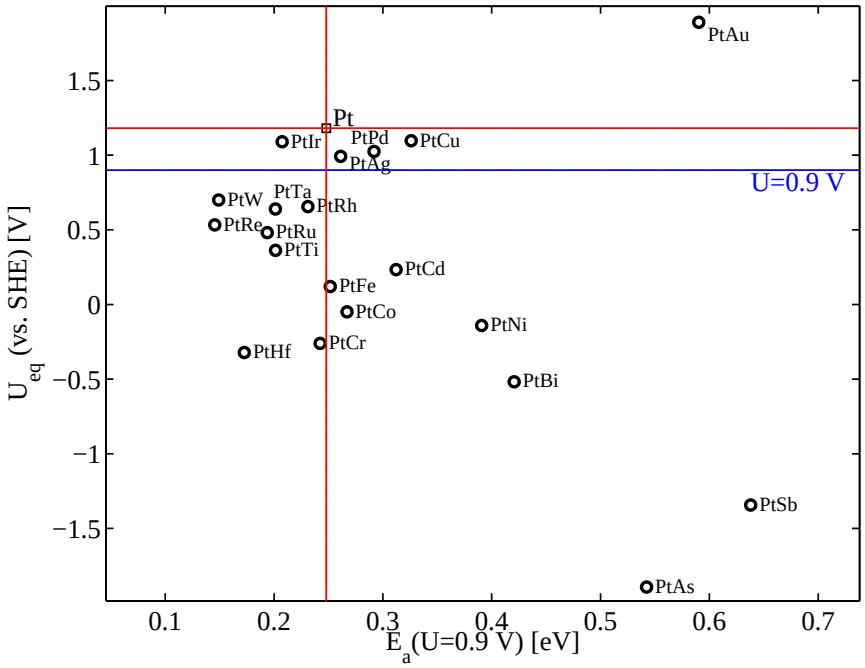

(a)

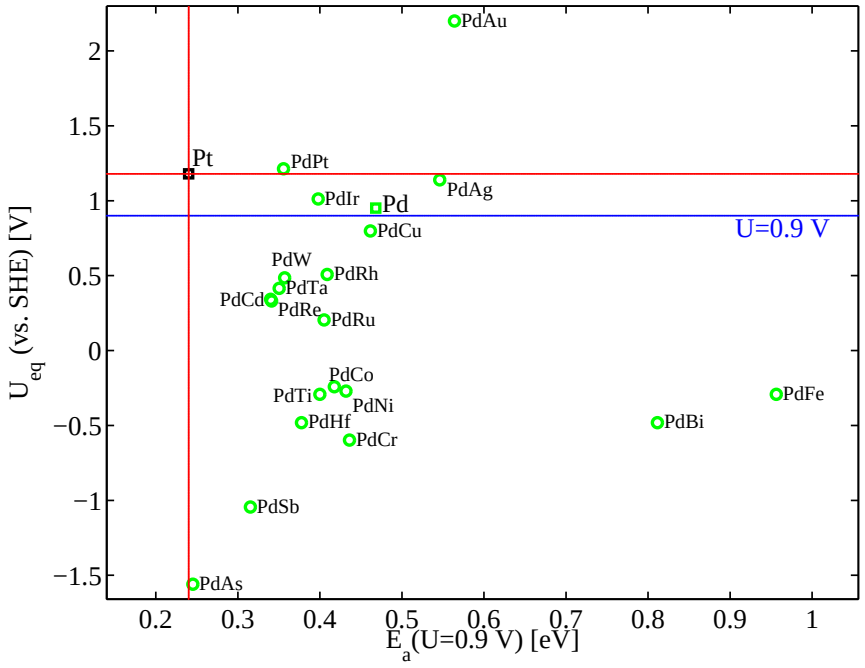

(b)

Figure 4.18: The activity and stability of (a) Pt and (b) Pd alloys in the structure of Fig. 4.17. The activity is shown along x-axis by the activation energy E_a of ORR when U = 0.9 vs. SHE, and the stability is shown along y-axis by U_{eq} for the corrosion of alloying element atoms.

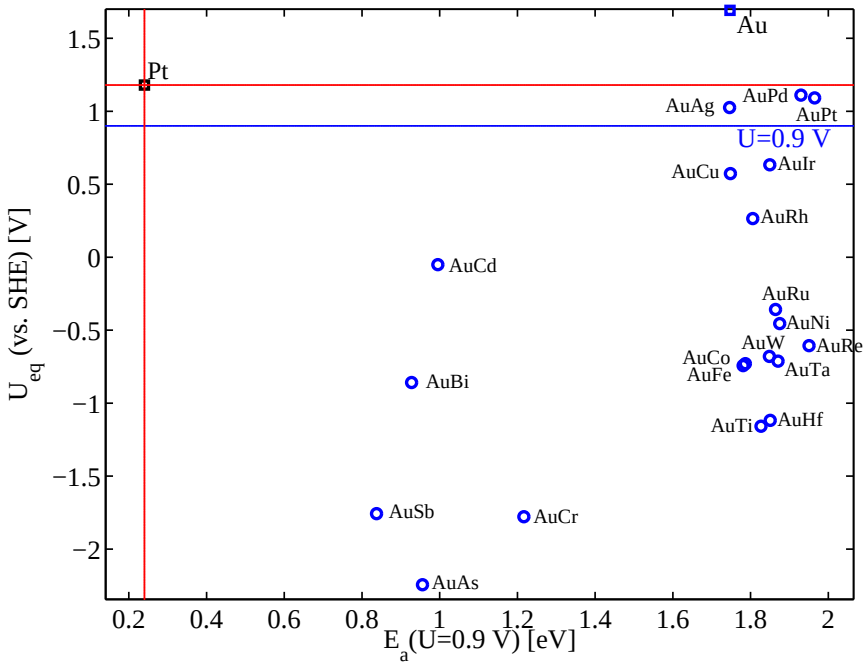

(a)

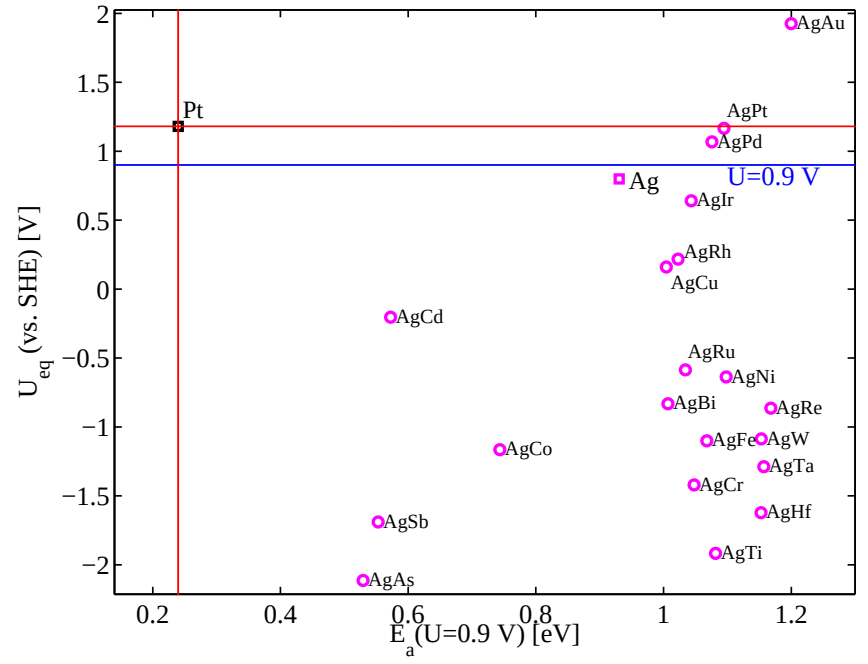

(b)

Figure 4.19: The activity and stability of (a) Au and (b) Ag alloys in the structure of Fig. 4.17. The activity is shown along x-axis by the activation energy E_a of ORR when U = 0.9 vs. SHE, and the stability is shown along y-axis by U_{eq} for the corrosion of alloying element atoms.

potential for PEM cathode, indicating it is always thermodynamically favorable for the corrosion reactions. In summary, no alloy structures of these (111) surface configurations are found to have both high catalytic activity and better anti-corrosion stability than (111) surface of pure Pt.

4.3.2 Pt Surface + Au Clusters

However, there could be other structures to reach these dual requirements. For example, oxide-Pt mixtures or Pt surfaces with deposited noble metal nano-clusters may be good candidates, since some oxide and noble metal themselves are quite stable in an acidic environment. It is reported that Pt surface partially covered with Au clusters has ORR activity almost equal to pure Pt[154]. To confirm and explain this result, we study different types of Au clusters on Pt (111) surface.

In our studies, we test different configurations of Au clusters on Pt (111) surfaces. As shown in Fig. 4.20, clusters with 3, 4, 7 and 10 atoms are placed on Pt (111) surfaces, also with oxygen atoms adsorbed at the most favorable sites on them. Surprisingly, the Au clusters with 3 and 4 atoms have oxygen adsorption energy $E_{\mathrm{ads}}^{\mathrm{O}^*}$ very close to the value on Pt (111) surface ($E_{\mathrm{ads}}^{\mathrm{O}^*}$ = -0.85 and -0.70 eV for 3-atom and 4-atom Au clusters), so they may have very good catalytic activity for ORR. However, once the Au cluster size increases a little bit to 7 and 10 atoms, $E_{\mathrm{ads}}^{\mathrm{O}^*}$ decreases dramatically to the low value of bulk Au ($E_{\mathrm{ads}}^{\mathrm{O}^*} \sim$ -0.40 and -0.05 eV for 7-atom and 10-atom Au clusters), so does its catalytic activity.

These high activities of small Au clusters seem to agree with the similar results of Au clusters on TiO_2 for CO oxidation[138], and it may explain the good catalytic activity of Au-deposited Pt surface. However, after more detailed studies, it is found that these small Au clusters are not stable on Pt surface. For example, there is -0.3 eV reaction energy benefits to combine a Au cluster with 3 atoms and another cluster with 4 atoms into a larger cluster with 7 atoms. In addition, unlike small metallic cluster on oxide support where

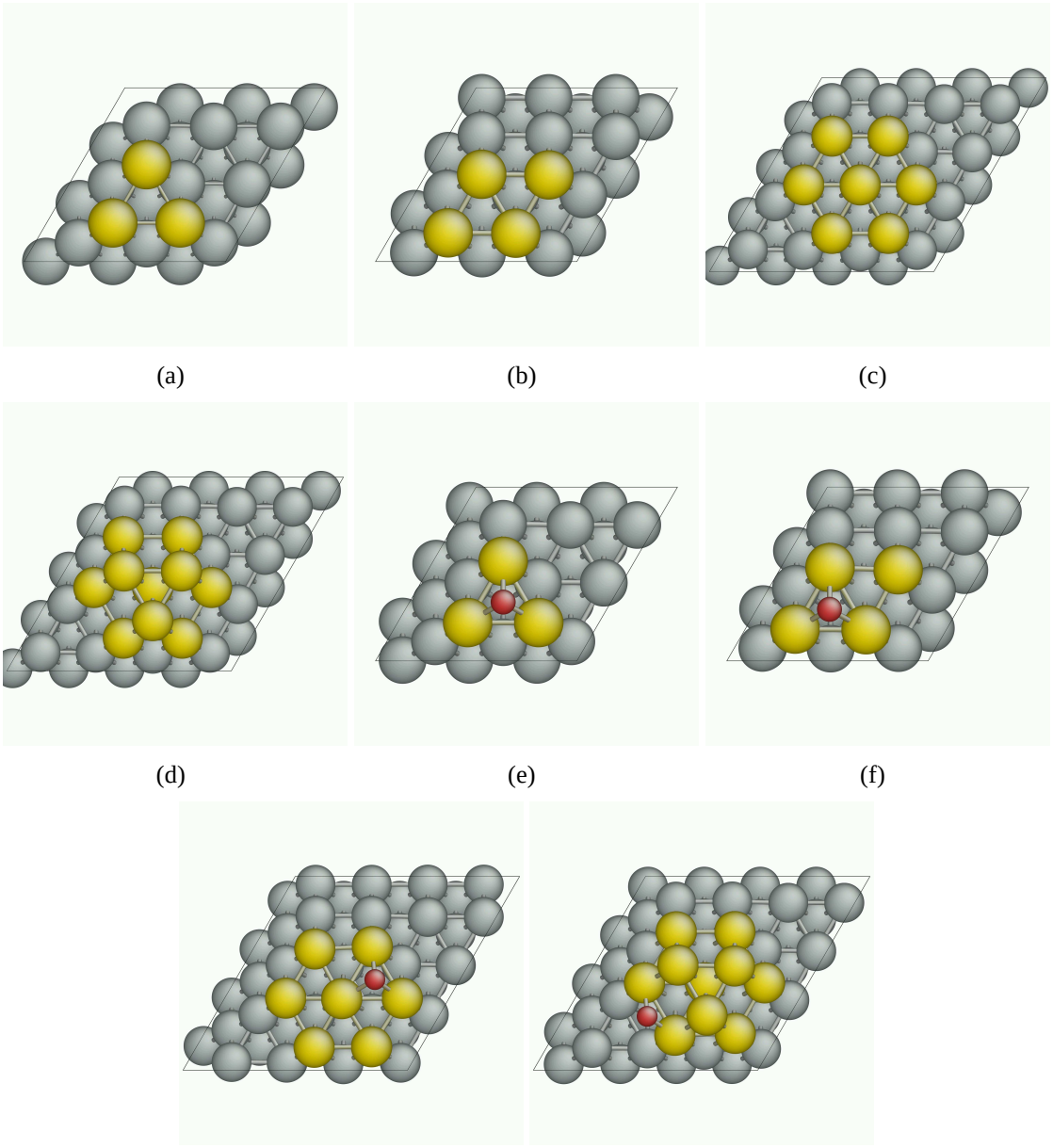

Figure 4.20: Au clusters on Pt (111) surface. (a)∼(d) are (3×3) super cell of Pt (111) surface with Au clusters composed of 3, 4, 7 and 10 Au atoms, respectively. (e)∼(f) are the configurations of the adsorption of oxygen atom on those Au clusters.

there are strong directional covalent bonds, the diffusion of Au cluster on Pt surface is relatively easy so that the cluster coarsening can occur at high rates. This is also confirmed by experimental observations[154], where most Au clusters are found to have diameters with 2$\sim$5 nm, containing hundreds or thousands Au atoms. Thus, these Au clusters themselves would not have good catalytic activity for ORR, and the areas of Pt surface which are covered by Au clusters may result in the degradation of Pt's catalytic performance.

However, there may also be some changes occurring to Pt surfaces. As shown in Fig. 4.21 (a), $E_{\text{ads}}^{\text{O}^*}$ on the Pt surface close to the Au cluster decreases to about 0.2 $\sim$ 0.3 eV compared with $E_{\text{ads}}^{\text{O}^*}$ on the Pt surface far away from Au cluster, as shown in Fig. 4.21 (b). This means that Pt surface near the Au cluster may have ORR activity better than pure Pt itself according to Nørskov's model[94, 123]. A simple back-of-envelope calculation indicates that it is possible to use the area of Pt surface near the Au cluster to compensate for the loss of catalytic activity from the area covered by the Au cluster. From the experimental measurement, about one third of total surface areas are covered by Au clusters. If all Au clusters are considered to be in round shapes with the diameter of 3 nm, and if we assume Pt surface area would have better activity if it is less than 0.5 nm away from a Au cluster, then these special Pt surface areas need to have activity per unit area of about 3 to 4 more times than the ordinary pure Pt surface, by which the activity of total surface areas can equal its counterpart on pure Pt surface. This 3$\sim$4 times activity increase is possible, because $E_{\text{ads}}^{\text{O}^*}$ on this special Pt surface is close to the corresponding values on (111) surface of Pt_3Co and Pt_3Ni, which are found by experiments to have 3$\sim$10 times higher activity than pure Pt (111) surface[125, 126].

Besides the activity issues, those Au clusters are found to increase the stability of Pt nanoparticles[154]. Usually, corrosion and dissolution of Pt nanoparticles are found during oxidation/reduction cycling in the turning-on/off processes of PEM fuel cell[119, 110, 11]. Especially if bulk oxide is formed on top of Pt surface, some Pt atoms have to move from

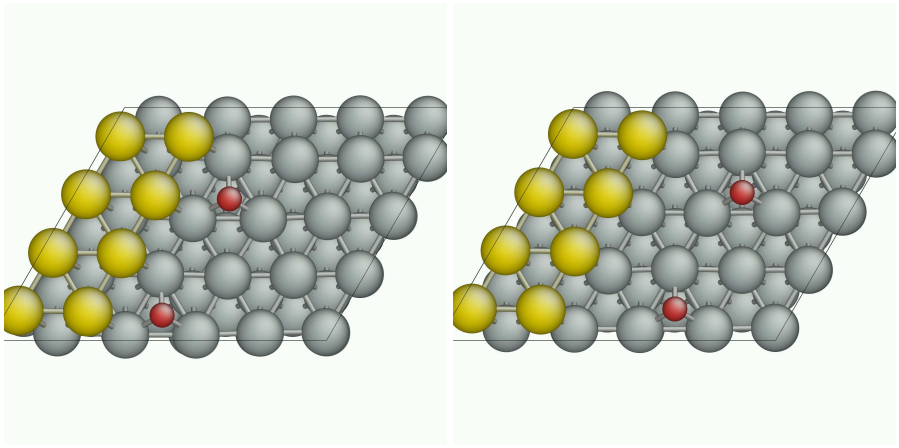

(a) (b)

Figure 4.21: Au steps on Pt (111) surface. (a) oxygen atom is adsorbed on Pt surface near Au steps, (b) oxygen atom is adsorbed Pt surface far from Au steps.

their original lattice sites and may not come back to these sites during the reversible reduction process; as a result, the dissolution rate of Pt atoms largely increases. Through our studies in Chapter 6, we find that the formation rate of bulk oxide depends on detailed surface structures and it is difficult for oxygen atoms to go through the top layer into the bulk lattice of Pt. Some surface defects may play the role of fast tunnel for the oxygen atoms to transfer into bulk Pt. If some stable Au clusters are deposited on Pt surface, most of these small surface defects could be covered by Au clusters, which impede the oxygen transfer through the top layer and the following oxidation. This defect passivation effect of the Au cluster may be the reason for the stability increase of Au-modified Pt surface, which will be investigated in future studies.

In summary, in this chapter, we mainly investigate electrochemical ORR mechanism. It is shown that all ORR intermediates (O_2^*, OOH^*, ...) are in near-neutral states so that electrons are transferred to them from the electrode by a proton-coupled (PCET) mechanism. We also study the dynamics of PCET near electrode surfaces and propose a hypothesis to describe its activation free energies, as shown in Eq. 4.19. All these results are useful for us to build a large-scale model to accurately describe ORR kinetics on different surfaces,

which is the main subject of Chapter 5. Before that, DFT methods themselves can be used to perform a quick and coarse search for new catalysts with better activity and stability based on some simple models of ORR kinetics and equilibrium corrosion potentials.

Chapter 5

Multiscale Modeling of Electrochemical Reactions

In the previous two chapters, we focus on how to use first-principles methods, such as DFT, to study the activity of oxygen reduction reaction (ORR) at both ultra-high-vacuum (UHV) and electrochemical conditions. However, to directly compare our results with experimental measurements, we need multiscale models beyond individual atomic reactions at specific surface sites. Here in Section 5.1, we first discuss how to obtain the total ORR rate and current density j at a given electrode potential U by considering the reaction networks on limited surface sites; in Section 5.2, by studying the structures of electrode-electrolyte interface, we try to obtain U and the corresponding differential capacitance C_{d} as functions of excess surface electron density σ^{M} on metallic electrode; finally, in Section 5.3 we discuss the principles of how to build a multiscale model to output both U and j in a self-consistent way.

5.1 Kinetic Model

Experimentally, it is found that Pt have the highest ORR catalytic activity among pure metals[33], and the rank of ORR activity of unit surface area for common Pt low-index facets is (110) $\approx>$ (111) $>$ (100) if there are no specifically adsorbed ions on Pt surfaces[125, 78, 79]; in addition, such high activity on Pt can be further increased to 2 $\sim$ 10 times by various Pt alloys[87, 88, 124, 33, 125, 126, 146]. So it is important to build an accurate ORR kinetics model, from which we can find the contributing factors for high ORR activity to explain these experimental results, and establish some general guidelines for the search of better ORR catalysts.

However, similar to the debates on charge states of ORR intermediates and the corresponding electron transfer mechanism discussed in the beginning of Chapter 4, the kinetics of ORR is another complex issue, on which consensus is generally lacking. Currently, there are three different theories on the rate-determining step in ORR and the reasons for activity increases in certain Pt alloys. The first one, which is widely accepted, was proposed by Nøskov et al.[94, 123]. In this model, on different surfaces both rate-determining step and the corresponding activation free energy $Q_{\mathrm{A}}^{\mathrm{RDS}}$ change with oxygen adsorption energy $E_{\mathrm{ads}}^{\mathrm{O}^*}$; on Pt surface the rate-determining steps are protonation of O^* as

$$\mathrm{O}^* + \mathrm{H}^+ + \mathrm{e}^- \rightarrow \mathrm{OH}^* \tag{5.1}$$

and OH^* as

$$\mathrm{OH}^* + \mathrm{H}^+ + \mathrm{e}^- \rightarrow \mathrm{H_2O} \tag{5.2}$$

because both of them have similar $Q_{\mathrm{A}}^{\mathrm{RDS}}$. On the surface of Pt alloys, such as $\mathrm{Pt_3Ni}$, $\mathrm{Pt_3Co}$ and $\mathrm{Pt_3Fe}$, the activity enhancement results from weaker adsorption strengths for both O^*

and OH^*, which not only change the rate-determining step to protonation of O_2^* as

$$O_2^* + H^+ + e^- \rightarrow OOH^* \tag{5.3}$$

but also reduce Q_A^{RDS} a little bit, about $0.03 \sim 0.05$ eV when electrode potential U = 0.9 V vs. SHE[123], thus, the total ORR activity increases by $3 \sim 10$ times calculated from Arrhenius equation $\exp\left(-\frac{\delta Q_A^{RDS}}{k_B T}\right)$ at room temperature (T = 300 K), matching the experiments perfectly.

The second theory was proposed by Markovic et al. [78, 79, 102, 126, 146]. They assumed the first electron transfer step as Eq. 5.3 to be the rate-determining step, which is supported by the first-order dependence of kinetic current on the O_2 concentration near the electrode[78, 79]. They also measured Q_A^{RDS} on surfaces of Pt, Pt-Ni and Pt-Co alloys[102], showing that there are no differences of Q_A^{RDS} beyond experimental uncertainty. So they argued that the activity increases in Pt alloys resulted from the pre-exponential factor υ of the conventional transition state theory rate expression $\upsilon \cdot \exp\left(-\frac{\delta Q_A^{RDS}}{k_B T}\right)$: because of weaker adsorption for both O^* and OH^* on Pt alloys, less surface areas are occupied by them at a steady state, so there are more empty adsorption sites available for the incoming reactant, O_2, resulting in an increase of υ[126].

The third one comes from Watanabe et al.[146]. They measured the amount of ORR intermediates on surfaces of Pt and Pt-Fe alloys during ORR at different U. The results showed that the more active Pt-Fe surface has more coverage of O^* than pure Pt. Thus, they proposed that oxygen protonation as Eq. 5.1 was the rate-determining step, and stronger adsorption of O^* on Pt-Fe surface increased O^*'s coverage, which further increased the Arrhenius pre-exponential factor of the rate-determining step.

Besides the above contradictions between different ORR kinetic theories, we have another concern about whether and how current DFT calculations can be used in ORR kinetic

model to accurately predict the reaction rate. For example, in Nøskov's model[94], the input parameters, such as $E_{\mathrm{ads}}^{\mathrm{O}^*}$ and O_2 dissociation barriers, are either directly obtained from DFT calculations or from certain linear relations extrapolated from many DFT calculations on different surfaces; and the final result, $Q_{\mathrm{A}}^{\mathrm{RDS}}$, equals these input parameters (or summation/subtraction between them) plus some surface-independent constants. However, DFT calculations themselves may have non-negligible errors ($\sim$ 0.1 eV) on surface adsorption energies because of the inaccuracies in the density functionals[44], and those extrapolated relations, although often correct in the general trends at large scales, may still have errors of $0.1 \sim 0.2$ eV for individual relation on a single surface, so it is difficult to make its final output of $Q_{\mathrm{A}}^{\mathrm{RDS}}$ in the accuracy of $\sim$ 0.03 eV, which is necessary to quantitatively explain the activity changes on Pt alloys[123].

In fact, if $Q_{\mathrm{A}}^{\mathrm{RDS}}$ depends linearly on the adsorption energies and the total ORR rate depends on $\exp\left(-\frac{\delta Q_{\mathrm{A}}^{\mathrm{RDS}}}{k_{\mathrm{B}}T}\right)$[94], the adsorption energy change of 0.2 eV means a reaction rate change by 3 orders of magnitude. Such high sensitivity of activity to adsorption energies brings us to another contradiction: the adsorption energy of single OH^* on Pt (100) is stronger than (111) by $\sim$ 0.6 eV from DFT calculations, which is so significant that the ORR rates may differ by several orders of magnitude; but in reality the ORR current density on Pt (100) surface is just about half of that on Pt (111) at U = 0.9 V[125]. This sensitivity difference between theories and experiments may be explained from two possible points of view: either in reality adsorption energies do not change so significantly as DFT predicts, or there may be some other factors, in addition to adsorption energies, which reduce the sensitivity of ORR rate to the adsorption energies.

To resolve these issues, we suggest a mean field kinetic model of ORR in Section 5.1.1. In this model, several elementary reaction steps are connected with each other within a reaction network through the competition of limited reaction sites. Besides adsorption energies, we also consider the lateral interaction energies between surface adsorbates, which

can also be computed from DFT calculations. The steady-state results at different electrode potential U are numerically calculated to obtain the total reaction rate and current density. Both numerical and analytical analyses show that although the reaction rate for individual elementary step may depend exponentially on the input parameters, such as adsorption energies of ORR intermediates, the final ORR rate does not have such significant changes. This insensitivity comes from "self-regulation" effects by the limited site competition (*entropic interactions*) and lateral repulsion of ORR intermediates on the surface (*enthalpic interactions*); both of them tend to equalize the reaction rate and the corresponding activation barriers of individual elementary steps so that there may be no obvious rate-determining steps at steady states. This mean field model can quantitatively explain the small activity difference between Pt (111) and Pt (100) surface. However, to obtain more accurate results on different Pt alloys, we should consider the lateral interactions between ORR intermediates in a more accurate way. Thus, a simple discrete kinetic Monte Carlo model is proposed in Section 5.1.4, where individual surface site is considered and the final result shows the possibility for a more accurate kinetic description. The detailed and complete studies on the discrete level are left for future work.

5.1.1 Mean Field Model

General Model

As discussed in Chapter 4, on Pt surface ORR occurs in "direct" four-electron reduction pathways through the mechanism of proton-coupled electron transfer (PCET). Here to simplify the input variables of kinetic model, we first assume that only the following elementary reactions would occur:

Step 1: Molecular Adsorption (**MA**): $O_2 + * \rightarrow O_2^*$

Step 2a: Direct Dissociation (**DD**): $O_2^* + * \rightarrow 2O^*$

Step 2b: Associated Dissociation (**AD**): $O_2^* + H^+ + e^- \rightarrow O^* + OH^*$

Step 3: Oxygen Protonation (**OP**): $O^* + H^+ + e^- \rightarrow OH^*$

Step 4: Hydroxyl Protonation (**HP**): $OH^* + H^+ + e^- \rightarrow H_2O$

Here we omit the intermediate OOH^*, because it can quickly dissociate or transform to other intermediates[108, 56]. The reaction rate for each elementary step is expressed as the following:

$$
\begin{aligned}
r_{\mathrm{MA}} &= k^+_{\mathrm{MA}}(1-\theta_{\mathrm{O}^*_2}-\theta_{\mathrm{O}^*}-\theta_{\mathrm{OH}^*}) - k^-_{\mathrm{MA}}\theta_{\mathrm{O}^*_2} && (5.4)\\
r_{\mathrm{DD}} &= k^+_{\mathrm{DD}}\theta_{\mathrm{O}^*_2}(1-\theta_{\mathrm{O}^*_2}-\theta_{\mathrm{O}^*}-\theta_{\mathrm{OH}^*}) - k^-_{\mathrm{DD}}\theta^2_{\mathrm{O}^*} && (5.5)\\
r_{\mathrm{AD}} &= k^+_{\mathrm{AD}}\theta_{\mathrm{O}^*_2}(1-\theta_{\mathrm{O}^*_2}-\theta_{\mathrm{O}^*}-\theta_{\mathrm{OH}^*}) - k^-_{\mathrm{AD}}\theta_{\mathrm{O}^*}\theta_{\mathrm{OH}^*} && (5.6)\\
r_{\mathrm{OP}} &= k^+_{\mathrm{OP}}\theta_{\mathrm{O}^*} - k^-_{\mathrm{OP}}\theta_{\mathrm{OH}^*} && (5.7)\\
r_{\mathrm{HP}} &= k^+_{\mathrm{HP}}\theta_{\mathrm{OH}^*} - k^-_{\mathrm{HP}}(1-\theta_{\mathrm{O}^*_2}-\theta_{\mathrm{O}^*}-\theta_{\mathrm{OH}^*}) && (5.8)
\end{aligned}
$$

where $\theta_{\mathrm{O}^*_2}$, θ_{O^*} and θ_{OH^*} is the surface coverage of O_2^*, O^* and OH^* on catalyst surface, respectively. The rate constants of forward and reverse reactions for each step are:

$$
\begin{aligned}
k^+_{\mathrm{MA}} &= \upsilon^+_{\mathrm{MA}}\exp\left(-\frac{Q^+_{\mathrm{MA}}}{k_{\mathrm{B}}T}\right), \quad k^-_{\mathrm{MA}} = \upsilon^-_{\mathrm{MA}}\exp\left(-\frac{Q^-_{\mathrm{MA}}}{k_{\mathrm{B}}T}\right) && (5.9)\\
k^+_{\mathrm{DD}} &= \upsilon^+_{\mathrm{DD}}\exp\left(-\frac{Q^+_{\mathrm{DD}}}{k_{\mathrm{B}}T}\right), \quad k^-_{\mathrm{DD}} = \upsilon^-_{\mathrm{DD}}\exp\left(-\frac{Q^-_{\mathrm{DD}}}{k_{\mathrm{B}}T}\right) && (5.10)\\
k^+_{\mathrm{AD}} &= \upsilon^+_{\mathrm{AD}}\exp\left(-\frac{Q^+_{\mathrm{AD}}}{k_{\mathrm{B}}T}\right), \quad k^-_{\mathrm{AD}} = \upsilon^-_{\mathrm{AD}}\exp\left(-\frac{Q^-_{\mathrm{AD}}}{k_{\mathrm{B}}T}\right) && (5.11)\\
k^+_{\mathrm{OP}} &= \upsilon^+_{\mathrm{OP}}\exp\left(-\frac{Q^+_{\mathrm{OP}}}{k_{\mathrm{B}}T}\right), \quad k^-_{\mathrm{OP}} = \upsilon^-_{\mathrm{OP}}\exp\left(-\frac{Q^-_{\mathrm{OP}}}{k_{\mathrm{B}}T}\right) && (5.12)\\
k^+_{\mathrm{HP}} &= \upsilon^+_{\mathrm{HP}}\exp\left(-\frac{Q^+_{\mathrm{HP}}}{k_{\mathrm{B}}T}\right), \quad k^-_{\mathrm{HP}} = \upsilon^-_{\mathrm{HP}}\exp\left(-\frac{Q^-_{\mathrm{HP}}}{k_{\mathrm{B}}T}\right) && (5.13)
\end{aligned}
$$

where Q_i^+ and Q_i^- are activation free energies of forward and reverse reactions at a single reaction site for step i, which means no configurational entropy is included; υ_i^+ and υ_i^-

are the pre-exponential constants of the forward and reverse reactions. Usually, for an individual step i, its activation free energies of forward and reverse reactions are related to each other by the following equation:

$$Q_i^- = Q_i^+ - \delta G_i \tag{5.14}$$

where δG_i is the reaction free energy of step i. As discussed in Section 4.2, Q_i^+ and Q_i^- depend on proton transfer barriers and energies of ORR intermediates, both of which may vary with electrode potential U. The detailed methods for calculating $Q_i^{+/-}$ will be discussed in the next sub-section of **Model Parameters**.

All the above rate equations are nonlinear functions. However, they are linearly related to each other by a reaction network, and the final output of ORR rate and current density j_k are also linear functions of the elementary step rates. In order to perform a mathematical analysis based on linear algebra, we define the following vectors of surface coverage changing rate and elementary step reaction rate:

$$\left[\vec{\lambda}_i\right] \equiv \begin{bmatrix} \frac{d\theta_{O_2^*}}{dt} \\ \frac{d\theta_{O^*}}{dt} \\ \frac{d\theta_{OH^*}}{dt} \end{bmatrix} \quad \text{and} \quad [\vec{r}_I] \equiv \begin{bmatrix} r_{MA} \\ r_{DD} \\ r_{AD} \\ r_{OP} \\ r_{HP} \end{bmatrix}, \tag{5.15}$$

Then based on these rate equations, the surface coverage would vary according to the following equation:

$$\left[\vec{\lambda}_i\right] = [A]\,[\vec{r}_I]\,, \tag{5.16}$$

where

$$A = \begin{bmatrix} 1 & -1 & -1 & 0 & 0 \\ 0 & 2 & 1 & -1 & 0 \\ 0 & 0 & 1 & 1 & -1 \end{bmatrix} \tag{5.17}$$

At a steady state, $\theta_{O_2^*}$, θ_{O^*} and θ_{OH^*} do not change ($\left[\vec{\lambda}_i\right] = [0]$). So we can use the above equations to obtain the reaction rate for each step by solving the following equation numerically

$$[\mathrm{A}]\,[\vec{r}_{\mathrm{I}}] \;=\; 0 \tag{5.18}$$

And the total current of ORR is calculated as the following equation:

$$j_k = [\vec{\mathrm{B}}]^{\mathrm{T}} \cdot [\vec{r}_{\mathrm{I}}] \times e/S_0 \tag{5.19}$$

where

$$[\vec{\mathrm{B}}] = \begin{bmatrix} 0 \\ 0 \\ 1 \\ 1 \\ 1 \end{bmatrix} \tag{5.20}$$

because electron transfer only occurs in three steps (**AD**, **OP** and **HP**). And S_0 is the surface area of one reaction site. Here we use j_k to denote the *kinetic current density* because it is determined only by the surface reaction kinetics. In the real PEM fuel cell, the real current density j is also limited by the mass transfer effects, which will be discussed in Section 5.3.

Model Parameters

To obtain accurate results from the above model, the first step is to find the correct parameters. There are two general types of parameters in this ORR model, $Q_i^{+/-}$ and $\upsilon_i^{+/-}$, in principle, all of which can be estimated either from experiments or first-principles calculation results.

First, we estimate the parameters in Eq. 5.9 for the molecular adsorption (**MA**) step. Usually there are negligible activation energies for the forward step of molecular adsorption if it is an exothermic process. So here we assume the activation free energy of MA, Q_{MA}^{+}, equals zero if the adsorption energy of O_2 molecule $E_{\mathrm{ads}}^{\mathrm{O_2^*}} < 0$, where $E_{\mathrm{ads}}^{\mathrm{O_2^*}}$ is defined in Eq. 3.6, otherwise $Q_{\mathrm{MA}}^{+} = E_{\mathrm{ads}}^{\mathrm{O_2^*}}$. For typical molecular adsorption at standard condition (room temperature and atmospheric partial pressure), the pre-exponential factor can be $\upsilon_{\mathrm{MA}}^{+} \sim 10^4$ $\mathrm{s^{-1}\cdot site^{-1}}$ for the forward step and $\upsilon_{\mathrm{MA}}^{-} \sim 10^{13}$ $\mathrm{s^{-1}\cdot site^{-1}}$ for the reverse step[122]. $\upsilon_{\mathrm{MA}}^{+}$ can also be accurately calculated from transition state theory by assuming that all the entropy is lost in the transition state for dissociation, and the result is $\upsilon_{\mathrm{MA}}^{+} = 3.0 \times 10^4$ $\mathrm{s^{-1}\cdot site^{-1}}$ for O_2 molecular adsorption when O_2 partial pressure is 1 atm and temperature T = 300 K[94]. $\upsilon_{\mathrm{MA}}^{-}$ approximately equals the vibrational frequency of adsorbed molecule perpendicular to the surface, which is 1.03×10^{13} $\mathrm{s^{-1}}$ for O_2^* at bridge site on Pt (111) surface. Here we only want a set of order-correct input parameters, so we rewrite the rate constants for molecular adsorption (**MA**) step as

$$k_{\mathrm{MA}}^{+} = 5 \times 10^4 \exp\left[-\frac{\max(0, \delta E^{\mathrm{MA}})}{k_{\mathrm{B}} T}\right] [\mathrm{s^{-1}site^{-1}}] \tag{5.21}$$

$$k_{\mathrm{MA}}^{-} = 10^{13} \exp\left[-\frac{\max(0, -\delta E^{\mathrm{MA}})}{k_{\mathrm{B}} T}\right] [\mathrm{s^{-1}site^{-1}}] \tag{5.22}$$

From DFT calculation,$E_{\mathrm{ads}}^{\mathrm{O_2^*}}$ =-0.65 eV for O_2^* at bridge site on Pt (111) surface.

Second, we estimate the parameters in Eq. 5.10 for the step of O_2^* direct dissociation

(**DD**). Since both reactant and product are surface adsorbates, the pre-exponential factor can be approximated by their vibrational frequencies. For O_2^* at bridge site on Pt (111) surface, the vibrational frequency along O_2^* bond direction is 2.78×10^{13} s^{-1}; for O^* at fcc site on Pt (111) surface, the vibrational frequency perpendicular to the surface is 1.29×10^{13} s^{-1}. In addition, the activation and reaction free energies can also be approximated as the activation and reaction energies ($Q_{DD}^{+} \approx E_a^{DD}$ and $\delta G_{DD} \approx \delta E_{DD} = 2 \cdot E_{ads}^{O^*} - E_{ads}^{O_2^*}$, where $E_{ads}^{O^*}$ is the adsorption energy of atomic oxygen O^* defined in Eq. 3.7). Then we rewrite the reaction constant of direct dissociation as

$$k_{DD}^{+} = 10^{13} \exp\left(-\frac{E_a^{DD}}{k_B T}\right) [s^{-1} site^{-1}] \tag{5.23}$$

$$k_{DD}^{-} = 10^{13} \exp\left(-\frac{E_a^{DD} + E_{ads}^{O_2^*} - 2 \cdot E_{ads}^{O^*}}{k_B T}\right) [s^{-1} site^{-1}]. \tag{5.24}$$

From DFT calculations in Section 3.1.2, $E_a^{DD} = 0.27$ eV on Pt (111) surface with low oxygen coverage, which also agrees with the experimental measurements (0.29 eV)[91]. Thus, the dissociation rate is $10^{13} \exp\left(-\frac{0.29 \text{ eV}}{k_B \cdot 300 \text{ K}}\right) \approx 9.3 \times 10^7$ $s^{-1} \cdot site^{-1}$, much larger than the corresponding O_2 adsorption rate ($\sim 10^4$ $s^{-1} \cdot site^{-1}$). On the other hand, $E_{ads}^{O^*}$ =-1.10 eV on Pt (111) surface from DFT calculation, so that δE_{DD} = -1.55 eV, which means that there is a huge barrier for the reverse reaction ($Q_{DD}^{-} = E_a^{DD} - \delta E_{DD} = 1.82$ eV). The rate differences indicate that O_2 will quickly dissociate after adsorption at low oxygen coverage.

Third, the remaining three reaction steps, associated dissociation (**AD**), oxygen protonation (**OP**) and hydroxyl protonation (**HP**), can all be considered as proton-coupled electron transfer (PCET). From the discussions in Section 4.2, the activation free energy for their forward steps can be written as

$$\begin{aligned} Q_i^{+} &= \beta(U - U^0)e \quad \text{if} \quad \delta G_i < \beta(U - U^0)e \\ &= \delta G_i \quad \text{otherwise} \end{aligned} \tag{5.25}$$

Here $\beta(U-U^0)e$ stands for the activation free energy for the proton to transfer from bulk electrolyte to the hydronium near the electrode surface, and δG_i is the reaction free energy for step *i* at individual reaction site, which means no configuration entropy is included. As shown in Section 4.2, once the proton is close to surface, there is almost no extra activation free energy except for some cases where there are up-hill reaction free energies. Thus, at low electrode potential U, δG_i is always negative and the proton transfer barrier is dominant. We can regard U^0 as electrode potential when $Q_i^+ = 0$. β is the *symmetry factor* on how the activation free energy changes with the reaction free energy[7], as defined in Section 2.2.3. From experimental measurements[40, 78, 79], we can set

$$U_0 = 0.3 \text{ [V vs. SHE]}, \ \beta = \frac{1}{2}. \tag{5.26}$$

The reverse activation free energy Q_i^- can be calculated based on Q_i^+ and δG_i as Eq. 5.14. However, because we always assume the activation free energy is a non-negative quantity, Q_i^+ is calculated as

$$Q_i^- \ = \ \max(0, Q_i^+ - \delta G_i) \tag{5.27}$$

The remaining uncertainties are the pre-exponential factors $\upsilon_i^{+/-}$. Since all the three steps (**AD**, **OP** and **HP**) are PCET, we assume all of their pre-exponential factors are equal, designated as υ_{H}. Then we rewrite the rate equations for these three steps as the following:

$$k_{\mathrm{AD}}^+ = \upsilon_{\mathrm{H}} \cdot \exp\left\{-\frac{\mathbf{max}[\beta(U-U_0)e, \delta G_{\mathrm{AD}}]}{k_{\mathrm{B}}T}\right\} \tag{5.28}$$

$$k_{\mathrm{AD}}^- = \upsilon_{\mathrm{H}} \cdot \exp\left\{-\frac{\mathbf{max}[0, \beta(U-U_0)e - \delta G_{\mathrm{AD}}]}{k_{\mathrm{B}}T}\right\} \tag{5.29}$$

$$k_{\mathrm{OP}}^+ = \upsilon_{\mathrm{H}} \cdot \exp\left\{-\frac{\mathbf{max}[\beta(U-U_0)e, \delta G_{\mathrm{OP}}]}{k_{\mathrm{B}}T}\right\} \tag{5.30}$$

$$k_{\mathrm{OP}}^- = \upsilon_{\mathrm{H}} \cdot \exp\left\{-\frac{\mathbf{max}[0, \beta(U-U_0)e - \delta G_{\mathrm{OP}}]}{k_{\mathrm{B}}T}\right\} \tag{5.31}$$

$$k_{\mathrm{HP}}^{+} = \upsilon_{\mathrm{H}} \cdot \exp\left\{-\frac{\mathbf{max}[\beta(U-U_0)e, \delta G_{\mathrm{HP}}]}{k_{\mathrm{B}}T}\right\} \tag{5.32}$$

$$k_{\mathrm{HP}}^{-} = \upsilon_{\mathrm{H}} \cdot \exp\left\{-\frac{\mathbf{max}[0, \beta(U-U_0)e - \delta G_{\mathrm{HP}}]}{k_{\mathrm{B}}T}\right\} \tag{5.33}$$

Here the reaction free energy for each step is determined by the chemical potentials of ORR intermediates on the surface, protons in the electrolyte and electrons in the cathode. Practically, it is difficult to use first-principles methods to calculate the free energy of protons or electrons, because there are long-range electric and solvation fields involved. Here we just use the method proposed by Nørskov[94]: instead of calculating the free energies of protons and electrons, we can use free energy of hydrogen oxidation reaction (HOR).

$$\mathrm{H_2} \rightarrow 2\mathrm{H^+} + 2e^- \tag{5.34}$$

Its reaction free energy is $\delta G = 2e\cdot(U \text{ vs. SHE})$. So we can calculate the reaction free energy for step **AD**, **OP** and **HP** as the following

$$\delta G_{\mathrm{AD}} = \mu_{\mathrm{O}^*} + \mu_{\mathrm{OH}^*} - \mu_{\mathrm{O_2^*}} - \frac{1}{2}\mu^0_{\mathrm{H_2}} + e\cdot U \tag{5.35}$$

$$\delta G_{\mathrm{OP}} = \mu_{\mathrm{OH}^*} - \mu_{\mathrm{O}^*} - \frac{1}{2}\mu^0_{\mathrm{H_2}} + e\cdot U \tag{5.36}$$

$$\delta G_{\mathrm{HP}} = \mu^0_{\mathrm{H_2O}} - \mu_{\mathrm{OH}^*} - \frac{1}{2}\mu^0_{\mathrm{H_2}} + e\cdot U \tag{5.37}$$

where $\mu_{\mathrm{O_2^*}}$, μ_{O^*} and μ_{OH^*} are the chemical potentials of $\mathrm{O_2^*}$, O^* and OH^* at individual reaction site, where no configurational entropy is included; $\mu^0_{\mathrm{H_2O}}$ and $\mu^0_{\mathrm{H_2}}$ is chemical potential of $\mathrm{H_2O}$ and $\mathrm{H_2}$, respectively, at standard conditions (T = 300 K, $p_{\mathrm{H_2}} = 1$ atm, $p_{\mathrm{H_2O}} = 0.035$ atm because it is the equilibrium pressure of liquid $\mathrm{H_2O}$ at 300 K). From DFT calculations (VASP with PAW-PBE methods) and thermodynamic corrections, we have

$$\mu^0_{\mathrm{H_2}} = -6.796 \text{ eV}, \mu^0_{\mathrm{H_2O}} = -14.203 \text{ eV} \tag{5.38}$$

On the other hand, because there may be strong repulsive lateral interactions between surface adsorbates as shown in Chapter 3 and 6, $\mu_{O_2^*}$, μ_{O^*} and μ_{OH^*} are variables depending not only on intrinsic surface properties, such as Pt (111) vs. Cu (111), but also on the surface adsorption configurations, such as surface adsorbate coverage $\theta_{O_2^*}$, θ_{O^*} and θ_{OH^*}. Here we use a mean-field approximation to express these chemical potentials as

$$\begin{bmatrix} \mu_{O_2^*} \\ \mu_{O^*} \\ \mu_{OH^*} \end{bmatrix} = \begin{bmatrix} h^0_{O_2^*} - (s^{vib}_{O_2^*} + s^{rot}_{O_2^*}) \cdot T \\ h^0_{O^*} - (s^{vib}_{O^*} + s^{rot}_{O^*}) \cdot T \\ h^0_{OH^*} - (s^{vib}_{OH^*} + s^{rot}_{OH^*}) \cdot T \end{bmatrix} + \begin{bmatrix} f_{O_2^*}(\theta_{O_2^*},\ \theta_{O^*},\ \theta_{OH^*}) \\ f_{O^*}(\theta_{O_2^*},\ \theta_{O^*},\ \theta_{OH^*}) \\ f_{OH^*}(\theta_{O_2^*},\ \theta_{O^*},\ \theta_{OH^*}) \end{bmatrix} \tag{5.39}$$

where $h^0_{i^*}$ is the enthalpy on clean surface; $s^{vib}_{i^*}$ and $s^{rot}_{i^*}$ are the vibrational and rotational entropies for surface adsorbate i^*; the functions $f_{i^*}(\theta_{i^*}, \theta_{j^*}, ...)$ describe how the chemical potentials change with surface coverage configurations. Generally, $h^0_{i^*}$ can be obtained from DFT calculations by the following equation:

$$h^0_{i^*} = E_{surface+i^*} + ZPE_{i^*} - E_{surface} \tag{5.40}$$

where $E_{surface+i^*}$ and $E_{surface}$ is the energy of surface with adsorbed i^* and clean surface itself, respectively; ZPE_{i^*} is the zero point energy from the vibration of i^*. Meanwhile, since the adsorbates are always constrained on the surface, their entropic contributions (except for configurational entropies) to chemical potentials are usually very small so that we will not consider $(s^{vib}_{i^*} + s^{vib}_{i^*}) \cdot T$ in the real calculation. In addition, if we take Taylor expansions of all $f_{i^*}(\theta_{i^*}, \theta_{j^*}, ...)$ on all variables θ_{j^*} and neglect all the higher order terms, we can obtain the following linearized equations:

$$\begin{bmatrix} \mu_{O_2^*} \\ \mu_{O^*} \\ \mu_{OH^*} \end{bmatrix} \approx \begin{bmatrix} h^0_{O_2^*} \\ h^0_{O^*} \\ h^0_{OH^*} \end{bmatrix} + \begin{bmatrix} \zeta^{O_2^*}_{O_2^*} & \zeta^{O^*}_{O_2^*} & \zeta^{OH^*}_{O_2^*} \\ \zeta^{O_2^*}_{O^*} & \zeta^{O^*}_{O^*} & \zeta^{OH^*}_{O^*} \\ \zeta^{O_2^*}_{OH^*} & \zeta^{O^*}_{OH^*} & \zeta^{OH^*}_{OH^*} \end{bmatrix} \begin{bmatrix} \theta_{O_2^*} \\ \theta_{O^*} \\ \theta_{OH^*} \end{bmatrix} \tag{5.41}$$

where $\zeta^{j^*}_{i^*}$ is the linear dependence coefficient of μ_{i^*} on θ_{j^*}.

In principle, all the 12 parameters (3 $h^0_{i^*}$ and 9 $\zeta^{j^*}_{i^*}$) can be obtained from DFT calculations. However, as shown in Chapter 6, to accurately calculate $\zeta^{j^*}_{i^*}$ requires extrapolation based on adsorption energies at many different surface coverages, so it would be a heavy task to calculate all $\zeta^{j^*}_{i^*}$. Then at first step we just make some simplifications. On Pt surface, because of the fast dissociation rate compared with adsorption rate at low surface coverage, we first assume that $\theta_{O_2^*} \ll \theta_{O^*}$ and θ_{OH^*} so that the affects of $\theta_{O_2^*}$ to $\mu_{O_2^*}$, μ_{O^*} and μ_{OH^*} are not considered (later we will find that this is a good assumption on Pt (111) surface at high U, but not so accurate for Pt (100) surface). For this reason, Eq. 5.41 can be rewritten as

$$\begin{bmatrix} \mu_{O_2^*} \\ \mu_{O^*} \\ \mu_{OH^*} \end{bmatrix} \approx \begin{bmatrix} h^0_{O_2^*} \\ h^0_{O^*} \\ h^0_{OH^*} \end{bmatrix} + \begin{bmatrix} 0 & \zeta^{O^*}_{O_2^*} & \zeta^{OH^*}_{O_2^*} \\ 0 & \zeta^{O^*}_{O^*} & \zeta^{OH^*}_{O^*} \\ 0 & \zeta^{O^*}_{OH^*} & \zeta^{OH^*}_{OH^*} \end{bmatrix} \begin{bmatrix} \theta_{O_2^*} \\ \theta_{O^*} \\ \theta_{OH^*} \end{bmatrix} \tag{5.42}$$

Now we start to calculate all these parameters in Eq. 5.42. Using (2×2) unit cell of Pt (111) surface with PAW-PBE methods as shown in Section 3.1.1, we can obtain $h^0_{O_2^*} = -10.362$ eV, $h^0_{O^*} = -6.034$ eV. But the case of OH^* is a little bit different, because in the electrolyte there would be a significant solvation energy for OH^* resulting from the hydrogen bond between OH^* and H_2O molecules. The accurate solvation free energy correction depends on the detailed electrode-electrolyte interface structure, which is very complex and may change with electrode potential. So we just use the hydrogen bonding energy between an isolated H_2O molecule and an OH, which is also connected with a Pt atom, as an approximation of the solvation free energy; the result is -0.3231 eV. With this

correction, DFT calculation of OH^* adsorbed on the top site of Pt (111) surface shows that $h^0_{OH^*}$ = -9.941 eV.

The repulsive interaction terms, $\zeta_{i^*}^{j^*}$, can be obtained from calculations of coverage-dependent adsorption. The detailed procedures to calculate $\zeta_{O^*}^{O^*}$ are described in Section 6.1.2. The estimation of $\zeta_{OH^*}^{OH^*}$ is based on the following approximation method: first, the adsorption energy of a single OH^* in (2×2) unit cell of Pt (111), $E_{ads}^{OH^*}(\theta_{OH^*} = \frac{1}{4}\ \text{ML})$, is calculated; then the most stable configurations of 3 and 4 OH^* in this (2×2) cell are also obtained, so that $E_{ads}^{OH^*}(\theta_{OH^*} = 1\ \text{ML})$ can be calculated from the energy difference of these two configurations; finally $\zeta_{OH^*}^{OH^*}$ = [$E_{ads}^{OH^*}(\theta_{OH^*} = 1\ \text{ML})$ - $E_{ads}^{OH^*}(\theta_{OH^*} = \frac{1}{4}\ \text{ML})$]/ $\frac{3}{4}$[ML]. Here the solvation energy correction (-0.3231 eV per OH^*) is added to any OH^* if its hydrogen atom does not connect with nearby OH^* by hydrogen bond. The final results show that $\zeta_{O^*}^{O^*} \approx$1.64 eV/ML, $\zeta_{OH^*}^{OH*} \approx$0.15 eV/ML, and we also assume $\zeta_{O^*}^{OH^*} \approx \zeta_{OH^*}^{O^*} \approx$ 0.15 eV/ML. These values indicate that O^* is much more sensitive to its surface coverage than OH^*. This sensitivity difference is reasonable, because O atom has stronger electronegativity than OH, and O^* at fcc site also has 3 Pt atoms as nearest neighbors, while OH^* at top site only connects with 1 Pt atom. For these reasons, O^* results in larger changes in local surface electronic structure and nearby O^*s have to share some Pt atoms as nearest neighbors, both of which largely affect the adsorption of O^*.

Furthermore, in order to obtain $\zeta_{O_2^*}^{O^*}$ and $\zeta_{O_2^*}^{OH^*}$, we calculate the adsorption energies of O_2 and O atom on (111) surface of different FCC metals, as shown in Fig. 5.1. It indicates an approximately linear relation between $E_{ads}^{O_2^*}$ and $E_{ads}^{O^*}$ as the following:

$$E_{ads}^{O_2^*} \approx 0.6328 \cdot E_{ads}^{O^*}\ [\text{eV}] + 0.1509\ [\text{eV}] \tag{5.43}$$

Since the differences between $E_{ads}^{O_2^*}$ and $\mu_{O_2^*}$ and the difference between $E_{ads}^{O^*}$ and μ_{O^*} are both constant, it can be deduced that $\zeta_{O_2^*}^{O^*} \approx$0.6328 $\cdot \zeta_{O^*}^{O^*}$ =1.04 eV/ML, and $\zeta_{O_2^*}^{OH^*} \approx$0.6328

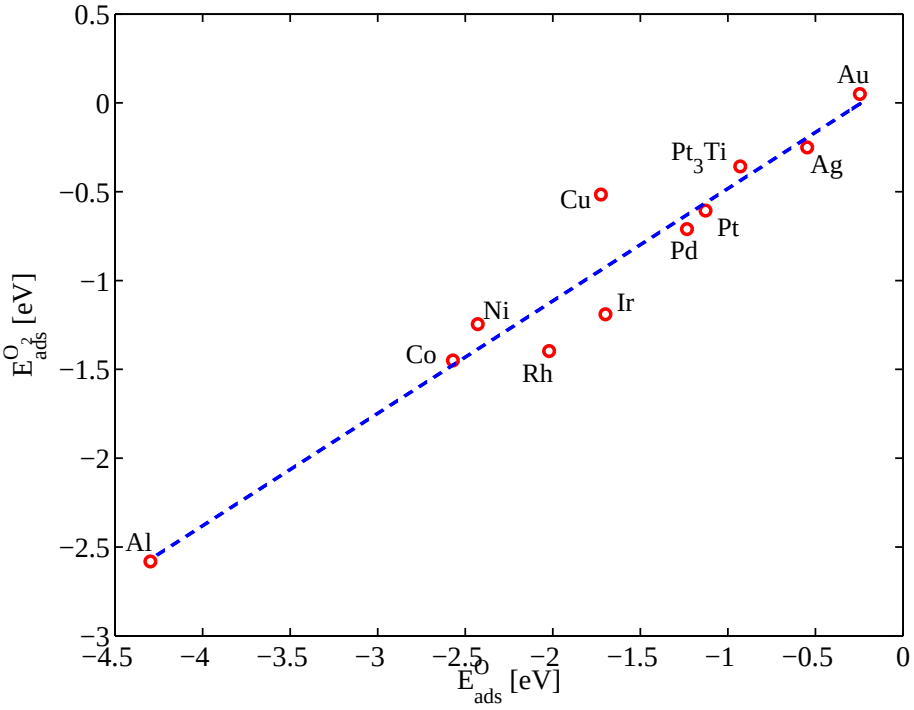

Figure 5.1: The relation between O_2 adsorption energy $E^{O_2^*}_{ads}$ and O adsorption energy $E^{O^*}_{ads}$ from DFT calculations.

$\cdot\zeta^{OH^*}_{O^*}$ =0.09 eV/ML. Thus, the reaction energy of O_2 molecular adsorption (step **MA**)and $E^{O^*}_{ads}$ changes with surface coverage as the following

$$\delta E^{MA} = \delta E^{MA}_0 + \zeta^{O^*}_{O^*_2}\theta_{O^*} + \zeta^{OH^*}_{O^*_2}\theta_{OH^*} \quad (5.44)$$

$$E^{O^*}_{ads} = E^{O}_{ads0} + \zeta^{O^*}_{O^*}\theta_{O^*} + \zeta^{OH^*}_{O^*}\theta_{OH^*} \quad (5.45)$$

Meanwhile, once $E^{O_2^*}_{ads}$ and $E^{O^*}_{ads}$ change, the activation free energy of O_2^* direct dissociation (step **DD**) will also change. Nørskov et al. found an approximately linear relation between $E^{DD}_a + \delta E^{MA}$ and $E^{O^*}_{ads}$ from the results on many different metallic surfaces as the following[93, 94]:

$$(E^{DD}_a + \delta E^{MA}) = 1.8 \cdot E^{O^*}_{ads} + \text{constant} \quad (5.46)$$

Plugging Eq. 5.44 and 5.45 into Eq. 5.46, we obtain the dependence O_2^* dissociation

barrier $E_{\mathrm{a}}^{\mathrm{DD}}$ on surface coverage as the following equation:

$$E_{\mathrm{a}}^{\mathrm{DD}} = E_{\mathrm{a0}}^{\mathrm{DD}} + 1.16 \cdot \zeta_{\mathrm{O}^*}^{\mathrm{O}^*}\theta_{\mathrm{O}^*} + 1.16 \cdot \zeta_{\mathrm{O}^*}^{\mathrm{OH}^*}\theta_{\mathrm{OH}^*} \tag{5.47}$$

We summarize all the parameters and express the rate constant k as functions of surface coverage θ here:

$$k_{\mathrm{MA}}^{+} = 5\times10^{4}\exp\left\{-\frac{\max(0,-0.65+1.04\theta_{\mathrm{O}^*}+0.09\theta_{\mathrm{OH}^*})[\mathrm{eV}]}{k_{\mathrm{B}}T}\right\}[\mathrm{s}^{-1}\mathrm{site}^{-1}] \tag{5.48}$$

$$k_{\mathrm{MA}}^{-} = 10^{13}\exp\left\{-\frac{\max(0,0.65-1.04\theta_{\mathrm{O}^*}-0.09\theta_{\mathrm{OH}^*})[\mathrm{eV}]}{k_{\mathrm{B}}T}\right\}[\mathrm{s}^{-1}\mathrm{site}^{-1}] \tag{5.49}$$

$$k_{\mathrm{DD}}^{+} = 10^{13}\exp\left\{-\frac{(0.27+1.92\theta_{\mathrm{O}^*}+0.18\theta_{\mathrm{OH}^*})[\mathrm{eV}]}{k_{\mathrm{B}}T}\right\}[\mathrm{s}^{-1}\mathrm{site}^{-1}] \tag{5.50}$$

$$k_{\mathrm{DD}}^{-} = 10^{13}\exp\left\{-\frac{(1.82-0.33\theta_{\mathrm{O}^*}-0.03\theta_{\mathrm{OH}^*})[\mathrm{eV}]}{k_{\mathrm{B}}T}\right\}[\mathrm{s}^{-1}\mathrm{site}^{-1}] \tag{5.51}$$

$$k_{\mathrm{AD}}^{+} = \upsilon_{\mathrm{H}}\exp\left\{-\frac{\max[\frac{1}{2}(U-0.3),-2.22+0.75\theta_{\mathrm{O}^*}+0.21\theta_{\mathrm{OH}^*}+U][\mathrm{eV}]}{k_{\mathrm{B}}T}\right\} \tag{5.52}$$

$$k_{\mathrm{AD}}^{-} = \upsilon_{\mathrm{H}}\exp\left\{-\frac{\max[0,2.07-0.75\theta_{\mathrm{O}^*}-0.20\theta_{\mathrm{OH}^*}-\frac{U}{2}][\mathrm{eV}]}{k_{\mathrm{B}}T}\right\} \tag{5.53}$$

$$k_{\mathrm{OP}}^{+} = \upsilon_{\mathrm{H}}\exp\left\{-\frac{\max[\frac{1}{2}(U-0.3),-0.51-1.49\theta_{\mathrm{O}^*}-0.00\theta_{\mathrm{OH}^*}+U][\mathrm{eV}]}{k_{\mathrm{B}}T}\right\} \tag{5.54}$$

$$k_{\mathrm{OP}}^{-} = \upsilon_{\mathrm{H}}\exp\left\{-\frac{\max[0,0.36+1.49\theta_{\mathrm{O}^*}+0.00\theta_{\mathrm{OH}^*}-\frac{U}{2}][\mathrm{eV}]}{k_{\mathrm{B}}T}\right\} \tag{5.55}$$

$$k_{\mathrm{HP}}^{+} = \upsilon_{\mathrm{H}}\exp\left\{-\frac{\max[\frac{1}{2}(U-0.3),-0.86-0.15\theta_{\mathrm{O}^*}-0.15\theta_{\mathrm{OH}^*}+U][\mathrm{eV}]}{k_{\mathrm{B}}T}\right\} \tag{5.56}$$

$$k_{\mathrm{HP}}^{-} = \upsilon_{\mathrm{H}}\exp\left\{-\frac{\max[0,0.71+0.15\theta_{\mathrm{O}^*}+0.15\theta_{\mathrm{OH}^*}-\frac{U}{2}][\mathrm{eV}]}{k_{\mathrm{B}}T}\right\} \tag{5.57}$$

Here the only unknown parameter is υ_{H}. In the numerical calculation we will adjust υ_{H} so that the final result of j_k when U = 0.9 V approximately matches the experimental results.

5.1.2 Results of Pt (111) and (100) Surfaces

Using the parameters obtained on Pt (111) surface as above, we can solve Eq. 5.18 to obtain surface coverage configuration θ_i and kinetic current density j_k. Here we set

$$\upsilon_{\mathrm{H}} = 5 \times 10^7 [\mathrm{s}^{-1}\mathrm{site}^{-1}], \tag{5.58}$$

so that when U = 0.9 V, j_k = 1.31 mA·cm^{-2}, comparable with experimental results[102, 33]. Then we calculate the changes in steady-state values when U increases from 0.3 V to 1.0 V, and the detailed results are shown in Fig. 5.2. It shows that at low U region (0.3 V $< U <$ 0.55 V), the surface is very clean (80% sites are empty) and j_k does not change very much because of the limitation of the maximum O_2 adsorption rate (υ_{MA} = 5×10^4 [s^{-1}site^{-1}] $\ll \upsilon_{\mathrm{H}}$). In the medium U region (0.55 V $< U <$ 0.8 V), j_k decreases because of the proton transfer barrier $\beta(U - U^0)e$, so

$$\frac{dU}{d\log_{10}(j_k)} = -\frac{\log(10)\cdot k_{\mathrm{B}}T}{\beta e} \tag{5.59}$$

When T = 300 K and $\beta = \frac{1}{2}$, the result is 117 mV/decade, agreeing with experiments[78, 79, 40]. Because of this proton transfer limitation, all ORR intermediates would accumulate on the surface so that θ_{i*} for each adsorbate i^* increases on the surface initially. However, the increasing coverage also decreases the surface adsorption energies for all adsorbates. As a result, $\theta_{\mathrm{O}_2^*}$ decreases dramatically to almost zero as $U >$ 0.65 V, because its desorption pre-exponential factor (10^{13}[s^{-1}site^{-1}]) $\gg \upsilon_{\mathrm{H}}$ so that O_2^* desorption process is more sensitive to adsorption energy changes.

In the high U region (0.8 V $< U <$ 1.0 V), $\theta_{\mathrm{O}_2^*}$ is almost zero because of fast desorption, but θ_{O^*} and θ_{OH^*} increase because at high U it is thermodynamically favorable to obtain OH^* and O^* from water dissociation as the reverse reactions of step **HP** and **OP**. Since

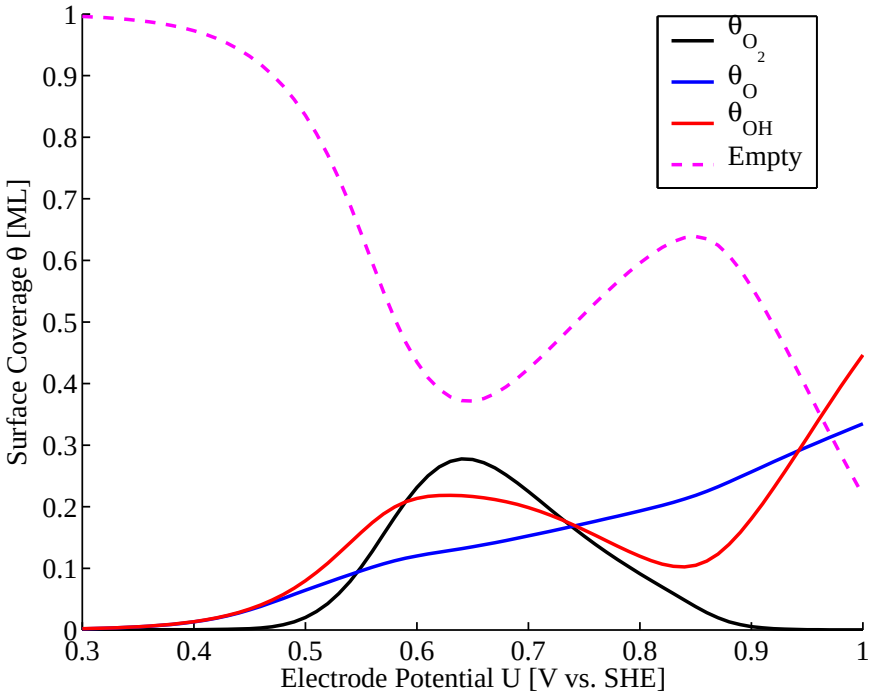

(a)

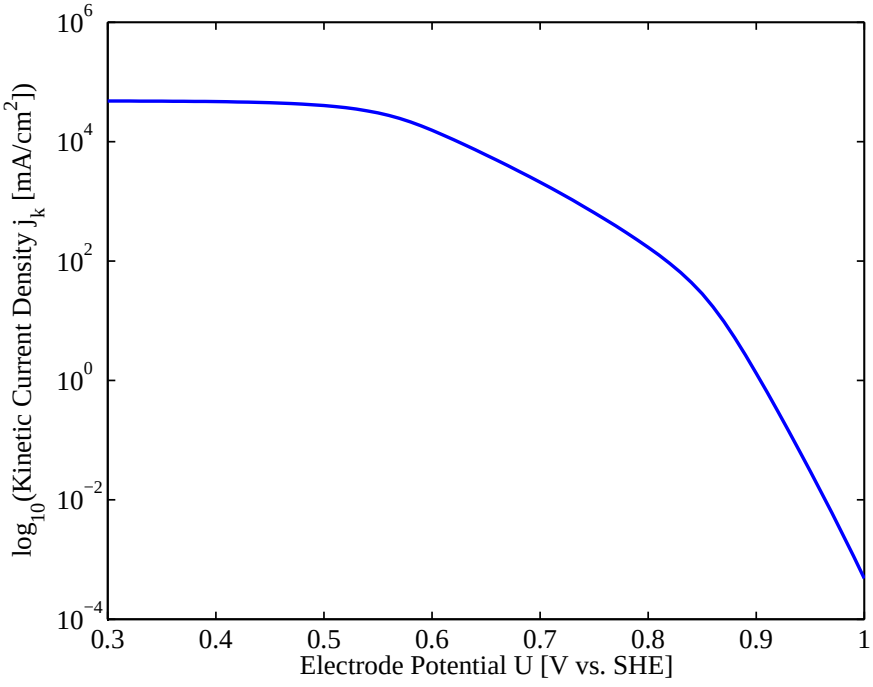

(b)

Figure 5.2: (a) Surface coverage of ORR intermediates vs. electrode potential U on Pt (111) surface at steady states. (b) Kinetic current density j_k vs. electrode potential U on Pt (111) surface at steady states.

the unoccupied surface sites also decrease as surface coverage increases, j_k now is not only limited by the proton transfer barrier, but also by the available reaction sites, so j_k decreases more rapidly at high U region. As shown in Fig. 5.2 (b), when 0.8 V $< U <$ 0.9 V $\frac{dU}{d\log_{10}(j_k)} \approx 70$ mV/decade, agreeing with experiments[78, 79]. However, at higher U (> 0.9 V), $\frac{dU}{d\log_{10}(j_k)} \approx 40$ mV/decade, which was not observed by experiments. This mismatch may result from our simplifications of functions $f_{i^*}(\theta_{i^*}, \theta_{j^*}, ...)$ in Eq. 5.39. Our assumption of linear relation between θ_{i^*} and chemical potential changes $\delta\mu_{j^*}$ may be only suitable at low surface coverage region when U is not too high, while at very high U the higher order terms of θ_{i^*} in $f_{i^*}(\theta_{i^*}, \theta_{j^*}, ...)$ must be considered. In Chapter 6 it is shown that μ_{j^*} depends on detailed local surface adsorption configuration and may be described as step functions of θ_{i^*}. So in the future, we can either use better approximation of $f_{i^*}(\theta_{i^*}, \theta_{j^*}, ...)$ or a discrete model to improve the kinetic results at high U region.

To understand the detailed reaction mechanism, we make further analyses on the kinetic of each elementary step. As shown in Fig. 5.3 (a), although different steps may have totally different activation energies and/or pre-exponential factors, at a steady state the reaction rate r_{I} for each step I is always comparable with each other ($r_{\mathrm{I}}/r_{\mathrm{J}} \approx 1\sim2$) because of the constraints imposed by Eq. 5.18. It also shows how O_2^* chooses its dissociation pathway. At low U where oxygen adsorption is strong, the direct dissociation (step **DD**) is dominant because of its large pre-exponential factor (10^{13} [$s^{-1}site^{-1}$]); as U increases so that the adsorption is weakened by repulsion between surface adsorbates, the activation barrier of **DD** increases significantly as Eq. 5.47. However, the barrier for associated dissociation (step **DD**) is not so sensitive to U, because it has a large negative reaction energy so that only the proton transfer barrier is important. As a result, the relative ratio of step **DD** increases with U and is dominant at high U region.

This pathway change is also confirmed by the activation free energy Q^+ of the forward reaction in each step at steady states of different U, as shown in Fig. 5.3 (c), where the

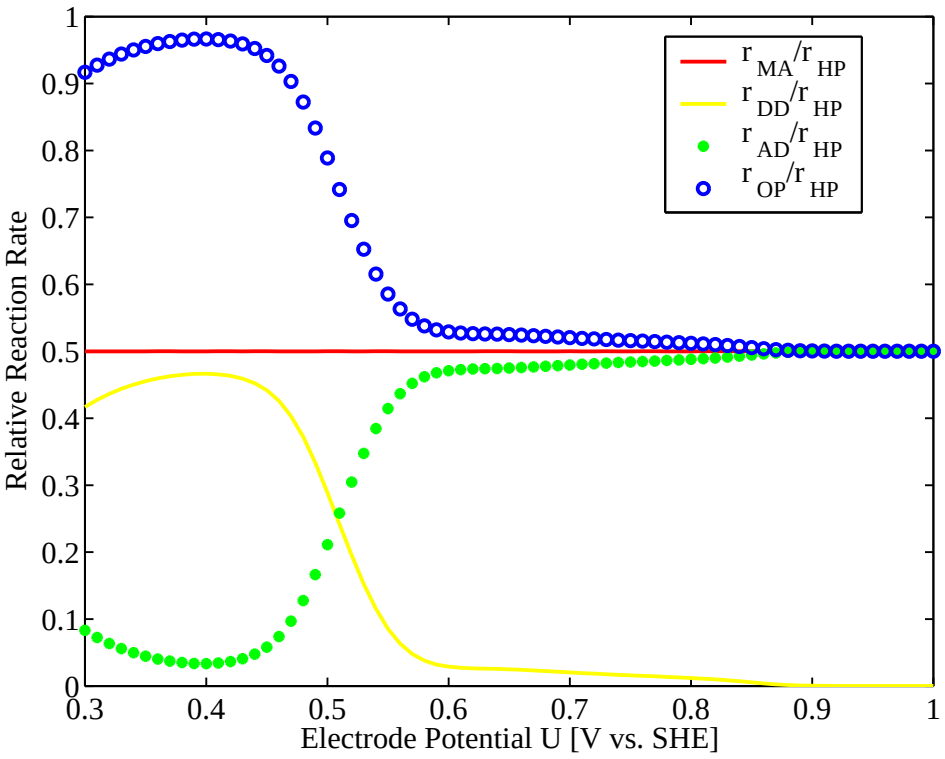

(a)

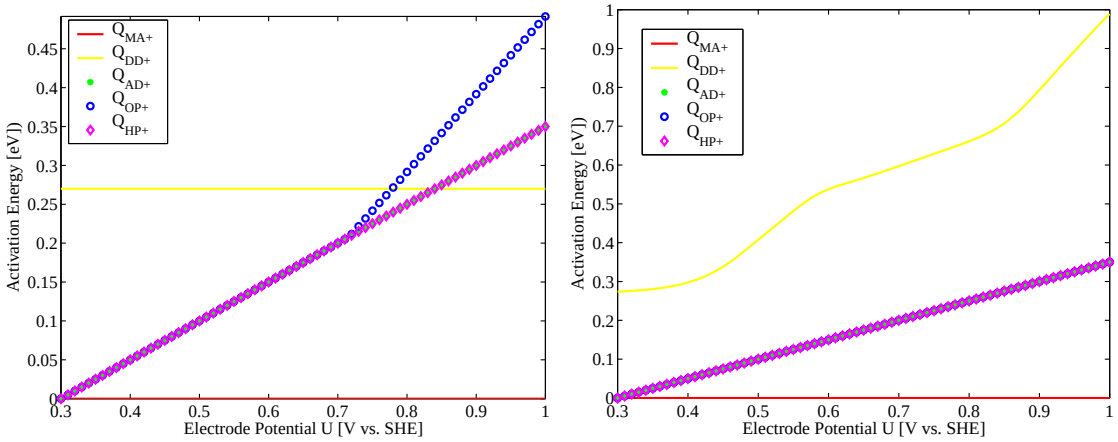

(b) (c)

Figure 5.3: (a) The ratio between reaction rate of each elementary step and that of hydroxyl protonation (**HP**) at steady states on Pt (111) surface at different U. Activation free energy for each elementary step at (b) zero surface coverage and (c) steady states on Pt (111) surface are also shown.

barrier of step **DD** is observed to increase more rapidly with U than other steps. It also shows that all PCET steps (**AD**, **OP** and **HP**) have almost the same Q^+ at given U, because all these steps have the same pre-exponential factors υ_H, so under the steady-state constraint of Eq. 5.18, their Q^+s become almost the same if all the involved ORR intermediates have similar surface coverage. Interestingly, if we also plot Q^+ of each step at zero-coverage surface as shown in Fig. 5.3 (b), these PCET steps may have different Q^+, because at high U some reactions, such as **OP**, can have large positive reaction free energy δG, which determines Q^+ instead of the proton transfer term $\beta(U-U^0)e$.

Finally, since we know Q^+ and δG for each step at different U, we can plot the whole reaction pathways for ORR, as shown in Fig. 5.4. Similar to ORR paths under ultra-high-vacuum (UHV) conditions as shown in Section 3.1, two different reaction pathways are plotted: the one with O_2^* direct dissociation in Fig. 5.4 (a) and the one with O_2^* associated dissociation in Fig. 5.4 (b). As discussed above, the first path is dominant at low U and the second one is dominant at high U. We also plot the reaction pathways at zero-coverage surface, as the dashed lines show in Fig. 5.4, which indicate that at high U the free energy of the total system from the initial state first goes down into a deep potential "well" because of the strong adsorption energies and low chemical potentials for ORR intermediates, then it has to overcome a huge barrier to jump up to the final state. For this reason, at the beginning of the reaction on clean surface, ORR intermediates with the lower chemical potentials will accumulate on the surface by either oxygen reduction (forward reaction) or water dissociation (backward reaction). As the reaction goes on, the surface coverages of these intermediates increase, so their chemical potentials increase because of stronger repulsive interactions with each other, which would reduce their accumulation rates in return. Finally, at the steady state zero accumulation rates are reached, at which the depths of potential "well" in reaction pathways are significantly reduced, as clearly shown in Fig. 5.4.

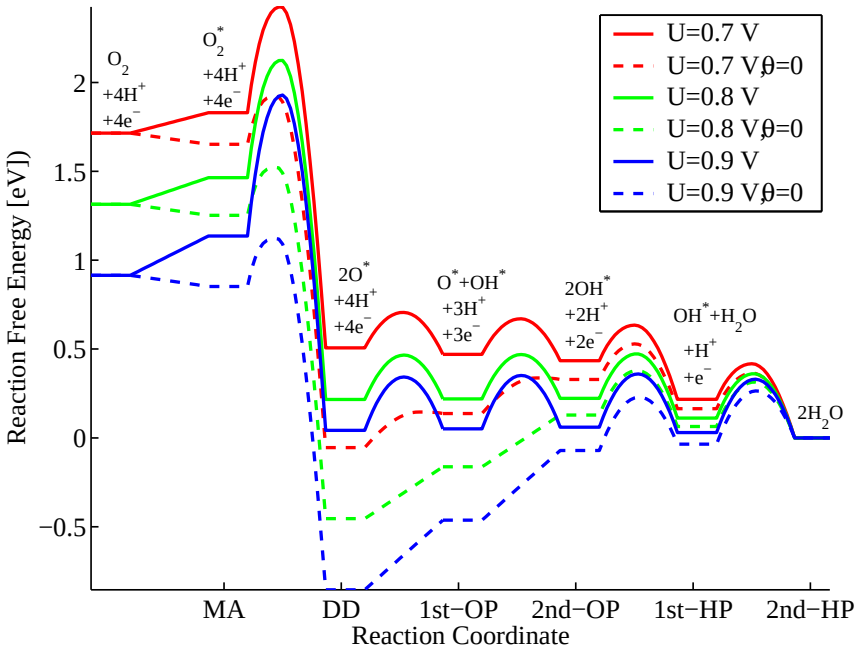

(a)

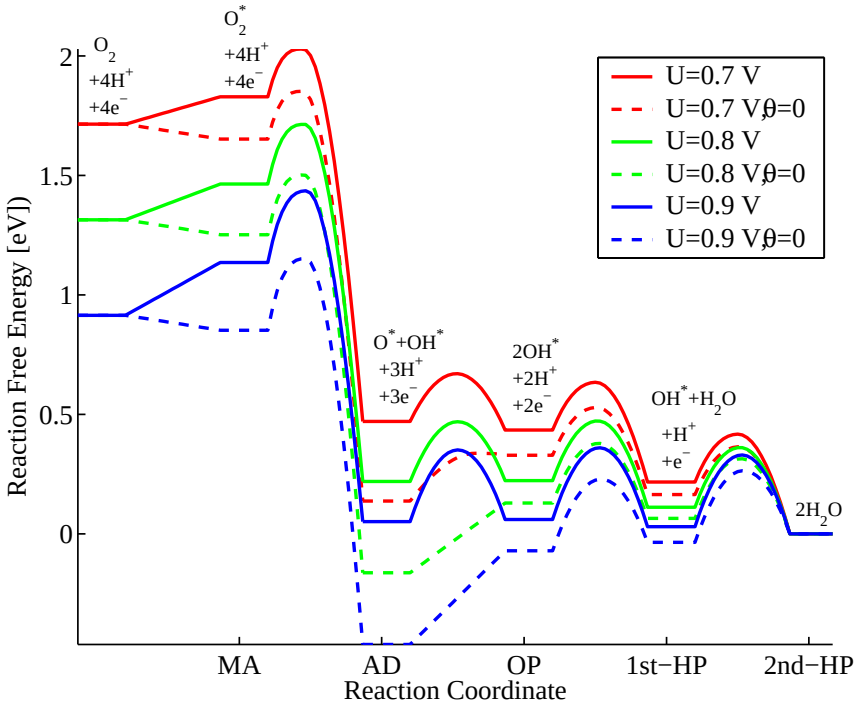

(b)

Figure 5.4: The reaction paths of ORR in different mechanisms by (a) O_2^* direct dissociation (**DD**) and (b) O_2^* associated dissociation (**AD**) on Pt (111) surface at different electrode potentials (U = 0.7, 0.8 and 0.9 V, respectively.). The dashed curves are the reaction paths at zero surface coverage, and solid curves are paths at steady states.

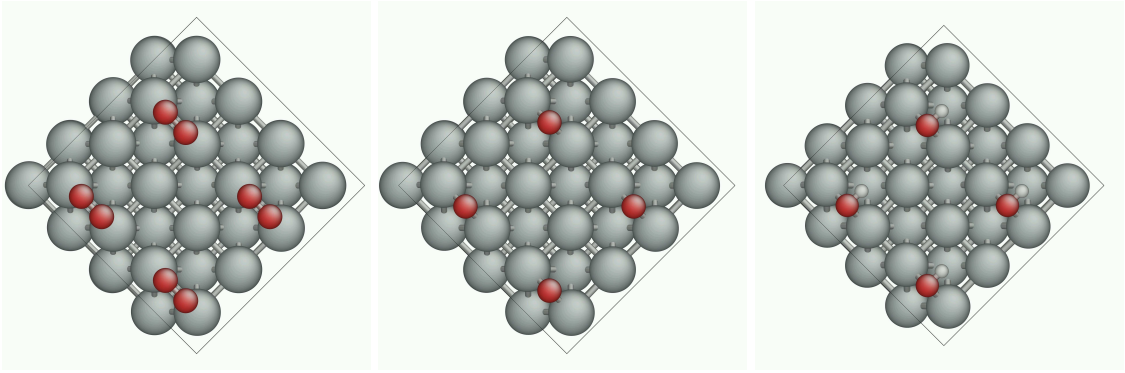

(a) (b) (c)

Figure 5.5: (2×2) unit cell of Pt (100) surface with (a) O_2^*, (b) O^* and (c) OH^* at the bridge site.

In the next step, we apply this model on Pt (100) surface. Because there are less coordination numbers (CN) on Pt (100) surface, it usually has stronger binding with certain atoms/molecules than Pt (111) surface. Fig. 5.5 shows the stable configurations of Pt (100) surface with O_2^*, O^* and OH^*, all of which are at the bridge site between two nearest Pt atoms. Compared with Pt (111) surface, DFT calculations show that $E_{\text{ads}}^{O_2^*}$ changes by -0.513 eV and $E_{\text{ads}}^{OH^*}$ changes by -0.587 eV, confirming the significant increase in adsorption strengths. On the other hand, $E_{\text{ads}}^{O^*}$ almost does not change ($\delta E_{\text{ads}}^{O^*}$ = +0.043 eV compared with Pt (111) surface), which probably is a result of the geometric changes of O^* adsorption sites: as shown in Fig. 3.1 and 5.5 (b), on Pt (111) surface, O^* is at fcc site with 3 Pt atoms as its nearest neighbors, while on Pt (100) surface O^* is at the bridge site with only two Pt atoms as nearest neighbors. Although each Pt atom on (100) surface has stronger binding with O^* than (111) surface, the decreasing number of Pt-O bonds introduces an opposite effect so that on two surfaces $E_{\text{ads}}^{O^*}$ are almost the same. Finally, we assume the differences between these adsorption energies and their corresponding enthalpies, such as $h_{O_2^*}^0$, $h_{O^*}^0$ and $h_{OH^*}^0$, are the same with those on Pt (111) surface.

We also estimate the 6 repulsive interaction terms in Eq. 5.42, $\zeta_{i^*}^{j^*}$, on Pt (100) surface. $\zeta_{O^*}^{O^*} \approx 1.08$ eV/ML from DFT calculations in Section 6.1.3, smaller than its counterpart

on Pt (111) surface. This may result from the difference in surface site density: Pt (100) has lower site density (The area per reaction site is 7.91 Å^2 vs. 6.85 Å^2 of Pt (111) surface) than (111) so that the average distance between nearby O*s increases to reduce their commutative repulsive energy. Similar to the (111) surface, the estimation of $\zeta_{\text{OH}^*}^{\text{OH}^*}$ is from the energy difference between $E_{\text{ads}}^{\text{OH}^*}(\theta_{\text{OH}^*} = \frac{1}{4}\ \text{ML})$ and $E_{\text{ads}}^{\text{OH}^*}(\theta_{\text{OH}^*} = 1\ \text{ML})$ in (2×2) unit cell of Pt (100) surface, and the result is $\zeta_{\text{O}^*}^{\text{O}^*} \approx 1.31$ eV/ML, which is much larger than its counterpart on Pt (111) surface (0.15 eV/ML). This significant change may also result from geometric differences: as shown in Fig. 5.5 (b), on Pt (100) surface OH* is fixed at the bridge site, so nearby OH*s have to share one Pt atom, inducing a large distortion of electronic structure near this Pt atom and a large increase in total system's energy; on the other hand, on Pt (111) surface OH* is at top site and each OH* only connects with one Pt atom below it, so the change of electronic structures due to OH* is a local effect and nearby OH*s have less repulsive interaction. Furthermore, here we assume $\zeta_{\text{OH}^*}^{\text{O}^*} \approx \zeta_{\text{O}^*}^{\text{OH}^*} \approx \zeta_{\text{O}^*}^{\text{O}^*} =$ 1.08 eV/ML, and $\zeta_{\text{O}_2^*}^{\text{O}^*} = 0.6308 \cdot \zeta_{\text{O}^*}^{\text{O}^*}$ and $\zeta_{\text{O}_2^*}^{\text{OH}^*} = 0.6308 \cdot \zeta_{\text{O}^*}^{\text{OH}^*}$ following the extrapolation relation of Eq. 5.43. Finally, we use DFT+NEB methods to obtain the dissociation barrier $E_{\text{a}}^{\text{DD}} = 0.15$ eV, smaller than that of Pt (111) surface because of stronger O_2 adsorption, and we assume E_{a}^{DD} changes with θ_{O^*} and θ_{OH^*} as Eq. 5.47. Except these different $h_{\text{OH}^*}^0$, $\zeta_{\text{i}^*}^{\text{j}^*}$ and E_{a}^{DD}, all other parameters used in the kinetic model for Pt (100) surface are the same as those of Pt (111) surface.

The results of kinetic current density j_k and surface coverage configuration θ_i are shown in Fig. 5.6. To directly compare with experimental results, we also add the mass transfer limitation to obtain the actual measured current density j by using the following relation:

$$\frac{1}{j} = \frac{1}{j_k} + \frac{1}{j_d} \tag{5.60}$$

where j_d is the maximum current density allowed by mass transfer, which is a U-independent

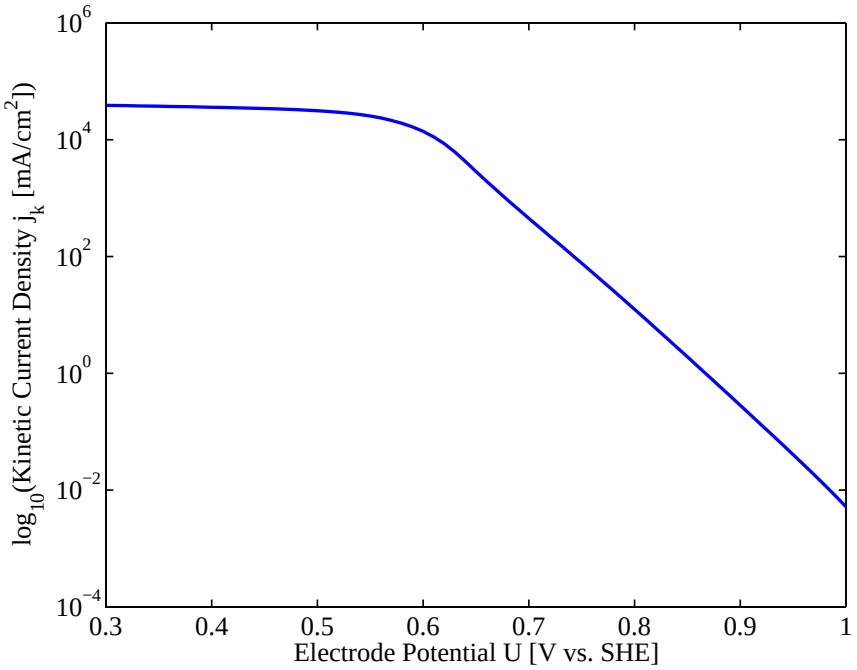

(a)

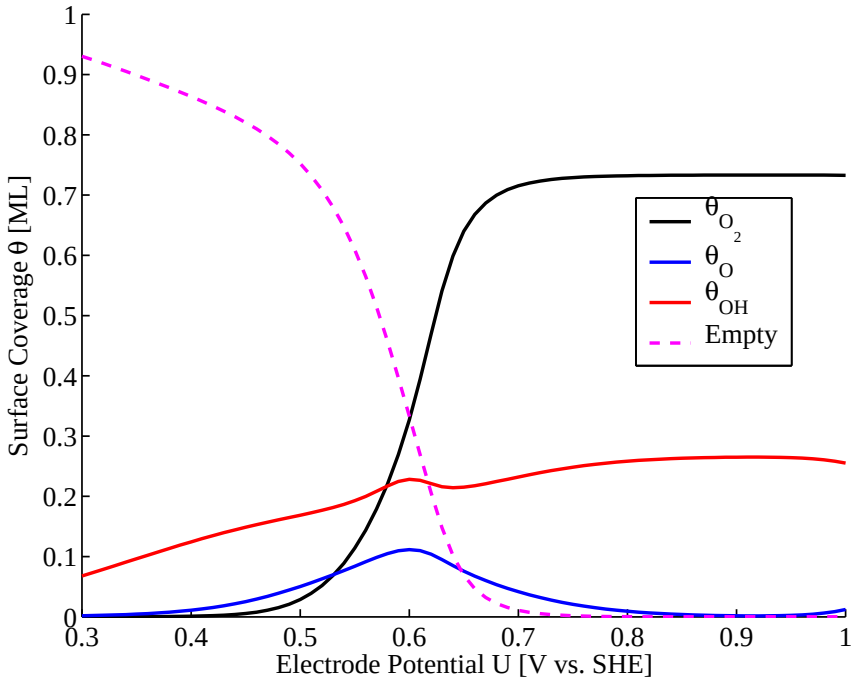

(b)

Figure 5.6: (a) Kinetic current density j_k vs. electrode potential U on Pt (100) surface at steady states. (b) Surface coverage of ORR intermediates vs. electrode potential U on Pt (100) surface at steady states.

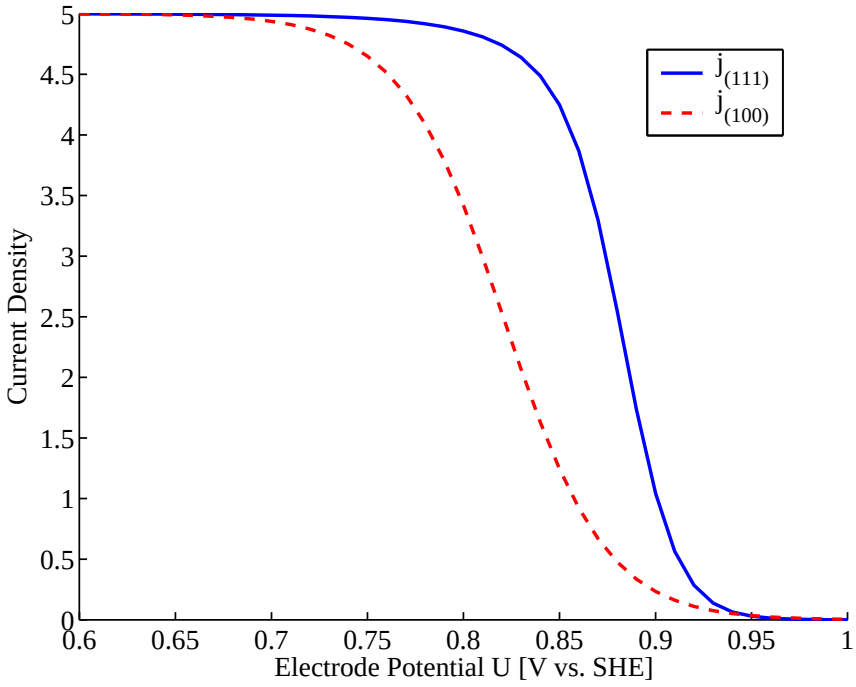

(a)

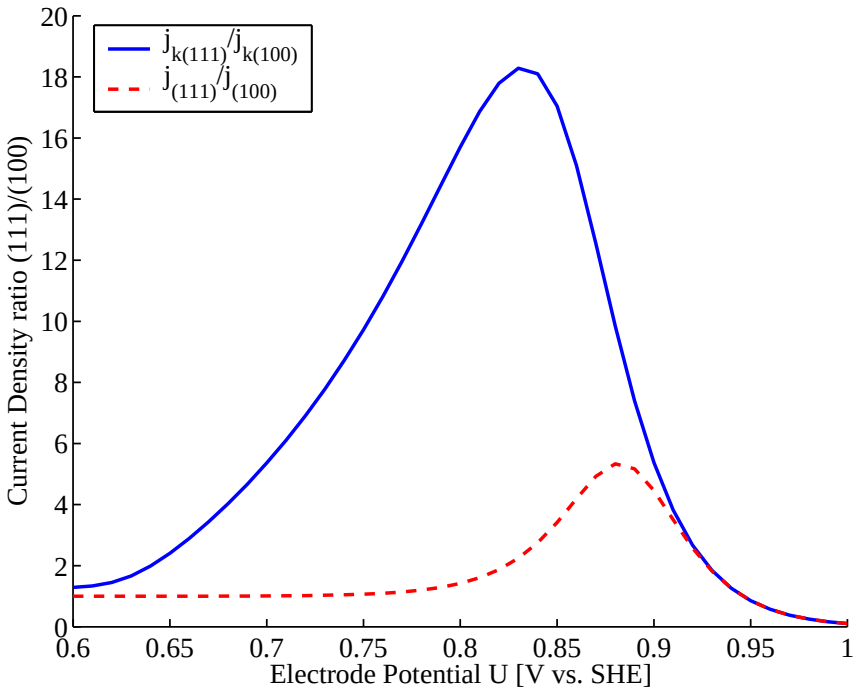

(b)

Figure 5.7: (a)Simulated current density $j = 1/(\frac{1}{j_k} + \frac{1}{j_d})$ on Pt (111) and (100) surfaces under the diffusion-limited current density j_d= 5 mA·cm^{-2}. (b) The ratios of j_k and j between Pt (111) and Pt (100) surfaces.

quantity that only changes with rotating frequency of certain rotating disk electrode (RDE)[7]. Here we set j_d = 5 mA·cm^{-2}, comparable with many experimental results[78, 79, 125, 126]. The results of j for both Pt (111) and (100) surface are shown in Fig. 5.7, where we also show the ratios of both j_k and j on two surfaces, defined as $j_{k(111)}/j_{k(100)}$ and $j_{(111)}/j_{(100)}$ under the same U. According to Nørskov's kinetic model[94], because there are huge changes of $E_{\text{ads}}^{\text{O}_2^*}$ and $E_{\text{ads}}^{\text{OH}^*}$, the reaction pathways will go into deeper potential "wells", shown by the paths on zero-coverage surfaces in Fig. 5.4 and 5.8: on Pt (111) surface, the rate-determining step is **OP** ($\text{O}^* + \text{H}^+ + \text{e}^- \rightarrow \text{OH}^*$) and $Q_{\text{A}}^{\text{RDS}}$ = 0.39 eV when U = 0.9 V; on Pt (100) surface, the rate-determining step is **HP** ($\text{OH}^* + \text{H}^+ + \text{e}^- \rightarrow \text{H}_2\text{O}$) and $Q_{\text{A}}^{\text{RDS}}$ = 0.62 eV when U = 0.9 V; so $Q_{\text{A}}^{\text{RDS}}$ increases by 0.23 eV; as a result, there would be huge decreases in the ORR rate and corresponding current density on the order of $\exp\left(-\frac{0.23\text{eV}}{k_{\text{B}}T}\right) \sim 10^{-4}$ when T = 300 K. However, the maximum ratio of $j_{k(111)}/j_{k(100)}$ and $j_{(111)}/j_{(100)}$ is only about 20 and 5, respectively, which suggests that we can not simply use the change in $Q_{\text{A}}^{\text{RDS}}$ estimated from changes of $E_{\text{ads}}^{\text{i}^*}$ to predict current density variations.

The insensitivity of j_k/j to changes in $E_{\text{ads}}^{\text{i}^*}$ can be qualitatively explained by the changes between reaction paths on zero-coverage surface vs. their counterparts at steady states because of a "self-regulation" effect. As shown in Fig. 5.4 and 5.8, at zero-coverage states Pt (111) and Pt (100) have different depths of potential "wells", resulting from different stabilities of ORR intermediates (O^* and OH^*) on these clean surfaces. As the reaction proceeds, more OH^* and O^* are deposited on the surface from either oxygen reduction or water dissociation reactions, so the stabilities of these intermediates decrease because of lateral repulsive interactions. Thus, a large parts of these potential "wells" are filled up to reach the steady states, and the energy barriers in the rate-determining steps are from proton transfers instead of positive reaction energies. As a result, the activation energy differences between Pt (111) and Pt (100) become much smaller, so do the total current density differences. These small differences satisfy with experimental results[125], where

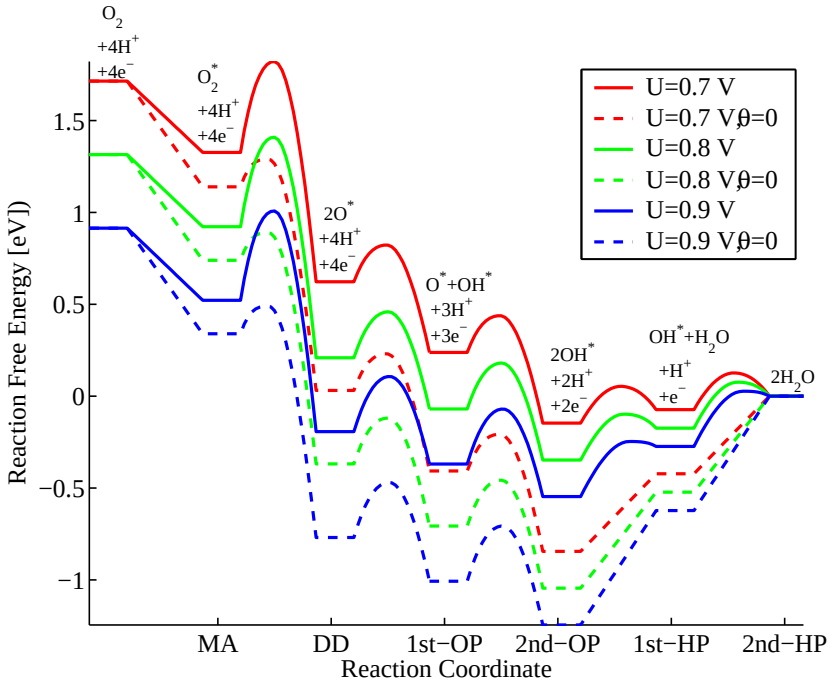

(a)

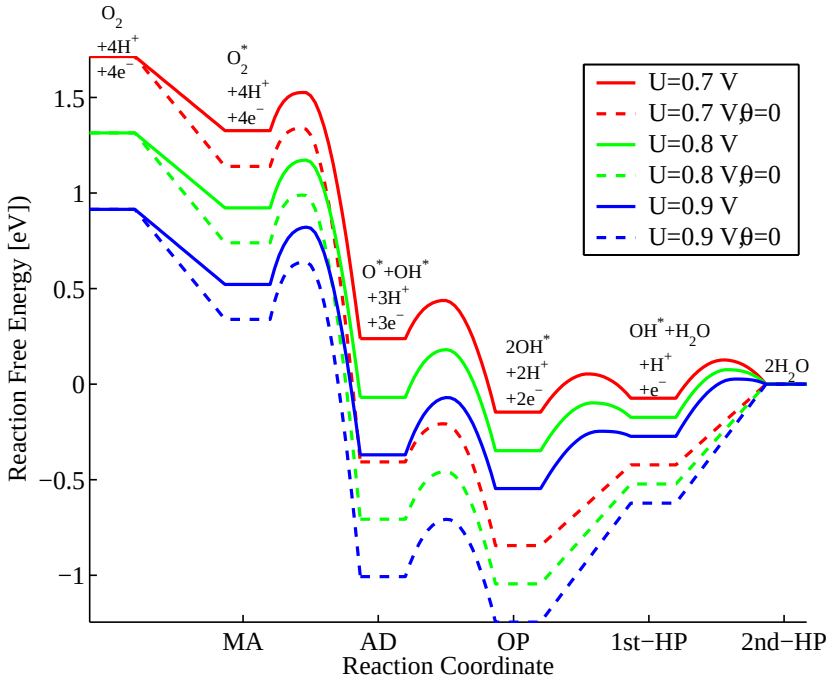

(b)

Figure 5.8: The reaction paths of ORR in different mechanisms by (a) O_2^* direct dissociation (**DD**) and (b) O_2^* associated dissociation (**AD**) on Pt (100) surface at different electrode potential (U = 0.7, 0.8 and 0.9 V respectively.). The dashed curves are the reaction paths at zero surface coverage, and solid curves are paths at steady states.

it was found that the kinetic current density j_k on Pt (111) surface is only about twice of j_k on Pt (100) surface when U = 0.9 V.

However, there are still two major problems in these results of Pt (100) surface. First, j_k drops too fast with U. As shown in Fig. 5.6 (a), $\frac{dU}{d\log_{10}(j_k)} \approx 60$ mV/decade when $U > 0.65$ V, much smaller than 120 mV/decade found in experiments[78, 79]. Second, as shown in Fig. 5.6 (b), when $U \sim 0.7$ V the surface would mainly be covered by O_2^* ($\theta_{O_2^*} \sim 0.7$ ML) resulting from larger $E_{\text{ads}}^{O_2^*}$. However, in order to simplify the procedures of our detailed parameter estimations, we set all three $\zeta_{i^*}^{O_2^*}$ as zero in Eq. 5.39 by assuming $\theta_{O_2^*}$ is small so that these terms are not important. This assumption is generally suitable on Pt (111) surface, but from Fig. 5.6 (b) it indicates that we must consider $\zeta_{i^*}^{O_2^*}$ for accurate results on Pt (100) surface. These two problems may be related to each other, because to use non-zero $\zeta_{i^*}^{O_2^*}$ may increase the coverage of empty surface sites and the corresponding j_k at given U, so $\frac{dU}{d\log_{10}(j_k)}$ may increase and become close to experimental values, and $j_{k(111)}/j_{k(100)}$ may become even smaller.

5.1.3 Sensitivity Analysis

General Equations

In Section 5.1.2, we perform a mean-field kinetic model based on a reaction network at limited reaction sites for both Pt (111) and (100) surfaces. It is found that in spite of significant differences in adsorption strengths and the corresponding reaction pathways at zero-coverage surface, the current densities on Pt (111) and Pt (100) surfaces are still comparable with each other at steady states, agreeing with experimental results[125]. A "self-regulation" effect on reaction pathways, shown in Fig. 5.4 and 5.8, can qualitatively explain this sensitivity decrease of total reaction rate to adsorption strengths. However, to quantitatively predict how total reaction rate changes when varying the input parameters,

such as adsorption energies of certain intermediates, and understand the physical origin of this "self-regulation" effect, a detailed mathematical analysis on this kinetic model is performed in this section.

When catalytic surface changes, its adsorption strengths to all adsorbed intermediates and their lateral interactions may all change. Here, to make a clear mathematical picture, we assume that we can change only one parameter, such as enthalpy $h^0_{i^*}$ for adsorbate i^* on clean surface, but keep all other parameters constant, then we want to know the derivative $\frac{d\ j_k}{d\ h^0_{i^*}}$, the first-order sensitivity of j_k to $h^0_{i^*}$ at steady states. From Eq. 5.19, we obtain

$$\begin{aligned}
\frac{d\ j_k}{d\ h^0_{i^*}} &\equiv [\vec{\mathrm{B}}]^{\mathrm{T}} \cdot \left[\frac{d\ \vec{r}_{\mathrm{I}}}{d\ h^0_{i^*}}\right] \times e/S_0 \\
&= [\vec{\mathrm{B}}]^{\mathrm{T}} \cdot \left\{\left[\frac{\partial \vec{r}_{\mathrm{I}}}{\partial h^0_{i^*}}\right] + \left[\frac{\partial \vec{r}_{\mathrm{I}}}{\partial \theta_{j^*}}\right] \cdot \left[\frac{d\ \theta_{j^*}}{d\ h^0_{i^*}}\right]\right\} \times e/S_0 \\
&= [\vec{\mathrm{B}}]^{\mathrm{T}} \cdot \left\{ \begin{bmatrix} \frac{\partial r_{\mathrm{MA}}}{\partial h^0_{i^*}} \\ \frac{\partial r_{\mathrm{DD}}}{\partial h^0_{i^*}} \\ \frac{\partial r_{\mathrm{AD}}}{\partial h^0_{i^*}} \\ \frac{\partial r_{\mathrm{OP}}}{\partial h^0_{i^*}} \\ \frac{\partial r_{\mathrm{HP}}}{\partial h^0_{i^*}} \end{bmatrix} + \begin{bmatrix} \frac{\partial r_{\mathrm{MA}}}{\partial \theta_{\mathrm{O}^*_2}} & \frac{\partial r_{\mathrm{MA}}}{\partial \theta_{\mathrm{O}^*}} & \frac{\partial r_{\mathrm{MA}}}{\partial \theta_{\mathrm{OH}^*}} \\ \frac{\partial r_{\mathrm{DD}}}{\partial \theta_{\mathrm{O}^*_2}} & \frac{\partial r_{\mathrm{DD}}}{\partial \theta_{\mathrm{O}^*}} & \frac{\partial r_{\mathrm{DD}}}{\partial \theta_{\mathrm{OH}^*}} \\ \frac{\partial r_{\mathrm{AD}}}{\partial \theta_{\mathrm{O}^*_2}} & \frac{\partial r_{\mathrm{AD}}}{\partial \theta_{\mathrm{O}^*}} & \frac{\partial r_{\mathrm{AD}}}{\partial \theta_{\mathrm{OH}^*}} \\ \frac{\partial r_{\mathrm{OP}}}{\partial \theta_{\mathrm{O}^*_2}} & \frac{\partial r_{\mathrm{OP}}}{\partial \theta_{\mathrm{O}^*}} & \frac{\partial r_{\mathrm{OP}}}{\partial \theta_{\mathrm{OH}^*}} \\ \frac{\partial r_{\mathrm{HP}}}{\partial \theta_{\mathrm{O}^*_2}} & \frac{\partial r_{\mathrm{HP}}}{\partial \theta_{\mathrm{O}^*}} & \frac{\partial r_{\mathrm{HP}}}{\partial \theta_{\mathrm{OH}^*}} \end{bmatrix} \begin{bmatrix} \frac{d\ \theta_{\mathrm{O}^*_2}}{d\ h^0_{i^*}} \\ \frac{d\ \theta_{\mathrm{O}^*}}{d\ h^0_{i^*}} \\ \frac{d\ \theta_{\mathrm{OH}^*}}{d\ h^0_{i^*}} \end{bmatrix} \right\} \times e/S_0 \quad (5.61)
\end{aligned}$$

where the elements in vector $\left[\frac{\partial\ \vec{r}_{\mathrm{I}}}{\partial\ h^0_{i^*}}\right]$ and matrix $\left[\frac{\partial \vec{r}_{\mathrm{I}}}{\partial \theta_{j^*}}\right]$ are partial derivatives of each elementary step's rate with respect to intermediates' enthalpy $h^0_{i^*}$ and coverage θ_{j^*}, respectively. All of them can be directly calculated because there are kinetic rate equations analytically expressed from Eq. 5.4 to 5.8. On the other hand, the elements in vector $\left[\frac{d\ \theta_{j^*}}{d\ h^0_{i^*}}\right]$ are the derivatives of coverage θ_{j^*} with respect to enthalpy $h^0_{i^*}$, which can not be calculated directly because there are no analytical expressions for θ_{j^*}.

However, because the constraints of steady states by Eq. 5.18 ($\left[\vec{\lambda}_i\right] = [\mathrm{A}]\,[\vec{r}_{\mathrm{I}}] = 0$), we

can obtain the following relation

$$\left[\frac{d\,\vec{\lambda}_i}{d\,h^0_{i^*}}\right] = [\mathrm{A}]\left[\frac{d\,\vec{r}_\mathrm{I}}{d\,h^0_{i^*}}\right] = [\mathrm{A}]\left\{\left[\frac{\partial \vec{r}_\mathrm{I}}{\partial h^0_{i^*}}\right] + \left[\frac{\partial \vec{r}_\mathrm{I}}{\partial \theta_{j^*}}\right]\cdot\left[\frac{d\,\theta_{j^*}}{d\,h^0_{i^*}}\right]\right\} = 0 \tag{5.62}$$

So $\left[\frac{d\,\theta_{j^*}}{d\,h^0_{i^*}}\right]$ can be written as a function of $\left[\frac{\partial \vec{r}_\mathrm{I}}{\partial h^0_{i^*}}\right]$ and $\left[\frac{\partial \vec{r}_\mathrm{I}}{\partial \theta_{j^*}}\right]$ as

$$\left[\frac{d\,\theta_{j^*}}{d\,h^0_{i^*}}\right] = -\left[[\mathrm{A}]\left[\frac{\partial \vec{r}_\mathrm{I}}{\partial \theta_{j^*}}\right]\right]^{-1}[\mathrm{A}]\left[\frac{\partial \vec{r}_\mathrm{I}}{\partial h^0_{i^*}}\right] \tag{5.63}$$

So the final results is

$$\begin{aligned}
\frac{d\,j_k}{d\,h^0_{i^*}} &= [\vec{\mathrm{B}}]^\mathrm{T}\cdot\left\{\left[\frac{\partial \vec{r}_\mathrm{I}}{\partial h^0_{i^*}}\right] + \left[\frac{\partial \vec{r}_\mathrm{I}}{\partial \theta_{j^*}}\right]\left[\frac{d\,\theta_{j^*}}{d\,h^0_{i^*}}\right]\right\}\times e/S_0 \\
&= [\vec{\mathrm{B}}]^\mathrm{T}\cdot\left\{\left[\frac{\partial \vec{r}_\mathrm{I}}{\partial h^0_{i^*}}\right] - \left[\frac{\partial \vec{r}_\mathrm{I}}{\partial \theta_{j^*}}\right]\left[[\mathrm{A}]\left[\frac{\partial \vec{r}_\mathrm{I}}{\partial \theta_{j^*}}\right]\right]^{-1}[\mathrm{A}]\left[\frac{\partial \vec{r}_\mathrm{I}}{\partial h^0_{i^*}}\right]\right\}\times e/S_0 \\
&= [\vec{\mathrm{B}}]^\mathrm{T}\cdot\left\{\mathbf{I} - \left[\frac{\partial \vec{r}_\mathrm{I}}{\partial \theta_{j^*}}\right]\left[[\mathrm{A}]\left[\frac{\partial \vec{r}_\mathrm{I}}{\partial \theta_{j^*}}\right]\right]^{-1}[\mathrm{A}]\right\}\left[\frac{\partial \vec{r}_\mathrm{I}}{\partial h^0_{i^*}}\right]\times e/S_0 \\
&= [\vec{\mathrm{B}}]^\mathrm{T}\cdot(\mathbf{I}-\mathbf{C})\left[\frac{\partial \vec{r}_\mathrm{I}}{\partial h^0_{i^*}}\right]\times e/S_0
\end{aligned} \tag{5.64}$$

where **I** is identity matrix, and

$$\mathbf{C} = \left[\frac{\partial \vec{r}_\mathrm{I}}{\partial \theta_{j^*}}\right]\left[[\mathrm{A}]\left[\frac{\partial \vec{r}_\mathrm{I}}{\partial \theta_{j^*}}\right]\right]^{-1}[\mathrm{A}] \tag{5.65}$$

To get a clear physical picture, we can further decompose $\left[\frac{\partial \vec{r}_\mathrm{I}}{\partial h^0_{i^*}}\right]$ into two parts as the following:

$$\left[\frac{\partial \vec{r}_\mathrm{I}}{\partial \theta_{j^*}}\right] = [\mathrm{D}] + [\mathrm{E}] \tag{5.66}$$

Here [D] describes that, when surface coverage changes, how reaction rate r_I of each elementary step changes because of the competition for limited reaction sites but without

considering changes in rate constant $k_{\mathrm{I}}^{+/-}$, so it can be called *entropic interactions*. On the other hand, [E] describes the other part, how the changes in rate constant $k_{\mathrm{I}}^{+/-}$ of each elementary step affect r_{I}; because changes in $k_{\mathrm{I}}^{+/-}$ result from the coverage-dependent lateral repulsion between surface adsorbates, it can be called *enthalpic interactions*. For this reason, [E] is a zero matrix if we do not consider any repulsive or attractive interactions between surface adsorbates. With this decomposition, we rewrite Eq. 5.64 as

$$\frac{d\ j_k}{d\ h_{i^*}^0} = [\vec{\mathrm{B}}]^{\mathrm{T}} \cdot \left\{ \mathbf{I} - ([\mathrm{D}] + [\mathrm{E}])\ [[\mathrm{A}]([\mathrm{D}] + [\mathrm{E}])]^{-1}\ [\mathrm{A}] \right\} \left[\frac{\partial \vec{r}_{\mathrm{I}}}{\partial h_{i^*}^0} \right] \times e/S_0 \tag{5.67}$$

Eq. 5.64 and 5.67 can be generally used in any reaction network on any catalyst surface with limited reaction sites. Here [A] describes how different elementary steps are related to each other in steady states as Eq. 5.18; $[\vec{\mathrm{B}}]$ describes the contribution of each elementary step to the total reaction rate as Eq. 5.19; [D], [E] and $\left[\frac{\partial \vec{r}_{\mathrm{I}}}{\partial h_{i^*}^0}\right]$ depend on the details in each elementary step and can be analytically obtained from rate equations from Eq. 5.4 to 5.8. So when the reaction system changes, we only need to change these matrices and vectors but not Eq. 5.64 or 5.67. For the detailed case of ORR reaction network from Eq. 5.4 to 5.8, we can get

$$[\mathrm{D}] = \begin{bmatrix} -k_{\mathrm{MA}}^{+} - k_{\mathrm{MA}}^{-} & -k_{\mathrm{MA}}^{+} & -k_{\mathrm{MA}}^{+} \\ k_{\mathrm{DD}}^{+}\theta_{*} - k_{\mathrm{DD}}^{+}\theta_{\mathrm{O}_2^*} & -k_{\mathrm{DD}}^{+}\theta_{\mathrm{O}_2^*} - 2k_{\mathrm{DD}}^{-}\theta_{\mathrm{O}^*} & -k_{\mathrm{DD}}^{+}\theta_{\mathrm{O}_2^*} \\ k_{\mathrm{AD}}^{+}\theta_{*} - k_{\mathrm{AD}}^{+}\theta_{\mathrm{O}_2^*} & -k_{\mathrm{AD}}^{+}\theta_{\mathrm{O}_2^*} - k_{\mathrm{DD}}^{-}\theta_{\mathrm{OH}^*} & -k_{\mathrm{AD}}^{+}\theta_{\mathrm{O}_2^*} - k_{\mathrm{AD}}^{-}\theta_{\mathrm{O}^*} \\ 0 & k_{\mathrm{OP}}^{+} & -k_{\mathrm{OP}}^{-} \\ k_{\mathrm{HP}}^{-} & k_{\mathrm{HP}}^{-} & k_{\mathrm{HP}}^{+} + k_{\mathrm{HP}}^{-} \end{bmatrix} \tag{5.68}$$

and

$$[\mathrm{E}] = \begin{bmatrix} \frac{\partial k^+_{\mathrm{MA}}}{\partial \theta_{\mathrm{O}^*_2}}\theta_* - \frac{\partial k^-_{\mathrm{MA}}}{\partial \theta_{\mathrm{O}^*_2}}\theta_{\mathrm{O}^*_2} & \frac{\partial k^+_{\mathrm{MA}}}{\partial \theta_{\mathrm{O}^*}}\theta_* - \frac{\partial k^-_{\mathrm{MA}}}{\partial \theta_{\mathrm{O}^*}}\theta_{\mathrm{O}^*_2} & \frac{\partial k^+_{\mathrm{MA}}}{\partial \theta_{\mathrm{OH}^*}}\theta_* - \frac{\partial k^-_{\mathrm{MA}}}{\partial \theta_{\mathrm{OH}^*}}\theta_{\mathrm{O}^*_2} \\ \frac{\partial k^+_{\mathrm{DD}}}{\partial \theta_{\mathrm{O}^*_2}}\theta_{\mathrm{O}^*_2}\theta_* - \frac{\partial k^-_{\mathrm{MA}}}{\partial \theta_{\mathrm{O}^*_2}}\theta^2_{\mathrm{O}^*} & \frac{\partial k^+_{\mathrm{DD}}}{\partial \theta_{\mathrm{O}^*}}\theta_{\mathrm{O}^*_2}\theta_* - \frac{\partial k^-_{\mathrm{MA}}}{\partial \theta_{\mathrm{O}^*}}\theta^2_{\mathrm{O}^*} & \frac{\partial k^+_{\mathrm{DD}}}{\partial \theta_{\mathrm{OH}^*}}\theta_{\mathrm{O}^*_2}\theta_* - \frac{\partial k^-_{\mathrm{MA}}}{\partial \theta_{\mathrm{OH}^*}}\theta^2_{\mathrm{O}^*} \\ \frac{\partial k^+_{\mathrm{AD}}}{\partial \theta_{\mathrm{O}^*_2}}\theta_{\mathrm{O}^*_2}\theta_* - \frac{\partial k^-_{\mathrm{AD}}}{\partial \theta_{\mathrm{O}^*_2}}\theta_{\mathrm{O}^*}\theta_{\mathrm{OH}^*} & \frac{\partial k^+_{\mathrm{AD}}}{\partial \theta_{\mathrm{O}^*}}\theta_{\mathrm{O}^*_2}\theta_* - \frac{\partial k^-_{\mathrm{AD}}}{\partial \theta_{\mathrm{O}^*}}\theta_{\mathrm{O}^*}\theta_{\mathrm{OH}^*} & \frac{\partial k^+_{\mathrm{AD}}}{\partial \theta_{\mathrm{OH}^*}}\theta_{\mathrm{O}^*_2}\theta_* - \frac{\partial k^-_{\mathrm{AD}}}{\partial \theta_{\mathrm{OH}^*}}\theta_{\mathrm{O}^*}\theta_{\mathrm{OH}^*} \\ \frac{\partial k^+_{\mathrm{OP}}}{\partial \theta_{\mathrm{O}^*_2}}\theta_{\mathrm{O}^*} - \frac{\partial k^-_{\mathrm{OP}}}{\partial \theta_{\mathrm{O}^*_2}}\theta_{\mathrm{OH}^*} & \frac{\partial k^+_{\mathrm{OP}}}{\partial \theta_{\mathrm{O}^*}}\theta_{\mathrm{O}^*} - \frac{\partial k^-_{\mathrm{OP}}}{\partial \theta_{\mathrm{O}^*}}\theta_{\mathrm{OH}^*} & \frac{\partial k^+_{\mathrm{OP}}}{\partial \theta_{\mathrm{OH}^*}}\theta_{\mathrm{O}^*} - \frac{\partial k^-_{\mathrm{OP}}}{\partial \theta_{\mathrm{OH}^*}}\theta_{\mathrm{OH}^*} \\ \frac{\partial k^+_{\mathrm{HP}}}{\partial \theta_{\mathrm{O}^*_2}}\theta_{\mathrm{OH}^*} - \frac{\partial k^-_{\mathrm{HP}}}{\partial \theta_{\mathrm{O}^*_2}}\theta_* & \frac{\partial k^+_{\mathrm{HP}}}{\partial \theta_{\mathrm{O}^*}}\theta_{\mathrm{OH}^*} - \frac{\partial k^-_{\mathrm{HP}}}{\partial \theta_{\mathrm{O}^*}}\theta_* & \frac{\partial k^+_{\mathrm{HP}}}{\partial \theta_{\mathrm{OH}^*}}\theta_{\mathrm{OH}^*} - \frac{\partial k^-_{\mathrm{HP}}}{\partial \theta_{\mathrm{OH}^*}}\theta_* \end{bmatrix} \tag{5.69}$$

and

$$\left[\frac{\partial \vec{r}_{\mathrm{I}}}{\partial h^0_{i^*}}\right] = \begin{bmatrix} \frac{\partial k^+_{\mathrm{MA}}}{\partial h^0_{i^*}}\theta_* - \frac{\partial k^-_{\mathrm{MA}}}{\partial h^0_{i^*}}\theta_{\mathrm{O}^*_2} \\ \frac{\partial k^+_{\mathrm{DD}}}{\partial h^0_{i^*}}\theta_{\mathrm{O}^*_2}\theta_* - \frac{\partial k^-_{\mathrm{MA}}}{\partial h^0_{i^*}}\theta^2_{\mathrm{O}^*} \\ \frac{\partial k^+_{\mathrm{AD}}}{\partial h^0_{i^*}}\theta_{\mathrm{O}^*_2}\theta_* - \frac{\partial k^-_{\mathrm{AD}}}{\partial h^0_{i^*}}\theta_{\mathrm{O}^*}\theta_{\mathrm{OH}^*} \\ \frac{\partial k^+_{\mathrm{OP}}}{\partial h^0_{i^*}}\theta_{\mathrm{O}^*} - \frac{\partial k^-_{\mathrm{OP}}}{\partial h^0_{i^*}}\theta_{\mathrm{OH}^*} \\ \frac{\partial k^+_{\mathrm{HP}}}{\partial h^0_{i^*}}\theta_{\mathrm{OH}^*} - \frac{\partial k^-_{\mathrm{HP}}}{\partial h^0_{i^*}}\theta_* \end{bmatrix} \tag{5.70}$$

where all the rate constants $k^{+/-}_{\mathrm{I}}$ and their partial derivatives with respect to either $h^0_{i^*}$ or θ_{i^*} can be easily calculated from Eq. 5.9 to 5.13 and their detailed expressions, such as Eq. 5.48 to 5.57.

Sensitivity on Pt (111) Surface: Effect of Lateral Repulsion

After obtaining the analytical equations, we calculate $\frac{dj_k}{dh^0_{i^*}}$ at steady states in two ways: first, $\frac{dj_k}{dh^0_{i^*}}$ can be analytically calculated by Eq. 5.67 based on steady-state solutions; second, $\frac{dj_k}{dh^0_{i^*}}$ can be numerically calculated from the differences between steady-state solutions with two sets of input parameters, where certain $h^0_{i^*}$ is set to be different by 1×10^{-5} eV but other parameters are unchanged. In addition, to clarify the physical origins of sensitivity, we calculate $\frac{dj_k}{dh^0_{i^*}}$ at steady states in two cases: ORR reaction on Pt (111) surface without

considering the lateral repulsion between adsorbates (only *entropic interactions*), which means $\zeta_{i^*}^{j^*} = 0$ in Eq. 5.41 and [E] = [0] in Eq. 5.67, and the same ORR reaction on Pt (111) surface but $\zeta_{i^*}^{j^*} \neq 0$ and [E] $\neq$ [0] (*entropic interactions* plus *enthalpic interactions*).

The results are shown in Fig. 5.9, where the sensitivity of j_k to both $h^0_{O^*}$ are $h^0_{OH^*}$ are calculated at steady states of different U, and the results from analytical methods (solid lines) and numerical methods (circles) match up with each other, confirming the validity of Eq. 5.67. Here because j_k changes with U significantly, in order to accurately compare the sensitivity at different U, we plot

$$\frac{d\log_{10}(j_k)}{dh^0_{i^*}} = \frac{dj_k}{dh^0_{i^*}}/[\log(10)\cdot j_k] \tag{5.71}$$

For a certain limiting case, if the change of activation energy of rate determining step is the same as the change in $h^0_{i^*}$, which means no "self-regulation" effect at all, the current can be approximately written as

$$j_k = j^0_k \cdot \exp\left(\frac{\pm h^0_{i^*}}{k_B T}\right) \tag{5.72}$$

similar to the express in Nøskov's kinetic model[94], then the absolute value of $\frac{d\log_{10}(j_k)}{dh^0_{i^*}}$ goes to a maximum as

$$\left|\frac{d\log_{10}(j_k)}{dh^0_{i^*}}\right| = \frac{1}{k_B T}/\log(10) \approx 16.80\ \mathrm{eV}^{-1} \text{ when } T = 300\mathrm{K} \tag{5.73}$$

Fig. 5.9(a) shows $\frac{d\log_{10}(j_k)}{dh^0_{i^*}}$ at steady states with $\zeta_{i^*}^{j^*} = 0$ and [E] = [0]. At low U region, because j_k is controlled by the maximum O_2 adsorption rate, so $\frac{d\log_{10}(j_k)}{dh^0_{i^*}} = 0$. At high U, $\frac{d\log_{10}(j_k)}{dh^0_{i^*}}$ becomes +16.8 eV^{-1} and -16.8 eV^{-1} for O^* and OH^*, respectively, which means the sensitivity goes to the maximum and there is no "self-regulation" effect (Here when $U > 0.85$ eV, $|\frac{d\log_{10}(j_k)}{dh^0_{i^*}}|$ decreases because of numerical errors to calculate j_k accurately, which is extremely small at such a high U). The +/- signs result from the fact that O^* and

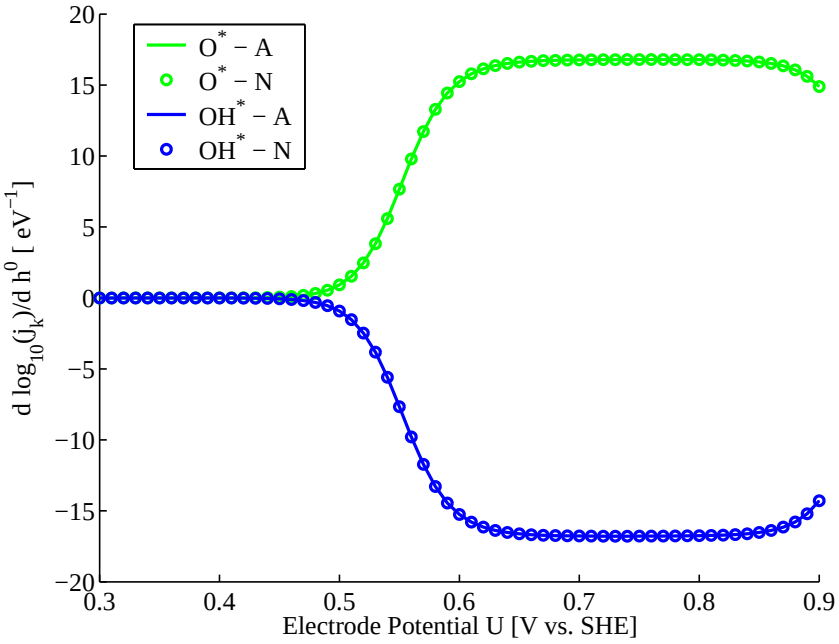

(a)

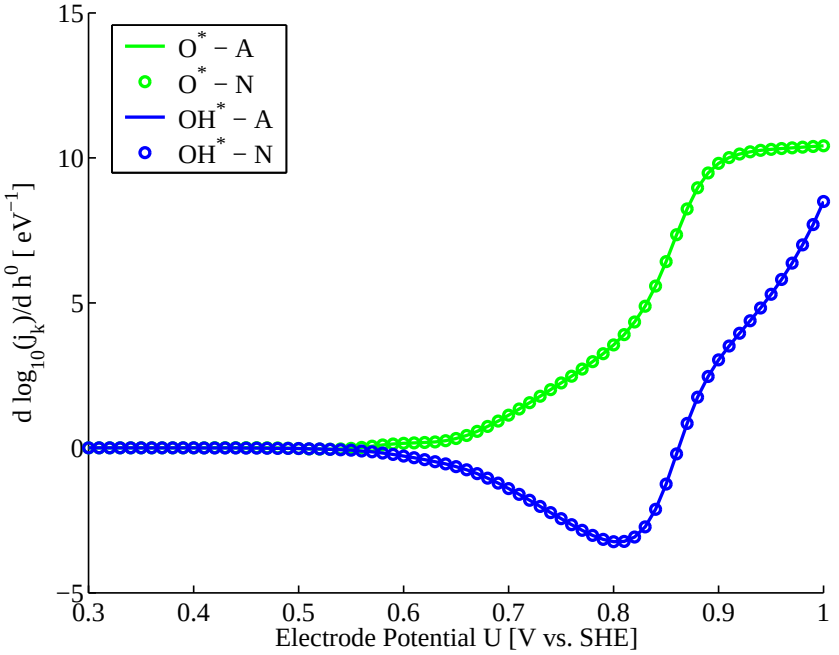

(b)

Figure 5.9: Sensitivity of kinetic current density j_k on adsorption energy of ORR intermediates O^* and OH^* (a) without considering their lateral interactions ($\zeta_{i^*}^{j^*} = 0$ and $[E] = [0]$) and (b) considering their lateral interactions ($\zeta_{i^*}^{j^*} \neq 0$ and $[E] \neq [0]$). Here "A" means analytical results from Eq. 5.67, "N" means numerical results by calculating steady states at different $h_{i^*}^0$.

OH^* are on the two different sides of the rate determining step: as shown in Fig. 5.3 (b), the rate determining step at high U region in ORR without considering lateral repulsion is the step **OP** ($O^* + H^+ + e^- \rightarrow OH^*$), which has positive reaction energy, so to increase $h^0_{i^*}$ of O^* or OH^* would make the activation/reaction free energy of this step vary in opposite directions. At the medium U region($0.5\ V < U < 0.65$ eV), $|\frac{d\log_{10}(j_k)}{dh^0_{i^*}}|$ increases from zero to the maximum, which shows the existence of "self-regulation" effects on the sensitivity. These effects totally result from the competition for limited reaction sites between different elementary steps (*entropic interactions*), but quickly vanish at high U, which means the "self-regulation" effect from *entropic interactions* is very weak.

On the other hand, Fig. 5.9 (b) shows $\frac{d\log_{10}(j_k)}{dh^0_{i^*}}$ at steady states of ORR on Pt (111) surface with $\zeta^{j^*}_{i^*} \neq 0$ and $[E] \neq [0]$, which means both *entropic interactions* and *enthalpic interactions* are considered. The results are quite different from those in Fig. 5.9 (a): at low U region, because j_k is controlled by the maximum O_2 adsorption rate, $\frac{d\log_{10}(j_k)}{dh^0_{i^*}}$ is still 0; as U increases, $|\frac{d\log_{10}(j_k)}{dh^0_{i^*}}|$ for both O^* and OH^* increase. However, even at very high U region, all $|\frac{d\log_{10}(j_k)}{dh^0_{i^*}}|$ values are still less than 10 eV^{-1}, much smaller than their counterparts in the cases of $\zeta^{j^*}_{i^*} = 0$ shown in Fig. 5.9 (a). These significant sensitivity decreases indicate that the "self-regulation" effects from *enthalpic interactions* are much stronger than those from *entropic interactions*, which is also confirmed by the reaction pathway changes shown in Fig. 5.4 and 5.8.

To understand how these "self-regulations" work, further detailed mathematical analyses are performed. Here we rewrite Eq. 5.67 as

$$\frac{d\ j_k}{d\ h^0_{i^*}} = [\vec{B}]^T \cdot [F] \left[\frac{\partial \vec{r}_I}{\partial h^0_{i^*}}\right] \times e/S_0 \tag{5.74}$$

where

$$[F] \equiv \left\{\mathbf{I} - ([D]+[E])\ [[A]([D]+[E])]^{-1}\ [A]\right\} \tag{5.75}$$

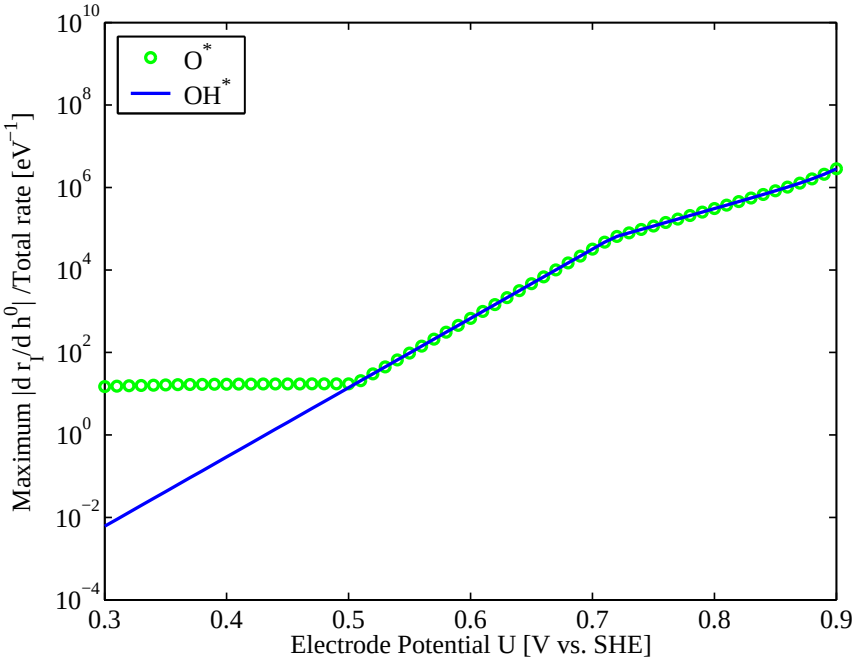

(a)

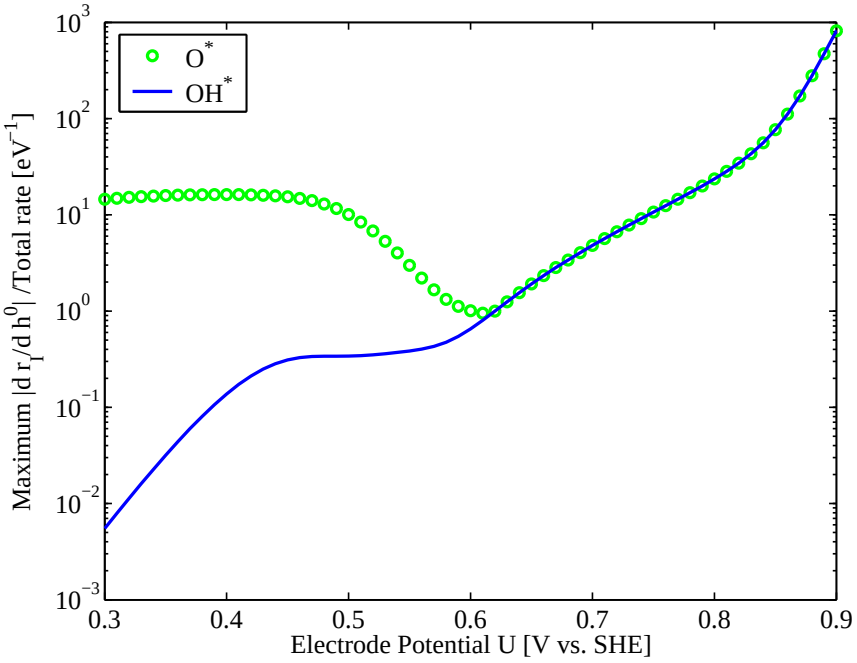

(b)

Figure 5.10: Maximum absolute value of elements in vector $\left[\frac{\partial \vec{r}_I}{\partial h^0_{i^*}}\right]$ relative to total ORR rate ($j_k \cdot S_0/e$) for (a) no-enthalpic-interaction cases ([E]=0) and (b) enthalpic-interaction cases ([E]≠0).

Because there are 5 different elementary steps in ORR, for a single variable $h^0_{i^*}$, $\left[\frac{\partial \vec{r}_{\rm I}}{\partial h^0_{i^*}}\right]$ is a 5×1 vector, [F] is a 5×5 asymmetric matrix. We first plot the ratio of the maximum absolute value of the 5 elements in $\left[\frac{\partial \vec{r}_{\rm I}}{\partial h^0_{i^*}}\right]$ to the total ORR rate, which equals $j_k \cdot S_0/e$, at different U in Fig. 5.10. These values describe the the maximum sensitivity of the reaction rates of individual elementary steps to the change of $h^0_{i^*}$. Surprisingly, it is found that they are much larger than $|\frac{d\log_{10}(j_k)}{dh^0_{i^*}}|$ as shown in Fig. 5.9, regardless of whether *enthalpic interactions* are considered. So there must be strong regulation effects resulting from matrix [F]. To clarify how it works, we perform **singular value decomposition** (SVD) to matrix [F] as

$$[\mathrm{F}] \;=\; [\bar{\mathrm{U}}][\mathrm{S}][\mathrm{V}]^{\mathrm{T}} \tag{5.76}$$

where both $[\bar{\mathrm{U}}]$ and [V] are 5×5 unitary matrices and [S] is a 5×5 diagonal matrix. The sensitivity equation can be again rewritten as

$$\frac{d\ j_k}{d\ h^0_{i^*}} = [\vec{\mathrm{B}}]^{\mathrm{T}} \cdot [\mathrm{U}][\mathrm{S}][\mathrm{V}]^{\mathrm{T}} \left[\frac{\partial \vec{r}_{\rm I}}{\partial h^0_{i^*}}\right] \times e/S_0 \tag{5.77}$$

To check the role of each matrix, we plot their values at different U. In Fig. 5.11, 5 diagonal elements in [S] are plotted, which show that the last three diagonal elements (S_{33}, S_{44} and S_{55}) are zero, resulting from 3 steady-state constraint equations in Eq. 5.18. Only the first 2 elements (S_{11}, S_{22}) are non-zero and there are no significant changes with U(S_{11} $\approx$ 2$\sim$4 and S_{22} $\approx$ 1$\sim$1.5), regardless of whether *enthalpic interactions* are considered. For these reasons, although there are 5 elements for vector ($[\mathrm{V}]^{\mathrm{T}} \left[\frac{\partial \vec{r}_{\rm I}}{\partial h^0_{i^*}}\right]$) in Eq. 5.77, only first two of them finally affect the sensitivity $\frac{d\ j_k}{d\ h^0_{i^*}}$. Thus, we plot these first 2 elements of ($[\mathrm{V}]^{\mathrm{T}} \left[\frac{\partial \vec{r}_{\rm I}}{\partial h^0_{i^*}}\right]$) divided by corresponding total ORR rate ($j_k \cdot S_0/e$) in Fig. 5.12 and the last 3 ones in Fig. 5.13. These figures show that although the last 3 elements are still as large as $\left[\frac{\partial \vec{r}_{\rm I}}{\partial h^0_{i^*}}\right]$ in Fig. 5.10 and oscillate violently, the first 2 elements become quite small,

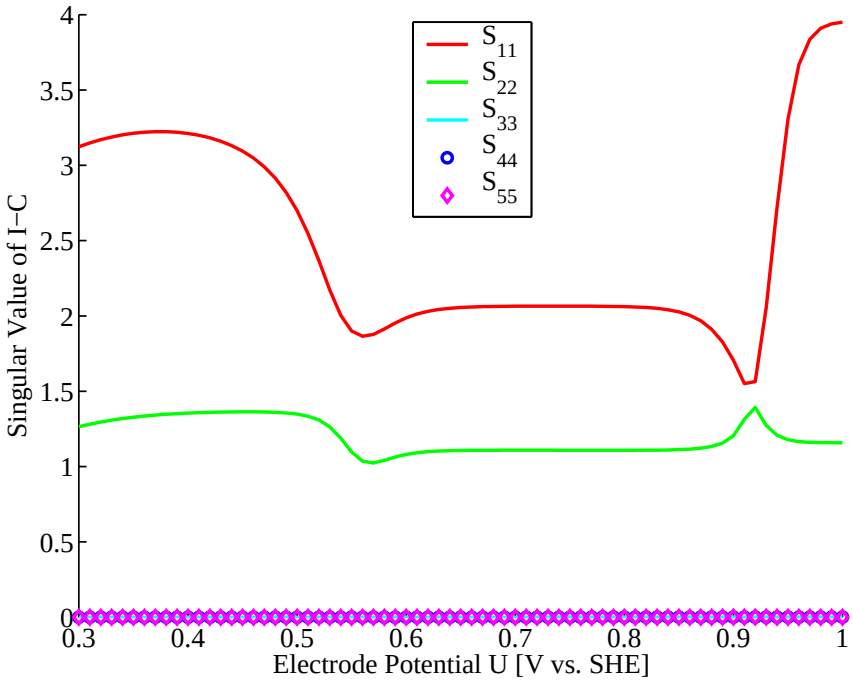

(a)

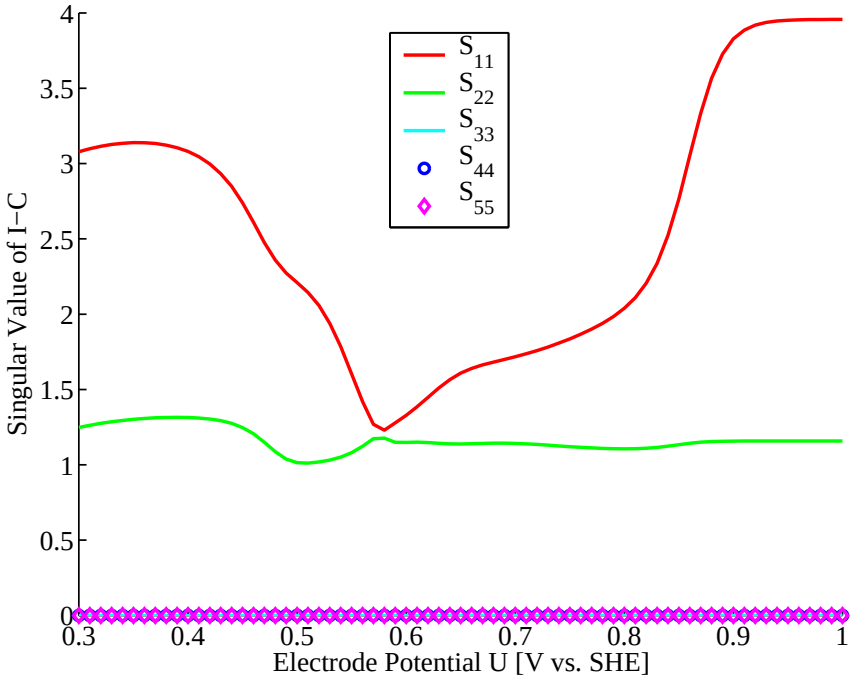

(b)

Figure 5.11: 5 elements of 5×5 diagonal matrix [S] in Eq.5.77 for (a) no-enthalpic-interaction cases ([E]=0) and (b) enthalpic-interaction cases ([E]≠0).

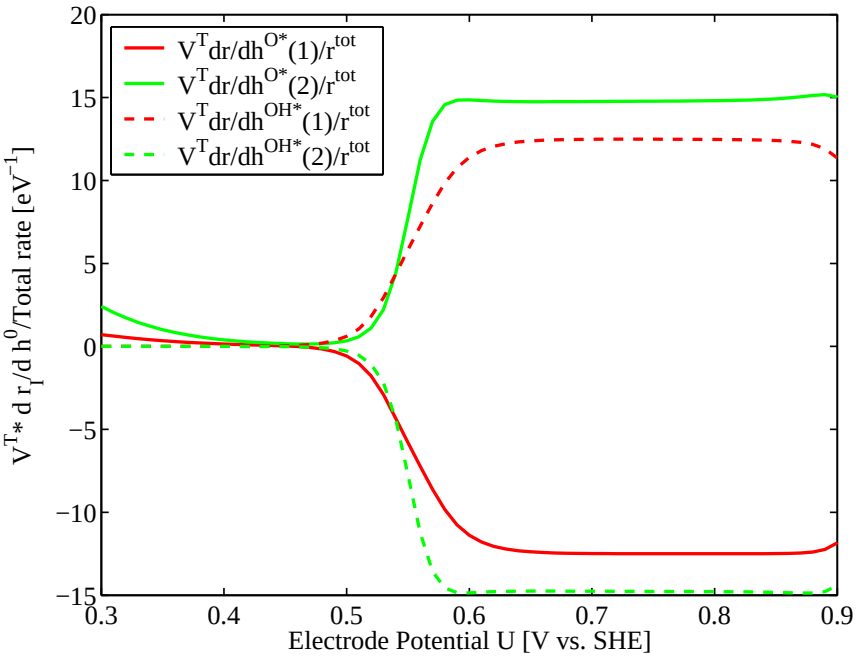

(a)

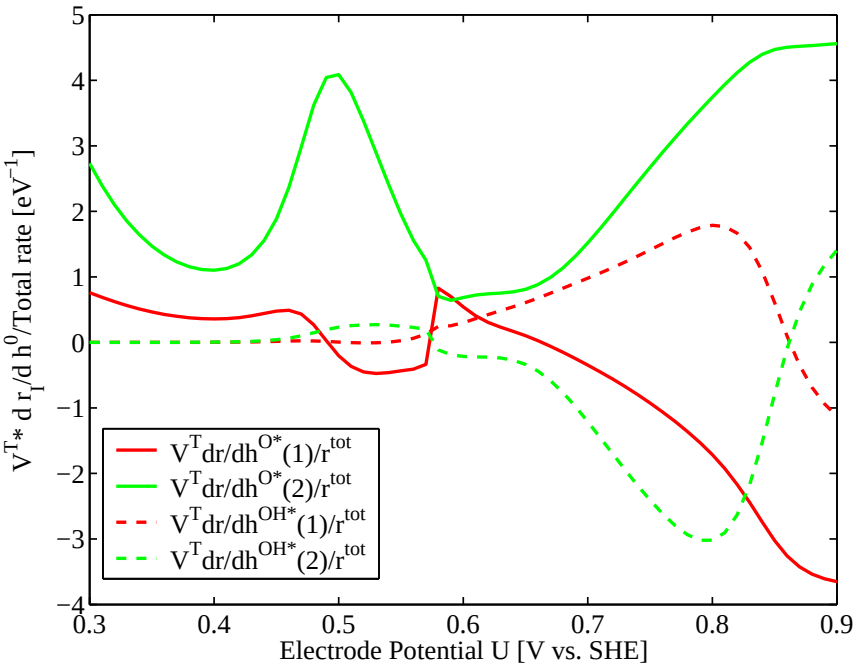

(b)

Figure 5.12: First two elements in vector $[\mathrm{V}]^{\mathrm{T}}\left[\frac{\partial \vec{r}_{\mathrm{I}}}{\partial h^{0}_{i^*}}\right]$ relative to total ORR rate ($j_k \cdot S_0/e$) for (a) no-enthalpic-interaction cases ([E]=0) and (b) enthalpic-interaction cases ([E]≠0).

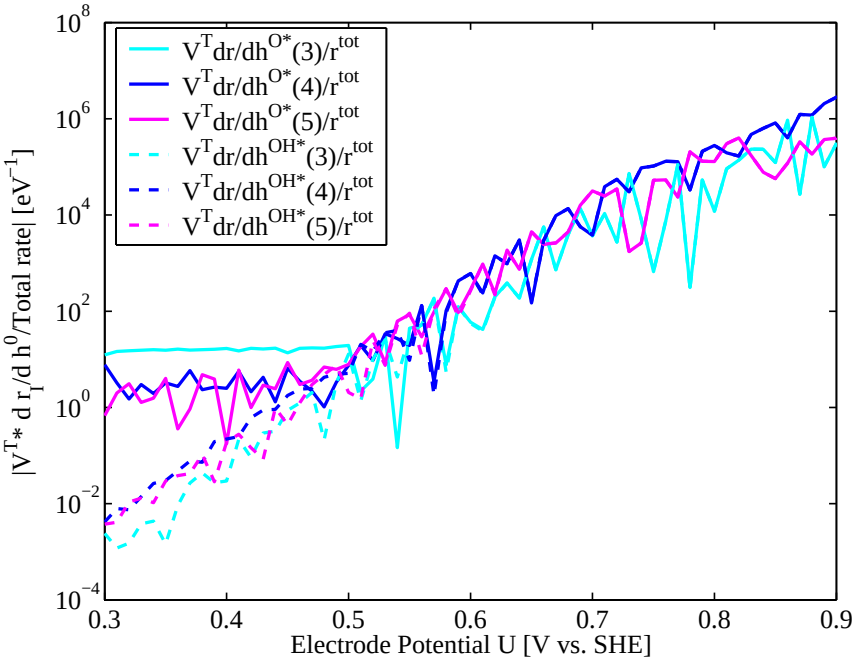

(a)

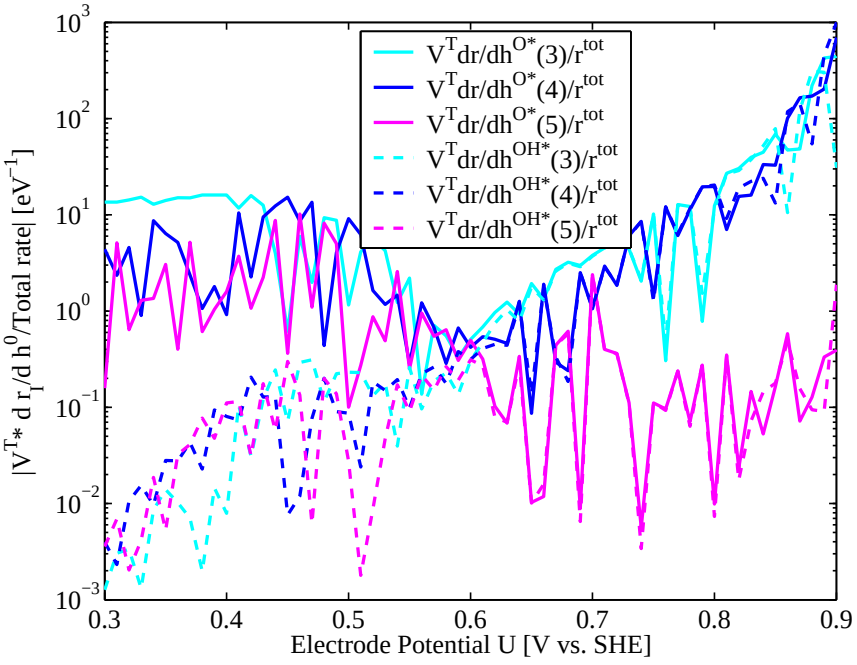

(b)

Figure 5.13: Magnitude of last three elements in vector $[V]^T \left[\frac{\partial \vec{r}_I}{\partial h^0_{i*}}\right]$ relative to total ORR rate ($j_k \cdot S_0/e$) for (a) no-enthalpic-interaction cases ([E]=0) and (b) enthalpic-interaction cases ([E]≠0).

which are comparable with the final sensitivity results $\frac{d\ j_k}{d\ h^0_{i^*}}$ shown in Fig. 5.9 and smoothly change with U. These results indicate that most "self-regulation" effect results from matrix $[\mathrm{V}]^{\mathrm{T}}$ in Eq. 5.77. It works like a rotation matrix in the activity-energy space to rotate only a small part of the huge vector of $\left[\frac{\partial \vec{r}_{\mathrm{I}}}{\partial h^0_{i^*}}\right]$ along the direction of total ORR rate, leaving other huge elements in perpendicular directions. This "rotation" effect comes from both entropic interactions and enthalpic interactions, as shown in Fig. 5.12 (a) and (b), which also indicates that enthalpic interactions would further strengthen this effect to obtain much smaller $[\mathrm{V}]^{\mathrm{T}}\left[\frac{\partial \vec{r}_{\mathrm{I}}}{\partial h^0_{i^*}}\right]$ along ORR rate direction and result in much smaller $\frac{d\ j_k}{d\ h^0_{i^*}}$.

The intrinsic origins of the 'rotation" matrix $[\mathrm{V}]^{\mathrm{T}}$ and the corresponding "self-regulation" effect are the steady-state requirements. When certain $h^0_{i^*}$ changes, the activation/reaction free energies of about one or two elementary steps in the whole ORR reaction network would correspondingly change, so their rates vary exponentially, but the rates of other elementary steps which do not involve the intermediate i^* do not change at all. However, because of the linear relations between all of these elementary steps as Eq. 5.18, the rate of each elementary step always tries to become almost equal to each other at steady states, so the changes in activation free energies and reaction rates of one or two steps would finally be averagely re-distributed to other steps. As a result, a large change of activation/reaction free energies of one or two steps would become several small changes of activation/reaction free energies of all elementary steps, and the final variation in total ORR rate becomes much smaller.

5.1.4 Discrete Model

As the discussions in both Section 5.1.2 and 5.1.3, the *enthalpic interactions* between ORR intermediates adsorbed on the surface are important not only for accurate reaction rate and kinetic current density j_k, but also for the determination of j_k's sensitivity on adsorption strengths varying with different surfaces. So we need to describe these lateral interactions

correctly. As an initial step, we just use a mean-field approximation as Eq. 5.39 and assume that these interactions are linearly proportional to the surface coverages as Eq. 5.41, then we use DFT calculations to estimate the corresponding linear coefficients $\zeta_{i^*}^{j^*}$. This method may be accurate enough when surface coverage is small at low U region.

However, there are two drawbacks with this approximation method. First, as shown in Section 6.1, between certain adsorbates, such as O^*, their repulsive interactions are more like increasing and discontinuous functions of surface coverage, which have several discontinuous increments at some critical coverages depending on detailed surface structures. Second, the mean-field approximation of lateral interactions itself, as shown in Eq. 5.39, may not be correct for certain adsorbates; for example, because OH^* is a polarized species with hydrogen atom, their mutual interactions depend not only on the distance, but also the angle between two OH bonds. As a result, the linear approximation method may not be accurate, especially when U is very high, generating some problems such as too low Tafel slopes ($\frac{dU}{d\log_{10}(j_k)}$) for Pt (111) and (100) surfaces at high U regions shown in Section 5.1.2.

To overcome these drawbacks, we need an accurate discrete description of ORR intermediates' interactions beyond the continuous mean-field approximation. One possible way is to use a large surface unit cell, such as (50×50) Pt (111) surface, to perform kinetic Monte Carlo simulation of ORR by considering detailed reactions on each reaction site. As an initial step, we use kinetic Monte Carlo method to simulate an anodic polarization process on Pt (111) surface in cyclic voltammetry measurement, where there is no supply of O_2, and we only consider the reaction of water dissociation into O^* as the following:

$$H_2O \leftrightarrow O^* + 2H^+ + 2e^-. \tag{5.78}$$

This reversible reaction is not only an elementary step involved in the reaction network of ORR, but also an initial step for Pt surface oxidation studied in Chapter 6. In this

simple model, all the parameters of activation/reaction free energies are the same as those in Section 5.1.2, except that the lateral repulsion is not calculated from the mean-field method but by considering the local adsorption configuration. Here we only consider the repulsion between two O^* as nearest neighbors, which is 0.20 eV obtained from DFT calculations on different O^* adsorption configurations in (3×3) unit cell of Pt (111) surface. Except the reaction in Eq. 5.78, we also consider the diffusion of O^* between different sites. The activation energy of O^* diffusion is 0.6 eV on clean Pt (111) surface from DFT+NEB calculations, but it may change on the surface with considerable O^* coverage, because different adsorption sites may have different repulsive energies.

The simulations are performed in (50×50) unit cell of Pt (111) surface with periodic boundary conditions and U is increased from 0.6 V to 1.4 V. Meanwhile, a model including no lateral repulsion is also considered. Because for the deposition of each O^* on the surface there are two electrons transferred to the electrode, we can express the final results as the relation between total charge transfer density Q and U, which is plotted in Fig. 5.14 (a) (here current density is not plotted because its value oscillates too rapidly for such a small unit cell). It is shown that if no lateral repulsion is considered, the surface is quickly covered with 1 ML O^* when $U > 0.8$ V, corresponding to $Q = 460\ \mu C/cm^2$, which totally disagrees with experimental measurement[80].

On the other hand, when lateral repulsion is considered, Q increases with U like a step function until surface is covered with 1 ML O^* when $U > 1.4$ V. When $0.6\text{ V} < U < 1.4\text{ V}$, there are two large steps of discontinuous increments. The first step is at $U \approx 0.8$ V and $Q \approx 150\ \mu C/cm^2$, equal to $\frac{1}{3}$ ML O^*; the corresponding surface configuration is shown in Fig. 5.14 (b), where Pt (111) surface is covered with O^* with $(\sqrt{3}\times\sqrt{3})$ lattice, indicating that each O^* from the further deposition reaction has to have at least 3 O^* as nearest neighbors. The second step is at $U \approx 1.1$ V and $Q \approx 300\ \mu C/cm^2$, equal to $\frac{2}{3}$ ML O^*; the corresponding surface configuration is shown in Fig. 5.14 (c), where Pt (111)

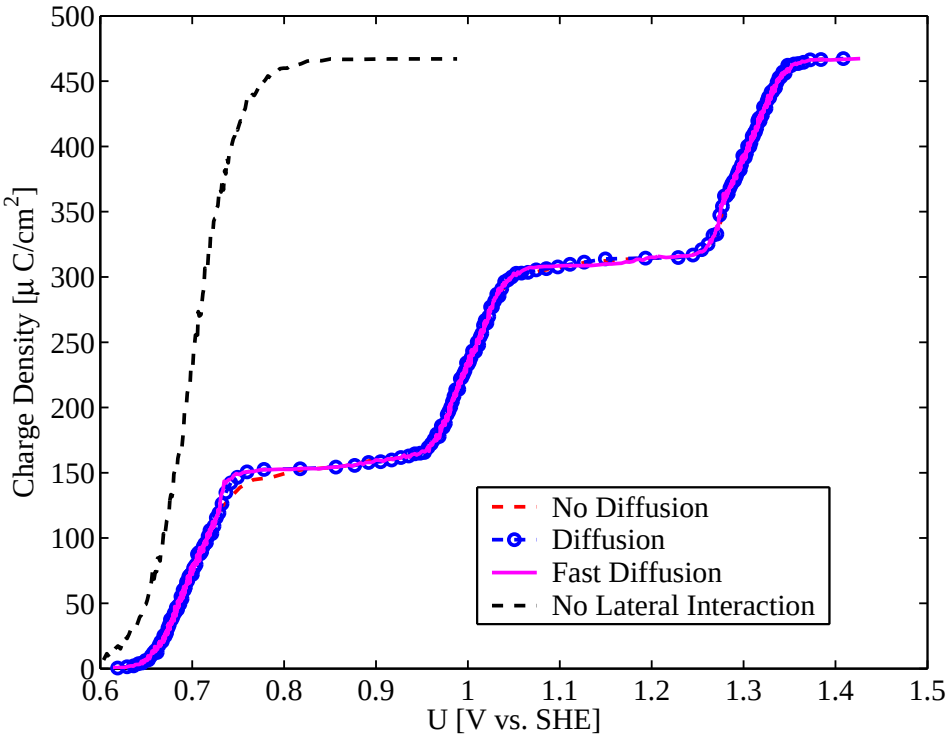

(a)

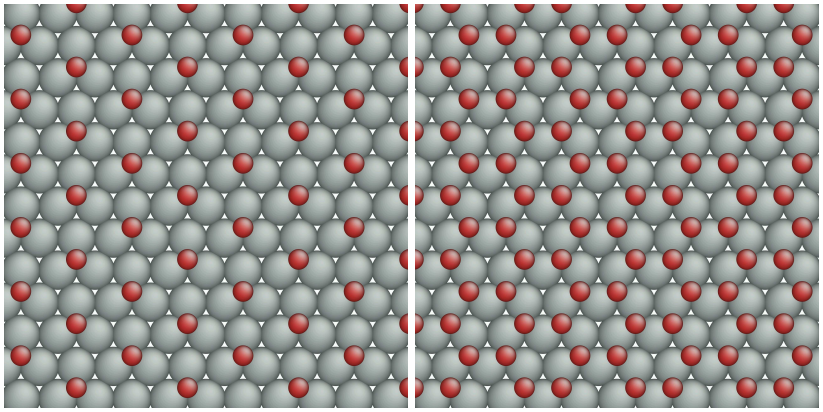

(b) (c)

Figure 5.14: Kinetic Monte Carlo (kMC) simulation of anodic polarization on Pt (111) surface: (a) total integrated charge density vs. electrode potential. (b) $(\sqrt{3}\times\sqrt{3})$ lattice of O* on Pt (111) surface, corresponding to the configuration when $U \approx 0.8 \sim 1.0$ V. (c) "Graphene-like" lattice of O* on Pt (111) surface, corresponding to the configuration when $U \approx 1.1 \sim 1.3$ V.

surface is covered with O^* with a "graphene-like" lattice, indicating that each O^* from the further deposition reaction has to have 6 O^* as nearest neighbors. Such two steps in *Q-U* relation were also observed from experiments at $U \approx 0.8$ V and 1.2 V, respectively[80]; however, the corresponding Q is not so high: at $U \approx 0.8$ V Q was found to be about 100 $\sim 120\ \mu C/cm^2$. The differences in Q between the simulation and the experiment may be due to two possible reasons: either other adsorbates such as OH^* in the simulation should be considered, or the interactions beyond nearest neighbors should be considered, because $\sim 100\ \mu C/cm^2$ corresponds to $\frac{1}{4}$ ML of O^*, which can only be obtained from simulation if the second nearest neighbors are taken into account.

In spite of these inaccuracies, such a simple kinetic Monte Carlo model still semi-quantitatively shows the key feature of "step-function-like" *Q-U* curve observed in experiments [80]. Such a discontinuous curve can not be produced in the continuous mean-field model, confirming the possibility of a discrete model to improve the description of ORR kinetics, where the lateral *enthalpic interactions* play important roles.

5.2 Model of Electrode-Electrolyte Interfacial Structures

In Section 5.1, electrode potential U is used as an external input to determine ORR kinetics and current density j. However, in the real PEM fuel cell, both U and j are the output of the total system at given reaction conditions, such as reactant concentration, mobility of ions in electrolyte, and properties of the external circuit. It is both intellectually and practically important to build a multiscale self-consistent model to output both U and j starting from first-principles calculation results. One of the critical step to achieve this goal is to understand the detailed structure of electrode-electrolyte interface and the origin of U.

To evaluate any potential, a well-defined reference is needed. In a full fuel cell system, U can be defined as the difference of Fermi level E_{F} between the working electrode and

a reference counterpart, such as standard hydrogen electrode (SHE) and saturated calomel electrode (SCE)[7], divided by electron charge $-e$. Unfortunately, such a macroscopic system with two electrodes is difficult to handle by first-principles or other microscopic methods; usually a half-cell with a single electrode is used in the simulation so that only one type of electrode-electrolyte interfacial structure is explicitly investigated.

However, in a half-cell with only one electrode, it is not so straightforward to find a good reference for U[135, 120, 131]. One practical method is to calculate U by two steps. First, we define half-cell electrode potential $\tilde{U}$ as the difference between E_{F} of the electrode and electrostatic potential energy E_{stat} in the electrolyte far away divided by electron charge $-e$, which can be directly calculated by using first-principles methods with the help of statistical mechanical methods. As shown in Section 2.2, when there are no excess or deficient electrons on the electrode, $\tilde{U}$ equals the potential of zero charge (PZC) of this electrode, which can be directly measured relative to any practical reference electrode (SHE or SCE) in experiments[152, 7], plus a constant that is independent of the electrode-electrolyte interfacial structure[135, 131]. Meanwhile, when the excess surface electron on the studied electrode changes, all the corresponding potential changes are located at this electrode-electrolyte interface. So we can write

$$\tilde{U} - \tilde{U}_{\mathrm{PZC}} = U - \mathrm{PZC} \tag{5.79}$$

where $\tilde{U}_{\mathrm{PZC}}$ is $\tilde{U}$ without excess or deficient electron on the electrode. By varying the amount of excess electrons on the electrode, we can obtain different $U - \mathrm{PZC}$. Second, we can calculate PZC of certain electrode relative to any practical reference electrode with the help of *absolute electrode potential*[135]. As a result, U of this electrode relative to any practical reference electrode can also be theoretically calculated by combing these two steps, which are discussed in Section 5.2.1 and 5.2.2, respectively.

5.2.1 Electrode Potential and Differential Capacitance

Physically, the change in $\tilde{U}$ results from the variation of opposite excess charges accumulated on the two sides of electrode-electrolyte interface, which is called *electrical double layer*[115, 114, 7]. As shown in Section 2.2, this double layer structure can be divided into two areas by the outer Helmholtz plane (OHP), which is the locus of the electrical centers of non-specifically adsorbed ions in their position of closest approach to the electrode. Away from electrode and outside OHP, it is the ion *diffusion layer*, which can be described by classical statistical mechanical methods, such as the Gouy-Chapman theory[38, 18]. Inside OHP it is a *compact layer* of solvent molecules and other adsorbates on the electrode surface. The electronic structure of this compact layer can be calculated by first-principles methods at specific configuration, but an accurate description of potential changes in this layer at room temperature is only possible when a statistical model is built to consider various co-adsorption configurations.

Figure 5.15: The symmetrical configuration of Pt-H_2O interfaces to simulate the compact layer in the double layer structure.

As an initial step, we use DFT methods to study a simple compact layer structure with excess surface electron density σ^{M} on the metallic electrode. Here σ^{M} can be either nega-

tive, meaning there are more electrons than the charges of positive metallic ions, or positive, meaning fewer electrons than the metallic ions' charges. As shown in Fig. 5.15, we create a symmetrical supercell of two Pt (111) surfaces plus adsorption of two monolayers of H_2O on each surface, and there is a large vacuum region in the middle. The surface of Pt is in a $(3\times\sqrt{3})$ unit cell as shown in Fig. 4.9 (a), and each monolayer of H_2O has the same structure with the H_2O monolayer observed on Pt (111) surface at vacuum condition[96]. In the following section, we call the water layer close to Pt surface the first water layer, and the one far away from Pt is the second layer. We add equal σ^M on two surfaces and compensating opposite charge as δ function in the middle of vacuum, which is closer to the charge distribution in *electrical double layer* than the method to use homogeneous compensating opposite charges in the whole unit cell[131]. As a result, two symmetrical compact layers are made and there is a homogeneous electric field applied on each of them, resulting in a charge redistribution and corresponding potential changes on the Pt-H_2O interfaces.

The changes in electron densities with both a positive and a negative σ^M are shown in Fig. 5.16 (a). Most of the changes occur around two layers of H_2O, especially the second layer which is far away from the surface, and there is a huge oscillation of electron density difference when a negative σ^M is applied. One thing we need to check is whether there is electron density in the center of vacuum for the negative σ^M case, because the positive compensation δ charge may cause electrons to spill out from Pt-H_2O layer so that the result can not accurately describe the electrical double layer structure with this negative σ^M. Here σ^M = -5.85 μC/cm^2 is the maximum negative value we used in this simulation, and there is still no electron distributed in the center of vacuum, which confirms the validity to use this result to evaluate potential changes.

The electrostatic energies E_{static} relative to corresponding Fermi levels E_F with the same positive and negative σ^M are shown in Fig. 5.16 (b). We can see that inside Pt layers E_{static} relative to E_F does not change with σ^M. However, compared with E_{static} in the vacuum, E_{static}

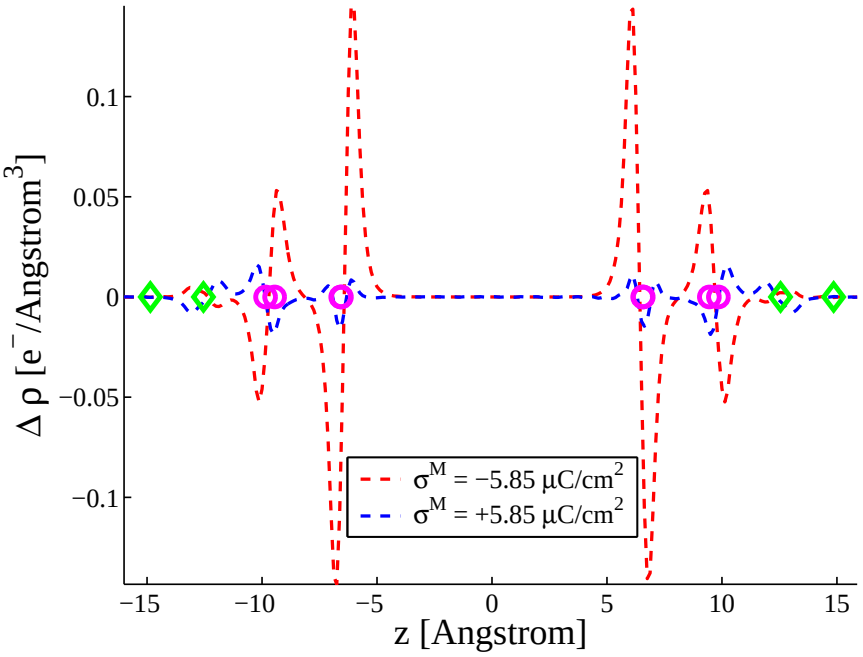

(a)

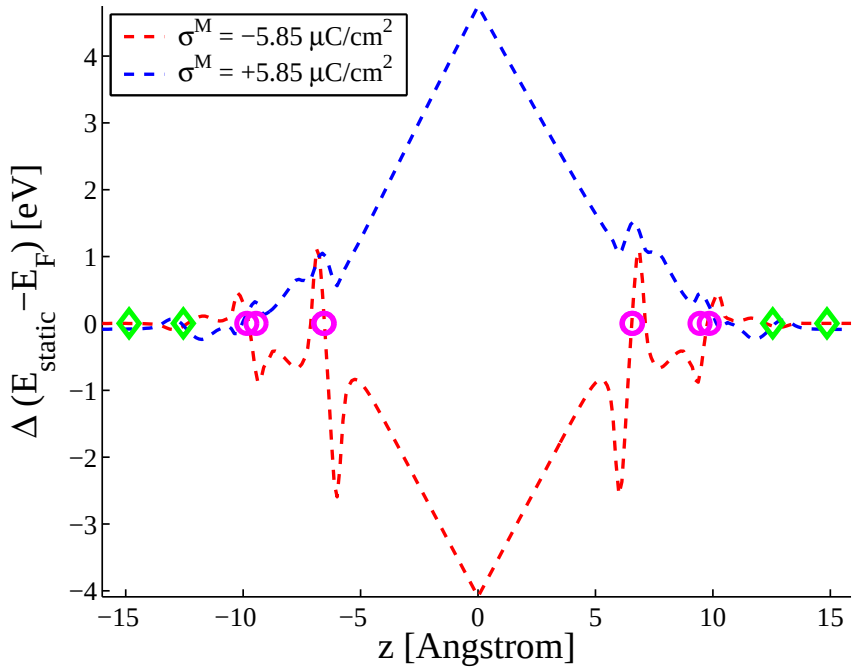

(b)

Figure 5.16: Average (a) electron density and (b) electrostatic potential energy differences at certain excess surface electron density σ^{M} along z-direction for the 2-layer H_2O configuration in Fig. 5.15. Here the green diamonds stand for z-coordinates of Pt atoms at neutral system, while magenta circles stand for z-coordinates of oxygen atoms at neutral system.

of Pt layers decreases/increases with positive/negative σ^{M}, indicating electrode potential increasing/decreasing. Here we want to use these potential distributions to describe the potential changes inside the *compact layer*, so we have to define the position of OHP. In the real electrode-electrolyte interface, OHP should result from the average sampling of the varying water structures near the electrode. Here we simply define the average position of all oxygen atoms in the first water layer as the position of OHP, and corresponding $E_{\text{static}}^{\text{OHP}}$ is calculated from the average value of E_{static} applied on every oxygen atom in the first water layer. By varying σ^{M} and corresponding compensating δ charge, we can obtain different $E_{\text{static}}^{\text{OHP}}$, and we define

$$\Delta U_{\text{H}}(\sigma^{M}) \equiv [E_{\text{static}}^{\text{OHP}}(\sigma^{M}) - E_{\text{F}}(\sigma^{M})] - [E_{\text{static}}^{\text{OHP}}(\sigma^{M}=0) - E_{\text{F}}(\sigma^{M}=0)] \tag{5.80}$$

as the compact layer's contribution to the potential, which is a function of σ^{M}. On the other hand, the potential changes from the *diffusion layer*, ΔU_{GC}, can be calculated from classical Gouy-Chapman theory by given σ^{M} and ion concentration of electrolyte as Eq. 2.12. Finally we can obtain electrode potential U as a function of σ^{M} by adding the contributions from both compact layer and diffusion layer together as the following:

$$U(\sigma^{M}) - \text{PZC} = \tilde{U}(\sigma^{M}) - \tilde{U}_{\text{PZC}} = \Delta U_{\text{H}}(\sigma^{M}) + \Delta U_{\text{GC}}(\sigma^{M}) \tag{5.81}$$

The results of ΔU_{H} and ΔU_{GC} as functions of σ^{M} are shown in Fig. 5.17. It can be seen that ΔU_{H} changes more rapidly with σ^{M} when $\sigma^{M} < 0$ than $\sigma^{M} > 0$: when $\sigma^{M} \approx$ -6 μC/cm^2 $\Delta U_{\text{H}} \approx$ -0.6 V, but σ^{M} should be as large as +12 μC/cm^2 so that ΔU_{H} can reach +0.6 V. This difference may result from the huge Coulomb repulsion between electrons at Pt-H_2O interface when excess electrons are added. On the other hand, ΔU_{GC} is a symmetric function of σ^{M} but changes rapidly with ion concentrations in the electrolyte. When ion concentration is very low (0.001 M), ΔU_{H} is only about twice of ΔU_{GC} so that both compact

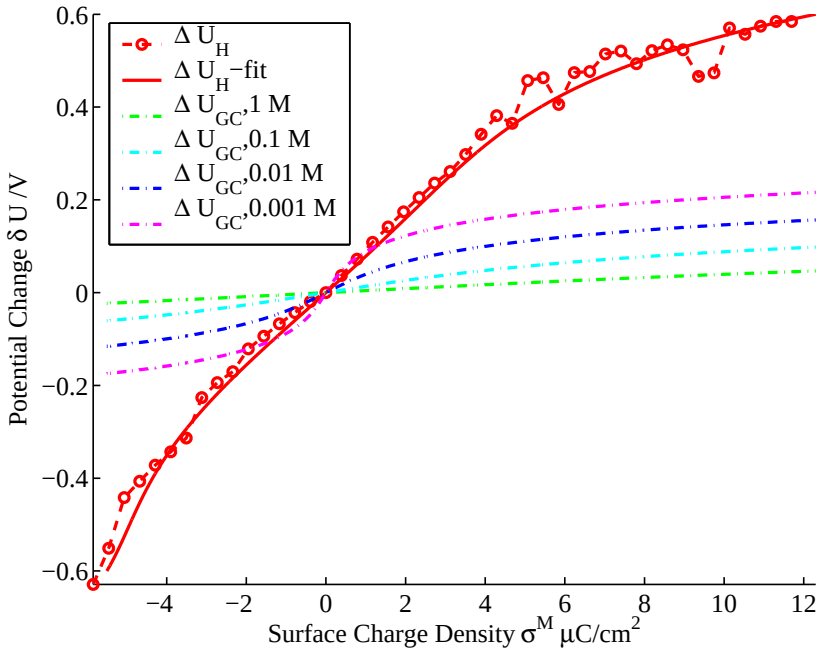

(a)

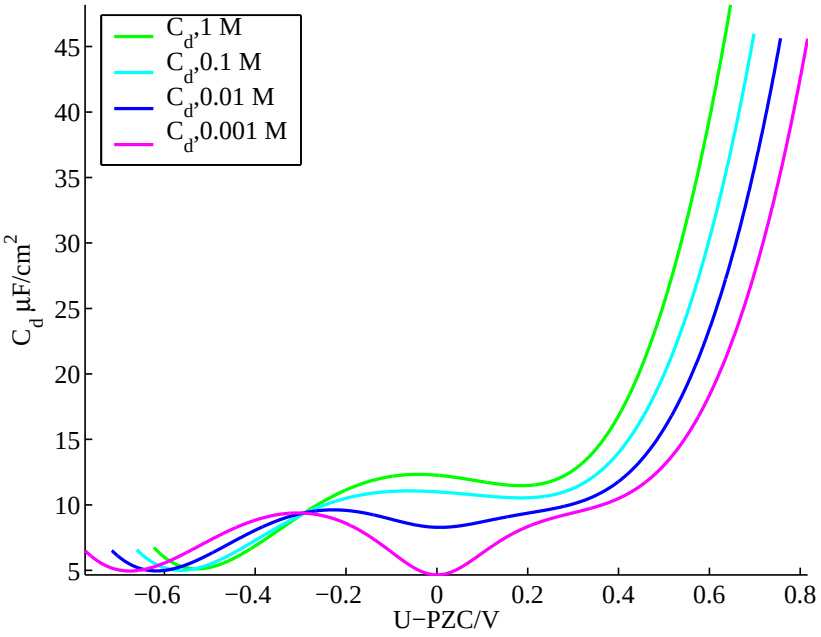

(b)

Figure 5.17: (a) Electrode potential changes ΔU as function of excess surface electron density σ^{M}. Here compact layer contribution ΔU_{H} is calculated by DFT methods from 2-layer H_2O configuration in Fig. 5.15, and diffusion layer contribution ΔU_{GC} is calculated by Gouy-Chapman theory for the completely dissociated 1-1 electrolyte with the ion concentration varying from 1 M to 0.001 M. (b) The corresponding differential capacitance C_d.

layer and diffusion layer make significant contributions to the total potential changes; when ion concentration is high (1 M), $\Delta U_{\mathrm{H}} \gg \Delta U_{\mathrm{GC}}$ so that most potential changes are inside the compact layer.

Meanwhile, from these $\Delta U(\sigma^{\mathrm{M}})$ functions we can obtain differential capacitance C_d defined as the following:

$$C_d = \frac{\partial \sigma^{\mathrm{M}}}{\partial U} \tag{5.82}$$

which can be directly measured from experiments[7]. Our calculation results of C_d at different ion concentrations (because U_{GC} depends on ion concentration) are shown in Fig. 5.17 (b). Since ΔU_{H} is an asymmetric function of σ^{M}, C_d is also asymmetrical with (U - PZC): when U is larger than PZC, C_d quickly goes up to $40 \sim 50$ μF/cm^2, which is comparable with experimental results on several types of metallic surfaces (Hg, Au or Ag)[39, 139, 64, 7]; when U is smaller than PZC, C_d becomes very small ($5 \sim 10$ μF/cm^2) and insensitive to the change of U, which qualitatively agrees with experiments but the quantities are different: in experiments, $C_d \approx 20$ μF/cm^2 at very negative U[39, 139, 64, 7].

This underestimate of C_d at negative σ^{M}(U - PZC < 0) indicates that the dielectric constant of the compact layer, ε_{H}, may be too low. For any condensed phase composed of polarized molecules such as H_2O, its dielectric constant comes mainly from two parts: the first part is from the electron redistribution under external field within each fixed molecule, which is automatically included in our simulation; the second part is from the re-organization of its atomic and molecular structures, which may not be adequately described by just a single configuration of compact layer as Fig. 5.15. Although such monolayer structure was observed on Pt (111) surface under vacuum condition, at the interface between Pt and bulk water such a compact layer structure may change with time. In fact, several simulations show that at various σ^{M} there are different ground states structures of water molecules close to metallic surface[131, 111, 58]. For this reason, the problem of

inadequate configuration sampling of water structures in compact layer may be solved or alleviated by *ab initio* molecular dynamics simulation of compact layer structures at finite temperature, so the structures of water molecules network could change with time. Then $[E^{\mathrm{OHP}}_{\mathrm{static}}(\sigma^{\mathrm{M}}) - E_{\mathrm{F}}(\sigma^{\mathrm{M}})]$ is calculated not from a single configuration, but from the average value of many configurations at equilibrium states, which may cancel out the effect of external field more significantly and give rise to larger value of dielectric constant and corresponding C_d.

5.2.2 Potential of Zero Charge

In Section 5.2.1, the methods to combine DFT with statistical methods to calculate the difference between electrode potential U and the potential of zero charge (PZC) are discussed. Then the remaining task is to calculate PZC relative to some typical reference electrodes (SHE or NCE) which can be directly measured by experiments[7].

Since we can only calculate the potential changes at one electrode, we should compare the calculation results with a similar reference system in which only one electrode is considered but the results can be measured from experiments. As shown in Section 2.2, A good choice is **absolute electrode potential**[135, 120], which can be calculated from the energy cost to move one electron from the vacuum area just outside the electrolyte-vacuum interface to the electrode. For the SHE, in which the electron has the equilibrium chemical potential with HOR as Eq. 1.1, its absolute electrode potential is 4.6$\pm$0.2 V, which is obtained from experimentally measurable values, such as solvation free energy of a bare proton[135, 136]. For this reason, for any single electrode in certain electrolyte (usually water), we can first calculate its absolute electrode potential with zero excess electron on the electrode, $\mathrm{PZC}_{\mathrm{abs}}$, then obtain its PZC vs. SHE as the following:

$$\text{PZC vs. SHE} = \mathrm{PZC}_{\mathrm{abs}} - \mathrm{PZC}_{\mathrm{SHE}} \approx \mathrm{PZC}_{\mathrm{abs}} - 4.6\ \mathrm{V} \tag{5.83}$$

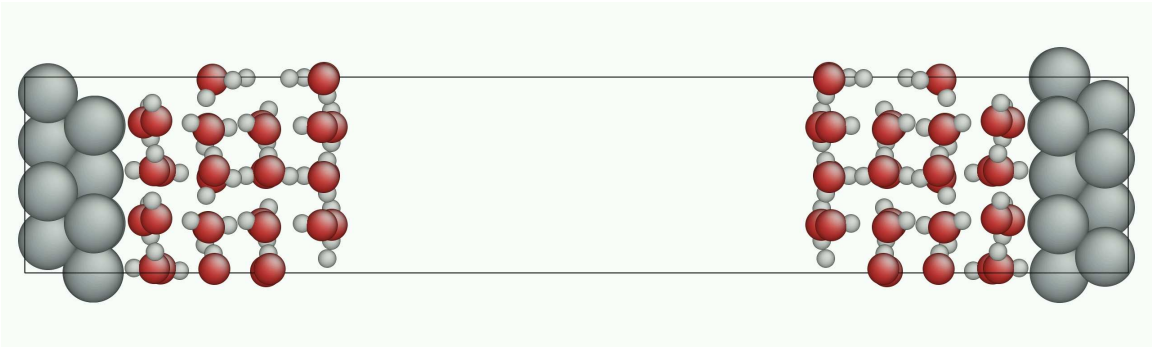

Figure 5.18: The symmetrical configuration of interfaces between Pt (111) surface and several layers of water molecules.

The next task is to determine PZC_{abs}. According to the definition of absolute electrode potential, we build two symmetrical interfaces between Pt (111) surfaces and several layers of water molecules, as shown in Fig. 5.18, where there is a large vacuum region between two symmetrical Pt-H_2O interfaces. The relaxed water layer structure is obtained by two steps: first, starting from a random initial configuration, *ab-initio* molecular dynamics based on DFT calculated potentials is performed in this unit cell at a high temperature (500 K) for several pico-seconds; second, we take the final configuration and make DFT relaxation to obtain a local minimum state of this water layer. We hope this relaxed water layer could reveal the correct dielectric properties of bulk water at room temperature, so that we can use the difference between Fermi level of the system and the electrostatic energy in the middle of the vacuum divided by charge $-e$ as PZC_{abs} of Pt (111) surface. Then it can be transferred to PZC vs. SHE by Eq. 5.83

However, the result is found to be very sensitive to the water configurations we finally use. If *ab-initio* molecular dynamics at a high temperature is performed with different lengths of times, the DFT relaxation at the next step would lead to different local minimum states, so the final calculated PZC can oscillate between -1.0 V and 1.2 V vs. SHE. If we want to get a constant value comparable with the experimental result (0.2 V vs. SHE)[152], a good sampling method should be applied for the future work. Similar to the case of C_d in

Section 5.2.1, a possible solution is to perform a long time *ab-initio* molecular dynamics at room temperature and PZC can be calculated from the time-average difference between vacuum electrostatic energy and the Fermi level. In addition, we also need to make sure that the water layer is thick enough so that it can simulate the behavior of bulk water phase.

5.3 Principles of Self-Consistent Multiscale Model

Until now, for all the electrochemical models discussed in this section, there are always some input parameters, such as electrode potential U and excess surface electron density σ^{M}, which should be the outputs of real fuel cell systems, because once two electrodes are connected together as a circuit, constant outputs of both U and electric current I would be reached at a steady state, so do σ^{M}s on two electrodes. Here we just discuss some principles to calculate U, I and σ^{M} in self-consistent methods.

For any electrode, there are both incoming and outgoing electron fluxes. For an electrode coupled with ORR, which consumes electrons from the electrode, the outgoing electron flux is the current density j determined by ORR kinetics; the incoming electron flux j_{I} is from the auxiliary electrode through the external circuit. Here we assume the auxiliary electrode has very high reaction rate and its electrode potential is almost constant during the reaction. At a steady state, there would be constant excess electron charge σ^{M} accumulated on the studied electrode and $j = j_{\mathrm{I}}$. If σ^{M} suddenly becomes more positive because of some external perturbation, the electrode potential U would increase. As a result, j would decrease because there is less thermodynamic driving force for ORR as shown in Fig. 5.4, but j_{I} would increase because the thermodynamic driving force to move electrons from the auxiliary electrode to this electrode increases. The net effect is that there would be more incoming electrons than the outgoing electrons because $j_{\mathrm{I}} > j$, so that σ^{M} finally reduces to its original value at the steady state. For the same reason, the steady state is also stable

under negative perturbation of σ^{M}.

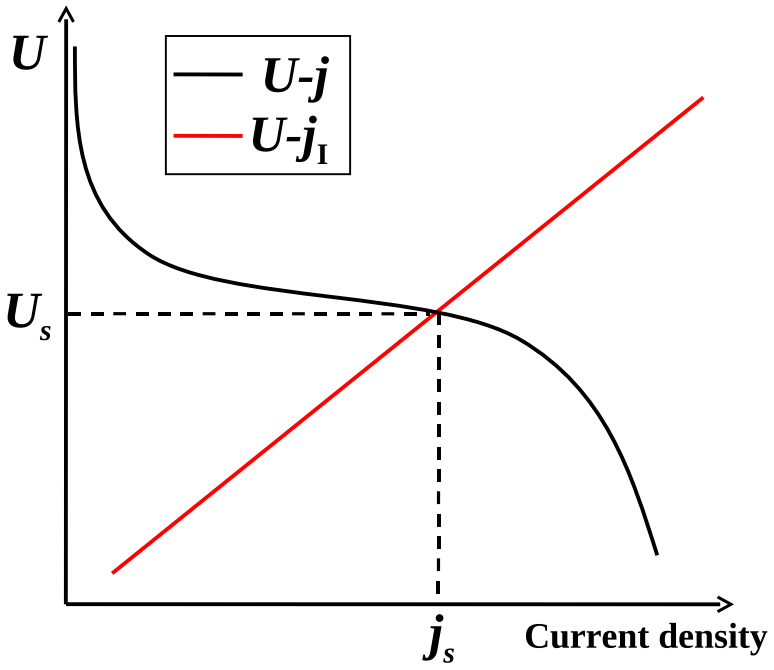

Figure 5.19: The functions of current density j from electrode reaction and incoming electron flux j_I from external circuit as electrode potential U. j_s and U_s are the output of this electrode at a steady state.

The requirement of $j = j_I$ can help us to obtain U and I at the steady state. As shown in Fig. 5.19, for a cathode coupled with ORR, j is a decreasing function of U, which can be calculated from ORR kinetics, as discussed in Section 5.1; j_I is an increasing function of U, which can be obtained from the electrical properties of the total circuit. For example, if the electrical resistance of total circuit is R and there is no other electrical elements, then j_I can be simply obtained by Ohm's law. So the steady state is at the intersection of U-j and U-j_I curves, where the outputs of this electrode, j_s and U_s, can be obtained.

Meanwhile, to obtain j in a wide range of U, we should consider the mass transfer effect, especially at high overpotential region where surface reaction is fast. Let's still take ORR for example. Its pre-exponential factors for rate constants of ORR elementary steps, such as υ^{+}_{MA} in Eq. 5.9 or υ^{+}_{HP} in Eq. 5.13, depend on the mass-transfer fluxes of O_2 and

H^+ from bulk electrolyte to the area close to the electrode surface, as shown in the whole electrode reaction pathway of Fig. 2.5. For certain species *i*, its flux is governed by the Nernst-Planck equation, written for one-dimensional mass transfer along the x-axis as

$$J_i(x) = -D_i\frac{\partial C_i(x)}{\partial x} - \frac{z_i}{k_B T}D_i\frac{\partial \phi(x)}{\partial x} + C_i v(x) \tag{5.84}$$

where $J_i(x)$ is the flux of species i at distance x from the electrode surface, D_i is the diffusion coefficient in the electrolyte, $\frac{\partial C_i(x)}{\partial x}$ is the concentration gradient at x, $\frac{\partial \phi(x)}{\partial x}$ is the electrostatic potential gradient in the electrolyte, z_i and C_i are the charge number and concentration of species i, respectively. The three terms on the right-hand side represent the contributions of diffusion, migration and convection, respectively, to the total flux. To consider the mass transfer, a full ORR reaction network should combine reaction network on the electrode surface in Section 5.1 and the mass transfer equation in Eq. 5.84. A steady-state solution can be obtained not only under the constraint of surface coverage changes in Eq. 5.18, but also the constraint that the consumption rates of reactants, such as O_2 and H^+, by kinetic current density j_k as Eq. 5.19, equal the rates of supplies given by Eq. 5.84. Eq. 5.60 is a special-case solution for ORR for a rotating disk electrode (RDE), where there are significant convection fields[7]. For a real fuel cell, where there is no external stirring effect such as electrode rotating, the diffusion and migration contributions may become important. So for a complete ORR kinetic model, we need to know the concentration and diffusion coefficients of O_2 and H^+ in the electrolyte to calculate the diffusion contribution; for the migration terms, $\frac{\partial \phi(x)}{\partial x}$ can be obtained from studies of $U(\sigma^M)$ and corresponding potential distribution in electrolyte as discussed in Section 5.2.

We can also use $U(\sigma^M)$ to study the kinetics of how a steady state is reached. Furthermore, we can abandon the assumption of constant potential for the auxiliary electrode in order to achieve a self-consistent model between two electrodes, which is a real fuel cell

simulator *in silico*. For this two-electrode model, the study of $U(\sigma^{M})$ for single electrode in Section 5.2 provides a useful reference system, because U can be calculated based on *absolute electrode potential* reference instead of any auxiliary electrode. In Fig. 5.20, we show a possible numerical double-loop model to reach a steady state for a two-electrode system: at initial state, anode and cathode have some excess surface electron density σ^{Ma} and σ^{Mc} respectively; then their own potentials, U_a and U_c, are determined by corresponding $U(\sigma^{M})$ relations; in the next step, these potentials themselves determine current densities on anode (j_a) and cathode (j_c), respectively, and their difference U_O produces the current density in the external circuit j_O; then the difference between j_a/j_c and j_O would result in the changes of σ^{Ma}/σ^{Mc}, which further change U_a/U_c until the steady state is reached.

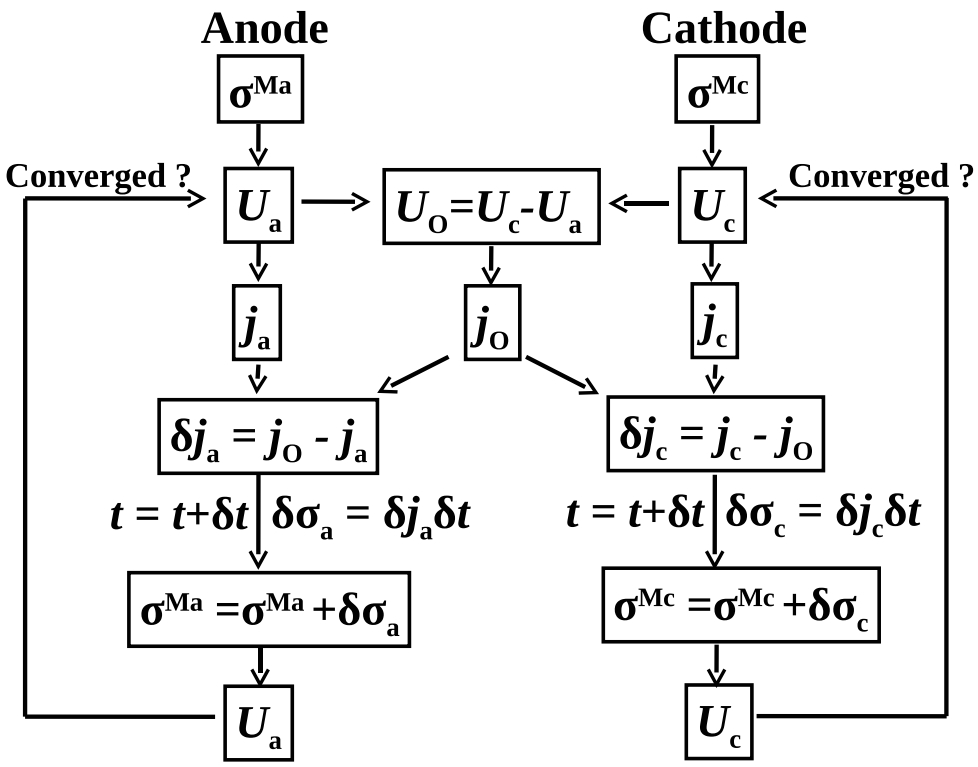

Figure 5.20: A self-consistent simulator for a fuel cell system. σ^{Ma}/σ^{Mc} is the excess surface electron density on anode/cathode; U_a/U_c is the potential for anode/cathode; j_a/j_c is the current density from anode/cathode reaction; U_O/j_O is the output potential/current of the fuel cell; t is time.

Chapter 6

Stability of Catalysts

Besides low ORR activity, low stability of catalysts in PEM fuel cell is another problem. For Pt or Pt alloy nanocrystals, the catalysts are found to lose electrochemical active surface area (ECSA) during long-time operation, resulting in severe catalytic performance degradation. This degradation mainly comes from two correlated effects, the dissolution (corrosion) of Pt atoms and the coarsening of nanocrystals, both of which will be discussed in this chapter.

6.1 Oxide Formation on Pt Surfaces

Pt is usually very stable in acidic electrolyte even at high electrode potential U. Only when $U > U_{\mathrm{eq}}^{\mathrm{Pt}} = 1.08$ V vs. SHE, Pt oxidation as the following equation:

$$\mathrm{Pt} \rightarrow \mathrm{Pt}^{2+} + 2\mathrm{e}^{-} \tag{6.1}$$

is thermodynamically favorable. On the other hand, the norm working potential of PEM fuel cell is only about 0.9 V, so in most cases Pt oxidation and corrosion do not occur. However, when PEM fuel cell is turned on/off, the cathode can go through a potential

cycling in which the maximum potential can reach so high value that oxidation/reduction of Pt can occur as the following:

$$H_2O + Pt \rightleftharpoons \text{Pt oxide} + 2H^+ + 2e^-, \tag{6.2}$$

Meanwhile, the dissolution of Pt atoms from the surface may occur in the reduction process of potential cycling[110, 11], because some Pt atoms have to move from their original lattice sites in the oxidation process and may not come back to these sites during the reversible reduction process. In addition, oxide formations on different Pt facets occur with different rates and reversibility, and this reaction anisotropy can be used as a new method to produce noble metal nanoparticles with stable high-index facets[132]. Therefore, to understand the mechanisms of Pt surface oxide formation on different Pt surfaces is a critical step to increase the stability of Pt catalysts in PEM fuel cell[154].

There have been a lot of experimental studies in this area. For Pt oxidation in anodic polarization, Conway provided a theory which considers OH^* from H_2O dissociation playing an important role in the initial and intermediate steps: OH is first adsorbed on the surface and then it changes the place with surface Pt atoms to form a quasi-3D lattice; final oxide formation is completed by the departure of H^+ from OH^{sub} (here ^{sub} means species absorbed into the surface) inside the lattice structures[4, 20]. Recently Jerkiewicz et al. combined cyclic-voltammetry (CV) and electrochemical quartz-crystal nanobalance (EQCN) to study surface-oxide growth at Pt electrodes[59]. It showed no evidence for OH^{sub} species, because during the whole anodic polarization process the mass of Pt electrode always increases at a constant rate of 15.8 g per two moles electron transferred. So they proposed that when U = 0.85 $\sim$ 1.10 V, the first half monolayer of O* from H_2O dissociation is adsorbed on the surface; when U = 1.20 $\sim$ 1.40 V, subsequent discharge of H_2O leads to the formation of Pt oxide at the top surface. Beside bulk Pt, similar CV

measurements between 0.0 V to ∼1.4 V were performed on different Pt surfaces[132], and it showed that Pt corrosion/dissolution during the oxidation/reduction cycles occurs in various rates ((111) ∼ (100) < (210) and other high-index facets), which suggests that the oxidation process depends on the detailed surface structures. There are also several studies in atmospheric pressure oxidation of Pt (111) and (110) surfaces, and α-PtO_2 as thin as several Å are observed on the top surface[28, 74].

Recently there have been several theoretical studies on Pt oxide. Seriani et al. performed DFT calculations to study the PtO, Pt_3O_4 and PtO_2 bulk oxide phases; they also discussed the relative thermodynamic stability of Pt oxide nanoparticles[117]. Jacob combined DFT calculations and *ab initio* atomistic thermodynamics approaches to obtain the interfacial structure of Pt oxide by studying the bulk and all low-index surfaces of α-PtO_2, β-PtO_2 and PtO oxides[57], whose lattice structures are shown in Fig. 6.1. However, there are few studies on the initial state of oxide formation on clean Pt surfaces. Gu et al. used DFT to study the absorption of atomic oxygen into Pt(100) and Pt(111) surfaces[41]. However, their proposed structures of oxygen interstitial atoms are too unstable to form when $U \sim 1.2$ V during anodic polarization.

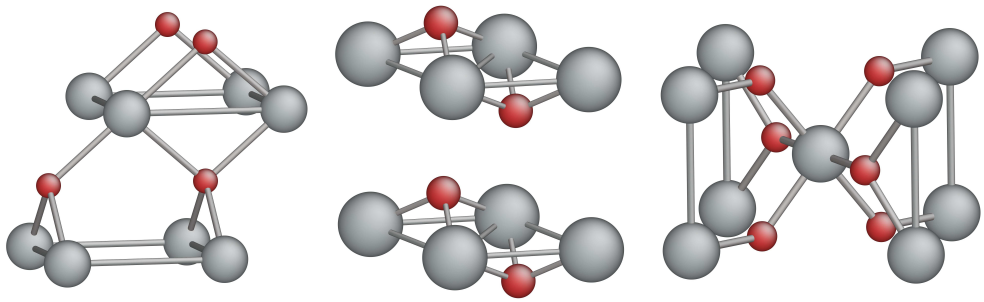

(a) (b) (c)

Figure 6.1: Lattice structures for different types of Pt oxides. (a) PtO in tetragonal lattice. (b) α-PtO_2 in hexagonal lattice. (c) β-PtO_2 in tetragonal lattice.

In this section, we try to clarify several problems. The first problem is how the ox-

idation starts from the initial clean Pt surfaces of different facets. The second one is to understand the atomic structures of thin oxide layers on top of metallic Pt surfaces. The third is how the oxidation processes affect the stability of different Pt surfaces during CV measurements. We perform systematic DFT calculations of oxygen adsorption/absorption under various surface coverages of adsorbed/absorbed oxygen atoms θ_{O^*}. Here we define that the **adsorption** is the accumulation of atoms or molecules on the top of a surface, but **absorption** is the process of atoms or molecules moving into the bulk phase below the top surface layer. The results show that at clean surface, oxygen adsorption is much more energy favorable than its absorption. However, surface adsorption becomes more and more difficult as θ_{O^*} increases; above certain critical oxygen coverage $\theta^{T}_{O^*}$, oxygen atoms prefer to lattice sites below Pt top layer on the surface, which indicates the beginning of absorption and bulk oxidation formation. On different surfaces, this transition coverage $\theta^{T}_{O^*}$ is different. Furthermore, the final product of oxide thin layers and their thermodynamic stabilities also change with the surface structures. We try to explain the anti-corrosion stability differences between various Pt surfaces in potential cycling based on the differences of both $\theta^{T}_{O^*}$ and surface oxide structures.

6.1.1 Computational Method

The calculations are performed using the Vienna Ab-Initio Simulation Package (VASP) [69, 67]. We use projector augmented wave (PAW) potentials[13] with Perdew-Burke-Ernzerhof (PBE) exchange-correlation functional[103] in spin-polarized condition. Both Pt(111) and (100) surfaces are modeled by a six-layer slab with a (2×2) unit cell of total 24 Pt atoms or (3×3) unit cell of total 54 Pt atoms, separated by a 12 Å thick vacuum layer. Oxygen atoms are on one side of the slab; both oxygen and Pt atoms at the top three layers are fully relaxed. Brillouin zone integrations are performed on a grid of $5\times5\times1/3\times3\times1$ $\vec{k}$ points for (2×2)/(3×3) unit cell, using first-order Methfessel-Paxton smearing of σ=0.2

eV. Meanwhile, Pt(210) surfaces is modeled by a nine-layer slab with a $(\sqrt{5} \times 2)$ unit cell of total 36 Pt atoms; its top five layers plus oxygen atoms are fully relaxed, and Brillouin zone integrations are performed on a grid of $4 \times 4 \times 1$ $\vec{k}$ points. The calculations are performed at equilibrium lattice constant of a_0=3.977 Å. Dipole correction[76] on the electric potential and total energy is imposed to eliminate dipole-dipole interactions between image supercells. The accuracy of VASP calculations is also verified by obtaining the formation energy of platinum bulk oxide in different phases. Using the same functional and similar parameters mentioned above, the formation energy, defined as the energy difference between bulk Pt oxide and bulk metallic Pt plus isolated O_2 molecule, is -0.53 eV, -0.69 eV and -0.71 eV per oxygen atom for PtO, α PtO_2 and β PtO_2 respectively (here negative value means oxidation is energy favorable), agreeing with previous DFT calculations and experimental results[57].

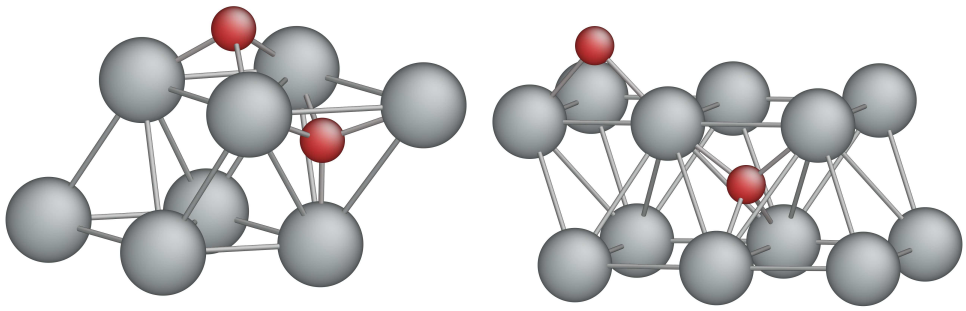

(a) (b)

Figure 6.2: Adsorption and absorption sites on Pt (a) (111) and (b) (100) surfaces.

The adsorption/absorption energies of oxygen atoms strongly depend on the adsorption/absorption lattice sites. On Pt surfaces there are two general types of lattice positions where oxygen atoms can be placed: adsorption sites on the top layer and absorption sites below the top layer, as shown in Fig. 6.2. On Pt (111) surface, the most favorable adsorp-

tion site on top layer for a single oxygen atom is the fcc hollow site in a triangle of three nearest Pt atoms, and the most favorable absorption site between the top and second top Pt layers is the tetrahedral interstitial site just below the hcp hollow site on the top layer; on Pt (100) surface, the most favorable adsorption site is the bridge site between two nearest Pt atoms, and the most favorable absorption site between the top and second top Pt layers is the tetrahedral interstitial site just below the bridge site on the top layer. These most favorable sites are also confirmed by other DFT calculations[41]. Adsorption/absorption sites on Pt (210) surface are much more complicated, which will be discussed in detail in Sec. 6.1.4.

The adsorption/absorption energies of oxygen atoms may also change rapidly with oxygen coverage and chemical potential of oxygen species in the reactants. It is convenient for us to define some uniform criteria to quantitatively determine the adsorption/absorption strengths and compare them with experimental measurements. In general, there are two kinds of oxygen adsorption/absorption reactions under two different environments. At solid-gas interface, it is the following reaction:

$$\mathrm{Pt}_{\theta_{\mathrm{O}^*}} + \frac{1}{2}\mathrm{O}_2 \rightarrow \mathrm{Pt}_{\theta_{\mathrm{O}^*}}\text{-}\mathrm{O}_{\mathrm{ads/abs}}. \tag{6.3}$$

At solid-water interface, the following electrochemical reaction may occur:

$$\mathrm{Pt}_{\theta_{\mathrm{O}^*}} + \mathrm{H_2O} \rightarrow \mathrm{Pt}_{\theta_{\mathrm{O}^*}}\text{-}\mathrm{O}_{\mathrm{ads/abs}} + 2\mathrm{H}^+ + 2\mathrm{e}^-_{E=-eU} \tag{6.4}$$

Here $\mathrm{Pt}_{\theta_{\mathrm{O}^*}}$ stands for the Pt surface with adsorbed oxygen coverage θ_{O^*}. This reaction may be accomplished in two steps. First, hydroxyl from water dissociation is adsorbed on Pt surface as the following:

$$\mathrm{Pt}_{\theta_{\mathrm{O}^*}} + \mathrm{H_2O} \rightarrow \mathrm{Pt}_{\theta_{\mathrm{O}^*}}\text{-}\mathrm{OH}_{\mathrm{ads}} + \mathrm{H}^+ + \mathrm{e}^-_{E=-eU} \tag{6.5}$$

Then, an adsorbed or absorbed oxygen atom appears from further dissociation of adsorbed hydroxyl:

$$\mathrm{Pt}_{\theta_{\mathrm{O}^*}}\text{-}\mathrm{OH}_{\mathrm{ads}} \rightleftharpoons \mathrm{Pt}_{\theta_{\mathrm{O}^*}}\text{-}\mathrm{O}_{\mathrm{ads/abs}} + \mathrm{H}^+ + \mathrm{e}^-_{E=-eU} \tag{6.6}$$

However, an accurate calculation of adsorbed hydroxyl needs a precise treatment of water solvation effect, which results from complex interactions between adsorbed hydroxyl and water molecules on or close to the electrode surface. To simplify calculation models and seize the intrinsic mechanism of surface oxidation, here we only study the reactions in Eq. 6.3 and 6.4.

In the real Pt surfaces with huge surface areas, θ_{O^*} is almost unchanged before and after one oxygen atom adsorption/absorption, which can not be valid in our limited DFT unit cells. So we calculate the reaction (free)-energy for the following two reactions:

$$\text{Pt-}n\mathrm{O}^* + \frac{1}{2}\mathrm{O}_2 \rightarrow \text{Pt-}n\mathrm{O}^*\text{-}\mathrm{O}_{\mathrm{ads/abs}} \tag{6.7}$$

and

$$\text{Pt-}n\mathrm{O}^* + \mathrm{H}_2\mathrm{O} \rightarrow \text{Pt-}n\mathrm{O}^*\text{-}\mathrm{O}_{\mathrm{ads/abs}} + 2\mathrm{H}^+ + 2\mathrm{e}^-_{E=-eU} \tag{6.8}$$

Here Pt-nO* stands for Pt surface unit cell with n oxygen atoms adsorbed on the top layer, and the (n+1)$^{\mathrm{th}}$ oxygen atom can be at either adsorption site or absorption site. We define the energy change of the reaction in Eq. 6.7, $E^{\mathrm{O}}_{\mathrm{diff}}$, corresponding to the adsorption/absorption energy for single oxygen atom at Pt surface with $\theta_{\mathrm{O}^*} = (n+1)/M$, where M is number of primitive cells in a unit cell of DFT calculations. Here "**diff**" means it is a differential other than average adsorption/absorption energy. This differential value is closer to experimental measurements, because the heat generated by the adsorption/absorption of one oxygen atom is quickly dissipated so that it does not affect the adsorption/absorption of next atom. Reaction in Eq. 6.8 is more complex since it involves liquid $\mathrm{H}_2\mathrm{O}$, hydrated

protons and electrons with energies depending on the electrode potential U. In order to compare directly with experiments, we need to calculate its reaction free energy $\delta G^{\mathrm{O}}_{\mathrm{diff}}$, or we can define $U^{\mathrm{O}}_{\mathrm{diff}}$, the equilibrium electrode potential to make $\delta G^{\mathrm{O}}_{\mathrm{diff}}$ equal to zero. It stands for the minimum possible potential, above which reaction of Eq. 6.4 or 6.8 will occur at Pt surface with oxygen coverage $\theta_{\mathrm{O}^*} = (n+1)/M$. In addition, $E^{\mathrm{O}}_{\mathrm{diff}}$ and $U^{\mathrm{O}}_{\mathrm{diff}}$ are linearly related with each other because of the similarity between Eq. 6.7 and 6.8.

Practically, it is difficult to use first-principles methods to calculate the free energy of protons or electrons, because there are long range of electric and solvation fields involved. So here we just use the method proposed by Nørskov[94]: instead of calculating the free energies of protons and electrons, we can use free energy of hydrogen oxidation reaction (HOR).

$$\mathrm{H_2} \rightarrow 2\mathrm{H^+} + 2\mathrm{e^-} \tag{6.9}$$

Its reaction free energy is $\delta G = 2e\cdot(U$ vs. SHE) at standard conditions. So we just need to calculate the free energy of the following reaction:

$$\text{Pt-}n\mathrm{O^*} + \mathrm{H_2O} \rightarrow \text{Pt-}n\mathrm{O^*\text{-}O_{ads/abs}} + \mathrm{H_2} \tag{6.10}$$

As proposed by Nørskov[94], the free energy of H_2O and H_2 are calculated by two steps. First, the absolute energies of isolated H_2O and H_2 molecules are calculated by VASP with PAW-PBE potentials; second, all the other free energy corrections are calculated based on classical statistical mechanics, as shown in Table 6.1. Here we take the partial pressure of H_2 as 1.0×10^5 Pa, and the the partial pressure of H_2O as 100 Pa, which is the vapor pressure of liquid H_2O when T = 300 K. The free energies of surface and surface plus adsorbates are approximated as the energies calculated by VASP with PAW-PBE potentials plus the corrections of zero point vibration energies (ZPE) of adsorbates. ZPE is found to be 0.07 eV for a single oxygen atom adsorbed at either fcc site on Pt (111) surface or bridge

site on Pt (100) surface. We also use this ZPE value as an approximation for the oxygen atom in absorption state. Other possible terms, such as configuration entropies, should be small values at T = 300 K ($k_{\mathrm{B}}T \sim 0.025$ eV). By using ZPE and free energies from Table 6.1, we can get the simple relation between $E^{\mathrm{O}}_{\mathrm{diff}}$ and $U^{\mathrm{O}}_{\mathrm{diff}}$ as the following:

$$U^{\mathrm{O}}_{\mathrm{diff}}[\mathrm{V\ vs.\ SHE}] = (E^{\mathrm{O}}_{\mathrm{diff}}[\mathrm{eV}] + 2.553[\mathrm{eV}])/(2e) \tag{6.11}$$

In the following sections, $E^{\mathrm{O}}_{\mathrm{diff}}$ and $U^{\mathrm{O}}_{\mathrm{diff}}$ on different surfaces with various adsorbed oxygen coverage θ_{O^*} are calculated. The results are discussed in order to understand the initial steps of Pt oxidation and stability in polarization cycling.

Table 6.1: Energies E and free energies G of molecules from DFT calculations plus free energy corrections at certain partial pressure p and temperature T.

	E[eV]	p [Pa]	T [K]	G[eV]
O_2	-9.8480	1.0×10^5	300	-10.2998
H_2	-6.7593	1.0×10^5	300	-6.7959
H_2O	-14.2199	100	300	-14.2031

6.1.2 Oxidation on Pt(111) Surface

(111) surface is the most stable facet of FCC lattice and contributes most of surface areas for bulk Pt. Coverage-dependent oxygen adsorptions were calculated by first-principles methods[35], which showed that all oxygen atoms prefer fcc hollow sites than any other adsorption sites on top layer of Pt (111) surface no matter how large θ_{O^*} is. Besides adsorption, the absorption of single oxygen atom on clean Pt (111) surface was also calculated[41], which showed that even at the most favorable site, tetrahedral site as shown in Fig. 6.2, oxygen absorption is still $\sim$ 2 eV unstable than its adsorption process. It suggests that on clean Pt (111) surface it is almost impossible for an oxygen atom to diffuse into the Pt bulk lattice. On the other hand, some thin oxide layers were found by oxidation of Pt (111) surface

when exposed to O_2 gas at high temperature, and stable structures of α-PtO_2 layer on Pt (111) surface were proposed by theoretical calculations[28]. So there may be a transition point of oxygen coverage, $\theta^{T}_{O^*}$, above which oxygen absorption becomes more energetically favorable than further oxygen adsorption on the top layer, indicating the beginning of bulk Pt oxide formation.

Oxygen adsorption and absorption on Pt (111) surface

In order to obtain $\theta^{T}_{O^*}$, we first calculate the changes of E^{O}_{diff} and U^{O}_{diff} on (2×2) unit cell of Pt (111) surface. Oxygen atoms are added one after another on the cell, so θ_{O^*} increases in a increment of $\frac{1}{4}$ monolayer (ML). The final results are shown Fig. 6.3 (a): E^{O}_{diff}/ U^{O}_{diff} for the first oxygen adsorption is -1.18 eV/0.68 V; because of lateral repulsion, E^{O}_{diff}/ U^{O}_{diff} for oxygen adsorption increases almost linearly as θ_{O^*} increases. On the other hand, E^{O}_{diff}/ U^{O}_{diff} for oxygen absorption has much smaller dependence on θ_{O^*} and just oscillates around the values at low θ_{O^*}. As a result, when θ_{O^*} is larger than $\frac{3}{4}$ ML, absorption of an oxygen atom in tetrahedral interstitial site, as shown in Fig. 6.4 (h), is more favorable than its adsorption at fcc site on the top layer, as shown in Fig. 6.4 (d).

However, because (2×2) Pt (111) surface is a small unit cell so that each additional oxygen atom would result in large coverage increment ($\frac{1}{4}$ ML), we repeat the similar calculations on (3×3) Pt (111) surface, as shown in Fig. 6.3 (b). The results are similar with (2×2) case but the detail transition point changes. Starting from clean surface, E^{O}_{diff}/ U^{O}_{diff} increases linearly with θ_{O^*} until θ_{O^*} reaches $\frac{1}{3}$ ML, where there is a small discontinuous increment in E^{O}_{diff}/ U^{O}_{diff}. This discontinuity results from the special configuration of O^* when $\theta_{O^*} = \frac{1}{3}$ ML, as shown in Fig. 6.5 (b), in which every Pt atom on the top layer have one adsorbed oxygen atom as its nearest neighbor. When θ_{O^*} continuously increases, E^{O}_{diff}/ U^{O}_{diff} still increases linearly until θ_{O^*} reaches $\frac{2}{3}$ ML, as shown in Fig. 6.5 (d), in which every Pt atom on the top layer have two adsorbed oxygen atoms as its nearest neighbors. At

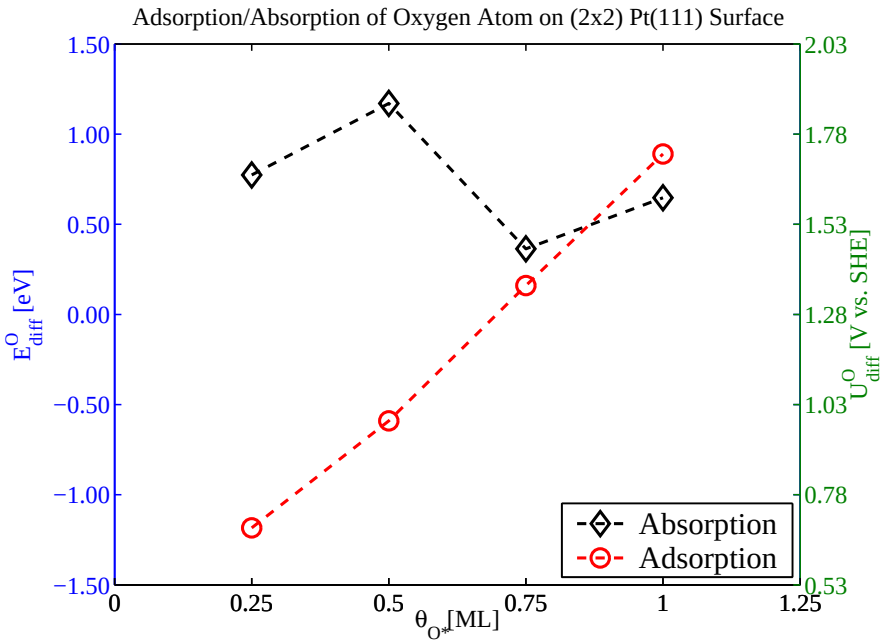

(a)

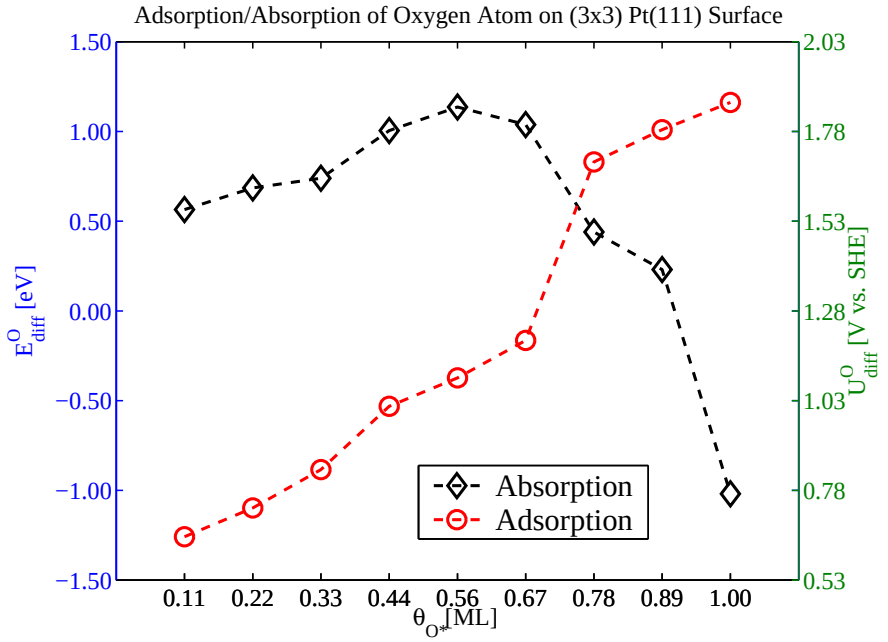

(b)

Figure 6.3: Changes of E^{O}_{diff}/ U^{O}_{diff} for oxygen adsorption/absorption on Pt (111) surface with oxygen coverage θ_{O^*}. The values of E^{O}_{diff} and U^{O}_{diff} are shown on the left and right y-axis, respectively. (a) Adsorption/absorption of oxygen atoms on (2×2) Pt (111) surface. The corresponding atomic configurations are shown in Fig. 6.4. (b) Adsorption/absorption of oxygen atoms on (3×3) Pt (111) surface. The corresponding atomic configurations are shown in Fig. 6.5.

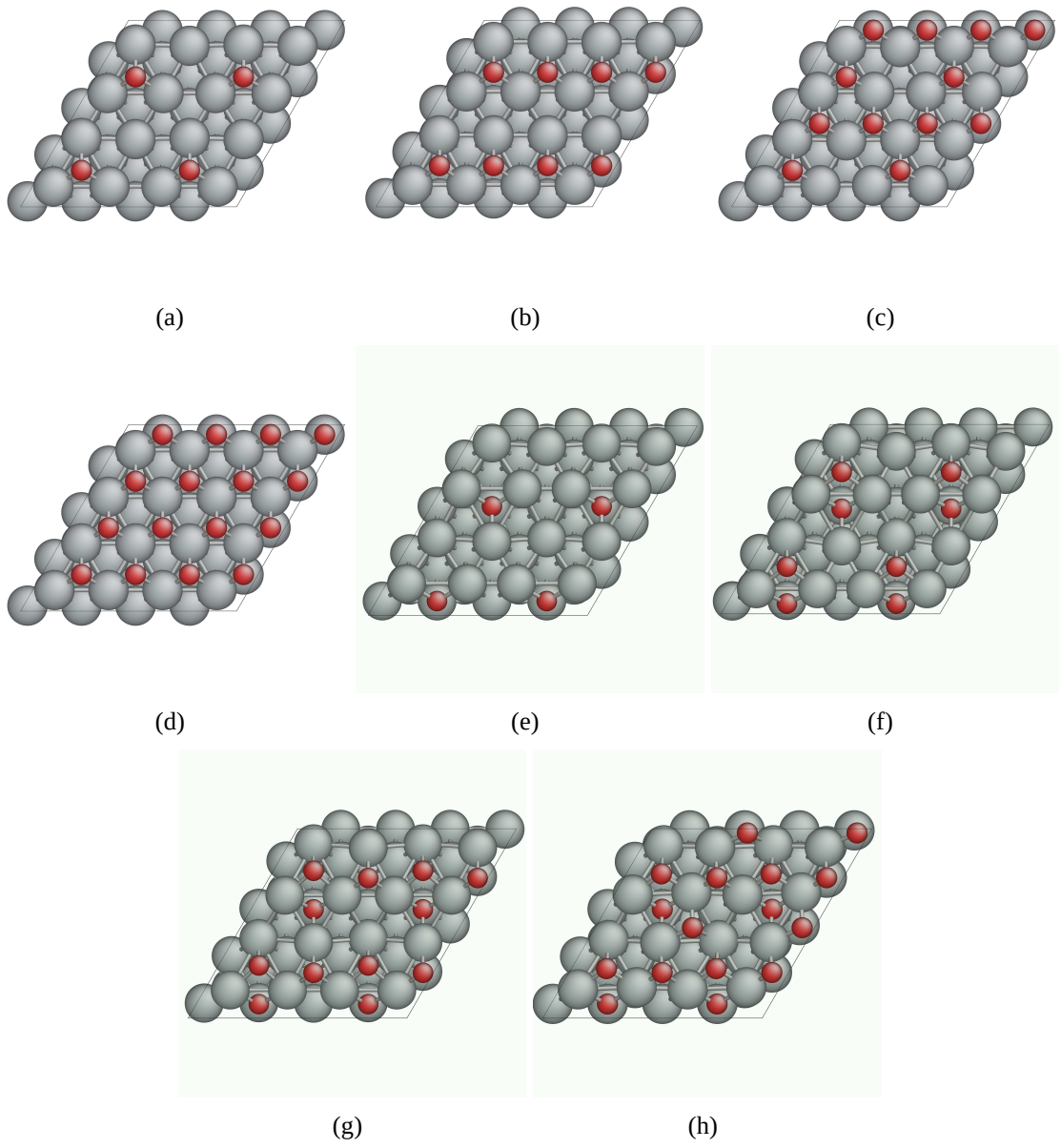

Figure 6.4: Configurations of adsorption/absorption of oxygen atoms on (2×2) Pt (111) surface. (a)-(d) Oxygen adsorption configurations when $\theta_{O^*} = \frac{1}{4}, \frac{1}{2}, \frac{3}{4}$ and 1 ML. (e)-(h) Absorption of one oxygen atom into tetrahedral site below the top hcp hollow site when $\theta_{O^*} = \frac{1}{4}, \frac{1}{2}, \frac{3}{4}$ and 1 ML.

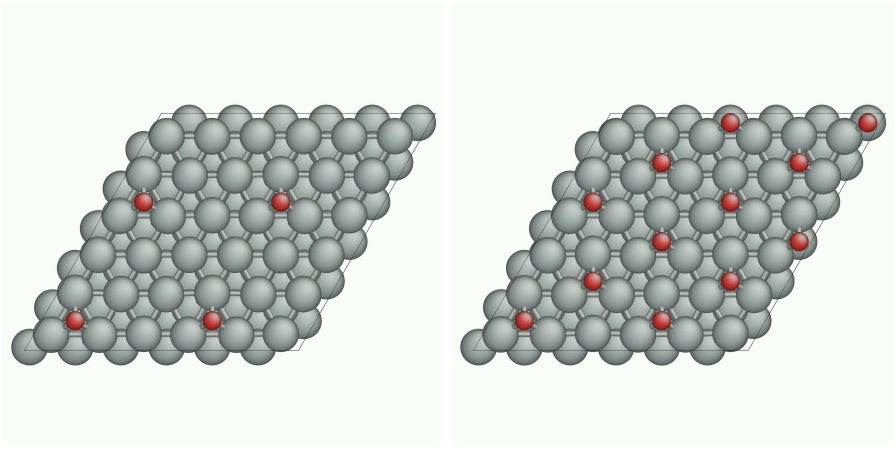

(a) (b)

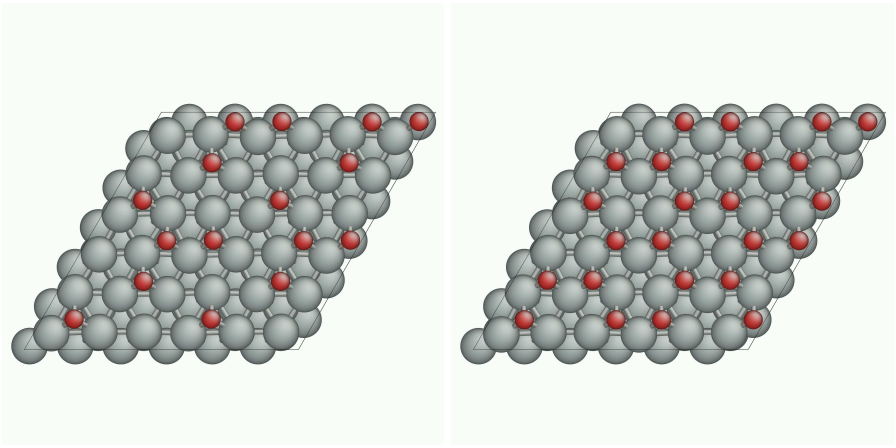

(c) (d)

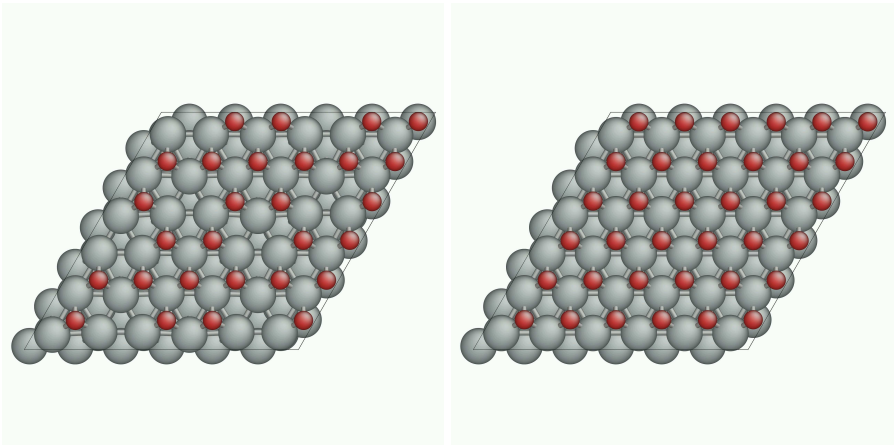

(e) (f)

Figure 6.5: Configurations of adsorptions of oxygen atoms on (3×3) Pt (111) surface when $\theta_{O^*} = \frac{1}{9}, \frac{1}{3}, \frac{4}{9}, \frac{2}{3}, \frac{7}{9}$ and 1 ML as shown from (a) to (f).

this critical θ_{O^*}, the E^{O}_{diff}/ U^{O}_{diff} to add one more oxygen atom at an adsorption site would suddenly increase more than 1 eV/0.5 V, even higher than E^{O}_{diff}/ U^{O}_{diff} of the corresponding absorption process for this oxygen atom. For this reason, it can be concluded that when θ_{O^*} is larger than $\frac{2}{3}$ ML, which corresponds to electrode potential U higher than 1.19 V for water dissociation reaction of Eq. 6.4, Pt (111) surface begins to transform into bulk Pt oxide. If we force all oxygen atoms still at adsorption sites above this critical $\theta_{O^*} = \frac{2}{3}$ ML, the energy difference between absorption and adsorption becomes more and more negative, as shown in Fig. 6.3 (b), indicating a stronger driving force for bulk oxide formation.

Epitaxial Oxide Layer on Pt (111) Surface

Once one oxygen atom is absorbed into the bulk lattice below (111) top layer, it usually results in large lattice distortion and accelerates the process of further oxygen absorption. For example, when there are 4 oxygen atoms adsorbed on (2×2) Pt (111) surface, as shown in Fig. 6.4 (d), the total energy will decrease 0.24 eV to transfer one oxygen atom from adsorption into absorption site, as shown in Fig. 6.4 (h); to transfer one more oxygen atom from adsorption into absorption site, the total energy drop would increase to 1.08 eV. This stable structure with $\frac{1}{2}$ ML adsorbed and $\frac{1}{2}$ ML absorbed oxygen atoms is shown in Fig. 6.6 (a) and (b). It can be seen that the distance between top and second-top Pt layers is much larger than its counterpart in pure metallic Pt, which is another indication of bulk oxide formation.

If more oxygen atoms are placed on Pt surface, the bulk oxide structure would continue to grow. When θ_{O^*} = 2 ML, if we force all Pt atoms to stay at or near their original lattice sites, the stable configuration would be 1 ML oxygen adsorbed on fcc sites and 1 ML oxygen absorbed on the tetrahedral sites below the nearby hcp hollow sites, which is just one (001) layer of α-PtO_2, as shown in Fig. 6.6 (c) and (d). Its formation energy from isolated O_2 molecule is -0.30 eV per oxygen atom, which is much more positive than

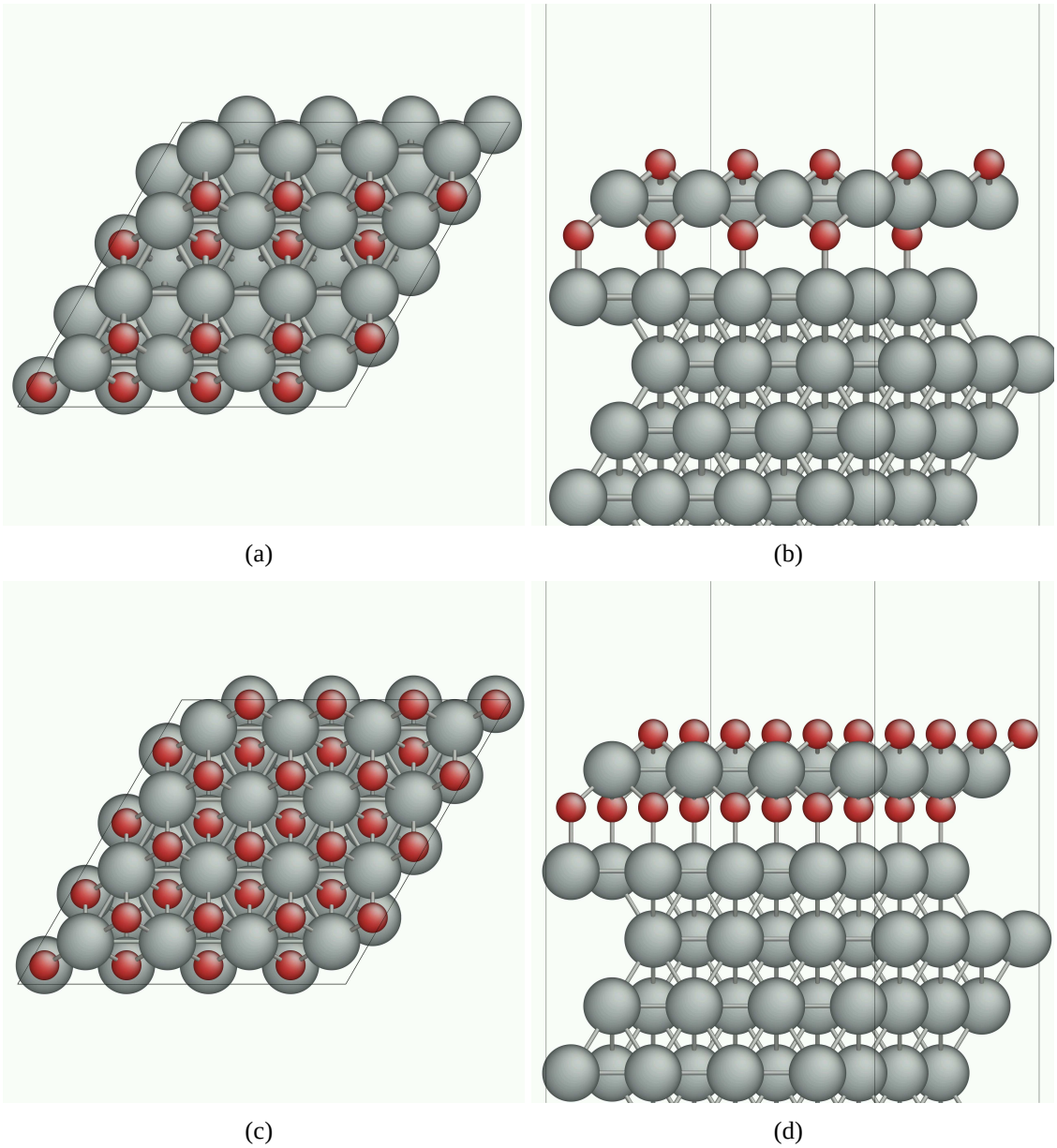

Figure 6.6: Epitaxial Oxide Layer on Pt (111) Surface. (a)-(b) top and side view of a thin oxide layer on Pt (111) surface with $\frac{1}{2}$ ML on fcc sites and $\frac{1}{2}$ ML at tetrahedral sites below the hcp sites. (c)-(d) top and side view of a thin oxide layer on Pt (111) surface with 1 ML on fcc site and 1 ML at tetrahedral sites.

the formation energy of pure bulk α-PtO_2 (-0.69 eV). This formation energy difference suggests significant instability of thin α-PtO_2 layer relative to bulk α-PtO_2. This instability may come from the large compressive strain applied on thin layer of α-PtO_2 by metallic Pt substrate. In bulk α-PtO_2, Pt-Pt bond distance on (001) surface is 3.14 Å from our DFT calculations, while on Pt (111) surface Pt-Pt distance is only 2.81 Å. Another difference is that in bulk α-PtO_2, which has hexagonal lattice, it is A-A stacking along [001] direction and the layer-layer distance is quite large (4.09 Å in our DFT calculation), while Pt (111) surface is A-B-C stacking along [001] direction, and two nearby Pt layers have a distance of 3.84 Å, as shown in Fig. 6.6 (d). Because of these lattice mismatch and energy instability, there will be significant lattice distortion occurring on this thin-oxide layer. A possible case is that this coherent Pt (111) + α-PtO_2 (001) interface structure would change into semi-coherent or incoherent structures, where the thin α-PtO_2 layer has lattice constant close to its bulk value in order to relieve the strong compressive strain energy; but the extra Pt atoms have to be repelled from this α-PtO_2 layer and accumulate as islands or clusters structures on the surface. These extra Pt islands or clusters may be very unstable and result in Pt atom dissolution in polarization cycling.

6.1.3 Oxidation on Pt(100) Surface

(100) is another common low-index surface. Because of low coordination number (CN) ($CN_{(111)}$=9 and $CN_{(100)}$=8 for FCC lattice), the adsorption energy for certain adsorbate may be stronger on (100) surface than (111) surface. This is supported by the cyclic voltammetry measurements on different Pt surfaces[79], which showed that the peak corresponding to water dissociation reactions (Eq. 6.5 and 6.6) was shifted to much less positive potential on Pt (100) surface than Pt (111) surface. The adsorption and absorption of a single oxygen atom on clean Pt (100) surface were also calculated; the results showed that even at the most favorable site, the tetrahedral site as shown in Fig. 6.2 (b), oxygen ab-

sorption is still $\sim$ 2 eV unstable than the adsorption on bridge site. In order to understand the initial step of oxide formation, we perform the similar calculations and analyses on Pt (100) surface as (111) in Section 6.1.2.

Oxygen adsorption and absorption on Pt (100) surface

Adsorption and absorption of oxygen atoms on (2×2) Pt (100) surface are shown in Fig 6.7 (a) and 6.8. In this unit cell, each oxygen atom is adsorbed on the most favorable adsorption site, the bridge site between two nearest Pt atoms. Each Pt atom shares 4 bridge sites with its 4 nearest Pt neighbors at the same layer, so that the maximum coverage of oxygen atoms at bridge sites of (100) surface is 2 ML. Different from Pt (111) surface, $E^{\mathrm{O}}_{\mathrm{diff}}$/ $U^{\mathrm{O}}_{\mathrm{diff}}$ for oxygen adsorption increases gradually without significant discontinuous increments until θ_{O^*} reaches 1 ML. Above this critical value, there is a huge jump in $E^{\mathrm{O}}_{\mathrm{diff}}$/ $U^{\mathrm{O}}_{\mathrm{diff}}$, as large as 2.57 eV/1.28 V. This rapid increment also results from the adsorbed oxygen arrangement when $\theta_{\mathrm{O}^*} = 1$ ML, as shown in Fig. 6.8 (d), where each Pt atom already has two oxygen atoms as nearest neighbors.

We also calculate the different absorption energies of single oxygen atom at tetrahedral interstitial sites below top Pt layer. Agreeing with the previous DFT calculation[41], at low θ_{O^*}, $E^{\mathrm{O}}_{\mathrm{diff}}$/ $U^{\mathrm{O}}_{\mathrm{diff}}$ for oxygen absorption is much higher than its adsorption counterpart. Similar to Pt (111) surface, the relative stability of absorbed oxygen atom to the adsorbed one increases when θ_{O^*} increases, as shown in Fig. 6.7 (a) and Fig. 6.8 (f)-(j), because $E^{\mathrm{O}}_{\mathrm{diff}}$/ $U^{\mathrm{O}}_{\mathrm{diff}}$ for oxygen absorption, unlike its adsorption process, does not strongly depend on θ_{O^*}. For this reason, after the huge increment of $E^{\mathrm{O}}_{\mathrm{diff}}$/ $U^{\mathrm{O}}_{\mathrm{diff}}$ for oxygen adsorption when adsorbed oxygen coverage is larger than 1 ML, its absorption process becomes energy favorable. This transition surface coverage $\theta^{\mathrm{T}}_{\mathrm{O}^*}$ is higher than the corresponding value on Pt (111) surface (less than 1 ML in (2×2) unit cell), which may be attributed to the smaller adsorption site density: a (1×1) Pt (100) surface has an area of 7.91 $\mathrm{\AA}^2$ while it is 6.85

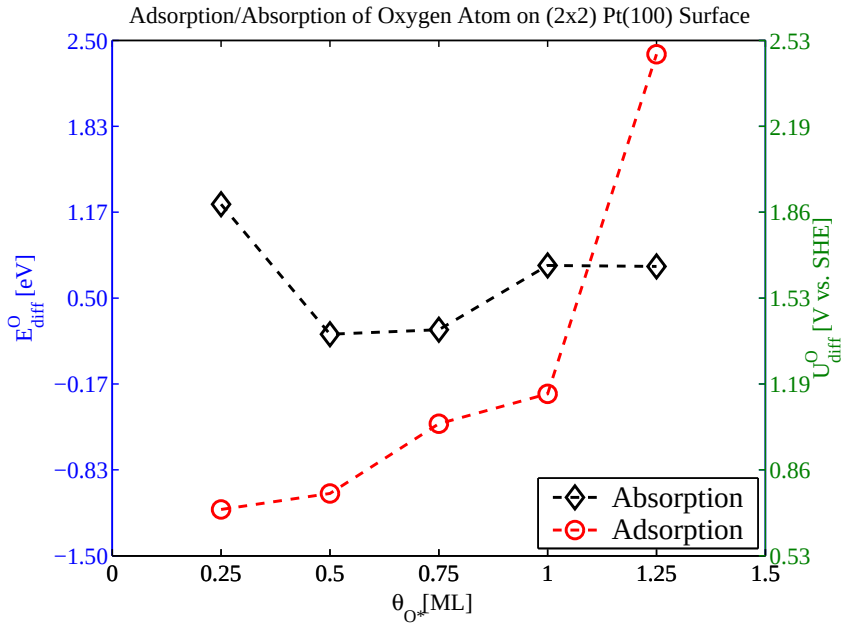

(a)

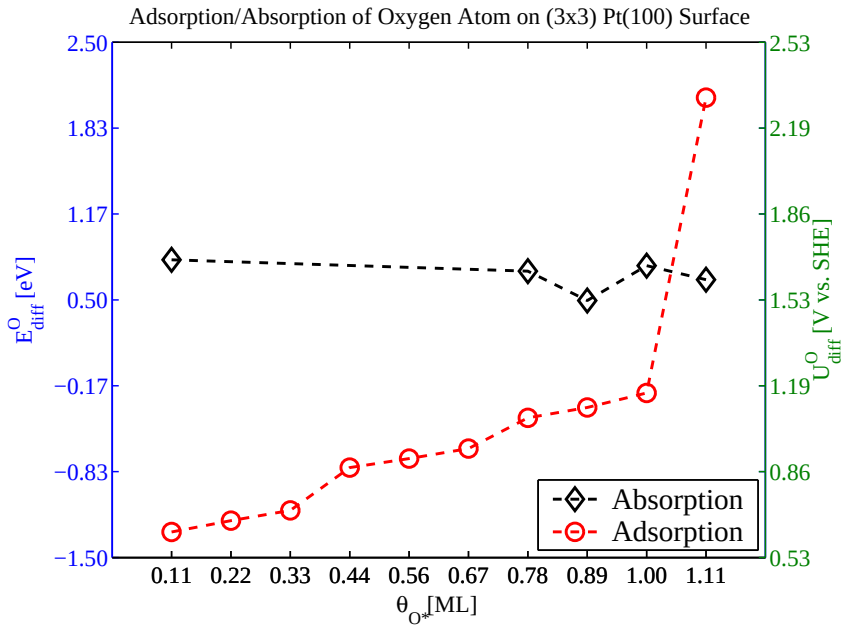

(b)

Figure 6.7: Changes of E^{O}_{diff}/ U^{O}_{diff} for oxygen adsorption/absorption at Pt (100) surface with oxygen coverage θ_{O^*}. The values of E^{O}_{diff} and U^{O}_{diff} are shown on the left and right y-axis, respectively. (a) Adsorption/absorption of oxygen atoms on (2×2) Pt (100) surface. The corresponding atomic configurations are shown in Fig. 6.8. (b) Adsorption/absorption of oxygen atoms on (3×3) Pt (100) surface. The corresponding atomic configurations are shown in Fig. 6.9.

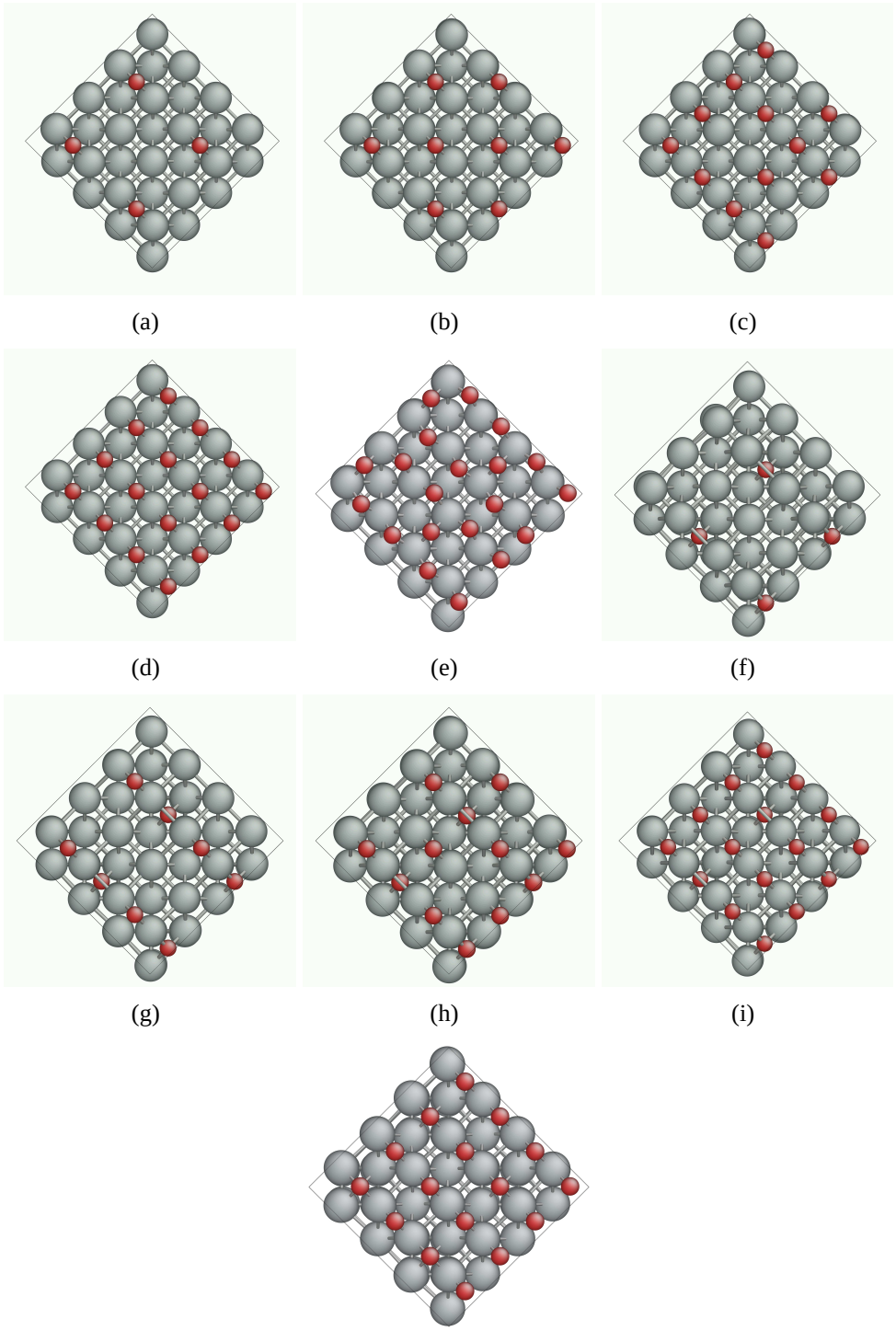

Figure 6.8: Configurations of adsorption/absorption of oxygen atoms on (2×2) Pt (100) surface. (a)-(e) Oxygen adsorption configurations when θ_{O^*} = $\frac{1}{4}$, $\frac{1}{2}$, $\frac{3}{4}$, 1 and $\frac{5}{4}$ ML. (f)-(j) Absorption of one oxygen atom into tetrahedral site below the top hcp hollow site when θ_{O^*} = $\frac{1}{4}$, $\frac{1}{2}$, $\frac{3}{4}$, 1 and $\frac{5}{4}$ ML.

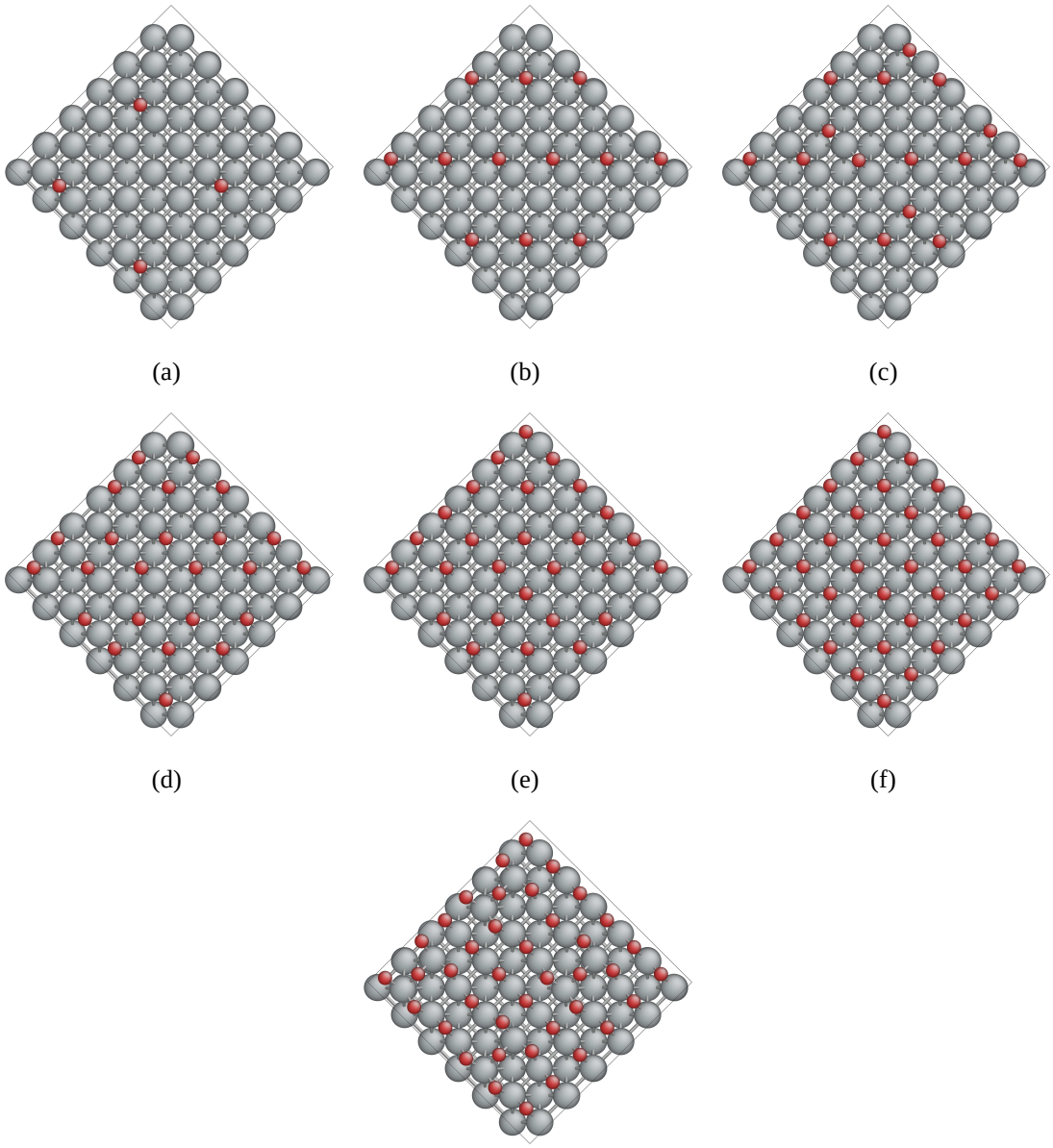

Figure 6.9: Configurations of adsorptions of oxygen atoms on (3×3) Pt (100) surface when θ_{O^*} = $\frac{1}{9}$, $\frac{1}{3}$, $\frac{4}{9}$, $\frac{2}{3}$, $\frac{7}{9}$, 1 and $\frac{10}{9}$ ML as shown from (a) to (g).

$Å^2$ for Pt (111) surface, so there is less lateral repulsion for nearby adsorbed oxygen atoms under the same θ_{O^*} on Pt (100) surface.

To obtain more accurate results of E^O_{diff}/ U^O_{diff} dependence on θ_{O^*}, (3×3) Pt (100) surface is also used and the results are shown in Fig. 6.7 (b) and 6.9. Similar to (3×3) Pt (111) surface, E^O_{diff}/ U^O_{diff} increases linearly at low θ_{O^*} with small discontinuous increments when $\theta_{O^*} = \frac{1}{3}$ and $\frac{2}{3}$ ML. These discontinuities also result from the specific geometric arrangements on Pt (100) surface: when $\theta_{O^*} < \frac{1}{3}$ ML there is available bridge adsorption site where neither of two nearest Pt atoms have adsorbed oxygen atoms as nearest neighbors, as shown in Fig. 6.9 (a) and (b); when $\frac{1}{3}$ ML $< \theta_{O^*} < \frac{2}{3}$ ML for every bridge adsorption site, there is at least one nearest Pt atom that has one adsorbed oxygen atom as nearest neighbor, as shown in Fig. 6.9 (c) and (d); when $\frac{2}{3}$ ML $< \theta_{O^*} < 1$ ML for every bridge adsorption site, both two nearest Pt atoms have at least one adsorbed oxygen atom as nearest neighbor, as shown in Fig. 6.9 (e) and (f). Finally, the same as (2×2) Pt (100) surface, its absorption process becomes energy favorable when adsorbed oxygen coverage is larger than 1 ML, corresponding to $U^O_{diff} = 1.17$ V, which is very close to the value on (3×3) Pt (111) surface (1.19 V). Since most of surfaces on Pt crystals are these two low-index surfaces, it means that bulk oxide structure with oxygen inside Pt lattice starts to form on bulk metallic Pt when U is larger than 1.2 V, agreeing with experimental measurement[59].

Epitaxial Oxide Layer on Pt (100) Surface

Similar as Pt (111) surface, this bulk oxide structure will continue to grow when more oxygen atoms are deposited in the tetrahedral sites below top Pt layer. As shown in Fig. 6.10, when oxygen coverage reaches to 2 ML, half of the oxygen atoms stay at the bridge sites on top of surface, and half of the oxygen atoms stay at the tetrahedral interstitial sites just below the top oxygen atoms, which is just like two epitaxial layers of (001) PtO. Its formation energy from isolated O_2 molecule is -0.51 eV per oxygen atom, very close to

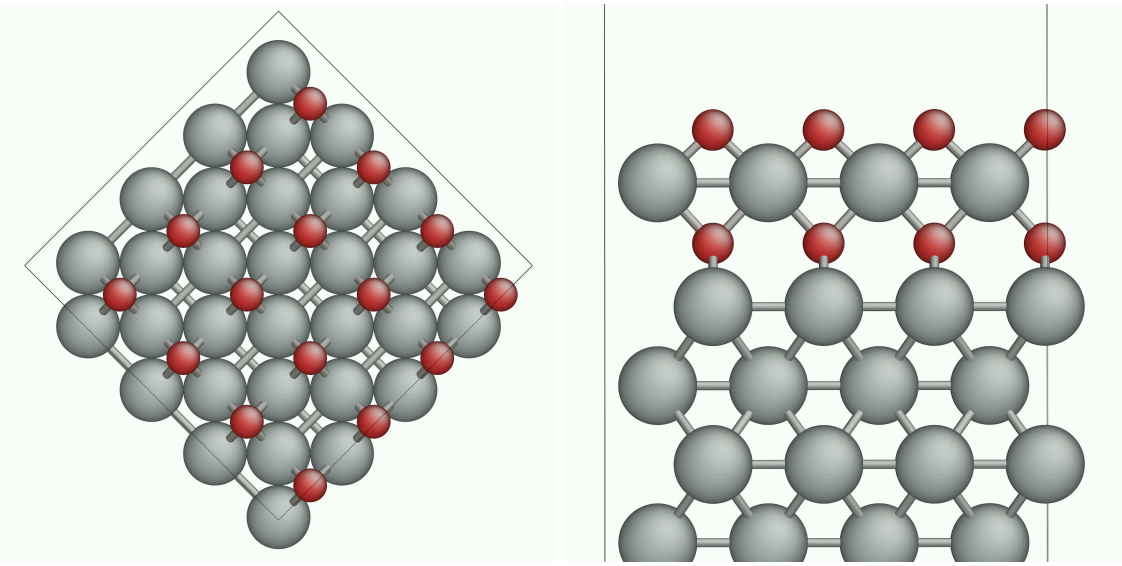

(a) (b)

Figure 6.10: Epitaxial Oxide Layer on Pt (100) Surface. (a)-(b) top and side view of a thin oxide layer on Pt (100) surface with 1 ML at bridge sites and 1 ML at tetrahedral sites just below the oxygen atoms on top layer.

bulk PtO atoms (-0.53 eV) and much stronger than the case of a (001) α-PtO_2 layer on Pt (111) surface (-0.31 eV), which suggests higher stability of this coherent epitaxial structure. Geometrically, although Pt-Pt bond length on Pt (100) surface is still much shorter than bulk PtO (2.81 vs. 3.12 Å), the layer-layer distance between these two PtO layers on top of Pt (100) surface is much larger than the corresponding value in bulk PtO(3.15 vs. 2.70 Å), so the planar compressive strain energy applied on these two PtO layers is significantly reduced. This high stability for this coherent epitaxial layer may result from the structural similarity between PtO (001) surface and Pt (100) surface, because both of them have A-B stacking sequence as shown in Fig. 6.1 (a) and Fig. 6.10 (a). This stable coherent structure indicates that when a thin oxide layer is produced on Pt (100) surface, all Pt atoms can still stay on the same lattice positions as metallic Pt other than extra clusters formation as Pt (111) surface, which increases its stability in oxidation/reduction cycling.

6.1.4 Oxidation on Pt(210) Surface

Pt (210) surface is a typical high-index surface, and its lattice structure is shown in Fig. 6.11. It can be regarded as narrow (100) terraces with 1-atom-step-height (010) steps, as shown in Fig. 6.11 (a). There are three types of unsaturated surface Pt atoms with different coordination numbers (CN): type A with CN = 6, type B with CN = 9 and type C with CN = 11. Type A atoms are located on the edge of the (010) steps, while type B and C are in the terraces. In the following all the oxygen adsorption/absorption calculations are performed in rectangular ($\sqrt{5}\times 2$) unit cell as shown in Fig. 6.11 (b).

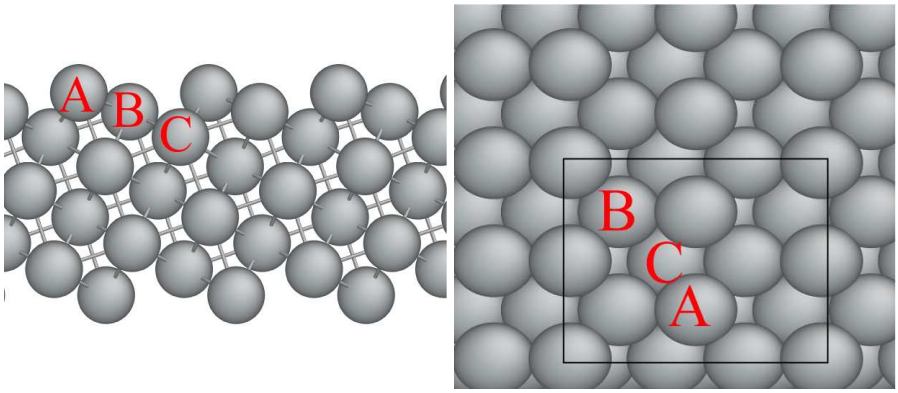

(a) (b)

Figure 6.11: Lattice structures of Pt (210) surface. (a) Side view of Pt (210) surface, composed of small Pt (100) facets. (b) Top view of Pt (210) surface, where $\sqrt{5}\times 2$ unit cell is shown in solid-line rectangle. There are also signs for Pt surface atoms with different CNs: A with CN = 6, B with CN = 9 and C with CN = 11.

The adsorption of oxygen atoms and the corresponding $E^{\mathrm{O}}_{\mathrm{diff}}$/ $U^{\mathrm{O}}_{\mathrm{diff}}$ on Pt (210) surface are shown in Fig. 6.12 and 6.13. At low θ_{O^*}, oxygen is initially adsorbed on Pt atoms with lower CN. As shown in Fig. 6.12 (a) and (b), the most favorable adsorption site for a single oxygen atom at low coverage (θ_{O^*} = $\frac{1}{4}$ and $\frac{1}{2}$) is the hollow site in the triangle composed of two nearest type A atoms and one type B atom. Its adsorption energy is -1.281 eV, $\sim$ 0.1 eV stronger than Pt (111) surface. When increasing θ_{O^*} to 1ML, the most stable configuration

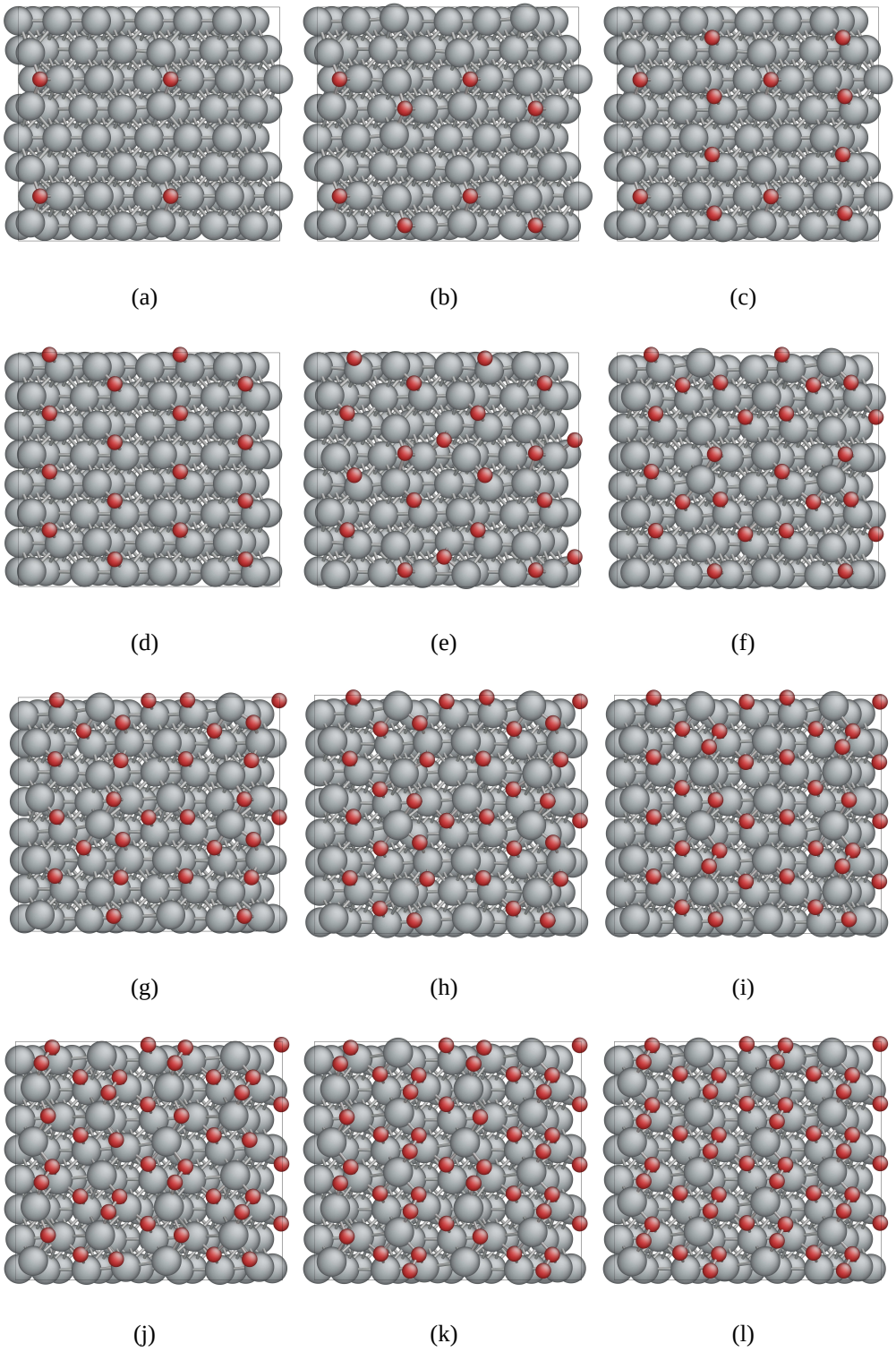

Figure 6.12: Configurations of adsorptions of oxygen atoms on ($\sqrt{5}\times2$) Pt (210) surface. (a)-(l) Oxygen adsorption configurations when θ_{O^*} increase from $\frac{1}{4}$ to 3 ML by constant increment of $\frac{1}{4}$ ML.

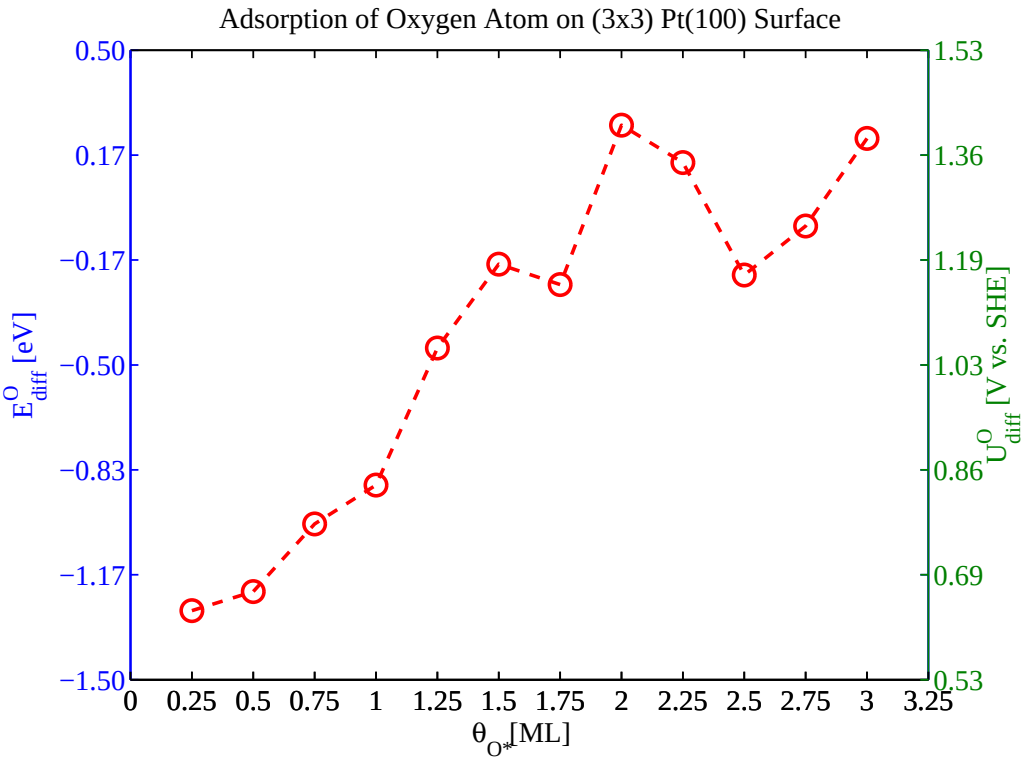

Figure 6.13: Changes of $E^{\mathrm{O}}_{\mathrm{diff}}$/ $U^{\mathrm{O}}_{\mathrm{diff}}$ for oxygen adsorption at Pt (210) surface with oxygen coverage θ_{O^*}. The values of $E^{\mathrm{O}}_{\mathrm{diff}}$ and $U^{\mathrm{O}}_{\mathrm{diff}}$ are shown on the left and right y-axis, respectively. The corresponding atomic configurations are shown in Fig. 6.12.

shows that each oxygen atom changes its adsorption site from the hollow site to nearby bridge site between one type A atom and one type B atom. This position shift occurs because it reduces the lateral repulsion energy between nearby oxygen atoms, otherwise they would connect with the same type A atom, which would largely increase the repulsion energies[35]. This new bridge adsorption site is the same as bridge site on flat (100) surface and there are 16 such bridge sites in a ($\sqrt{5}\times 2$) unit cell. When θ_{O^*} increases to more than 1 ML, oxygen atoms would be added on other bridge sites, similar to flat (100) surfaces: when $\theta_{\mathrm{O}^*} = 2$ ML, the most stable configuration is the oxygen atom covered half of the bridge sites on (100) terraces, as shown in Fig. 6.12 (h); when $\theta_{\mathrm{O}^*} = 3$ ML, oxygen atoms would cover $\frac{3}{4}$ of the bridge sites on (100) terraces, as shown in Fig. 6.12 (l), where oxygen atoms near type A Pt atoms re-bind to each other to form adsorbed oxygen molecules.

Here we did not calculate the absorption of one oxygen atom at different θ_{O^*}, because there are too many possible adsorption/absorption sites and their combinations. On the other hand, we can see a critical difference between E^{O}_{diff}/ U^{O}_{diff} of oxygen adsorption on Pt (210) surface and the counterparts on low-index surfaces: as shown in Fig. 6.13, there is no significant discontinuous increments in E^{O}_{diff} for oxygen adsorption as θ_{O^*} increases to 3 ML, corresponding to U^{O}_{diff} ≈1.40 V. Because there may be a large energy barrier for single oxygen atom to penetrate the top layer into the interstitial site in bulk lattice[41], this means oxygen atoms can be continuously deposited on Pt (210) top surface layer without bulk oxide formation as U increases to 1.40 V, since there are always adsorption sites with proper E^{O}_{diff} available. Furthermore, because surface adsorption/desorption is usually a reversible process without large distortion in surface structure, this continuous E^{O}_{diff}/ U^{O}_{diff} curve may explain the high stability of Pt (210) during polarization cycling.

6.1.5 Oxidation and Polarization Curves on Different Surfaces

In this section, we study the adsorption and absorption of single oxygen atom on Pt (111), (100) and (210) surfaces with pre-adsorbed oxygen atoms. The results are evaluated by differential oxygen adsorption/absorption energy E^{O}_{diff} for reaction in Eq. 6.7 and corresponding equilibrium electrode potential U^{O}_{diff} for reaction in Eq. 6.8 as functions of oxygen coverage θ_{O^*}. However, these relations can not easily be compared with electrochemical experimental measurements, unless we transfer the oxygen coverage data into total charge transfer through water dissociation reaction in Eq. 6.8, where two electrons are transferred in the adsorption/absorption process of each oxygen atom. So we plot the total charge transfer densities Q as functions of electrode potential U for three different surfaces studied above, as shown in Fig. 6.14, which are the thermodynamically equilibrium polarization curves on different Pt surfaces and directly measurable in electrochemical experiments. Here U starts from the starting potential of oxygen adsorption through reaction in Eq. 6.4,

and ends at the potential where the formation of bulk oxide begins (except Pt (210)). For both Pt (111) and (100) this potential range is between 0.6 V and 1.2 V vs. SHE, while for Pt (210) this range starts from 0.6 V and extends at least to 1.4 V. Here we want to emphasize that the detailed curve may be different from experiments, mainly because here we do not consider hydroxyl adsorption as reaction in Eq. 6.5, which may strongly affect the curves when 0.6 V$< U <$ 1.2 V.

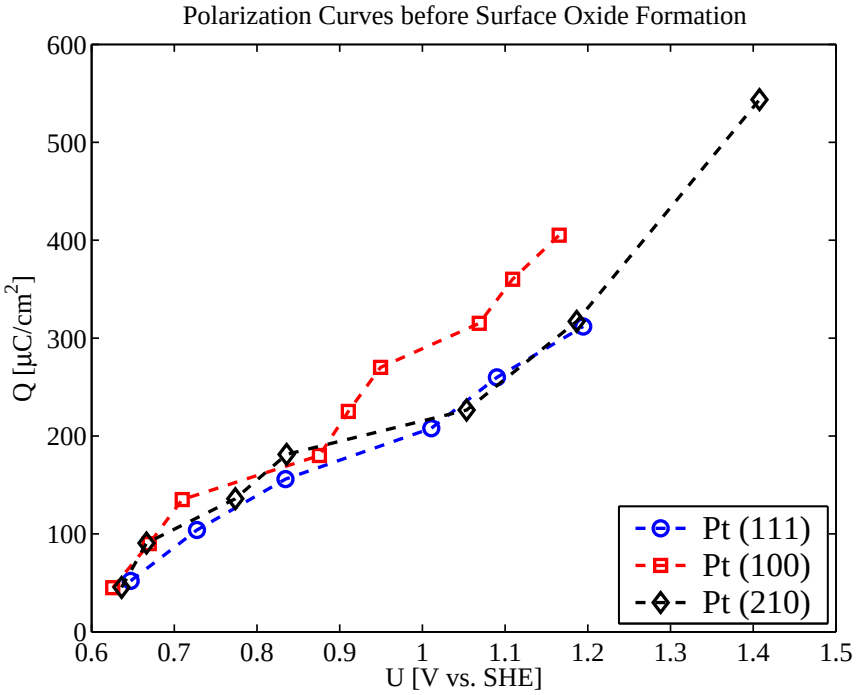

Figure 6.14: Curves of total charge transfer Q vs. electrode potential U on different Pt surfaces. U reaches the starting point of bulk oxide formation on Pt (111) and (100) surfaces; on Pt (210), even when U = 1.4 V, oxygen adsorption may still be more favorable than its absorption.

Because in the process of oxygen adsorption Pt atoms on the surface do not change their lattice positions, in the reversible reduction process, oxygen atoms are removed from the surface by water formation reaction and Pt can still keep its original lattice. The results show that in the polarization cycling when $0 < U <$ 1.2 V, all the surfaces have good reversibility in keeping their original lattice structures. However, if the maximum U is more

than 1.2 V, oxygen atoms adsorbed on Pt (111) and (100) surface start to penetrate into Pt bulk lattice and change top Pt layers into oxides. These thin oxide layers will destabilize Pt lattice through two steps. First, at high U when Pt oxide is thermodynamically stable, the thin oxide layers are under huge compressive strains applied by bulk metallic Pt if the oxide layers and metallic bulk keep 1:1 coherent relation, especially on Pt (111) surface. To relieve the strains, there would be large lattice expansion for the thin oxide layers so that there is no more 1:1 coherent relation between oxides and bottom Pt surface, and the extra Pt atoms from original Pt oxides may stay as islands and clusters on top of the surface. Second, when U decrease to lower values in the reverse cycling, Pt oxides will be reduced so that oxygen will "escape" from Pt bulk lattice, which may make the left Pt atoms hardly return to the original metallic lattice positions, especially for those in clusters or islands on top surface. For these reasons, after many cycles, Pt surfaces can become very rough, and some Pt atoms would be dissolved as ions in the electrolyte. However, for Pt (210) surface, oxygen absorption may not occur at large scale even U increases to 1.4 V, because oxygen atoms can be continuously deposited on Pt (210) surface without abrupt increase of the differential adsorption energy. So Pt (210) surface has good reversibility in potential cycling even when maximum U is as high as 1.4 V.

6.2 Coarsening of Pt Nanocrystals

Besides corrosion, coarsening of Pt nanocrystals is another reason that the catalysts lose electrochemical active surface area (ECSA). Coarsening always occurs because of Ostwald ripening. It can be accomplished by two distinct mass-transport mechanisms: (*i*) surface-diffusion transport where smaller grains emit adatoms that diffuse on the crystal surface to larger grains, and (*ii*) a dissolution-redeposition process, where atoms undergo random detachment and attachment at the electrode-electrolyte interface. Recently Xu et

al. used in-situ electrochemical scanning tunneling microscopy to observe the coarsening phenomena of Pt nanocrystals at different U[153]: a rapid coarsening of nanocrystals was observed in the double-layer region ($U \approx 0.5$ V); no obvious crystal size changes were observed for potentiostat in the oxygen-adsorption regime ($U \approx 0.8$ V) or the hydrogen-adsorption regime ($U \approx 0.25$ V). The kinetics of the coarsening process suggests that its dominant mechanism is potential-induced surface-diffusion transport, and the adsorption of oxygen/hydrogen atoms on Pt surface at high/low U would impede this surface-diffusion and final crystal coarsening. To verify this theory, first-principles calculations are performed to understand different surface-diffusion processes at different U.

6.2.1 Pt Adatom Diffusion

In this section, we use DFT+NEB methods as Section 3.1.1 to obtain the minimum energy paths of Pt adatom diffusion on Pt (111) surface at different surface coverage conditions. We first start from clean Pt (111) surface, which corresponds to double-layer region ($U \approx 0.5$ V). The results are shown in Fig. 6.15. At the initial state, Pt atom stays at fcc hollow site like O^* atom, and hcp hollow site is another type of stable adsorption position where the energy of Pt adatom is 0.20 eV higher than the fcc site. So in a full diffusion path, a Pt adatom would first jump to one nearby hcp hollow site and then to another fcc site, which makes the minimum energy path symmetric along the reaction coordinate, as shown in Fig. 6.15. The activation barrier is 0.26 eV higher than the initial state. Considering a pre-exponential factor of 10^{13} s^{-1}, it means that Pt adatom can diffuse extremely fast at T = 300 K.

If we change U, the surface would be deposited with many other adsorbates. As shown in Section 6.1.2, when $U \approx 0.8$ V, there are O^* atoms with coverage $\theta_{O^*} = \frac{1}{4} \sim \frac{1}{3}$ ML from water dissociation reaction as Eq. 6.5. For the similar reason, when U decreases to small

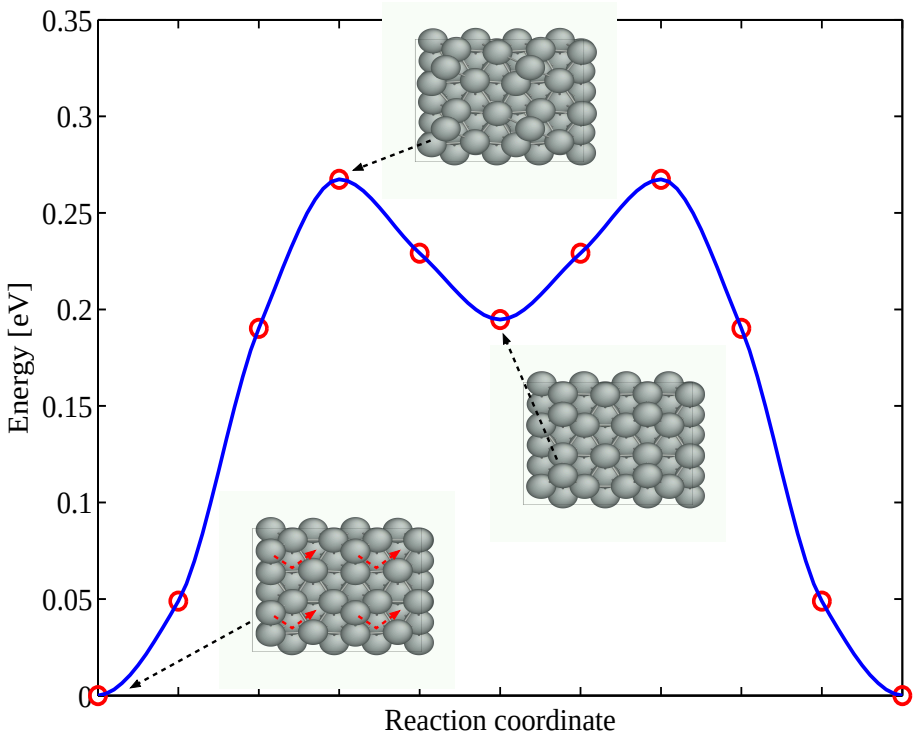

Figure 6.15: Minimum energy path of Pt adatom diffusion on clean Pt (111) surface. The curved arrows in the initial configuration shows the diffusion path of Pt atom from one fcc hollow site to a nearby fcc site.

value, H^* can be deposited on Pt (111) surface through the following reaction:

$$H^+ + e^- \rightarrow H^* \tag{6.12}$$

Because we have not performed the calculations on coverage-dependent adsorption energy for H^*, the accurate coverage of H^* at certain U is unknown. In order to easily compare the results, we perform the calculations of Pt adatom diffusion on Pt (111) surface with either $\frac{1}{4}$ ML H^* or $\frac{1}{4}$ ML O^*. The minimum energy paths are shown in Fig. 6.16. The configurations show that Pt adatom has different interactions with different adsorbates. H^* always prefers to connect with Pt adatom, and they move together in the whole diffusion process. On the other hand, O^* repels to the Pt adatom, and they stay away from each other in the diffusion process. Except for this difference, both H^* and O^* largely increase the diffusion barrier of Pt adatom: the activation energy is 0.44 eV for $\frac{1}{4}$ ML H^* and 0.49 eV for $\frac{1}{4}$ ML O^*. This means that Pt adatom diffusion rates decrease at least 1000 times at 300 K in both cases, agreeing with experimental observations of slow coarsening rates.

Strictly speaking, these diffusion barriers are *migration* energies for Pt adatoms on the surface; another critical issue is the formation mechanism of Pt adatoms and the related energy changes, so-called *formation* energies. Currently, it is assumed that most of Pt adatoms come from relatively unstable places, such as grain boundaries or surface steps. The surface adsorbates may also affect the adatom formation through oxide/hydride formation process. The detailed mechanism and the effects of surface adsorbates will be left for future studies.

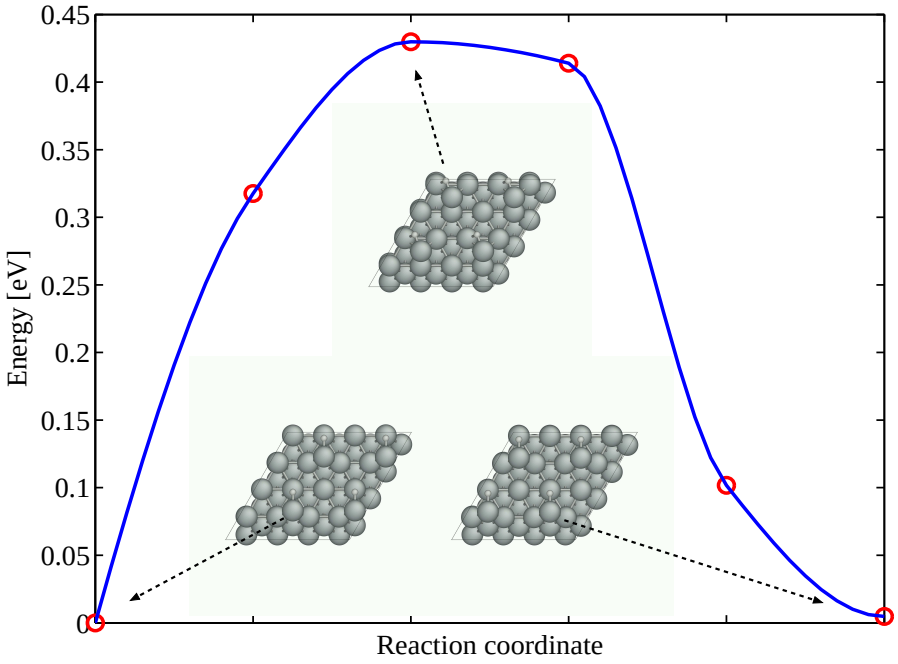

(a)

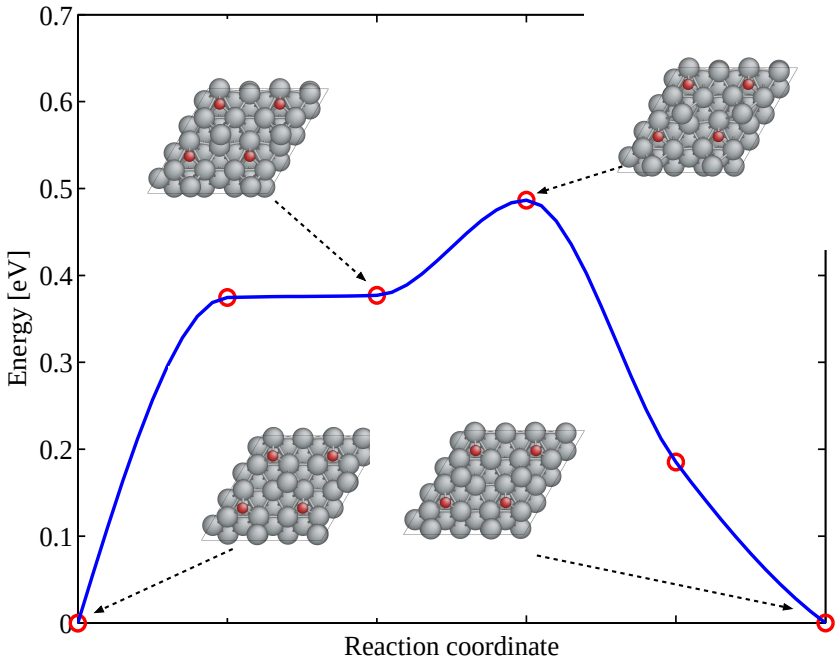

(b)

Figure 6.16: Minimum energy path of Pt adatom diffusion on Pt (111) surface with $\frac{1}{4}$ ML (a) H^* or (b) O^*.

Chapter 7

Summary and Future Work

7.1 Summary

Current catalysts used for oxygen reduction reaction (ORR) on the cathode of PEM fuel cell are Pt and Pt alloys. However, for industrial-scale applications of PEM fuel cell, we need to find catalysts with higher activity and better stability in order to reduce both the usage of precious metals and the degradation rate of catalytic performance. Thus, theoretical tools at different scales are discussed in this thesis in order to understand the corresponding mechanisms and speed up the search for new catalysts.

In Chapter 3, we use DFT to study a simple model reaction similar with electrochemical ORR, oxygen reduction by hydrogen molecule under ultra-high-vacuum (UHV) conditions. Its reaction pathways on (111) surface of different metals illustrate the origin of good catalytic activity. On Au (111) surface, where the adsorptions of atoms and molecules are generally very weak, O_2 and H_2 have few possibilities to be adsorbed on the surface and huge barriers to dissociate for the further reactions. Oppositely, on Cu (111) surface, which has strong binding with atoms/molecules, O_2 and H_2 easily dissociate and form OH^* adsorbed on the surface, which is so stable that there is a huge barrier for its reaction to form

water. Only on Pt (111) surface, because of its moderate adsorption strength, a full reaction pathway with low activation barriers can be found, confirming its good catalytic activity at room temperature. In addition, the reaction pathways on (111) surface of Pt alloys may have activation barriers even lower than those on pure Pt surface, which suggests the possibility to obtain catalysts with better activity by manipulating the surface compositions, structures and corresponding adsorption strengths.

In Chapter 4, we mainly focus on the reaction mechanism of electrochemical ORR and corresponding dynamics. We still use DFT calculations as tools to obtain electronic structures and energetics. The analyses of electronic structures of possible ORR intermediates (O_2^*, OOH^*, $H_2O_2^*$, O^* and OH^*) suggest that they are all in near-neutral states at different reaction environments (strong external electric fields and solvation fields of water molecules), which indicate that all the electron transfers in ORR should occur through proton-coupled (PCET) mechanisms like $A^* + H^+ + e^- \rightarrow A\text{-}H^*$. Then the dynamics of such PCET reactions are investigated near metallic surface based on a simple hydrated proton (hydronium) model. The results show that the near-surface PCET is accomplished by proton transfer along a hydrogen-bond network from hydronium to the ORR intermediate on the surface, and there is no significant extra barrier except a possible positive reaction energy. However, besides the near-surface reaction part, a full PCET path is completed by considering proton transfer from hydronium in the bulk electrolyte to hydronium near the surface, which may require extra energy cost. This dynamic picture is used in the ORR kinetic model in Chapter 5. Before that, because there is a simple ORR kinetic model whose input parameters are just the adsorption energies of critical ORR intermediates[94], we use it and a simple thermodynamic model of equilibrium corrosion potential to make a quick and coarse search for new catalysts with better activity and stability. The results, although possibly not accurate, suggest that it is difficult to find alloys to satisfy these dual requirements. Future candidates may be the combination of Pt with oxides, or Au-modified

Pt surfaces.

Based on the reaction mechanisms and corresponding dynamics discussed above, in Chapter 5 we try to build multiscale models in order to connect DFT data at atomic scale with experimentally measurable results, such as polarization curves and differential capacitances. We build a reaction network composed of ORR elementary steps by considering both the limited surface site competition and the repulsive interaction between ORR intermediates on the surface. We also develop a mathematical framework to perform the analyses on how each input parameter, such as adsorption energy of certain intermediate, can affect the final output of this reaction network. Under mean-field approximation, the steady-state solution of this model not only gives the ORR rate and current density j at given electrode potential U, but also suggests that there are strong "self-regulation" effects, which always try to equalize the reaction rates and corresponding activation barriers for different elementary steps. As a result, the sensitivity of ORR activity on adsorption energy of certain intermediate decreases significantly, which can explain why the ORR rate does not change exponentially with the adsorption energies of critical ORR intermediates on different surfaces. In addition, the accuracy of this model can be improved by discrete descriptions of the lateral interactions and site competitions. In the next step, we can generalize the reaction network model and sensitivity analyses to other catalytic surface reactions, because they can help us discover the correct directions to search for catalysts with both higher activity and selectivity.

Beside surface kinetics, in Chapter 5 we also study the structure of electrode-electrolyte interface in order to determine U as a function of excess surface electron density σ^{M} on metallic electrode. There DFT is used to investigate the potential change in the "compact layer" region near metallic surface, while statistical theories are applied to obtain the potential changes in the "diffusion layer" region far from surface. However, the differential capacitance C_d extrapolated from U-σ^{M} relation only agrees well with experiments when

$\sigma^{M} > 0$ (positive excess charge on the surface); when $\sigma^{M} < 0$ the calculated C_d is too small because of inadequate configurational sampling of water structures in the "compact layer", which may be improved by *ab initio* molecular dynamics simulation at finite temperature. Similar sampling problems exist in the first-principles calculation of potential of zero charge (PZC) for certain surfaces. Finally, because σ^{M} is determined by the electron consumption rate of j plus the supply rate of incoming external current I from circuit, we discuss the principles to achieve a self-consistent multiscale ORR model to output both U and I for the future work.

In Chapter 6 we study two different phenomena to induce the instability of Pt nanocrystals as (electro-)catalysts: surface oxidation and adatom diffusion. Because of different maximum abilities to keep oxygen atoms on the top surface layer, (111), (100) and (210) surfaces have different starting U ($\sim$ 1.20 V vs. SHE for (111) and (100), at least 1.44 V for (210)) above which bulk oxide formation begins. The thin oxide layers on (111) and (100) surfaces also have different structures and stabilities due to the lattice mismatch between Pt oxides and metallic Pt substrates. Since oxidation and subsequent reduction of Pt surface result in Pt atom dissolution, these differences can explain the relative stability of different Pt surfaces during polarization cycling and help us find possible mechanisms to impede Pt corrosion. Meanwhile, at low and high U, Pt surface is deposited with adsorbates, such as H^* and O^*. Both of them are found to significantly increase the diffusion barrier of Pt adatom on Pt (111) surface compared with a clean surface situation, which is a possible reason that the coarsening rate varies with U.

7.2 Future Work

There are still many unsolved problems in the computational modeling of electrocatalysis. Here we just outline several of them, which will be explored in future work.

First, we would like to understand the intrinsic mechanisms in determining the charge states of adsorbates. Although the electronic structures from DFT calculations have confirmed that all ORR intermediates (O_2^*, OOH^*, O^*, ...) are almost neutral, the physical origin of the near-neutrality properties is still unknown. Recently, Raebiger et al. analyzed a similar correlation between changes of the oxidation state and charge transfer in an similar system: transition metal ions in insulators. They demonstrated a tendency of the transition metal atom to maintain a constant charge as the oxidation state is altered[109]. This is achieved by a re-hybridization of the bonding and antibonding orbitals formed by the transition metal atom. We would like to develop a similar theory for the charge states of surface adsorbates. There may exist a "self-regulation" effect just like the surface reaction kinetics discussed in Section 5.1: a small amount of electron would transfer between surface and the atom/molecule once they contact each other; however, from some unknown "feedback" mechanism, further transfer of more electrons becomes very difficult, which is related to the concept of electron *hardness* defined as following[101]

$$\eta_h = \left.\frac{\partial^2 E}{\partial N^2}\right|_{V_{\text{ext}}} \tag{7.1}$$

where E is total energy of certain species and N is number of electrons in such species, while V_{ext} is the external potential field. Such "feedback" mechanisms will help us to understand the general tendency of charge states for different adsorbates on various types of surfaces.

Second, more fundamental studies are needed to understand the dynamics of proton-coupled electron transfer (PCET). In Section 4.2, an assumption of activation free energy Q_{PT} of proton transfer from bulk electrolyte to the area near electrode surface is proposed as Eq. 4.18 and 4.19. Although such assumptions seem to be consistent with experiments[40, 78, 79, 80], we want to verify these assumptions theoretically and calcu-

late the related parameters, such as symmetry factor β and electrode potential U^0 at which Q_{PT} equals zero. Such parameters can be calculated from the free energies of hydrated proton (hydronium) in the bulk electrolyte and the electrolyte near electrode surface with various excess surface electron density σ^{M}. To obtain accurate free energies, we need to perform molecular dynamics (based on first-principles or accurate classical potentials) at finite temperature or Monte Carlo simulations with proper sampling methods, such as Umbrella sampling[121]. Thus, we can obtain the relation between Q_{PT} and σ^{M}, which can be transformed as function $Q_{\mathrm{PT}}(U)$ with the help of the function $U(\sigma^{\mathrm{M}})$ from studies of electrode-electrolyte interfaces discussed in Section 5.2.

Third, besides the free energy changes in the whole path of proton-coupled electron transfer, its pre-exponential factor is another important issue to determine kinetics of ORR. In our mean-field kinetic model, the pre-exponential factor for all PCET steps, υ_{H} from Eq. 5.28 to Eq. 5.33, is chosen so that the calculated kinetic current density on Pt (111) surface at U = 0.9 V vs. SHE agrees with experimental value. It can also be estimated from the proton diffusivity and pH value of the electrolyte. In the future, we should calculate υ_{H} from first principles. Such calculations can not be performed by DFT ground state calculations based on *Born-Oppenheimer approximation*, which is accurate only for heavy nuclei[101]. For proton, its transfer process involves thermal hopping[53, 127], proton tunnelling[8, 149] and solvation effect[54], thus its dynamics can be accurately calculated by considering both thermal and quantum fluctuations of all nuclei. Such calculations have been performed in bulk water by *ab initio* path integral methods[83, 82, 137]. We want to explore the similar process of proton transfer between surface adsorbates and water molecules in the electrode-electrolyte interfacial structures, and check whether different types of adsorbates and surfaces would affect proton transfer rate.

Fourth, to obtain more accurate kinetics of oxygen reduction reaction, we need to consider the lateral *enthalpic* and *entropic* interactions more carefully. Currently, we just use

mean-field approximation and assume enthalpic interactions between surface adsorbates depend linearly on their coverage as Eq. 5.41, which makes our kinetic model predict too low slopes in Tafel plot of potential-current relations at high potential regions. From the studies of coverage-dependent adsorption of oxygen atoms O^* on Pt surfaces in Section 6.1, it is found that energies (enthalpies) of O^* is more sensitive to local adsorption configurations and can be described by discontinuous step functions of surface coverages. The lateral interactions of other surface adsorbates, such as O_2^* and OH^*, are more complex, because they may even depend on the relative orientations between nearby adsorbates, such as hydrogen bond formation between nearby OH^* and adsorbed H_2O molecules[96]. We need to include these effects to precisely predict the ORR kinetics and sensitivity as defined in Eq. 5.61, which may guide the development of catalysts with better activity and selectivity[128, 92].

Fifth, electrode-electrolyte interface and corresponding relation between electrode potential U and excess surface electron density σ^M need to be further investigated. As mentioned in Section 5.2.1, inadequate configurational sampling of water structures in *compact layer* may be solved by *ab initio* molecular dynamics simulation of compact layer structures at finite temperature. In addition, besides water molecules, we should consider other species in the compact layer, such as surface adsorbates from ORR intermediates or specially adsorbed ions from the electrolyte. Meanwhile, for the diffusion layer, Gouy-Chapman theory usually overestimates the ion concentration near the electrode surface because it considers all the ions in the solution as point charges. To solve this problem, we should use modified Poisson-Boltzmann equations in which all ions have finite sizes[15].

Sixth, because we have studied the thermodynamics of coverage-dependent oxygen adsorption/absorption in Section 6.1, which may determine the rates of oxidation processes on various Pt surfaces, in next step we want to understand their corresponding dynamics and kinetics. DFT + NEB methods can be used to calculate the activation energy of certain

oxygen adsorption process. However, the calculated activation barrier may be sensitive to the size of unit cell, so large unit cell should be used to obtain the accurate dynamic information. Meanwhile, besides intact surfaces with compact structures, there may be some other "fast channels" for oxygen transfer from the top surface to the bulk lattice, such as surface defects, edges between two facets and grain boundaries. The increasing stability of Au-modified Pt surface may result from the blocking effects of Au clusters on these fast channels[154], which need to be confirmed by detailed calculations.

Seventh, in Section 6.2 we have studied the Pt adatom diffusion on Pt (111) surface covered with different adsorbates, and the diffusion barrier changes may explain the coarsening rate differences under various electrode potentials[153]. However, all the calculations for diffusion barriers are performed on neutral Pt (111) surface, but at the real electrode-electrolyte interface there are excess/deficient surface electrons, which may also affect the diffusion of adatoms. In addition, these diffusion barriers are *migration* energies for Pt adatoms on the surface; another critical issue is the formation mechanism of Pt adatoms and the related energy changes, so called *formation* energies. These formation energies may also depend on the coverage of adsorbates, which could be another possible reason of the differences in coarsening rates. Furthermore, if the formation energies are too high for the surface to achieve reasonable production rate of adatoms, we should consider other mass transfer mechanisms for the coarsening processes, such as surface vacancy diffusion. All these hypotheses need to be further investigated by first-principles and other methods.

Bibliography

[1] R. R. Adzic. Chapter 5 in *Electrocatalysis*. Editors: J. Lipkowski and P. N. Ross. Wiley, New York, 1998.

[2] A. B. Anderson and T. V. Albu. Catalytic effect of platinum on oxygen reduction - An *ab initio* model including electrode potential dependence. *J. Electrochem. Soc.*, 147:4229–4238, 2000.

[3] P. W. Anderson. Localized magnetic states in metals. *Phy. Rev.*, 124:41–53, 1961.

[4] H. Angerstein-Kozlowska, B. E. Conway, and W. B. A. Sharp. Real condition of electrochemically oxidized platinum surfaces .1. resolution of component processes. *J. Electroanal. Chem.*, 43:9–36, 1973.

[5] P. Atkins. *Physical Chemistry*. W.H. Freeman and Company, New York, 6th edition, 1997.

[6] F. Barbir. *PEM Fuel Cells: Theory and Practice (Sustainable World Series)*. Academic Press, 1st edition, 2005.

[7] A. J. Bard and L. R. Faulkner. *Electrochemical Methods: Fundamentals and Applications*. Wiley, 2nd edition, 2000.

[8] J. D. Bernal and R. H. Fowler. A theory of water and ionic solution, with particular reference to hydrogen and hydroxyl ions. *J. Chem. Phys.*, 1:515–548, 1933.

[9] J. J. Berzelius. *J. Jber. Chem.*, 15:237, 1837.

[10] J. Biener, E. Lang, C. Lutterloh, and J. Küppers. Reactions of gas-phase H atoms with atomically and molecularly adsorbed oxygen on Pt(111). *J. Chem. Phys.*, 116:3063–3074, 2002.

[11] V. I. Birss, M. Chang, and J. Segal. Platinum oxide film formation reduction - an in-situ mass measurement study. *J. Electroanal. Chem.*, 355:181–191, 1993.

[12] T. Bligaard, J. K. Nørskov, S. Dahl, J. Matthiesen, C. H. Christensen, and J. Sehested. The Bronsted-Evans-Polanyi relation and the volcano curve in heterogeneous catalysis. *J. Catal.*, 224:206–217, 2004.

[13] P. E. Blöchl. Projector augmented-wave method. *Phys. Rev. B*, 50:17953–17979, 1994.

[14] J. O'M Bockris, A. K. N. Reddy, and M. Gamboa-Aldeco. *Modern Electrochemistry 1: Ionics*. Springer, 2nd edition, 1998.

[15] I Borukhov, D Andelman, and H Orland. Steric effects in electrolytes: A modified Poisson-Boltzmann equation. *Phys. Rev. Lett.*, 79:435–438, 1997.

[16] S. K. Burke, B. D. Rainford, D. E. G. Williams, P. J. Brown, and D. A. Hukin. Magnetization density in ferrimagnetic Pt_3Cr. *J. Magn. Magn. Mater.*, 15:505–506, 1980.

[17] D. M. Ceperley and B. J. Alder. Ground State of the Electron Gas by a Stochastic Method. *Phys. Rev. Lett.*, 45:566–569, 1980.

[18] D. L. Chapman. *Phil. Mag.*, 25:475, 1913.

[19] L. A. Cole and J. P. Perdew. Calculated electron affinities of the elements. *Phys. Rev. A*, 25:1265–1271, 1982.

[20] B. E. Conway. Electrochemical oxide film formation at noble-metals as a surface-chemical process. *Prog. Surf. Sci.*, 49:331–452, 1995.

[21] R. I. Cukier and D. G. Nocera. Proton-coupled electron transfer. *Annu. Rev. Phys. Chem.*, 49:337–369, 1998.

[22] A. Damjanovic, A. Dey, and J. O'M Bockris. Kinetics of oxygen evolution and dissolution on platinum electrodes. *Electrochim. Acta*, 11:791–814, 1966.

[23] S. L. Dudarev, G. A. Botton, S. Y. Savrasov, C. J. Humphreys, and A. P. Sutton. Electron-energy-loss spectra and the structural stability of nickel oxide: An LSDA+U study. *Phys. Rev. B*, 57:1505–1509, 1998.

[24] A. Eichler and J. Hafner. Molecular precursors in the dissociative adsorption of O_2 on Pt(111). *Phys. Rev. Lett.*, 79:4481–4484, 1997.

[25] A. Eichler, F. Mittendorfer, and J. Hafner. Precursor-mediated adsorption of oxygen on the (111) surfaces of platinum-group metals. *Phys. Rev. B*, 62:4744–4755, 2000.

[26] M. Eigen. Proton transfer, acidbase catalysis and enzymatic hydrolysis. *Angew. Chem. Int. Edn Engl.*, 3:1–19, 1964.

[27] M. S. El-Deab and T. Ohsaka. An extraordinary electrocatalytic reduction of oxygen on gold nanoparticles-electrodeposited gold electrodes. *Electrochem. Commun.*, 4:288–292, 2002.

[28] C. Ellinger, A. Stierle, I. K. Robinson, A. Nefedov, and H. Dosch. Atmospheric pressure oxidation of Pt(111). *J. Phys.: Condens. Matter.*, 20:184013, 2008.

[29] M. Faraday. *Experimental Researches in Electricity*, 1844.

[30] P. J. Feibelman. d-electron frustration and the large fcc versus hcp binding preference in O adsorption on Pt(111). *Phys. Rev. B*, 56:10532–10537, 1997.

[31] P. J. Feibelman. Partial dissociation of water on Ru(0001). *Science*, 295:99–102, 2002.

[32] K. A. Fichthorn and W. H. Weinberg. Theoretical foundations of dynamical Monte Carlo simulations. *J. Chem. Phys.*, 95(2):1090–1096, 1991.

[33] H. A. Gasteiger, S. S. Kocha, B. Sompalli, and F. T. Wagner. Activity benchmarks and requirements for Pt, Pt-alloy, and non-Pt oxygen reduction catalysts for PEM-FCs. *Appl. Catal. B-Environmental*, 56:9–35, 2005.

[34] Y. Gauthier, M. Schmid, S. Padovani, E. Lundgren, V. Bus, G. Kresse, J. Redinger, and P. Varga. Adsorption sites and ligand effect for CO on an alloy surface: a direct view. *Phys. Rev. Lett.*, 87:036103, 2001.

[35] R. B. Getman, Y. Xu, and W. F. Schneider. Thermodynamics of environment-dependent oxygen chemisorption on Pt(111). *J. Phys. Chem. C*, 112(26):9559–9572, 2008.

[36] D. T. Gillespie. General method for numerically simulating the stochastic time evolution of coupled chemical reactions. *J. Comput. Phys.*, 22(4):403–434, 1976.

[37] J. L. Gland, B. A. Sexton, and G. B. Fisher. Oxygen interactions with the Pt(111) surface. *Surf. Sci.*, 95:587–602, 1980.

[38] G. Gouy. *J. Phys.*, 9:457, 1910.

[39] D. C. Grahame. . *Chem. Rev.*, 41:441, 1947.

[40] B. N. Grgur, N. M. Markovic, and P. N. Ross. Temperature-dependent hydrogen electrochemistry on platinum low-index single-crystal surfaces in acid solutions. *J. Phys. Chem. B*, 101:5405–5413, 1997.

[41] Z. Gu and P. B. Balbuena. Absorption of atomic oxygen into subsurfaces of Pt(100) and Pt(111): Density functional theory study. *J. Phys. Chem. C*, 111:9877–9883, 2007.

[42] D. R. Hamann, M. Schlüter, and C. Chiang. Norm-Conserving Pseudopotentials. *Phys. Rev. Lett.*, 43:1494–1497, 1979.

[43] B. Hammer, L. B. Hansen, and J. K. Nørskov. Improved adsorption energetics within density-functional theory using revised Perdew-Burke-Ernzerhof functionals. *Phys. Rev. B*, 59:7413–7421, 1999.

[44] B. Hammer and J. K. Nørskov. Theoretical surface science and catalysis - Calculations and concepts. volume 45 of *Advances in catalysis*, pages 71–129. 2000.

[45] B. Hammer and J. K. Nϕrskov. Electronic factors determing the reactivity of metal surfaces. *Surf. Sci.*, 343:211–220, 1995.

[46] B. Hammer and J. K. Nϕrskov. Why gold it the noblest of all the metals. *Nature*, 376:238–240, 1995.

[47] T. He, E. Kreidler, L. Xiong, and E. Ding. Combinatorial screening and nanosynthesis of platinum binary alloys for oxygen electroreduction. *J. Power Sources*, 165:87–91, 2007.

[48] M. A. Henderson. The interaction of water with solid surfaces: fundamental aspects revisited. *Surf. Sci. Rep.*, 46:5–308, 2002.

[49] G. Henkelman and H. Jonsson. Improved tangent estimate in the nudged elastic band method for finding minimum energy paths and saddle points. *J. Chem. Phys.*, 113:9978–9985, 2000.

[50] G. Henkelman, B. P. Uberuaga, and H. Jonsson. A climbing image nudged elastic band method for finding saddle points and minimum energy paths. *J. Chem. Phys.*, 113:9901–9904, 2000.

[51] P. Hohenberg and W. Kohn. Inhomogeneous electron gas. *Phys. Rev.*, 136:B864–B871, 1964.

[52] K. Honkala and K. Laasonen. Oxygen molecule dissociation on the Al(111) surface. *Phys. Rev. Lett.*, 84:705–708, 2000.

[53] E Hückel. Theorie der Beweglichkeiten des Wasserstoff- und Hydroxylions in wässriger Lösung. *Z. Elektrochem.*, 34:546–562, 1928.

[54] M. L. Huggins. Hydrogen bridges in ice and liquid water. *J. Phys. Chem.*, 40:723–731, 1936.

[55] M. P. Hyman and J. W. Medlin. Theoretical study of the adsorption and dissociation of oxygen on Pt(111) in the presence of homogeneous electric fields. *J. Phys. Chem. B*, 109:6304–6310, 2005.

[56] M. P. Hyman and J. W. Medlin. Mechanistic study of the electrochemical oxygen reduction reaction on Pt(111) using density functional theory. *J. Phys. Chem. B*, 110:15338–15344, 2006.

[57] T. Jacob. Theoretical investigations on the potential-induced formation of Pt-oxide surfaces. *J. Electroanal. Chem.*, 607:158–166, 2007.

[58] M. J. Janik, C. D. Taylor, and M. Neurock. First-Principles Analysis of the Initial Electroreduction Steps of Oxygen over Pt(111). *J. Electrochm. Soc.*, 156:B126–B135, 2009.

[59] G. Jerkiewicz, G. Vatankhah, J. Lessard, M. P. Soriaga, and Y. S. Park. Surface-oxide growth at platinum electrodes in aqueous H_2SO_4 Reexamination of its mechanism through combined cyclic-voltammetry, electrochemical quartz-crystal nanobalance, and Auger electron spectroscopy measurements. *Electrochim. Acta*, 49:1451–1459, 2004.

[60] R. W. Joyner, E. S. Shpiro, P. Johnston, and G. J. Tuleuova. Intermetallic pt-cr clusters in zeolites as models of bimetallic aromatization and reforming catalysts .1. characterization of oxidation-states, dispersion, and local-structure. *J. Catal.*, 141:250–265, 1993.

[61] W. Kohn and L. Sham. Self-consistent equations including exchange and correlation effects. *Phys. Rev.*, 140:A1133–A1138, 1965.

[62] A. Kokalj. Computer graphics and graphical user interfaces as tools in simulations of matter at the atomic scale. *Comp. Mater. Sci.*, 28:155–160, 2003.

[63] K. W. Kolasinski. *Surface Science: Foundations of Catalysis and Nanoscience*. Wiley, 2nd edition, 2008.

[64] D. M. Kolb and J. Schneider. Surface Reconstruction in Electrochemistry - Au(100)-(5×20), Au(111)-(1×23) and Au(110)-(1×2). *Electrochim. Acta.*, 31:929–936, 1986.

[65] M. T. M. Koper and G. A. Voth. A theory of adiabatic bond breaking electron transfer reactions at metal electrodes. *Chem. Phys. Lett.*, 282:100–106, 1998.

[66] G. Kresse and J. Furthmüller. Efficiency of *ab initio* total energy calculations for metals and semiconductors using a plane-wave basis set. *Comput. Mater. Sci.*, 6:15–50, 1996.

[67] G. Kresse and J. Furthmüller. Efficient iterative schemes for *ab initio* total-energy calculations using a plane-wave basis set. *Phys. Rev. B*, 54:11169–11186, 1996.

[68] G. Kresse, A. Gil, and P. Sautet. Significance of single-electron energies for the description of CO on Pt(111). *Phys. Rev. B*, 68:073401, 2003.

[69] G. Kresse and J. Hafner. *Ab initio* molecular-dynamics for liquid-metals. *Phys. Rev. B*, 47:558–561, 1993.

[70] G. Kresse and D. Joubert. From ultrasoft pseudopotentials to the projector augmented-wave method. *Phys. Rev. B*, 59:1758–1775, 1999.

[71] A. Leach. *Molecular Modelling: Principles and Applications*. Prentice Hall, 2nd edition, 2001.

[72] S. J. Lee, S. Mukerjee, E. A. Ticianelli, and J. McBreen. Electrocatalysis of CO tolerance in hydrogen oxidation reaction in PEM fuel cells. *Electrochim. Acta*, 44(19):3283–3293, 1999.

[73] S. Lehwald, H. Ibach, and H. Steininger. Overtones and multiphonon processes in vibration-spectra of adsorbed molecules. *Surf. Sci.*, 117:342–351, 1982.

[74] W. Li, L. Osterlund, E. K. Vestergaard, R. T. Vang, J. Matthiesen, T. M. Pedersen, E. Laegsgaard, B. Hammer, and F. Besenbacher. Oxidation of Pt(110). *Phys. Rev. Lett.*, 93:146104, 2004.

[75] P. Liu and J. K. Nϕrskov. Ligand and ensemble effects in adsorption on alloy surfaces. *Phys. Chem. Chem. Phys.*, 3:3814–3818, 2001.

[76] G. Makov and M. C. Payne. Periodic boundary-conditions in ab-initio calculations. *Phys. Rev. B*, 51:4014–4022, 1995.

[77] R. A. Marcus and N. Sutin. Electron transfers in chemistry and biology. *Biochim. Biophys. Acta*, 811, 1985.

[78] N. M. Markovic, H. A. Gasteiger, and P. N. Ross. Oxygen reduction on platinum low-index single-crystal surfaces in sulfuric-acid-solution - rotating ring-Pt(hkl) disk studies. *J. Phys. Chem.*, 99:3411–3415, 1995.

[79] N. M. Markovic, H. A. Gasteiger, and P. N. Ross. Kinetics of oxygen reduction on Pt(hkl) electrodes: Implications for the crystallite size effect with supported Pt electrocatalysts. *J. Electrochem. Soc.*, 144(5):1591–1597, 1997.

[80] N. M. Markovic, T. J. Schmidt, B. N. Grgur, H. A. Gasteiger, R. J. Behm, and P. N. Ross. Effect of temperature on surface processes at the Pt(111)-liquid interface: Hydrogen adsorption, oxide formation, and CO oxidation. *J. Phys. Chem. B*, 103(40):8568–8577, 1999.

[81] R. M. Martin. *Electronic Structure: Basic Theory and Practical Methods*. Cambridge University Press, 1st edition, 2009.

[82] D. Marx and M. Parrinello. Ab initio path integral molecular dynamics: basic ideas. *J. Chem. Phys.*, 104:4077–4082, 1996.

[83] D. Marx, M. E. Tuckerman, J. Hutter, and M. Parrinello. The nature of the hydrated excess proton in water. *Nature*, 397:601–604, 1999.

[84] M. Mavrikakis, B. Hammer, and J. K. Nϕrskov. Effect of strain on the reactivity of metal surfaces. *Phys. Rev. Lett.*, 81:2819–2822, 1998.

[85] A. Michaelides and P. Hu. Catalytic water formation on platinum: A first-principles study. *J. Am. Chem. Soc.*, 123:4235–4242, 2001.

[86] H. J. Monkhorst and J. D. Pack. Special points for brillouin-zone integrations. *Phys. Rev. B*, 13:5188–5192, 1976.

[87] S. Mukerjee and S. Srinivasan. Enhanced electrocatalysis of oxygen reduction on platinum alloys in proton-exchange membrane fuel-cells. *Journal of Electroanalytical Chemistry*, 357:201–224, 1993.

[88] S. Mukerjee, S. Srinivasan, M. P. Soriaga, and J. Mcbreen. Role of structural and electronic-properties of pt and pt alloys on electrocatalysis of oxygen reduction - an in-situ XANES and EXAFS investigation. *J. Electrochem. Soc.*, 142:1409–1422, 1995.

[89] D. M. Newns. Self-consistent model of hydrogen chemisorption. *Phy. Rev.*, 178:1123–1135, 1961.

[90] M. D. Newton and N. Sutin. Electron-transfer reactions in condensed phases. *Annu. Rev. Phys. Chem.*, 35:437–480, 1984.

[91] P. D. Nolan, B. R. Lutz, P. L. Tanaka, J. E. Davis, and C. B. Mullins. Molecularly chemisorbed intermediates to oxygen adsorption on Pt(111): A molecular beam and electron energy-loss spectroscopy study. *J. Chem. Phys.*, 111:3696–3704, 1999.

[92] J. K. Nørskov, T. Bligaard, and J. Kleis. Rate Control and Reaction Engineering. *Science*, 324:1655–1656, JUN 26 2009.

[93] J. K. Nørskov, T. Bligaard, A. Logadottir, S. Bahn, L. B. Hansen, M. Bollinger, H. Bengaard, B. Hammer, Z. Sljivancanin, M. Mavrikakis, Y. Xu, S. Dahl, and

C. J. H. Jacobsen. Universality in heterogeneous catalysis. *J. Catalysis*, 209:275–278, 2002.

[94] J. K. Nørskov, J. Rossmeisl, A. Logadottir, L. Lindqvist, J. R. Kitchin, T. Bligaard, and H. Jonsson. Origin of the overpotential for oxygen reduction at a fuel-cell cathode . *J. Phys. Chem. B*, 108:17886–17892, 2004.

[95] P. R. Norton. A photoelectron spectroscopic study of adsorption and reactivity of oxygen on platinum. *J. Catal.*, 36:211–223, 1975.

[96] H. Ogasawara, B. Brena, D. Nordlund, M. Nyberg, A. Pelmenschikov, L. G. M. Pettersson, and A. Nilsson. Structure and bonding of water on Pt(111). *Phys. Rev. Lett.*, 89:276102, 2002.

[97] S. Ogata, J. Li, and S. Yip. Ideal pure shear strength of aluminum and copper. *Science*, 298:807–811, 2002.

[98] R. O'Hayre, W. Colella, S. W. Cha, and F. B. Prinz. *Fuel Cell Fundamentals*. Wiley, 2nd edition, 2009.

[99] R. A. Olsen, G. J. Kroes, and E. J. Baerends. Atomic and molecular hydrogen interacting with Pt(111). *J. Chem. Phys.*, 111:11155–11163, 1999.

[100] D. A. Outka, J. Stohr, W. Jark, P. Stevens, J. Solomon, and R. J. Madix. Orientation and bond length of molecular-oxygen on Ag(110) and Pt(111) - a near-edge x-ray-absorption fine-structure study. *Phys. Rev. B*, 35:4119–4122, 1987.

[101] R. G. Parr and W. Yang. *Density-functional theory of atoms and molecules*. Clarendon Press, Oxford, 1989.

[102] U. A. Paulus, A. Wokaun, G. G. Scherer, T. J. Schmidt, V. Stamenkovic, V. Radmilovic, N. M. Markovic, and P. N. Ross. Oxygen reduction on carbon-supported Pt-Ni and Pt-Co alloy catalysts. *J. Phys. Chem. B*, 106:4181–4191, 2002.

[103] J. P. Perdew, K. Burke, and M. Ernzerhof. Generalized gradient approximation made simple. *Phys. Rev. Lett.*, 77:3865–3868, 1996.

[104] J. P. Perdew, J. A. Chevary, S. H. Vosko, K. A. Jackson, M. R. Pederson, D. J. Singh, and C. Fiolhais. Atoms, molecules, solids, and surfaces: Applications of the generalized gradient approximation for exchange and correlation. *Phys. Rev. B*, 46:6671–6687, 1992.

[105] J. P. Perdew and Y. Wang. Accurate and simple analytic representation of the electron-gas correlation energy. *Phys. Rev. B*, 45:13244–13249, 1992.

[106] J. P. Perdew and A. Zunger. Self-interaction correction to density-functional approximations for many-electron systems. *Phys. Rev. B*, 23:5048–5079, 1981.

[107] L. Qi, X. F. Qian, and J. Li. Near-neutrality of oxygen molecule adsorbed on Pt(111) surface. *Phys. Rev. Lett.*, 101:146101, 2008.

[108] L. Qi, J. Yu, and J. Li. Coverage dependence and hydroperoxyl-mediated pathway of catalytic water formation on Pt (111) surface. *J. Chem. Phys.*, 125:054701–054708, 2006.

[109] H. Raebiger, S. Lany, and A. Zunger. Charge self-regulation upon changing the oxidation state of transition metals in insulators. *Nature*, 453:763–766, 2008.

[110] D. A. J. Rand and R. Woods. Study of dissolution of platinum, palladium, rhodium and gold electrodes in 1 M sulfuric-acid by cyclic voltammetry. *J. Electroanal. Chem.*, 35:209, 1972.

[111] J. Rossmeisl, J. K. Nørskov, C. D. Taylor, M. J. Janik, and M. Neurock. Calculated phase diagrams for the electrochemical oxidation and reduction of water over Pt(111). *J. Phys. Chem. B*, 110:21833–21839, 2006.

[112] P. Sabatier. *La catalyse en chimie organique*. Bérange, Paris, 1920.

[113] E. Santos, M. T. M. Koper, and W. Schmickler. A model for bond-breaking electron transfer at metal electrodes. *Chem. Phys. Lett.*, 419:421–425, 2006.

[114] W. Schmickler. Electronic effects in the electric double layer. *Chem. Rev.*, 96:3177–3200, 1996.

[115] W. Schmickler. *Interfacial Electrochemistry*. Oxford University Express, 1996.

[116] D. B. Sepa, M. V. Vojnovic, L. M. Vracar, and A. Damjanovic. Different views regarding the kinetics and mechanisms of oxygen reduction at pt and pd electrodes. *Electrochim. Acta*, 32:129–134, 1987.

[117] N. Seriani, Z. Jin, W. Pompe, and L. Colombi Ciacchi. Density functional theory study of platinum oxides: From infinite crystals to nanoscopic particles. *Phys. Rev. B*, 76(15):155421, OCT 2007.

[118] M. H. Shao, P. Liu, and R. R. Adzic. Superoxide anion is the intermediate in the oxygen reduction reaction on platinum electrodes. *J. Am. Chem. Soc.*, 128:7408–7409, 2006.

[119] Y. Y. Shao, G. P. Yin, and Y. Z. Gao. Understanding and approaches for the durability issues of Pt-based catalysts for PEM fuel cell. *J. Power Sources*, 171:558–566, 2007.

[120] R. A. Sidik and A. B. Anderson. Density functional theory study of O_2 electroreduction when bonded to a Pt dual site. *J. Electroanal. Chem.*, 528:69–76, 2002.

[121] B. Smit and D. Frenkel. *Understanding Molecular Simulation (Computational Science Series, Vol 1).* Academic Press, 2nd edition, 2001.

[122] G. A. Somorjai. *Chemistry in two dimensions : surfaces.* Cornell University Press, 1981.

[123] V. Stamenkovic, B. S. Mun, K. J. J. Mayrhofer, P. N. Ross, N. M. Markovic, J. Rossmeisl, J. Greeley, and J. K. Nørskov. Changing the activity of electrocatalysts for oxygen reduction by tuning the surface electronic structure. *Angew. Chem. Int. Ed.*, 45:2897–2901, 2006.

[124] V. Stamenkovic, T. J. Schmidt, P. N. Ross, and N. M. Markovic. Surface composition effects in electrocatalysis: Kinetics of oxygen reduction on well-defined Pt_3Ni and Pt_3Co alloy surfaces. *J. Phys. Chem. B*, 106:11970–11979, 2002.

[125] V. R. Stamenkovic, B. Fowler, B. S. Mun, G. Wang, P. N. Ross, C. A. Lucas, and N. M. Markovic. Improved oxygen reduction activity on $Pt_3Ni(111)$ via increased surface site availability. *Science*, 315:493–497, 2007.

[126] V. R. Stamenkovic, B. S. Mun, M. Arenz, K. J. J. Mayrhofer, C. A. Lucas, G. Wang, P. N. Ross, and N. M. Markovic. Trends in electrocatalysis on extended and nanoscale Pt-bimetallic alloy surfaces. *Nature Materials*, 6:241–247, 2007.

[127] A. E. Stearn and J. Eyring. The deduction of reaction mechanisms from the theory of absolute rates. *J. Chem. Phys.*, 5:113–124, 1937.

[128] Carsten Stegelmann, Anders Andreasen, and Charles T. Campbell. Degree of Rate Control: How Much the Energies of Intermediates and Transition States Control Rates. *J. Am. Chem. Soc.*, 131:8077–8082, JUN 17 2009.

[129] H. Steininger, S. Lehwald, and H. Ibach. Adsorption of oxygen on Pt(111). *Surf. Sci.*, 123:1–17, 1982.

[130] B. C. Stipe, M. A. Rezaei, W. Ho, S. Gao, M. Persson, and B. I. Lundqvist. Single-molecule dissociation by tunneling electrons. *Phys. Rev. Lett.*, 78:4410–4413, 1997.

[131] C. D. Taylor, S. A. Wasileski, J. S. Filhol, and M. Neurock. First principles reaction modeling of the electrochemical interface: Consideration and calculation of a tunable surface potential from atomic and electronic structure. *Phy. Rew. B*, 73:165402, 2006.

[132] N. Tian, Z. Y. Zhou, S. G. Sun, Y. Ding, and Z. L. Wang. Synthesis of tetrahexahedral platinum nanocrystals with high-index facets and high electro-oxidation activity. *Science*, 316:732–735, 2007.

[133] M. D. Tissandier, K. A. Cowen, W. Y. Feng, E. Gundlach, M. H. Cohen, A. D. Earhart, J. V. Coe, and T. R. Tuttle. The proton's absolute aqueous enthalpy and Gibbs free energy of solvation from cluster-ion solvation data. *J. Phys. Chem. A*, 102:7787–7794, 1998.

[134] T. Toda, H. Igarashi, H. Uchida, and M. Watanabe. Enhancement of the electroreduction of oxygen on Pt alloys with Fe, Ni and Co. *J. Electrochem. Soc.*, 146(10):3750–3756, 1999.

[135] S. Trasatti. The absolute electrode potential - an explanatory note (recommendations 1986). *Pure and applied chemistry*, 58:955–966, 1986.

[136] S. Trasatti. Structure of the Metal Electrolyte Solution Interface - New Data for Theory. *Electrochimica. Acta.*, 36(11-12):1657–1658, 1991.

[137] M. E. Tuckerman, D. Marx, M. L. Klein, and M. Parrinello. Efficient and general algorithms for path integral Car-Parrinello molecular dynamics. *J. Chem. Phys.*, 104: 5579–5588, 1996.

[138] M. Valden, X. Lai, and D. W. Goodman. Onset of catalytic activity of gold clusters on titania with the appearance of nonmetallic properties. *Science*, 281:1647–1650, 1998.

[139] G. Valette and A. Hamelin. Structure and properties of electrochemical double film on interphase of aqueous sodium-fluoride solutions and silver. *J. Elelctroanal. Chem.*, 45(2):301–319, 1973.

[140] D. Vanderbilt. Soft self-consistent pseudopotentials in a generalized eigenvalue formalism. *Phys. Rev. B*, 41:7892–7895, 1990.

[141] L. K. Verheij, M. Freitag, M. B. Hugenschmidt, I. Kempf, B. Poelsema, and G. Comsa. Autocatalytic behavior and role of oxygen diffusion in the hydrogen oxygen reaction on Pt(111). *Surf. Sci.*, 272:276–282, 1992.

[142] L. K. Verheij and M. B. Hugenschmidt. On the mechanism of the hydrogen-oxygen reaction on Pt(111). *Surf. Sci.*, 416:37–58, 1998.

[143] S. Völkening, K. Bedürftig, K. Jacobi, J. Wintterlin, and G. Ertl. Dual-path mechanism for catalytic oxidation of hydrogen on platinum surfaces. *Phys. Rev. Lett.*, 83:2672–2675, 1999.

[144] S. H. Vosko, L. Wilk, and M. Nusair. Accurate spin-dependent electron liquid correlation energies for local spin density calculations: a critical analysis. *Can. J. Phys.*, 58:1200, 1980.

[145] Z. Šljivančanin and B. Hammer. Oxygen dissociation at close-packed Pt terraces, Pt steps, and Ag-covered Pt steps studied with density functional theory. *Surf. Sci.*, 515:235–244, 2002.

[146] M. Wakisaka, H. Suzuki, S. Mitsui, H. Uchida, and M. Watanabe. Increased oxygen coverage at Pt-Fe alloy cathode for the enhanced oxygen reduction reaction studied by EC-XPS. *J. Phys. Chem. C*, 112:2750–2755, 2008.

[147] Y. X. Wang and P. B. Balbuena. Roles of proton and electric field in the electroreduction of O_2 on Pt(111) surfaces: Results of an *ab-initio* molecular dynamics study. *J. Phys. Chem. B*, 108:4376–4384, 2004.

[148] Y. X. Wang and P. B. Balbuena. Ab initio molecular dynamics simulations of the oxygen reduction reaction on a Pt(111) surface in the presence of hydrated hydronium $H_3O^+(H_2O)_2$: Direct or series pathway? *J. Phys. Chem. B*, 109:14896–14907, 2005.

[149] G. Wannier. Die Beweglichkeit des Wasserstoff- und Hydroxylions in wäβriger Lösung. *Ann. Phys. (Leipz.)*, 24:545–590, 1935.

[150] A. Warshel and W. W. Parson. Computer-simulations of electron-transfer reactions in solution and in photosynthetic reaction centers. *Annu. Rev. Phys. Chem.*, 42:279–309, 1991.

[151] G. W. Watson, R. P. K. Wells, D. J. Willock, and G. J. Hutchings. A comparison of the adsorption and diffusion of hydrogen on the 111 surfaces of Ni, Pd, and Pt from density functional theory calculations. *J. Phys. Chem. B*, 105:4889–4894, 2001.

[152] M. Weaver. Potentials of zero charge for platinum(111)-aqueous interfaces: A combined assessment from in-situ and ultrahigh-vacuum measurements. *Langmuir*, 14:3932–3936, 1998.

[153] Q. Xu, E. Kreidler, D. O. Wipf, and T. He. In situ electrochemical stm study of the coarsening of platinum islands at double-layer potentials. *J. Electrochem. Soc.*, 155:B228–B231, 2008.

[154] J. Zhang, K. Sasaki, E. Sutter, and R. R. Adzic. Stabilization of platinum oxygen-reduction electrocatalysts using gold clusters. *Science*, 315:220–222, 2007.

[155] T. Zhu, J. Li, and S. Yip. Atomistic study of dislocation loop emission from a crack tip. *Phys. Rev. Lett.*, 93:025503, 2004.

[156] G. Zundel and H. Metzger. Energiebänder der tunnelnden Überschu$_\beta$-Protenon in flüssigen Süuren. Eine IR-spektroskopische Untersuchung der Natur der Gruppierungen $H_5O_2^+$. *Z. Physik. Chem. (N.F.)*, 58:225–245, 1968.